DENSITY MEASUREMENT OF MULTIPHASE PIPE FLOWS

OGHENEOCHUKO OBIE
B.Eng., MSc

A thesis submitted to the University of Huddersfield

in partial fulfilment of the requirements for

the degree of Doctor of Philosophy

The University of Huddersfield
September 2017

Copyright statement

Abstract

Density is an important physical property and its measurement has wide application in a vast number of industries including; oil and gas, petrochemical, pharmaceutical, brewing, food & beverage production and mining. Density is often required to be accurately measured either as a standalone property or in combination with other flow properties for the purpose of quality assessment, process control, and custody transfer. Given the increasing importance of density measurement, extensive research has been conducted over recent years to develop newer and more accurate density measurement sensors and to improve the accuracy of existing sensors.

This thesis describes the design and development of a novel, non-invasive, non-radioactive Vibrating Density Measurement System (VDMS) capable of measuring fluid density in both single phase and multiphase flows. The device is also capable of measuring mean in-situ phase volume fractions in two-phase flows. The VDMS comprises three sub-units; (i) a measurement unit which includes a straight length of sensing pipe with corrugated bellows at both ends, an actuator and relevant sensors; (ii) a signal conditioning and processing unit; and (iii) a data acquisition unit.

The thesis also reports the development of a novel mathematical density prediction model which is used in conjunction with the VDMS. It then goes on to report the results of static bench test experiments that were conducted on the VDMS using a bespoke test rig. These tests were performed (i) to obtain the mass of the sensing pipe, its stiffness constant and damping constant; (ii) to investigate the frequency response characteristics of the VDMS; (iii) to obtain the VDMS constant; (iv) to investigate the sensing pipe displacement pattern; (v) to investigate the capability of the VDMS to give accurate density measurements of static fluids and (vi) to define the optimal VDMS operating conditions. Computation of density was achieved using the VDMS, the density prediction model and a novel signal processing technique. This signal processing technique used the Discrete Fourier Transforms (DFTs) of the measured force, used to mechanically excite the sensing pipe at its centre, and the measured displacement at the sensing pipe centre.

Next, the thesis reports a novel computer based control system that was developed to ensure that the VDMS automatically operated at its optimal operating conditions, so that errors in the density measurement were minimised. The control system was also capable of providing online computation of the flow mixture density.

Results are reported of several experiments conducted by the author on the VDMS to measure the fluid density in a range of "water only" flows, "solids-in-water" flows and "air-in-water" flows. These flows were all vertically upward and were established in the working section of a multiphase flow loop. These multiphase flow experiments were subsequently extended to compute the mean in-situ phase volume fraction of the solids phase in "solids-water" flows and the gas phase in "air-water" flows. For the "water only" and "solids-water" flow experiments, the mean error in the predicted density was consistently within $\pm 0.5\%$ of the reference density and the standard deviation of the error was less than 1%. For "air-in-water" flows the predicted density was within 1% of the reference density for flows where the air volume fraction in the mixture was less than 10%.

The mean in-situ volume fractions, measured by the VDMS, of the dispersed solids in "solids-in-water" flows and of the dispersed air in "air-in-water" flows were within 10% of the reference measurements for the vast majority of measurements taken.

Finally, the thesis describes a modified mathematical model, used with the VDMS, for predicting mixture density in "air-in-water" flows. This modified model is extended to make use of the predicted coupling stiffness between the VDMS sensing pipe and the multiphase mixture. The modified model gave density measurements with a higher order of accuracy than the earlier model which did not consider the effect of the flow compressibility on the coupling between the sensing pipe and the pipe contents.

Table of Contents

List of Figures

List of Tables

Acknowledgements

Firstly, my unreserved thanks and praises are given to God Almighty for the grace to start and successfully complete this research.

I would also like to express my sincere and heartfelt gratitude to the following persons;

- My supervisor, Prof. Gary Lucas, for the continuous support of my PhD research, for his motivation and vast knowledge and experience shared. His guidance was instrumental throughout this research and also writing up of this thesis. I could never have asked for a better supervisor and mentor for my PhD.

- My friends and research colleagues in the Systems and Engineering Research Group SERG Dr Yousif Muhamedsaleh, Dr Michael Agolom, Mr Raymond Webilor and Mr Ayodele Onilude who have been very supportive throughout this research work.

- Mr Richard Midlans for the countless support offered during the period of developing the electronic circuits used in this research and not forgetting to mention borrowing me several measurement equipment for the duration of the research. Mr Robert Harding, Mr Steven Goldstein and Mr Philips Holdworth for their unflinching help in the manufacture of the varied mechanical parts used in the research.

- The University of Huddersfield for the award of a fee waiver scholarship to carry out this research.

- Lastly, but by no means least, I would like to thank my family for the immeasurable support, love and prayers always. I am extremely thankful to my wonderful and darling wife, Sylvia, for her continuous support, advice and patience through the period of this research. In a million years I will still struggle to come up with the right words to duly appreciate you for "everything" you have done and particularly for taking of care of our son, Seifried, while I was preoccupied with a pipe, some plastic balls and water over 3000miles away from home.

List of abbreviations

CMM	coordinate measurement machine
DAQ	data acquisition
DFT	digital Fourier Transform
DP	differential pressure
ED	excitation signal duty cycle
EVP	electromagnetic velocity profiler
FCC	fluid catalytic cracker
FC	flow condition
FFT	fast Fourier Transform
HDPE	high density polyethylene
ICC	impedance cross correlation
LDPE	low density polyethylene
LVDT	linear variable differential transformer
MDPE	medium density polyethylene
NI	national instrument
PID	proportional integral and derivative
TM	Test mixture
VCA	voice coil actuators
VDMS	vibrating density measurement system

List of symbols

Δ	Deflection at the pipe centre
ΔP	Differential pressure
Δt	Time interval
Δt_s	Time intervals taken to acquire a predetermined mass of solids
Δt_w	Time intervals taken to acquire a predetermined mass of water
ρ	Density
ρ_{i}	Density of the ith phase
ρ_f	Fluid density
ρ_o	Oil density
ρ_p	Pipe density
ρ_{mix}	Mixture density
ρ_{ref}	Reference density
$\rho_{w,ref}$	Reference water density
$\rho_{tm,m,j,i}$	Measured/predicted density of test mixture
$\rho_{tm,ref,j}$	Reference density of test mixture
$\rho_{aw,m,n,i}$	Measured/predicted air-water mixture density
$\rho_{aw,ref,n,i}$	Reference air-water mixture density
$\rho_{sw,ref,n,i}$	Reference solids-water mixture density
$\rho_{w,m,n,i}$	Measured/predicted water density
$\bar{\rho}_{aw,m,n}$	Mean of measured/predicted air-water mixture density
$\bar{\rho}_{aw,ref,n}$	Mean of reference air-water mixture density
$\bar{\rho}_{sw,m,n}$	Mean of measured/predicted solids-water mixture density

$\bar{\rho}_{sw,ref,n}$	Mean of reference solids-water mixture density
Θ	Measured phase difference
$\bar{\theta}$	Mean of measured phase difference
$\theta(\omega_k)$	Phase difference at ω_k
$\theta_F(\omega_k)$	Phase of force phasor at ω_k
$\theta_F(s)$	Laplace transform of the phase of the force signal
$\theta_x(\omega_k)$	Phase of displacement phasor at ω_k
$\theta_x(s)$	Laplace transform of the phase of the displacement signal
α_i	Phase volume fraction
α_g	Gas volume fraction
α_o	Oil volume fraction
α_a	Air volume fraction
$\alpha_{g,ref}$	Reference gas volume fraction
$\alpha_{a,m,n,i}$	Measured/predicted air volume fraction
$\alpha_{a,ref,n,i}$	Reference air volume fraction
$\alpha_{s,m,n,i}$	Measured/predicted solids volume fraction
$\alpha_{s,ref,n,i}$	Reference solids volume fraction
$\bar{\alpha}_{a,m,n}$	Mean of measured/predicted air volume fraction
$\bar{\alpha}_{a,ref,n}$	Mean of reference air volume fraction
$\bar{\alpha}_{s,m,n}$	Mean of measured/predicted solids volume fraction
$\bar{\alpha}_{s,ref,n}$	Mean of reference solids volume fraction
β	VDMS constant
β_{mod}	Modified VDMS constant

β_{opt}	Optimal VDMS constant
ζ	Damping ratio
λ_{opt}	Optimal lambda value
ω	excitation frequency
Ω	Angular velocity
ω_k	VDMS operating frequency
ω_n	Fundamental frequency
μ_m	Mass attenuation coefficient
τ_{vca}	VCA rise time
$\bar{\Gamma}$	Density measurement parameter
$\chi_{sw,ref,n}$	Ratio of mean reference solids-water mixture density
$\chi_{sw,m,n}$	Ratio of mean predicted solids-water mixture density to mean reference solids-water mixture density
γ	Ratio of specific heats for air
$\bar{\hat{a}}$	Mean of $\hat{a}$
$\hat{a}_{meas}(t)$	Controlled variable
$\hat{a}_{opt}$	Optimal $\hat{a}$ value
$\hat{a}_{sp}(t)$	Process set point
$\hat{a}$	Density measurement parameter
A	Cross sectional area
$\hat{b}$	Density measurement parameter
b_x	VDMS constant optimization factor
B	Magnetic flux density
c	Sound wave velocity

C_p	Specific heat of the gas at constant pressure
C_v	Specific heat of the gas at constant volume
$C_1, C_2, C_3\ C_4$	Constants of integration
D	Flow pipe diameter
dF	Change in applied force
dP	Change in pressure
dV	Change in volume
dx	Change in displacement
$e_{tm,j}$	Error in the measured density of a test mixture
$\bar{e}_{tm}$	Mean error in the measured density of test mixture
$\bar{e}_{tm,t}$	Overall mean error in the measured densities of test mixtures
$e_{a,n,i}$	Error in the measured air volume fraction
$e_{s,n,i}$	Error in the measured solids volume fraction
$e_{w,n,i}$	Error in the measured water density
$e_{aw,n,i}$	Error in the measured air-water mixture density
$e_{sw,n,i}$	Error in the measured solids-water mixture density
$\bar{e}_{w,n}$	Mean error in the measured water density
$\bar{e}_{aw,n}$	Mean error in the measured air-water mixture density
$\bar{e}_{sw,n}$	Mean error in the measured solids-water mixture density
$\bar{e}_{w,t}$	Overall mean error in the measured water density
$\bar{e}_{aw,t}$	Overall mean error in the measured air-water mixture density
$\bar{e}_{sw,t}$	Overall mean error in the measured solids-water mixture density
$e(t)$	PI controller error

E	Modulus of elasticity
E_{out}	Differential voltage
$\hat{f}$	Modified damping constant
f_s	Sampling frequency
f_t	Turbine meter frequency output
f	Damping constant
f_2	True damping constant associated with the coupling between the pipe and the pipe contents
f_b	Buoyant force
$\hat{f}_2$	Modified damping constant of pipe contents
f	Frequency
$\hat{f}_1$	Sensing pipe modified damping constant
f_1	Sensing pipe true damping constant
F	Force generated
$F(t)$	External forcing excitation
$\|F\|$	Force magnitude
$F_d\ (t)$	Force due to damping element
F_m	Frictional pressure loss
$F_m(t)$	Force due to inertial element
$F_s(t)$	Force due to spring element
$\|F_{max}\|_{\omega_k}$	Peak force at ω_k
F, $\mathbf{F}_k$	Force phasor
$\sum F_x(t)$	Resultant force in x- direction

G	Acceleration of gravity
$\mathrm{G_{s-pipe}}(s)$	Sensing pipe transfer function
$\mathrm{G_{vca}}(s)$	VCA transfer function
$G_{ol}(s)$	Open loop transfer function
H	Axial length
I	Moment of inertia
I	Current
$\mathrm{Im\{X_k\}}$	Imaginary component of the DFT of x(n)
I_0	Intensity of emitted radiation particles
I_d	Intensity of transmitted radiation particles
I_{exc}	Excitation current
K	Stiffness constant
K_1	Sensing pipe stiffness constant
K_2	Stiffness constant of sensing pipe contents
K_2^*	Stiffness constant of a single gas bubble in the air-in-water flow
K_{bias}	Controller bias
$K_c(t)$	Controller algorithm
K_p	Proportional gain
K_t	Turbine flow meter constant
k_{vca}	VCA force constant
L	Beam length
L	Effective length of the moving coil in magnetic field
L	Axial length
L_{vca}	VCA coil winding inductance

L_w	Displacer working length
m	Mass
$\widehat{M}$	Modified mass
M	Mass
m_1	Sensing pipe true mass
m_2	True mass of sensing pipe contents
$M_{s_{(L)}}$	Lower mass limit of solids in the solids hopper
$M_{s_{(U)}}$	Upper mass limit of solids in the solids hopper
$M_{w_{(L)}}$	Lower mass limit of water in water hopper
$M_{w_{(U)}}$	Upper mass limit of water in the water hopper
M_{50mL}	Mass of water added to the standard 50mL conical flask
$\overline{Mr}$	Mean of magnitude ratio
M_s	True mass of the sinker
M_s	Mass of water added to solids hopper
M_w	Mass of water added to water hopper
$\dot{M}_i$	Measured mass flow rate of i^{th} phase
M^*_s	Apparent mass of the sinker
$\widehat{m}_1$	Sensing pipe modified mass
$\widehat{m}_2$	Modified mass of sensing pipe contents
$\dot{m}_t$	Total mass flow rate
Mr	Magnitude ratio
n	ADC resolution
N	Number of samples

N	Number of turns of the coil windings
P	Primary coil
P,p	Pressure
P	Gas pressure
P_1	Static pressure at the upstream of flow loop working section
P_2	Static pressure at the downstream of flow loop working section
q	Distributed weighted
Q_g	Air volumetric flow rate
$Q_{s,ref}$	Reference solids volumetric flow rate
$Q_{w,ref}$	Reference water volumetric flow rate
$Q_{a,ref}$	Reference air volumetric flow rate
Q_w	Water volumetric water flow rate
R	Reflection coefficient
R_1	Inner radius
R_2	Outer radius
R_{C1},R_{C2}	Resistances of the strain gauges in compression
R_{T1},R_{T2}	Resistances of the strain gauges in tension
R_s	Precision resistor
R_t	Total resistance
R_{vca}	VCA coil winding resistance
$\mathrm{Re}\{X_k\}$	Real component of the DFT of x(n)
S_1 , S_2	Secondary coils
$S_{g(m)}$	Specific gravity of milk
S_g	Specific gravity

S_{tm}	Standard deviation of errors in the measured densities of a test mixture
$S_{tm,t}$	Overall standard deviation of errors in the measured densities of a test mixture
$S_{a,n}$	Standard deviation of errors in the measured air volume fractions
$S_{s,n}$	Standard deviation of errors in the measured solids volume fractions
$S_{a,t}$	Overall standard deviation of errors in the measured air volume fractions
$S_{s,t}$	Overall standard deviation of errors in the measured solids volume fractions
$S_{aw,n}$	Standard deviation of errors in the measured air-water mixture densities
$S_{sw,n}$	Standard deviation of errors in the measured solids-water mixture density
$S_{w,t}$	Overall standard deviation of errors in the measured water densities
$S_{aw,t}$	Overall standard deviation of errors in measured air-water mixture densities
$S_{sw,t}$	Overall standard deviation of errors in measured solids-water mixture densities
t_r	Discrete time
t	Time
T	Temperature
T	Sampling period
T_i	Controller integral time
u_h	Mixture homogeneous velocity
u_g	Air velocity
u_{sp}	Slip velocity
u_w	Water velocity
V	Volume
V_s	Volume of the sinker
V_s	Voltage dropped across precision resistor

V_s	Output voltage from the load cell signal conditioning circuit connected to the solids hopper
V_w	Output voltage from the load cell signal conditioning connected to the water hopper
V^*	Volume of a single gas bubble
V_a	Volume occupied by air
V_{50mL}	Volume of standard conical flask
V_{dc}	Analogue output voltage
V_{exc}	Excitation voltage
V_{min}	Minimum voltage measured using NI USB 6211 DAQ card
V_{mix}	Mixture flow velocity
V_{pipe}	Volume of sensing pipe
W_s	True weight of sinker
$W^*{}_s$	Apparent weight of sinker
W	Total weight of the pipe and pipe contents
$\ddot{x}_1$(t)	Acceleration of sensing pipe
$\dot{x}_1$(t)	Velocity of sensing pipe
$\ddot{x}_2$(t)	Acceleration of sensing pipe contents
$\dot{x}_2$(t)	Velocity of the sensing pipe contents
$x_2(t)$	Displacement of sensing pipe contents
$x_1(t)$	Displacement of sensing pipe
X_k	Discrete Fourier Transform of X
$\ddot{x}(t)$	Acceleration
$\dot{x}(t)$	System velocity

x'	Path length of the scattered photons
x_r	rth term of the discrete signal
$\|X\|$	Magnitude of displacement
$\left\|X_{\max(\omega_k)}\right\|$	Peak displacement at ω_k
$\mathbf{X}, \mathbf{X}_\mathrm{k}$	Displacement phasor
$\boldsymbol{X_1}$	Sensing pipe displacement phasor
$\mathbf{X}_2$	Sensing pipe contents displacement phasor
$Y(x)$	Transverse displacement at a distance *x*
y	Transverse deflection
$y_1(t_1)$	Sensing pipe displacement at time t_1
$y_2(t_2)$	Sensing pipe displacement at time t_2
y_{mp}	Transverse deflection at the centre of the beam
z_1	Magnitude of the first overshoot
z_2	Magnitude of the first undershoot

Subscripts

1	Refers to sensing pipe
2	Refers to sensing pipe contents
F	Applied force
a	Air phase
aw	Air-water mixture
exc	Excitation signal
i	i^{th} density measurement
j	j^{th} frequency point
k	DFT index
m	Measured/predicted quantity
mix	mixture
mod	modified
n	Flow condition number
r	Discrete signal index
ref	Reference quantity
s	Solids phase
sw	Solids-water mixture
t	Total value
tm	Test mixture
w	Water phase

Chapter 1

1.1 Introduction

The primary objective of this thesis is to describe the research work that was carried out in order to design and develop a novel densitometry system based on the vibration characteristics of a mechanical system. The densitometry system developed makes use of a novel signal processing technique to non-invasively predict density in single phase and multiphase pipe flows. The measurement technique was also extended to measure the mean volume fraction in two-phase (solids-liquid and gas-liquid) pipe flows. A motivation factor for this research work was to develop a relatively accurate and low cost densitometry system without the need for a radioactive source. A densitometry system based on the mechanical vibration principle will be seen as a game changer in density measurement. This technique could be used to develop accurate density measurement instruments which do not require a radioactive source and hence do not require the bureaucracy that is involved with getting clearance for usage of radioactive densitometry systems. Even more importantly, they pose no health risk to personnel and the environment. The densitometry system developed in this research can also be combined with an impedance cross correlation (ICC) meter [1] and an electromagnetic velocity profiler (EVP) [2], two parallel research programmes going on at the University of Huddersfield, to develop a standalone multiphase flow meter.

Density measurements in single-phase flows are relatively well understood with numerous known measurement techniques (intrusive and non-intrusive) and commercial solutions available. Conversely, the mixture density in multiphase pipe flows cannot be simply computed by combining the density of the individual components of the flow, thus making it difficult to predict and measure. Given the challenge mentioned, there is increased need for both novel mathematical models and measurement techniques to accurately predict the mixture density in multiphase pipe flows. Over the last two decades, quite a number of measurement techniques, both intrusive and non-intrusive, have been developed and used to predict the mixture density in multiphase flows. However, these techniques have been besieged

by several notable drawbacks. For example, the use of differential pressure sensors are notable for inaccurate density measurements due to plugging/fouling of the pressure lines [3-5]; the use of radioactive densitometers poses great danger to the health of personnel and the environment and requires strict safety requirement for usage [6]; densitometry systems based on acoustic techniques are not well developed and are noted for high inaccuracy and tend to require extensive testing and calibration under the anticipated operating conditions [7, 8]. Density measurement of multiphase pipe flows nevertheless, has become increasingly important in the operation of many industrial processes. Its applications are evident across a wide range of industries, namely; oil and gas, chemical/petrochemical, pharmaceutical, pulp and paper, food processing, mining industry and these will be discussed in section 1.4. Given the diverse application areas of density measurement, the need for density measurement in multiphase flows and the types of two phase flow patterns relevant to this research work will be presented in section 1.2 and section 1.3 respectively.

1.2 Need for density measurement in multiphase flows

The term multiphase flow has generally been used to describe any flow containing two or more phases, where phases here are used to indicate the individual components of the flow. This type of flow is very common in nature and our environment, examples include; the flow of blood in the human body, snow, fog, mudslides and steam condensation on windows. The phases in a multiphase pipe flow comprise of any combination of solids, liquids and gases, and the properties of the flow are greatly dependent on the nature of the individual phases, their distribution and the interaction between the different phases [9]. For example, in a marginal oil field, two phase oil-water flow is commonly encountered, with the flow rate of water known to increase with time. If the flow is assumed to be homogeneous, then the total mass flow rate $\dot{m}_t$ of the oil-in-water mixture can be obtained from,

$$\dot{m}_t = AV_{mix}\rho_{mix} \qquad \text{Equation 1-1}$$

where A is the cross sectional area of the flow pipe, ρ_{mix} is the homogenous mixture density of the flow and V_{mix} is the homogenous mixture flow velocity. From equation 1-1, it is clear that in addition

to knowing the flow velocity V_{mix} of the homogenous mixture and the flow pipe cross sectional area A, knowledge of the homogeneous density ρ_{mix} of the oil-in-water mixture is also required to be able to compute its total mass flow rate $\dot{m}_t$. Equation 1-1 can also be extended to compute the mass flow rate $\dot{m}_i$ of the ith phase in a homogeneous oil-in-water pipe flow using the expression,

$$\dot{m}_i = AV_{mix}\rho_i\alpha_i \qquad \text{Equation 1-2}$$

where the subscript *i* can be either "o" for oil or "w" for water, ρ_i is the density of the ith phase and α_i is the mean volume fraction of the ith phase. If the individual densities of the oil and water are known a-priori, then both α_w and α_o can be obtained from ρ_{mix} (see equation 1-3 and equation 1-4) allowing m_w and m_o to be measured. In applications where mass flow rate measurements are required, e.g. custody transfer and material balance estimation, it is important that the mixture density ρ_{mix} can be accurately measured without any attendant health and environmental risk. This has greatly increased the industrial need for accurate instrumentation to predict the mixture density in multiphase flow. In addition, most industries are embracing a cost optimization process, which involves using less expensive and more accurate instrumentation for process measurement. For example, the recent fall in crude oil prices has seen the oil industry give more attention to developing cheaper and more accurate instrumentation to reduce the per barrel cost of producing crude oil.

Mixture density measurement can also be used to determine phase volume fraction in two-phase pipe flow. For example, the mean volume fraction of the oil phase in two-phase oil-in-water pipe flow can be obtained from

$$\alpha_o = \frac{\rho_w - \rho_{mix}}{\rho_w - \rho_o} \qquad \text{Equation 1-3}$$

where ρ_{mix} is mixture density of the oil and water flow, α_o and ρ_o are the mean volume fraction and density of the oil phase respectively and α_w and ρ_w are the mean volume fraction and density of the water phase respectively. The oil volume fraction α_o and water volume fraction α_w are related by the expression

$\alpha_o + \alpha_w = 1$. Equation 1-4

From equation 1-3 and equation 1-4, it is clearly seen that to determine the mean volume fraction of the oil phase α_o or water phase α_w in the mixture, the respective phase densities of oil ρ_o and water ρ_w and the mixture density ρ_{mix} are required. Since the phase densities of oil and water can be obtained from standard charts, measurement of the mixture density ρ_{mix} is crucial to estimate the mean volume fraction of oil or water in the flow. Once the mean volume fraction of the measured phase is obtained from equation 1-3, it can then be applied to equation 1-4 to obtain the mean volume fraction of the other phase. Recently, gamma ray based densitometers have been used to provide mixture density measurement in a multiphase flow meter [10-12] for estimating the mean volume fraction of the phases in the mixture.

1.3 Multiphase flow patterns in vertical pipes

Multiphase flow can uniquely be described by the respective distributions of the different phases in the flow. This description, based on the distribution of the different phases of the flow, is referred to as its flow pattern and it can be influenced by a number of factors namely; fluid properties, flow pipe inclination, flow rates and pipe geometry [13]. Two-phase flows are very predominant in many industries and can include; gas-liquid flows, gas-solids flows, liquid-solids flows and liquid-liquid flows. Here, the discussion on two-phase flow patterns in vertical pipes will be limited to gas-liquid flows and solids-liquid flows, which are obtainable from the flow loop at the University of Huddersfield [14].

1.3.1 Gas-in-liquid flow patterns

Two-phase gas-liquid flow can often be described as a flow of a liquid continuum carrying dispersed gases. Hewitt and Hall-Taylor [15] have classified the flow patterns in two-phase gas-liquid flows in vertical pipes into four categories namely; bubbly flow, slug flow, churn flow and annular flow. However, in separate work by Spedding et al [16] and Bratland [17], the gas-liquid flow patterns were extended into five categories. The fifth flow pattern, called the wispy annular flow pattern, was included

in the flow pattern categories. These flow patterns form recognisable geometries as shown in figure 1-1.

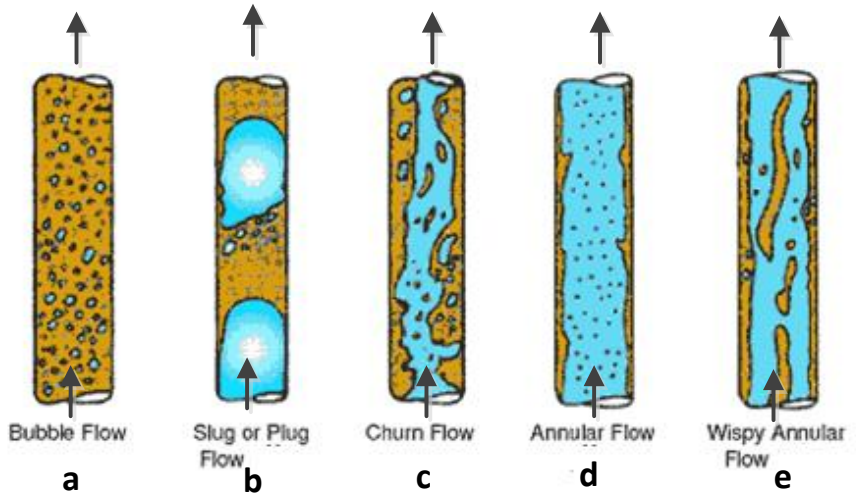

Figure 1-1: Two-phase flow patterns in gas-liquid vertically upward flow [18]

Bubbly flow

This type of flow is characterised with dispersed gas bubbles approximately uniformly distributed within a liquid continuum. The motion of the bubbles within the flow is often complex, maybe coalescing, and the bubbles generally have non-uniform size. This flow pattern occurs at relatively low gas flow rates and is shown in figure 1-1 (a).

Slug flow

Slug flow is mainly caused by the interaction of gas bubbles within the liquid continuum, which coalesce to form larger bullet-shaped bubbles (referred to as Taylor bubbles) that occupy almost the entire cross sectional area of the flow pipe, as is illustrated in the diagram shown in figure 1-1(b). These Taylor bubbles are often separated by a dispersion of smaller bubbles in the liquid and occur intermittently within the flow. Taylor bubbles are known to cause large pressure and liquid flow rate fluctuations and slug flow generally occurs at relatively moderate gas flow rates.

Churn flow

As the gas flow rate increases in a slug flow, the Taylor bubbles are known to grow larger and eventually start to break up into a more random and unstable flow pattern referred to as a churn flow. The motion of the liquid at this stage is very complex and oscillatory. The churn flow pattern usually occurs as an intermediate flow pattern between slug flow and annular flow and appears chaotic and frothy. This flow pattern is shown in figure 1-1(c).

Annular flow

The annular flow pattern, shown in figure 1-1(d), is characterised by the liquid phase flowing on the wall of the flow pipe as a thin film and the less dense gas phase flows in the centre of the pipe. This flow pattern occurs when the gas phase has a high flow velocity relative to the liquid phase and usually some of the liquid phase is entrained as small droplets in the gas core.

Wispy annular flow

This flow pattern occurs when the liquid flow rate in an annular flow is increased further. The entrained liquid droplets in the gas core coalesce to form large concentrations of liquid droplets in the central gas core which are referred to as wisps. This flow pattern is shown in figure 1-1(e).

1.3.2 Solids-in-liquid flow patterns

Solids-in-liquid flow can be described as the flow of a liquid continuum carrying dispersed solid particles which are conveyed by the drag forces due to the liquid and the pressure gradient of the flow. Not much literature is available on solids-liquid flow patterns in vertical pipes, however, for such flow types the flow patterns generated can be influenced by a number of factors, namely; pipe diameter and orientation, the solid and liquid flow rates, properties of the solid phase (e.g. size, density and concentration), properties of the liquid phase (e.g. density, viscosity) and flow direction (i.e. upward or downward) [19]. In solids-in-liquid vertically upward flow, it is critical that the pressure gradient generated by the flow is sufficient to overcome gravity and maintain upward flow. Garic-Grulovic et al [20] have grouped the flow patterns observed in solid-in-liquid flows into two, namely; turbulent and

parallel flow patterns. The turbulent flow patterns were described to occur at relatively lower liquid and solids velocities, where the solids suspension flows chaotically relative to the pipe walls. Conversely, the parallel flow pattern was said to occur at very high liquid and solids velocities and the solids tend to move vertically along paths parallel to the pipe walls. Hu [21] showed in his work that the flow patterns generated in solids-in-liquid flows were influenced by the pressure gradient generated by the flow. He concluded that solid-in-liquid flows, with a large enough pressure gradient to overcome gravity, the dispersed solid phase migrates away from the flow pipe wall and a clear liquid layer appears next to the wall. Additionally, as the pressure gradient increases, the dispersed phase interacts more strongly and forms large clusters in the flow. The flow patterns described by Garic-Grulovic et al. (turbulent and parallel) in solids-in-liquid vertically upward flow are shown in figure 1-2.

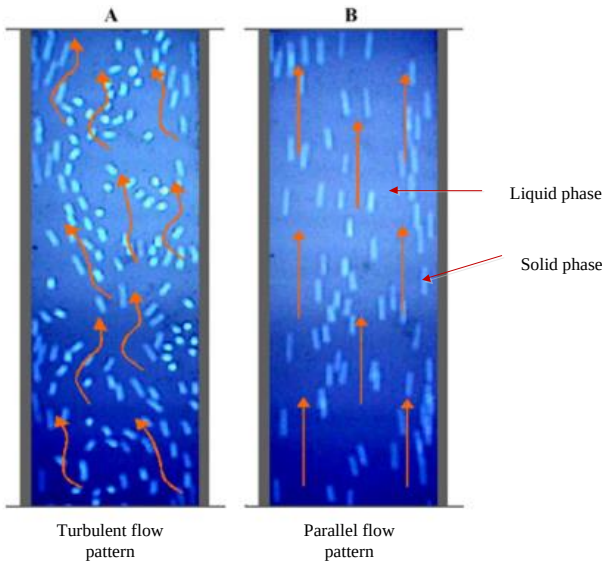

Figure 1-2: Flow patterns in solid-in-liquid vertically upward flow [20]

1.4 Applications of density measurement

Density is an important physical property in flow measurement and it is used in several application areas to describe, monitor and control certain properties of a material/product or process. This section will review the need for density measurement in a selection of industrial processes. The main intention here is not to provide a comprehensive listing of applications where density measurement is needed,

but to show a range of application areas where the output from this research work and other density measurement techniques could be applied.

1.4.1 Application of density measurement in the oil and gas industry

The oil and gas industry is a diverse industry with two key sectors- 'upstream' and 'downstream' - involving the exploration, development, production, processing and distribution of an expansive variety of hydrocarbon fluids, gases, contaminants and produced water [22]. Water often co-exists with gaseous hydrocarbons and crude oil in geologic formations and as such, a mixture of water, gaseous hydrocarbons and liquid hydrocarbons are often contained in a producing oil and gas well. Each sector of the oil and gas industry has unique density measurement needs which has been a catalyst to this industry playing a key role in the advancement of research to improve and develop density measurement techniques.

1.4.1.1 Need for density measurement in oil and gas exploration

Oil and gas exploration includes every activity involved in the process of finding and identifying oil and gas reserves. In a typical geological formation, crude oil and natural gas are produced from an irreversible process by source rocks such as diatomite, dolomite and limestone [23, 24]. It is common knowledge that in a typical hydrocarbon reservoir, the hydrocarbon mixture is separated into different layers depending on the density of the constituent fluids. Gaseous hydrocarbon is located at the top of the reservoir because of its lower density, oil stays in between the gas and water and water, being the densest, stays beneath as shown in figure 1-3.

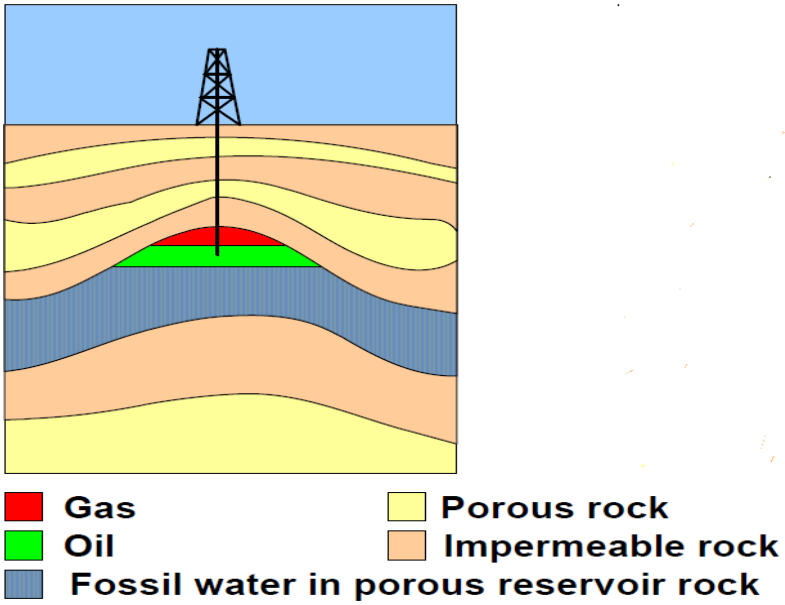

Figure 1-3: Picture of a reservoir formation [25]

Once a prospective oil reservoir has been identified, further analysis of the reservoir characteristics requires that an exploration well, often referred to as a wildcat well, is drilled into the formation. Geologists, geophysicists, and reservoir engineers will generally require a measure of the density of a sample of the hydrocarbon oil from the reservoir to determine its grade, hence its market value. Furthermore, information on the crude density is also useful when deciding on the type of drilling technology to deploy when drilling oil wells [24, 26]. Radioactive densitometry systems have commonly been applied down hole to measure hydrocarbon formation density [27, 28].

1.4.1.2 Need for density measurement in oil and gas reservoir development

The development of oil and gas reservoirs becomes an important requirement once a reservoir has been ascertained to contain economically viable quantities of oil and/or gas and it is safe to produce. This process usually involves drilling of appraisal and production wells. The relationship between reservoir fluid properties and hydrostatic gradient down hole in a reservoir plays a critical role in drilling an oil and gas well. Drilling operations involve using a drill bit attached to a drill pipe (parts of a drilling rig) to bore a hole through the earth formation. An important element of the drilling process is the drilling fluid (mud) which is continuously pumped down the drill pipe and circulated back to the surface during

drilling operation. Drilling fluid plays a very important role in the drilling process and is used for control of subsurface formation fluid pressure, drill bit lubrication, wellbore stability, fluid loss control, cooling and retrieval of drilled cuttings [25, 29, 30]. According to Bloys et al, drilling mud may represent 5% to 15% of the drilling cost, but may cause 100% of drilling problems if not properly managed [31]. Efficient management of drilling fluid becomes a major requirement when planning an optimal drilling program for a well. It is in this process that density measurement gets to play a significant role. For example, a drilling program would include a means to continuously monitor and control the density of the drilling mud (mud weight) to ensure its specification is always maintained. This is usually essential to mitigate the risk of critical drilling events occurring, to improve drilling performance and to optimize well control [29, 32]. When a well is being drilled, the density of the drilling mud is continually managed in a mud control system to ensure its specification (density and viscosity) is maintained and to ensure it always exerts a greater hydrostatic pressure than the down hole hydrostatic pressure of the reservoir, thus preventing the borehole from caving in and keeping formation fluids from entering the wellbore. It also prevents "blow outs" if a gas pocket is unexpectedly encountered. According to Azar and Robello [29], a major challenge associated with drilling fluid management is offline measurement of drilling fluid density. Inaccurate measurements can be caused by the presence of contaminants. Bloys et al [31] have described a drilling fluid management system with an online density measurement system at the mud feed line that provides real time information on the drilling fluid density before it is pumped into the well and at the return line from the well. The data provided by this system can be used to ensure safe and optimized drilling operation and can result in saving substantial amounts in the cost of drilling a well [30, 31]. An example of a mud control system using mechanical vibration densitometry to measure drilling fluid density as it is pumped into a well and at the return line from the well is shown in figure 1-4.

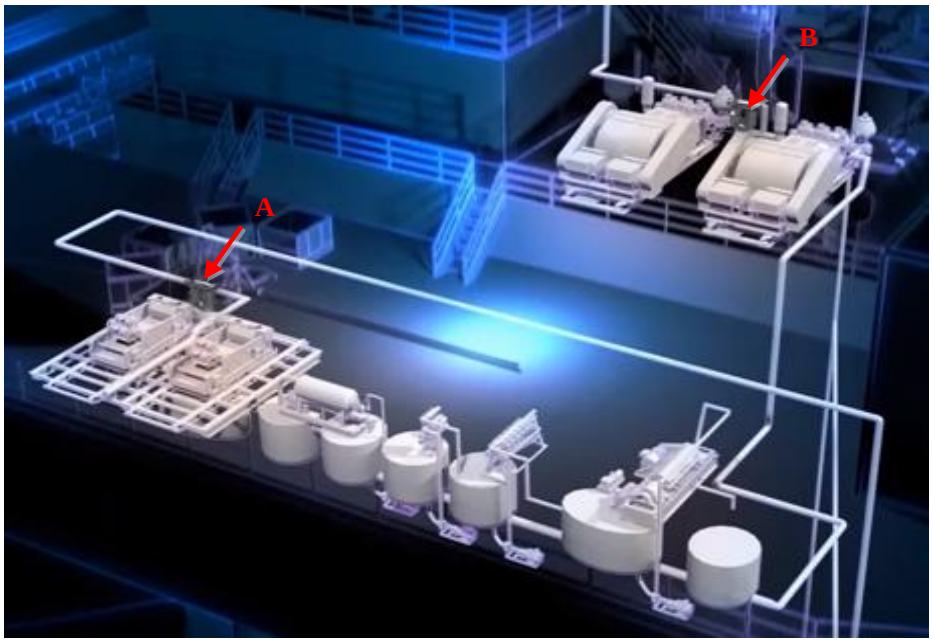

Figure 1-4: Picture of a drilling fluid management system comprising two densitometers A & B used to measure the density of drilling mud pumped into and out of a wellbore [33]

1.4.1.3 Need for density measurement in oil and gas production

Oil and gas production involves the processes of extracting the hydrocarbon mixture from a reservoir. In an oil and gas production platform, the hydrocarbon mixture extracted from the reservoir is usually separated into its constituent phases in a separator. A separator is a pressure vessel that uses the physical density properties of the constituent elements in a hydrocarbon mixture to separate the mixture into its individual (gas, oil and water) phases. When used as a well testing instrument, separators are known to be very expensive, occupy a vast area on the rig floor due to their large "footprint" and do not provide real time information on hydrocarbon properties because of the stabilization conditions required for their use [34]. However, densitometry systems can be used with auxiliary instrumentation for determining phase velocities and phase volume fractions, to provide real time, accurate mass and volumetric flow rate measurements of the individual phases of a hydrocarbon mixture from a reservoir without the need for a separator. Such techniques can provide information that is key to optimal field management and production optimization, mostly in marginal oil and gas fields [9, 34]. Note, however, that measurement of the density profile of a hydrocarbon stream in a separator can open a window to

the internal separation process and can help to visualize layers of sediments and crude oil emulsions with water, which aids optimization of the separation process [35].

1.4.2 Application of density measurement in the chemical/petrochemical industry

Density as a function of temperature and pressure is an important physical property used to classify and characterise fluids in the petrochemical industry. An example of a petrochemical process where density measurement gets to play a significant role is the production of polyethylene and its derivatives. Polyethylene is the most commonly used thermoplastic which has use in a wide range of applications. A thermal catalytic cracking process known as polymerization is used to produce polyethylene. During the polymerization process, accurate measurement and control of the density of polymer granules is necessary to sustain the fluidization in the reactor. A sharp increase/decrease in density can result in the polymer granules becoming too heavy/light and the loss of fluidization [36]. The ASTM D-3550 standard classifies polyethylene by density as high density polyethylene (HDPE), medium density polyethylene (MDPE) and low density polyethylene (LDPE) [37, 38]. Methods for measuring the density of a polymer melt have been described in [39, 40].

Figure 1-5: Picture of a radiometric density measurement device installed in a polymerization reactor [41]

The refining of hydrocarbon oil (crude) is a further example of an application in the petrochemical industry where density measurement is needed. The fluid catalytic cracker (FCC) unit, a workhouse of

an integrated refinery, plays a key role in the primary conversion process of crude oil to lighter hydrocarbons (gasoline and liquefied petroleum gas (LPG)) [42]. Given the high capital and operating cost (CAPEX and OPEX) required to set-up and operate a refinery, oil and gas refiners are continually seeking ways to optimize the refining process so as to maximize profit. Density measurement, in turn, plays a pivotal role in optimizing the operation of a fluid catalytic cracker during crude oil refining. When combined with the volumetric flow rate of the feedstock and catalyst to the FCC unit and its refined product, density measurement can be used to obtain accurate material mass flow rate measurement in the FCC unit. Since important decisions such as catalytic additions, feed throughput versus conversion, feed purchases, downstream processing and emission management are based on accurate material mass balance measurements, it is important that density is accurately measured in a FCC unit [42-44].

1.4.3 Application of density measurement in the pharmaceutical industry

Accurate and reliable instrumentation is an important cornerstone of pharmaceutical production, where high quality and traceability count above all else. Density measurements has come to play a significant role in ensuring high quality control in pharmaceutical production. It is also known to play a central role in pharmaceutical calculations, a key process in the pharmaceutical production process [45, 46]. Furthermore, density measurement has been used to provide insight into the condition of raw materials used in pharmaceutical production. This has made it possible to intervene to decide whether the final product is within the defined specifications for continuing the process and approving the product [47]. For example, during the production of compressed tablets (a complex mix of active drug, binders, disintegrants, flow acids, pigments and sweeteners) the bulk density of the powder formulation is actively measured and controlled to ensure consistency and correctness of the pharmaceutical products [45, 48, 49]. Variation in the bulk density of the formulation can lead to many production problems. Density measurement has also been deployed in tablet coating processes to monitor and control the real

thickness of the coating polymer to be deposited on the tablet surface [50, 51]. It has also been used to ensure precise density monitoring in liquid vitamin and syrup production [41].

1.4.4 Application of density measurement in the food and beverage processing industry

Ensuring consistently high quality and safety of products is an essential legal and business requirement for food and beverage manufacturers. Within this industry, density measurement can be used in several applications for quality control of a large number of products [52]. An example of an application where density measurement has found growing need is in beer production. Density measurement information is a critical parameter required to monitor the progress of the fermentation process of wort into beer. Olaniran et al [53] and Yokogawa [54] stated that a correlation exists between the density of wort (the liquid mixture that is used to produce beer) and a decrease in the extract (sugar) value during the fermentation process, hence the progress of a fermentation process can be monitored by measuring the density of the wort.

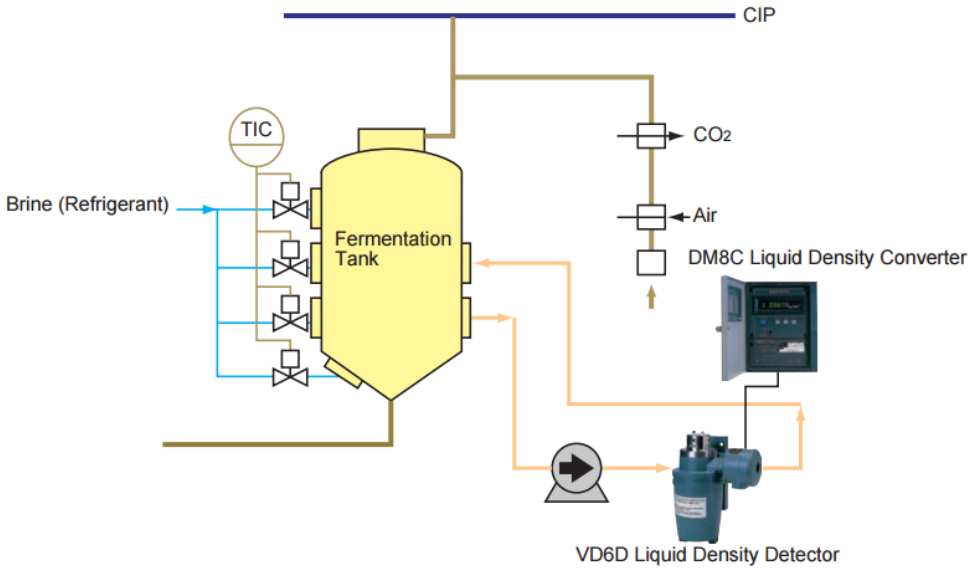

Figure 1-6: Picture of a fermentation process with density measurement device to monitor the degree of fermentation [54]

In figure 1-6, the fermentation process is controlled by a computer program that regulates the process temperature and pressure inside the tank based on measurement of changes to the density of the wort inside the tank.

Density measurement is also used as an officially acceptable method to determine the amount of alcohol (ethanol) present in beer for quality control, to ensure that product labels have the correct declaration of alcohol content and to establish an accurate basis for the payment of tax [55, 56]. Additionally, density measurement is frequently used in the determination of Brix value, a quantity used to express the sugar content in food, raw materials, ingredients, and beverages. An accurate estimation of the Brix value of a product is essential for cost and quality control in the food and beverage industry. For example the density of syrup, a concentrate used in soft drink production, is tightly monitored and controlled during soft drinks production to ensure that the finished product has the correct concentration of sweetener. Consequently, the density of the syrup used in the production of the soft drink must be in correct mixing proportion with water in order to maintain a consistent product quality [57, 58]. Density measurement can also be used to ensure quality control in milk production by monitoring the deviation in density of the milk composition due to the addition of water and skimming [59].

1.4.5 Application of density measurement in the pulp and paper industry

Paper making processes use pulp produced from wood chips to manufacture different grades of paper. Measurement of the wood chip density prior to cooking in a pressurized vessel called a digester, is essential to ensure that homogenous pulps are produced for the kraft process (the process of converting wood into wood pulp) [60]. Wood chip density is highly correlated with features that determine paper quality. Pecora et al. [61] reported that inconsistency in the wood chip density could result in either undercooked or overcooked pulp, which consequently degrades the quality of the pulp produced. Hence, if the wood chip density is not accurately measured it can result in economic losses in production. Also, the spent liquor (also referred to as black liquor) from the cooked pulp contains valuable chemicals and organic substances as well as oxidized sulphur known to be harmful to the environment. Energy efficient pulp and paper production requires that the black liquor is treated in a chemical plant and recycled to the digester. Density measurement is required to optimize the black liquor regeneration process [62, 63]. Density measurement can also be used to ascertain the

concentration of lime mud used in the wood chip cooking and the homogeneity of brines in wood chip bleaching processes [41].

1.4.6 Application of density measurement in the mining industry

Being able to determine the density of slurry is crucial in the mining industry for analysis of product flow and tailings. According to Australian Mineral Development Laboratories Ltd, (Amdel), over nine hundred and eighty density gauges are currently installed across mines in Australia [64]. Also, disposal of mine waste is an important subject of concern to environmentalists and mine operators. Inappropriate or unsafe disposal of mine waste from mining operations has continued to generate backlash from the public and to attract fines from government environmental protection agencies. Mine waste management is therefore an important subject in the mining industry. Density measurement can be used in combination with volumetric flow rate measurement to determine accurate mass flow rates during mine waste transportation. This information can also be used for selecting suitable pumps to transport the mine waste and to optimize energy consumption [65]. Furthermore, density measurement can be used to optimize water usage and to prevent pipe and pump blockage during mining operations. For example, large volume thickening tanks are used in mining to concentrate the solids (ore, minerals) contained in sludge, producing a stream of clarified water from the top of the tank overflow outlet and a thick sludge of settled solids from the underflow outlet (see figure 1-7) [66]. These solids settle on the bottom of the thickening tank and are removed from the tank via an underflow outlet. Excessive density of the solids may result in the pump and pipe becoming clogged while low density may cause erosion damage [35, 65]. Thus, the solid content in the underflow is continuously monitored by monitoring the density of the sludge.

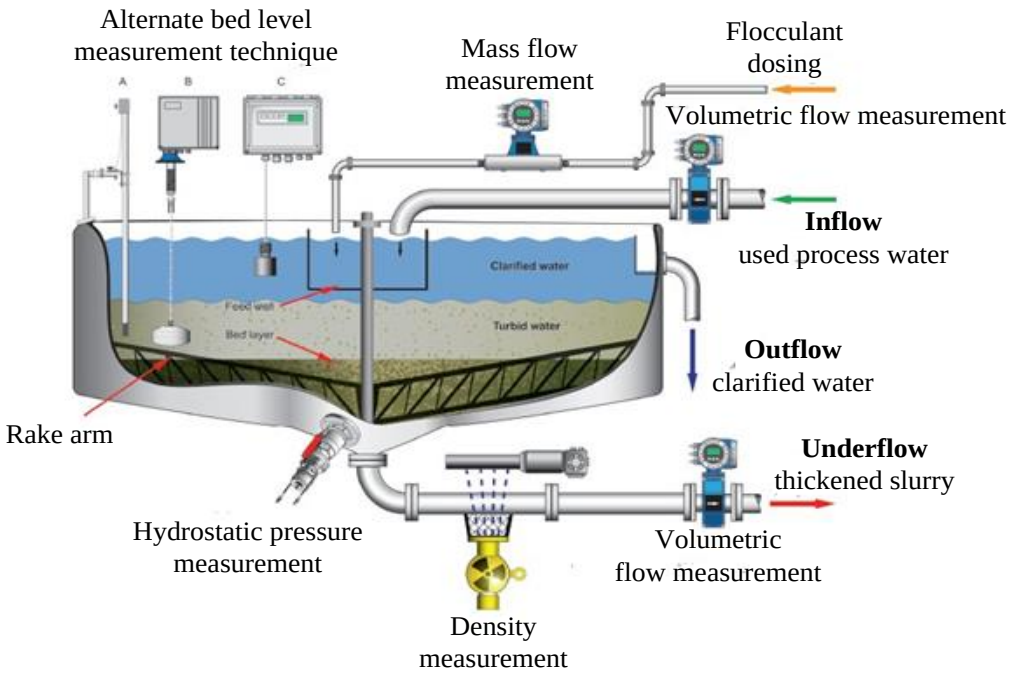

Figure 1-7: Picture showing density measurement device in thickening tank used in mining operations [66]

1.5 Motivation for the research presented in this thesis

Given the many application areas of density measurement discussed in section 1.4, it is important to mention some of the many problems associated with existing density measurement techniques (which will also be described in detail in chapter 2) and which formed the motivation for this research. Some of these problems include the use of radioactive sources, fouling of pressure lines, inaccuracy and high cost. This research was therefore focused on the design and development of a novel densitometry system that (i) does not include a radioactive source, (ii) gives relatively accurate measurements which are not affected by the flow type and flow regime, (iii) can provide online density measurement and (iv) is relatively inexpensive. The overall aims and methodology of the current research are presented in section 2.4 and 2.5 respectively.

1.6 Summary

An introduction to density measurement techniques applicable to the current research and the need for mixture density measurement in multiphase flows have been discussed in section 1.1 and 1.2.

Additionally, the different types of flow pattern applicable to the current research were described in section 1.3. These include gas-in-liquid and solids-in-liquid vertical upward flow patterns. Several application areas where density measurement is used were discussed in section 1.4. Some of the industrial applications considered include density measurement in the oil and gas industry, petrochemical industry, pharmaceutical industry, food and beverage industry, pulp and paper industry and mining industry. Lastly, the motivation for the current research was presented.

Chapter 2

REVIEW OF EXISTING METHODOLOGIES USED IN DENSITY MEASUREMENT IN MULTIPHASE PIPE FLOW

2.1 Introduction

In this chapter, a range of existing methodologies that could be conceivably used, or extended, or developed to address mixture density measurement needs in multiphase pipe flow are presented. The methods are discussed in terms of their fundamental principles of operation, design and construction and shortcomings in providing mixture density measurements in specific application areas. A critical discussion on the methodology chosen to address mixture density measurement needs in multiphase pipe flow as applicable to the current research is also discussed in this chapter. Lastly, based on the literature review a summary of the work packages that were undertaken in the program of research reported in this thesis are presented.

The density of a substance is a fundamental physical property generally described as its mass to volume ratio ($\rho = m/V$) under fixed conditions of temperature and pressure and it is expressed in units such as kg/m^3, g/l, g/ml, lb/ft^3 and lb/gal [67]. Density can also be expressed as a dimensionless quantity called specific gravity which is defined as the ratio of the density of a substance to that of water. Given the diverse areas of application of density measurement, its unit of measurement can also be expressed in different scales depending on the application areas [68, 69]. For example, the American Petroleum Institute (API) uses the degree API (°API) unit to measure density. This unit is defined as follows,

$$°API = \frac{141.5}{S_g@60°\text{F}} - 131.5 \qquad \text{Equation 2-1}$$

where $S_g@60°\text{F}$ is the specific gravity of the fluid at 60°F. Additionally, the brewing and sugar industry uses Balling degrees (°Ba) to express the density of a substance as a weight percentage of dissolved solids at 60°F and this is given by

$$°Ba = \%\ by\ weight\ of\ dissolved\ solids. \qquad \text{Equation 2-2}$$

In the dairy industry, most lactometers used to measure milk density uses the degrees Quevenne (°Q) scale, where 1 degree Quevenne represents an increase of 0.001 in the specific gravity of milk $S_{g(m)}$ when compared with water and it is defined by

$$^{\circ}Q = \left(S_{g(m)} - 1\right)(1000). \quad \text{Equation 2-3}$$

For example, a quantity of milk with a density of $10^{\circ}Q$ has a specific density of 1.010. The Sikes, Richter, or Trallers scales are used to determine the volumetric percentage of ethyl alcohol in water, a unit used to measure the concentration of alcohol. This is given by

$$^{\circ}S, ^{\circ}R, ^{\circ}T = Volume\ \%\ of\ ethyl\ alcohol. \quad \text{Equation 2-4}$$

These density conversion scales, and several others, make the transfer of density measurement from one scale to another relatively easy to implement. A density conversion table for converting from one measurement scale to another is given in [69]. Density measurement has continued to generate considerable interest since the pioneering works of Archimedes [70]. Researchers and scientists alike have kept seeking ways to develop more accurate and less costly density measurement methods and to improve on the existing methods. A great variety of instruments (both dynamic and static) for measuring the density of a substance have been developed using different sensing techniques. Some of the measurement methods developed are custom designed for specific fluids, while others have had similar operating principles and technology and are applicable to a wide range of fluids [67].

2.2 Density measurement techniques

This section describes a range of existing measurement methodologies used in density measurement in both single phase and multiphase pipe flow. An effort is made here to describe their fundamental principles of operation, design and construction features and known drawbacks when used in a specific application area.

2.2.1 Hydrostatic head techniques

This technique is one of the oldest available methods for density measurement and it is mainly suited for measuring the density of an incompressible and clean fluid. It is cheap, simple and non-intrusive.

The hydrostatic head technique has been applied to measure density in both static and flowing fluids and these applications will be discussed in sections 2.2.1.1 and 2.2.1.2 respectively.

2.2.1.1 Density measurement using hydrostatic head technique in static fluids

Over the years, the hydrostatic head technique has been used to measure the density of fluids stored in tanks and vessels. This type of fluid is referred to as a static fluid because it has no shearing force acting on it and the velocity is zero. The hydrostatic head technique uses the relationship between the variation in the differential pressure exerted by a column of fluid between two fixed vertically separated points in a tank/vessel (either open or closed) to the specific weight of the fluid, where specific weight as used here means the product of the fluid density and acceleration due to gravity. The static fluid density is given by

$$\rho = \frac{\Delta P}{gH} \qquad \text{Equation 2-5}$$

where ΔP is the differential pressure, in Pascal, measured across the two fixed points in the tank/vessel, H is the vertical distance between the two fixed points, in meters, g is acceleration due to gravity and ρ is the fluid density in kgm^{-3}. A number of configurations exist for determining the density of a static fluid using the hydrostatic head technique and these can be found in [68, 71]. The choice of system configuration that can be applied when using the hydrostatic head technique to measure density of static fluids depends on the measurement conditions and the nature of the fluid [68]. One form of density measurement system that uses the hydrostatic head technique to predict the density of static fluid in tanks/vessels comprises a differential pressure (DP) sensor with tappings connected with a fixed vertical separation H in the fluid column. A liquid purging system is also generally used as shown in figure 2-1.

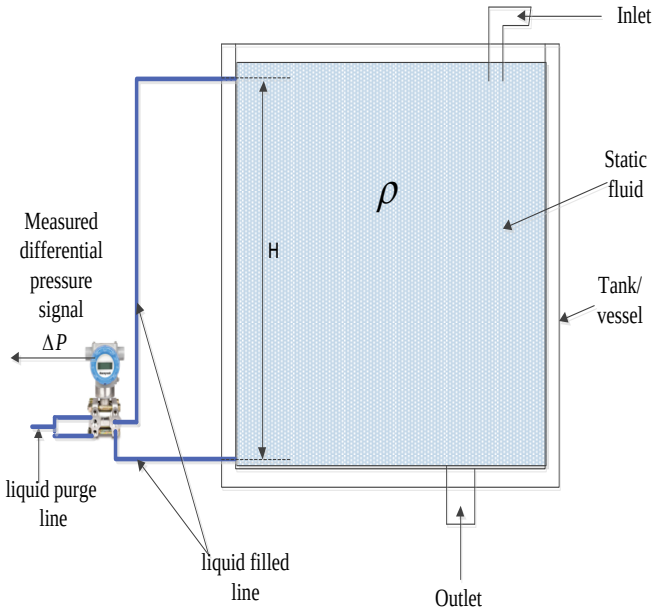

Figure 2-1: Density measurement in a tank/vessel using a DP sensor with a liquid purge system [72]

For a fluid with known density range and for a given span of the differential pressure transducer, the minimum column height H required for density measurement setup can be obtained from a standard plot of density span against the required hydrostatic head as shown in figure 2-2.

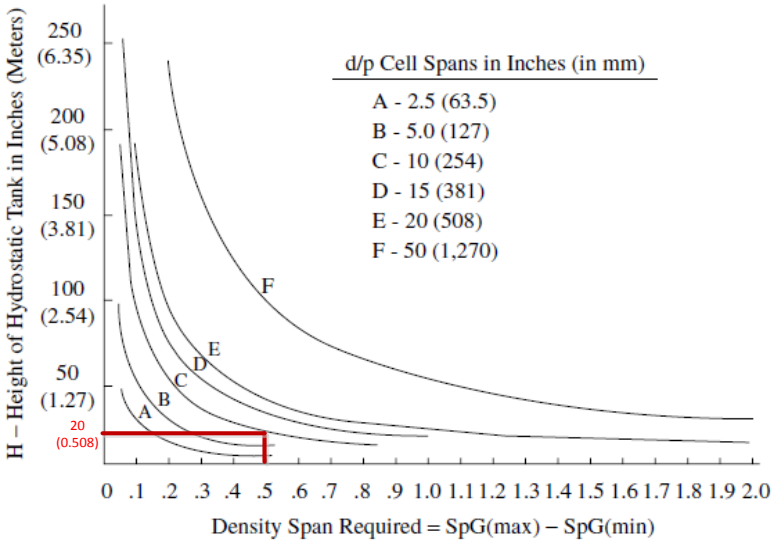

Figure 2-2 Plot of Relative density span versus H for various d/p sensor span [69]

In figure 2-2, SpG(max) and SpG(min) represents the maximum and minimum specific densities respectively, of the fluid and the letters "A" to "F" represent different DP sensors' minimum span. An example is given here to illustrate how the minimum column height H, which is an important factor

when using this technique to measure fluid density, can be determined. Assume a differential pressure (DP) sensor with a minimum span of 10inches of H_20 is required to measure the density of a fluid with minimum and maximum specific gravity values of 0.3 and 0.8 respectively. Then the minimum column height H required to measure the density of a fluid with the above mentioned specific gravity range is given by

$$H = \frac{span\ of\ DP\ sensor}{Specific\ density\ span}\ .$$ Equation 2-6

By substituting the values for the DP sensor span and the minimum and maximum specific densities of the fluid, in the current example, into equation 2-6, H was obtained as 20inches (50.8mm). Thus, a minimum column height of 50.8mm will be required when setting up the hydrostatic head density measurement system. Alternatively, H can be read-off from figure 2-2 using the following steps; (i) identify the curve which represents the minimum span of the DP cell (plot C), (ii) compute the specific density span (0.5) of the fluid and (iii) draw a vertical line starting from 0.5 on the horizontal axis (representing the fluid specific density span) until it touches plot C and draw a horizontal line from the same point on plot C to the vertical axis. The point where this line touches the vertical axis represents the value of H required. This is indicated by the red line in figure 2-2 and was obtained also as 50.8mm.

2.2.1.2 Density measurement using the hydrostatic head technique in flowing fluids

The hydrostatic head technique can also be used to measure the density of fluid flowing through a pipe. Supposing that the fluid flowing through the pipe shown in figure 2-3 is a multiphase mixture comprising of solids as the dispersed phase and water as the continuous phase and the liquid in the purge system is water. Then the density of the flowing multiphase mixture cannot be computed using equation 2-5 because it does not account for the multiphase pipe flow dynamics resulting in frictional pressure loss in the flowing mixture.

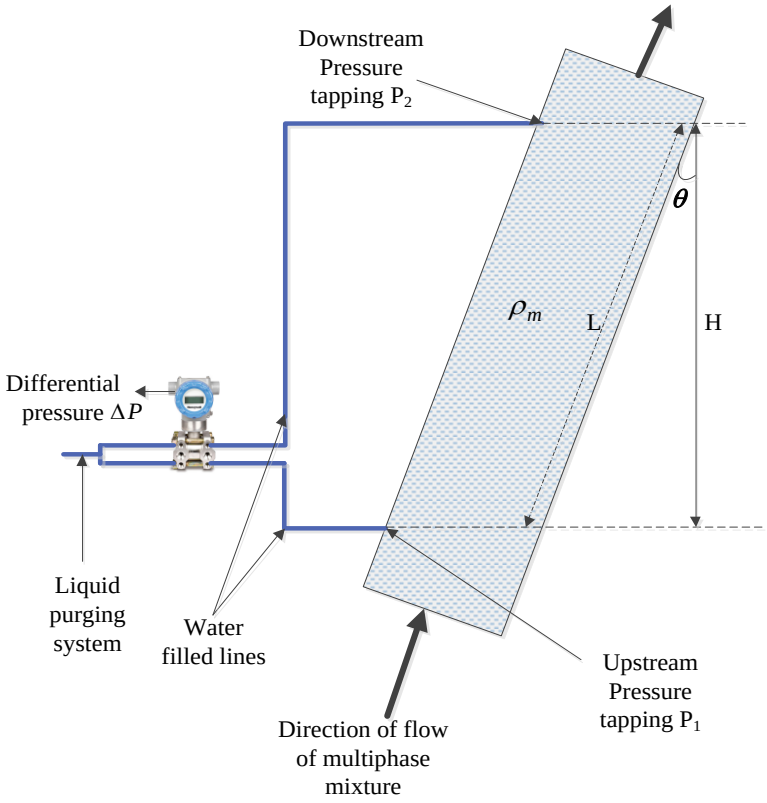

Figure 2-3: Diagram showing the set up to measure the density of a fluid flowing in a pipe using a DP sensor with a liquid purge system

Cory [14] showed that the mixture density ρ_{mix} of a homogeneous solids-water mixture flowing in an inclined pipe can be obtained using the hydrostatic head technique, where the liquid in the purging system is water as follows,

$$\rho_{mix} = \rho_w + \frac{\Delta P - F_m}{gH} \qquad \text{Equation 2-7}$$

where ρ_w is the water density, ΔP is the measured differential pressure between two fixed points in the flow pipe, H $(L\cos\theta)$ is the vertical separation between the fixed points, F_m is the Darcy-Weisbach friction loss in the flow, g is acceleration due to gravity and θ is the angle of inclination of the measurement system from the vertical. Typically H, L, g, ρ_w and θ are known for a given hydrostatic head density measurement system. Thus in order to ensure the mixture density ρ_{mix} of the flow is correctly predicted, it is important that ΔP obtained from the DP sensor and F_m are accurately estimated. This technique is commonly used in research laboratories to provide reference mixture density

measurements of flowing multiphase mixtures due to its relatively low cost, simplicity and ease of installation [68]. This technique shall be used in this investigation to provide reference density measurements of multiphase pipe flows. However, it is important to state here that the accuracy of the density measurement obtained using this technique can be affected by fouling of the pressure lines, inaccurate calibration of the DP sensor and poor estimation of the friction losses in the flow.

2.2.2 Buoyancy/hydrostatic balance techniques

The buoyancy technique is one of the earliest methods for measuring density and it is based on the famous Archimendes principle. This principle states that the upward buoyant force exerted on a body immersed in a fluid is exactly equal to the weight of the fluid displaced [73]. Thus, by either measuring the upward buoyant force or the apparent loss of the weight of an object immersed in a fluid, the density of the fluid can be determined [74]. Several types of buoyancy based densitometry system have been described in the literature [73, 75-77]. According to Liptak [69], one version of the buoyancy densitometer which uses the measured buoyant force to determine density of a fluid consists of a displacer and a force-balance mechanism to convert the buoyant force on the displacer to a pneumatic or electronic signal (e.g. see figure 2-4). The displacer is mounted either on the side or top of a vessel and is fully submerged in the process fluid. The cross sectional area of the displacer is kept constant over its working length so that the buoyant force is proportional to the fluid density. The buoyant force f_b exerted on a displacer is given by [69],

$$f_b = V\left(\frac{L_w}{L}\right)(B)(S_g) \qquad \text{Equation 2-8}$$

where V is the total volume of the displacer (m^3), L_w is the working length of the displacer (m), L is the total length of the displacer (m), B is a constant (N/m^3) and S_g is the specific gravity of the fluid. The buoyant force f_b required for a particular measurement determines the size of the displacer to use. Figure 2-4 shows a buoyancy based densitometer with the displacer mounted on the top of the vessel.

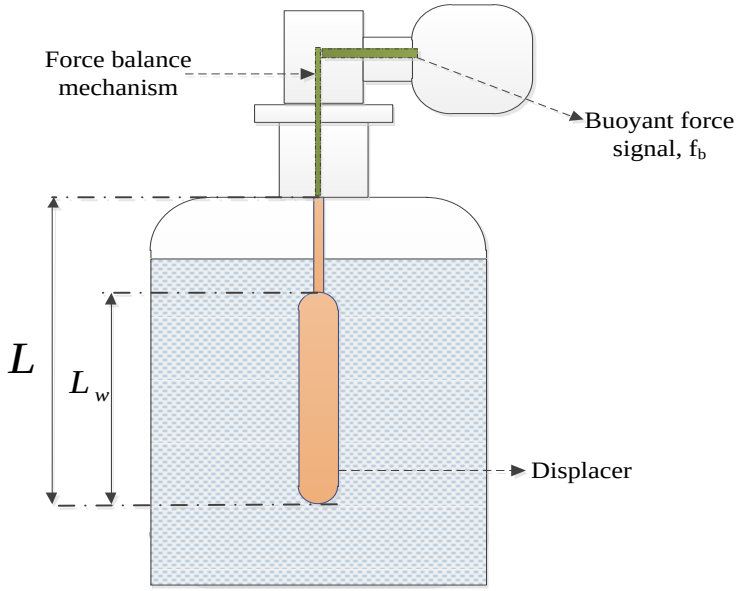

Figure 2-4: Buoyancy based densitometry system [69]

A slightly different version of this measurement technique that was described by Wagner [78] and Wagner and Kleinrahm [76] requires that an object (called a sinker) of known mass M_s is weighed while it is totally immersed in a fluid whose density is to be determined. The sinker is mostly made of glass or metal and is spherical or cylindrical in shape. The apparent loss in the true weight of the sinker immersed in the fluid is used to estimate the density of the fluid. The density is obtained as follows,

$$\rho = \frac{W_s - W^*_s}{gV_s} = \frac{M_s - M^*_s}{V_s} \qquad \text{Equation 2-9}$$

where $M_s = \frac{W_s}{g}$ is the true mass of the sinker, $M^*_s = \frac{W^*_s}{g}$ is the apparent mass of the sinker surrounded by the fluid, g is the acceleration due to gravity and V_s is the volume of the sinker. W_s and W^*_s are the true weight and apparent weight of the sinker respectively. The true mass M_s can be determined by weighing the sinker in vacuum or air and V_s can be determined by measuring the dimensions of the sinker. This technique is best suited for measuring the density of clean, non-viscous fluids in an enclosed vessel. It is an intrusive measurement technique and it is most suited to measuring the density of a stationary fluid. When this density measurement technique is used in applications with turbulent process conditions, the measurement accuracy can be significantly affected as turbulence may cause

the displacer to swing erratically and to give erroneous density measurements [79]. Also, particle build up on the displacer can result in changes to its weight and hence cause the densitometer to give inaccurate measurements [69]. Additionally, the surface tension force between the sample fluid and the displacer affects the accuracy of density measurements obtained [76]. Due to the drawbacks mentioned here, this technique was not considered suitable for the current investigation and was not investigated further.

2.2.3 Weighing techniques

The weighing technique is one of the most commonly used and oldest techniques for measuring density. In principle, the density ρ of a fluid can be determined from its mass m and its fixed volume V using the expression

$$\rho = \frac{m}{V}. \qquad \text{Equation 2-10}$$

The weighing technique is based on gravity or weighing principles and it is suitable for measuring a wide range of fluid densities. A weighing type densitometer, as shown in figure 2-5, generally consists of a fixed volume vessel or pipe section and a means for measuring the mass of the vessel or pipe section and its contents, usually with a load cell [80]. This technique could be applied to both static and flowing fluids. The design features of a typical weighing densitometer include a means of mechanically isolating the vessel or pipe section, mounted on load cells, by means of flexible end couplings (usually bellows). The load cell continuously measures the weight of the vessel/pipe section and its contents and generates an output signal which is used to compute the density of the process fluid. Since the volume of the vessel/pipe section is fixed, changes in density of the fluid are indicated by changes in the total weight of the isolated vessel/ pipe section.

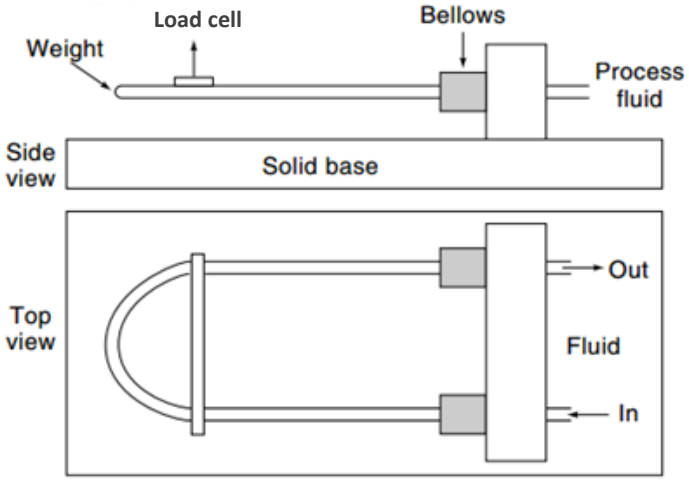

Figure 2-5: Front view and side view of a weighing densitometer [80]

A version of the weighing densitometer described by Falcone et al. [9] includes a horizontal pipe section with a deflection meter attached to the centre of the pipe section as shown in figure 2-6. The density of a fluid flowing through the horizontal pipe can be determined by using the elasticity of the pipe section L as a spring balance and measuring the deflection at its center.

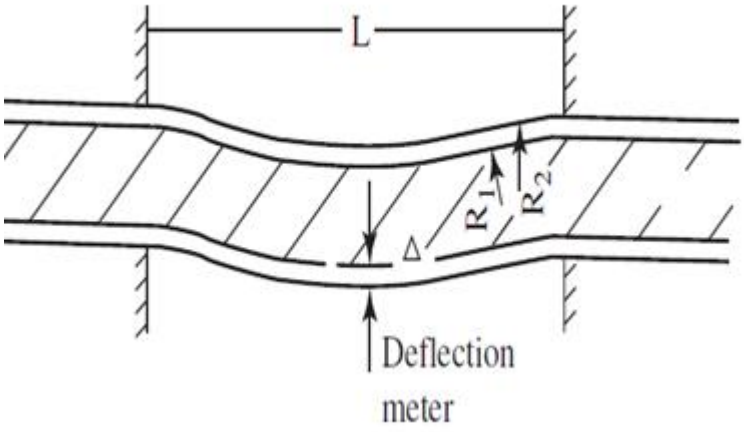

Figure 2-6: Weighing type densitometer [9]

Under the combined weight of the pipe and its contents W, the deflection Δ at the centre of the pipe section of length L is given by [9],

$$\Delta = \frac{1}{384}\frac{WL^3}{EI}$$ Equation 2-11

where E is the modulus of elasticity of the pipe material in [Nm^{-2}] and I is the moment of inertia of the pipe in [m^4]. The total weight W of the pipe and its contents is given by,

$$W = \{\pi(R_2{}^2 - R_1{}^2)\rho_p g + \pi R_1{}^2 \rho_f g\}L$$ Equation 2-12

where R_1 and R_2 are the inner and outer radii of the pipe, respectively, g is acceleration due to gravity, ρ_p is pipe density and ρ_f is density of the pipe contents. Also, the moment of inertia I of the pipe is given by,

$$I = \left\{\frac{\pi}{2}\left(R_2{}^4 - R_1{}^4\right)\right\}.$$ Equation 2-13

By substituting equation 2-12 and equation 2-13 into equation 2-11 and rearranging the resulting expression, a linear equation to compute the density ρ_f of the contents of the pipe is obtained as shown below,

$$\Delta = A + B\rho_f$$ Equation 2-14

where A and B are referred to as the densitometer constants and are defined in equation 2-15 and equation 2-16 respectively,

$$A = \frac{\pi L^4 g \rho_p}{192E(R_2{}^2 + R_1{}^2)}$$ Equation 2-15

$$B = \frac{\pi L^4 g R_1{}^2}{192E(R_2{}^4 - R_1{}^4)}\ .$$ Equation 2-16

From equation 2-14, it can be seen that provided A and B remain constant, changes in the density of the fluid flowing through the pipe will result in changes in the measured deflection. From equation 2-16, the constant B will become larger as the difference between the pipe inner and outer radii becomes smaller. Hence, pipes with thin walls are often used to obtain signals with high signal to noise ratio in a weighing densitometer. Batey [81] has also described a weighing densitometer for measuring the density of slurries flowing through a pipe. The densitometer described continuously measures the weight of slurry, flowing through a flexible flow pipe with defined volume, using a weight measuring

transducer. The transducer output is sent to a microcontroller to compute the density of the slurries. A limitation of the weighing densitometer is that it requires a very precise weight measuring transducer to give accurate density measurements. The weighing densitometer must also be installed horizontally on a solid base in order to be able to measure the weight of the flow pipe and its contents. Consequently, this densitometer is not flexible enough to be adapted to any process [82]. Particle accumulation in the weighing section of the flow pipe used in the densitometer can cause the density measurement errors to increase [83]. Some of the design features of this density measurement technique were adapted for use in the current investigation. These include the use of a flow pipe with thin walls to ensure the amplitude of the deflection at the flow pipe centre is measurable.

2.2.4 Acoustic techniques

This technique uses changes in the characteristics of a sound wave as it passes through different media to provide non-invasive characterization of fluid properties. This technique has been applied by several authors [8, 84-86] using different variations in the measurement configuration and Bjorndal [74] has provided a summary of some of the existing work done using the acoustic technique to measure density. The acoustic measurement technique is applied in the development of ultrasonic densitometers and the working principles of these densitometers is described here. The working principle of the ultrasonic densitometer is based on the transmission or reflection of an ultrasonic wave when it makes contact with an object in its path of travel. Typically, the design features of an ultrasonic densitometer primarily consist of ultrasonic transducers to function as sound emitter(s) and receiver(s) and signal processing electronics. These transducers are arranged using different sensor configurations and layouts across a vessel or flow pipe to optimize the strength of the acoustic signal obtainable [87]. One configuration where the sound emitter and receiver are arranged diametrically across the flow pipe wall is shown in figure 2-7.

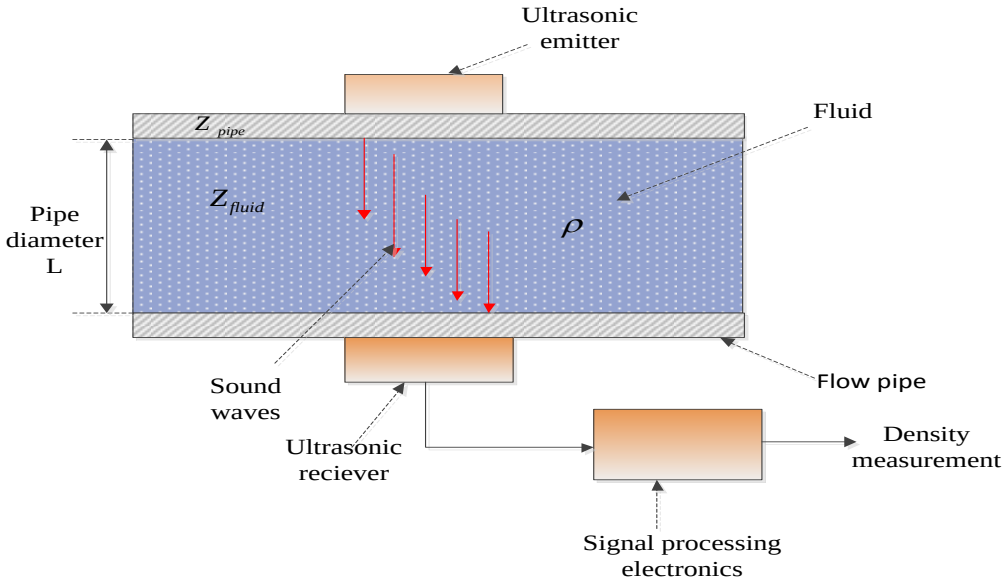

Figure 2-7: Diagram of ultrasonic densitometry system

Generally, the density ρ of a fluid measured using the acoustic technique can be determined from its acoustic impedance Z and sound wave velocity c using the relationship

$$\rho = {}^{Z}/_{c}\,. \qquad \text{Equation 2-17}$$

One version of the ultrasonic densitometer described separately by Puttmer et al [88] and Greenwood and Bamberger [89] requires that the acoustic impedance Z and sound wave velocity c of the fluid be measured simultaneously and these measurements inputted into equation 2-17 to compute the unknown density of the fluid through the pipe. Greenwood and Bamberger [89] used a single ultrasonic sensor acting as a transceiver to transmit pulse signals to the pipe wall as well as to record the multiple reflections at the flow pipe wall-fluid interface. The transmitted and reflected acoustic signals were recorded and used to compute the acoustic impedance of the fluid. Additionally, the speed of sound in the fluid was simultaneously estimated using the time taken for a pulse wave to be reflected back to the transceiver. Kazys et al [87] also described a different version of the ultrasonic densitometer which is set up to measure the sound wave velocity c of the fluid only. In this setup, the propagation time t of an ultrasonic pulse across the flow pipe diameter L (see figure 2-7) is used to compute the sound wave velocity c. This is given by,

$$c = \frac{L}{t}$$ Equation 2-18

and the acoustic impedance is determined by calibration using a sample of the fluid. Generally, the reflection coefficient R of a sound wave at the flow pipe-sample fluid interface is measured and used to compute the acoustic impedance using equation 2-19 [90]. Note that in this calibration, the flow pipe acts as a reference material and its acoustic impedance Z_{ref} is usually known.

$$Z_{fluid} = Z_{ref}\left(\frac{1-R}{1+R}\right)$$ Equation 2-19

where Z_{fluid} is the acoustic impedance of the fluid with unknown density and Z_{ref} is the acoustic impedance of the flow pipe (reference material). The acoustic impedance Z_{fluid} of the fluid that is obtained from calibration and the measured sound wave velocity c are then used to compute the fluid density using equation 2-17. The ultrasonic densitometer configuration described by Kazys et al [87] has gained wide acceptance because it is easy to implement.

Since the publication of the first patented ultrasonic densitometer [91], a great number of publications [7, 88, 89, 92-98] have described different applications of the acoustic technique to predict the density of a fluid. However, acoustic density measurement techniques are not fully developed and are known to give large measurement errors. Rowell et al [92] and Higuti and Adamowski [99] separately reported measurement accuracy that is greater than 2% when they used the ultrasonic densitometer to measure fluid density. This percentage accuracy is relatively poor compared to the accuracy obtainable from the vibration based densitometry system described in section 2.2.6. Common limitations encountered when using the acoustic technique to predict the density of a fluid are the need for extensive testing and calibration under the anticipated operating conditions [9, 100], increased measurement error due to drift effect of the acoustic impedance of the reference material used and the measurement electronics [7, 88]. Given that this technique is not fully developed and it is known to have poor accuracy, it was not considered suitable for this research.

2.2.5 Radiometric based techniques

Despite the inherent hazards and strict government regulations associated with the use of radioactive substances, radiometric based techniques are still being applied in several industries to non-invasively characterise the properties of fluids in enclosed pipes. This measurement technique is commonly used in the oil and gas industry to measure the void fraction and mixture density of multiphase process fluids [101]. Because of the aforementioned reasons, it is not an attractive option for food, beverage and pharmaceutical industries. For convenience, the discussion in this section will generally refer to vessels, containers, flow pipes, and all other enclosed objects as a pipe. The principle of operation of a radiometric densitometer is based on the transmission or backscattering of carefully generated mono-energetic radiation particles (such as gamma rays and X-rays) passing through the pipe walls and a multiphase mixture of unknown density. Previous literature has described density measurement instruments developed using the radiometric technique and a good summary of this literature has been provided by Hewitt [102]. Radiometric densitometers based on radiation particle transmission techniques are very common, though more recent developments have seen an increase in the use of the backscattering technique or a combination of both [103, 104]. The main design features of a radiometric densitometer based on the transmission of radiation particles consist of a shielded radiation source and collimated detector placed diametrically across a pipe containing the multiphase mixture. The radiation source is used to generate radiation particles which are transmitted through the near pipe wall, the multiphase process fluid, and the far pipe wall (see figure 2-8). The collimated detector is used to measure the resultant intensity of the collimated particle emissions received at the detector [104-106]. The diagram in figure 2-8 shows a general arrangement of a transmission type radiometric densitometer.

For a transmission type radiometric densitometry system (see figure 2-8), Lambert-Beer's law is used to describe the relationship between the intensity of the transmitted radiation particles I_d received at the detector and the density ρ of the multiphase mixture [107]. This is given by,

Equation 2-20

$$\rho = \frac{ln\left(\frac{I_d}{I_0}\right)}{(-\mu_m x)}$$

where I_0 is the intensity of the radiation particles from the radiation source, μ_m is the mass attenuation coefficient and *x* is the length of the absorbing media.

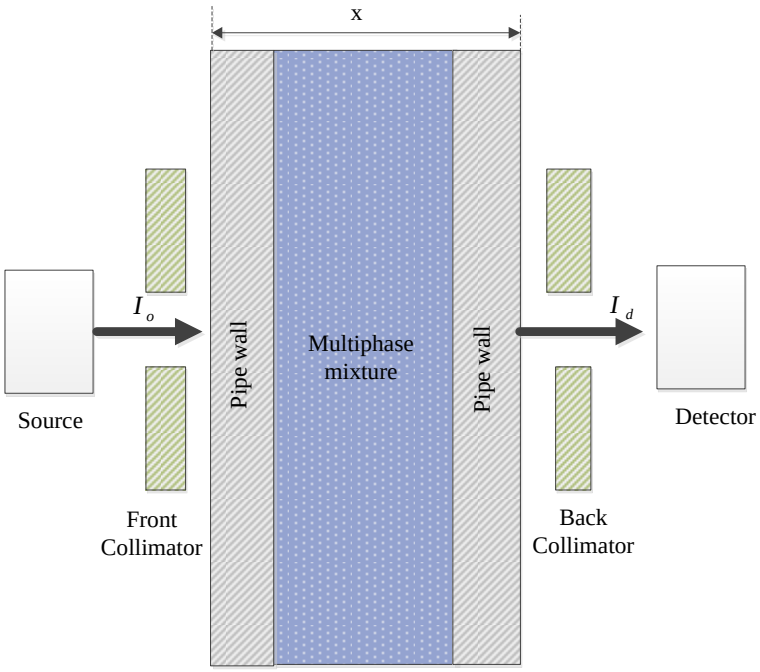

Figure 2-8: Typical arrangement of a transmission type radiometric densitometer [9]

From equation 2-20, if the mass attenuation coefficient μ_m and beam path length *x* are known for a given set up, then the density of the multiphase mixture in the pipe can be obtained by measuring the intensities of the particle radiation from the source and that reaching the detector. The accuracy of the radiometric densitometer is therefore dependent on accurate measurement of the intensities of the radiation particles at the densitometer source and detector. The intensity of the radiation particles reaching the detector from the source is proportional to the mass attenuation coefficient of the pipe and multiphase mixture as well as the length *x* of the absorbing media. Hence, in addition to being able to accurately measure the radiation particle intensity at the source and detector, a thin pipe wall and short beam path length are also requisites for obtaining stronger measurement signals of the radiation particle intensity at the detector, consequently ensuring more accurate density measurement [69, 108].

When a transmission based radiometric densitometry system is used in an application having large pipe size and relatively high multiphase mixture density, the intensity of the radiation particles reaching the detector can be significantly reduced due to higher attenuation, thereby affecting the accuracy of the densitometer. An alternative design of radiometric densitometers, which is based on the backscattering technique, can be used instead. Unlike the transmission type radiometric densitometers, where the radiation source, multiphase mixture and collimated detector must have a linear arrangement (see figure 2-8), radiometric densitometers based on the backscatter technique have their source and detector on the same side of the pipe. This configuration offers the advantage of being able to apply the radiometric based density measurement technique in applications where two sided access to the flow pipe is restricted or where the pipe diameter is very large or where the fluid has relatively high density. With backscatter radiometric densitometers, the radiation particles from the radiation source are either scattered in the multiphase mixture, or lost by scattering and attenuation in the multiphase mixture, or stopped by the source shielding. The scattered radiation particles received at the detector are used to compute the density of the multiphase mixture [104, 109]. The diagram in figure 2-9 shows an arrangement of a radiometric densitometer using the backscatter technique where the radiation particles are generated from a gamma source.

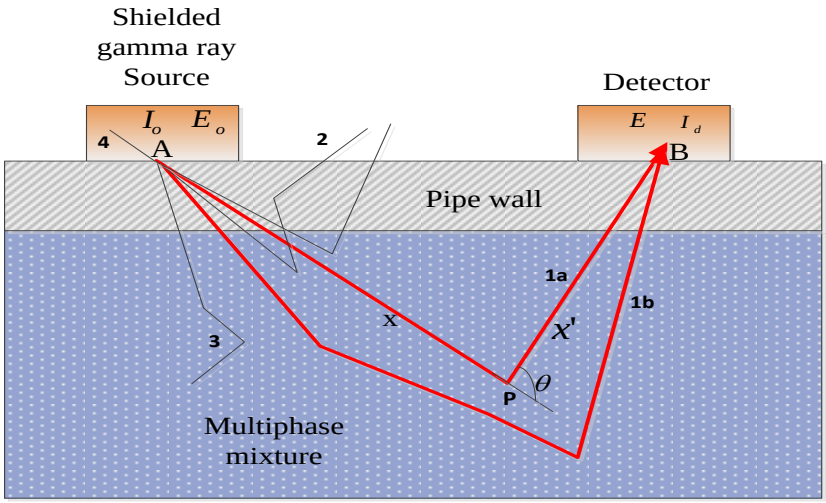

Figure 2-9: Schematic diagram of a gamma backscatter densitometry system. [109]

In figure 2-9, "1a" and "1b" represent photons detected having undergone (a) single or (b) multiple scattering in the multiphase mixture, "2" represents photons lost through the surface by single or multiple scattering, "3" represents photons lost by scattering and absorption in the multiphase mixture and "4" represents photons stopped by the source shielding. The intensity of the scattered photons reaching the detector is influenced by the following; (i) the incident energy of these photons from the source to the scattering point *P*, (ii) scattering at the point *P* towards the detector and (iii) attenuation of the scattered photons received at the detector. The Klein-Nishina relationship [104] can be used to compute the density of the multiphase mixture. This relationship is given by

$$I_d = KI_0\rho e^{-\left[\left(\frac{\mu(E_0)}{\rho}\right)\rho x\right]}e^{-\left[\left(\frac{\mu(E)}{\rho}\right)\rho x'\right]} \qquad \text{Equation 2-21}$$

where I_d is the intensity of scattered photons received at the detector, I_0 is the intensity of the photons leaving the source, $\frac{\mu(E)}{\rho}$ is the mass attenuation coefficient of the multiphase mixture for the scattered energy, $\frac{\mu(E_0)}{\rho}$ is the mass attenuation coefficient of the multiphase mixture for the incident energy, ρ is the density of the multiphase mixture, x is the path length of the primary photons (see AP in figure 2-9) and x' is the path length of the scattered photons (see PB in figure 2-9). *K* is a constant for a given geometrical set up and is defined by

$$K = \frac{d\sigma(E_0,\Omega)}{d\Omega}S(E_0,\theta,Z)d\Omega\rho_e(P)V \qquad \text{Equation 2-22}$$

where $\frac{d\sigma(E_0,\Omega)}{d\Omega}$ is the differential cross section for Compton scattering given by Klein-Nishina [104], V is the pipe volume , θ is the scattering angle, $\rho_e(P)$ is the electron density at the scattering point *P*, $S(E_0,\theta,Z)$ is the scattering function with respect to the atomic number *Z*, the incident photon energy E_0 and the final energy of the scattered photon *E*.

Quite a number of radiation sources have been used to generate the required radiation particles applied in radiometric densitometers and these include gamma ray [107, 110], X-ray [111], beta ray [112] and neutron [113, 114]. The use of gamma sources in radiometric densitometers has gained wider

acceptance and is better developed, compared to the other available radiation sources, because of the ease of selecting gamma sources with different and well-defined energies suitable for a given process. The most commonly used gamma source is caesium 137 which has a half-life of 30 years, an energy level of 662KeV and a mass absorption coefficient of $8.6m^{-1}$ [9, 69]. Other isotopes which have also been used include thulium-170, iridium-192, selenium-75, cobalt-57 and barium-133. X-ray sources have recently been used as an alternative to gamma sources by Tjugum et al [111]. The use of X-rays as the radioactive source has the advantage that they can be switched off, thus allowing the photon radiation to be stopped when the densitometer is not in use. As mentioned earlier in this section, the attraction for the industrial use of radiometric densitometers continues to decline by the day because of strict government regulations on handling radioactive substances, the need to stop the production of radioactive wastes and the inherent health and safety concerns to personnel and the environment from the radioactive emissions [115]. Additionally, due to the random nature of radioactive emission, statistical errors associated with the measured photons received at the detector can affect the measurement accuracy of the radiometric densitometers as reported in [9, 116, 117]. Khorsandi et al [107] also reported that the geometrical parameters of a radiometric densitometer such as distance between radiation source and detector, pipe diameter and wall thickness influence the densitometer calibration. Any changes in these parameters can cause the density measurement to change and hence affect the accuracy of the radiometric density measurement. For example, erosion and corrosion can affect the dimensions of the pipe thickness and hence the photon path length. Consequently, this effect can cause the instrument calibration to change and therefore to increase the measurement errors. Sharaf et al. [116] and Peyvandi et al. [118] have also reported that temperature can affect the measurement accuracies of gamma radiation densitometers. Because of these disadvantages, the radiometric densitometry method was not considered suitable for the current investigation.

2.2.6 Mechanical vibration based techniques

The fundamental theory of operation of mechanical vibration type densitometers is based on the natural phenomenon that a body vibrating at its natural frequency will have its mass related to its frequency of vibration. This technique has gained wide acceptance in the measurement of density due to the simplicity of the underlying physics, its robustness and its suitability for a wide range of applications as well as the absence of radioactive sources. The design of a mechanical vibration densitometer comprises a mechanical vibrating element, usually a vibrating tube or tuning fork, a means for setting the mechanical body into vibration and a means for sensing some chosen property (frequency, period, phase, or amplitude) of the mechanical vibrations. Inspired by the pioneering design of the first vibrating tube densitometer by Kratky et al [119] in 1969, several other designs have been developed and described in the literature [73, 76, 120-123]. These designs have used different structural shapes for the vibrating elements, besides having different types of sensing element(s) located at different positions in the sensing tube. In all of these designs, vibrations are maintained in the mechanical body either through magnetic or piezoelectric drives. The density of a fluid contained in the vibrating mechanical body is computed by relating the chosen property (e.g. frequency, period, phase, or amplitude) of the vibrating body that is measured to its mass [67, 69, 124].

The vibrating densitometers are grouped into four categories in this thesis, according to the type of mechanical vibrating element used. These categories of vibrating densitometers include (i) the vibrating straight tube type [120, 125], (ii) the vibrating U-tube type [126], (iii) the vibrating twin-tube type [127-129] and (iv) the vibrating fork type [121, 130, 131]. The working theory behind these densitometers can be derived from the mathematical relationship between the frequency f of the vibrating element and its total mass m. A straight tube type vibrating densitometer is shown in figure 2-10.

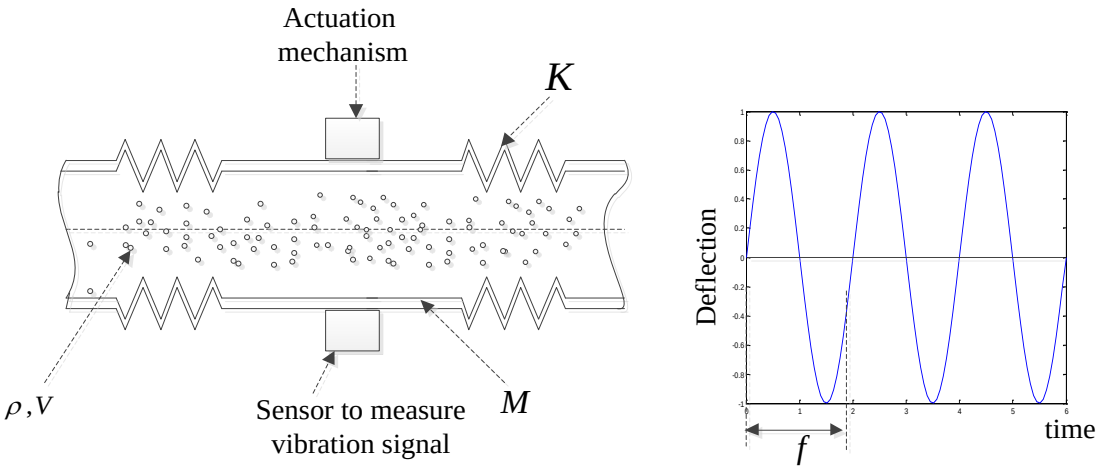

Figure 2-10: Diagram of a straight tube type vibrating densitometer and the recorded vibration signal

In the vibrating densitometer shown in figure 2-10, the actuation mechanism is used to set the flow pipe and its contents into vibration and an appropriate sensor is used to measure the period of the vibrating pipe and hence its frequency. The frequency f of vibration of the pipe and its contents is related to its total mass by,

Equation 2-23

$$f = \frac{1}{2\pi}\sqrt{\frac{K}{m}}$$

where K is pipe stiffness constant and m is the total mass of the flow pipe and its contents as defined in equation 2-24. The total mass of the vibrating densitometer consists of the mass M of the flow pipe and the mass ρV of the fluid contained in the pipe and is given by,

Equation 2-24

$$m = M + \rho V$$

where ρ is the density of the contents of the pipe and V is the fixed volume of the flow pipe. By substituting equation 2-24 into equation 2-23 and rearranging the resulting expression, the frequency f of the vibrating flow pipe can be related to the density ρ of its contents by,

Equation 2-25

$$\rho = \frac{A}{f^2} - B$$

where A and B are referred to as the densitometer calibration constants and are given by,

Equation 2-26

$$A = \frac{K}{4\pi^2 V}$$

$$B = \frac{M}{V}.$$ Equation 2-27

These constants are temperature T and pressure p dependent. Since this technique does not use a radioactive source and its underpinning physics is relatively well understood, it ticks all the boxes for a technique that could be extended or modified in this research to develop a novel densitometry system.

2.3 Review of density measurement techniques relevant to the current investigation

In order to achieve the research aims stated in section 2.4, it was important to comparatively evaluate the pros and cons of the different density measurement techniques reviewed in sections 2.2.1 to 2.2.6 and to decide on which technique or combination of techniques was best suited to meet the aims of the current work. From the evaluation of the pros and cons of the different density measurement techniques reviewed, it was decided that the mechanical vibration densitometer technique will be most suited to achieve the aims of the current research because (i) it is well developed (ii) it can give highly accurate density measurement (iii) its design is simple and robust (iv) it is relatively low cost (v) it is non-intrusive (excluding the vibrating turning fork type) and (vi) it does not require a radioactive source. The mechanical vibration density measurement technique will be extended in this research to develop a densitometry system to predict the mixture density in multiphase pipe flow. Next, a review of the principles of operation of existing mechanical vibration density measurement techniques was required to provide an insight into the problems encountered in the use of these densitometers to measure mixture density. Furthermore, potential drawbacks associated with the chosen density measurement technique for the current research were reviewed. The straight tube vibrating densitometer shown in figure 2-10 can be modelled as a spring mass damper system and the frequency of the vibrating mass of the system can be described using equation 2-23. This equation was used to obtain the expression in equation 2-25 which serves as the fundamental building block for the design of vibrating densitometers. From this equation, it is apparent that accurate estimation of the density of the flow pipe contents is dependent on accurate measurement of the flow pipe stiffness constant K and its fixed volume V, which

are both functions of temperature and pressure. Additionally, it is expedient that the calibration constants A and B given in equation 2-26 and equation 2-27 are correctly estimated and the influence of changes in ambient temperature and pressure on the measured density should be correctly compensated. When using the vibrating densitometer, measured fluid densities have been reported to vary slightly due to changes in the stiffness constant and fixed volume of the vibrating element as its temperature changes. However, these effects can be appropriately accounted for by compensating for the effects of temperature changes in the stiffness constant and fixed volume [132-134]. The effects can be minimized by using invar [135], a material known for its uniquely low thermal expansion coefficient, to design the vibrating element of the densitometer. Previous research efforts have identified some shortcomings of the vibrating densitometer when used in multiphase pipe flows [136]. Billingham and Gysling for example, reported in [137] and [138] respectively that the measurement errors associated with the use of vibrating densitometers to predict density in two-phase air-in-water flow, where air forms the dispersed phase, increase dramatically as the volume fraction of the air increases. According to Gysling [138], the cause of the increased density measurement error can be linked to the mathematical model given in equation 2-25. Gysling argued that the assumption that the mass of the vibrating element is inelastically coupled to the mass of its contents is inaccurate for air-in-water flows because of the mixture coupling stiffness constant between the flow pipe walls and the flow mixture introduced the air compressibility. For the vibrating densitometry system shown in figure 2-10, the generalized model of the flow pipe and the coupled mass of its contents is shown in figure 2-11 where K, f and M are the vibrating element (flow pipe) stiffness constant, damping constant and mass whilst ρV is the mass of its contents.

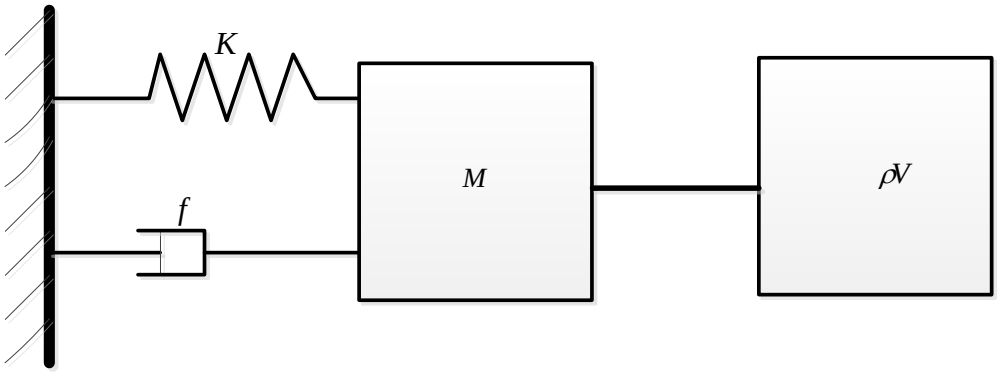

Figure 2-11: Generalised model for the vibrating flow pipe and its contents

If the contents of the vibrating element is an incompressible homogeneous fluid (e.g. "liquid only", liquid-liquid and solids-liquid flows), the total mass of the vibrating system is defined by equation 2-24 and equation 2-25 can be used to obtain accurate density measurement [139]. Conversely, if the content of the vibrating element is a compressible fluid (e.g. an air-water flow) the compressibility of the flow mixture tends to change the overall dynamics of the vibrating system and hence the mathematical model defined in equation 2-25 may not be able to give an accurate description of the dynamics of the flow pipe and the compressible mixture. Therefore, using equation 2-25 to predict the fluid density in such flow type's results in reduced density measurement accuracy. For example, in a two-phase air-in-water flow where air forms the dispersed phase, the fluid mixture contained in the flow tube is compressible. At 20°C, air is known to be approximately 15,000 times more compressible than water thus, an in-situ air volume fraction of 1% will increase the compressibility of the mixture by a factor of 150. Gysling [136, 138] has shown that the compressibility of the air-in-water mixture is inversely proportional to the mixture coupling stiffness constant. Hence, an increase in the compressibility of the flow mixture by a factor of 150 will result in changes to the overall system stiffness constant which will consequently affect the accuracy of the model defined in equation 2-25. Furthermore, for inhomogeneous multiphase flows where a slip velocity exists, the components of the flow move at different velocities through the vibrating pipe. Hence, the components of the mixture will have varying participation in the flow tube oscillation thereby resulting in reduced apparent system inertia [138]. It is therefore important that, for

equation 2-25 to give correct density measurement in single phase and multiphase flow, the model for predicting fluid density should account for the effects of both compressibility and inhomogeneity.

Additionally, most vibrating densitometers described in the literature [120, 140] have employed positive feedback control to the drive coils to maintain the amplitude of vibration of the flow pipe and its contents at the relevant natural frequency. The sensed vibration signal serves as an input to the drive coil amplifier and its gain is set by the damping properties of the fluid. This design configuration also ensures minimal drive coil power requirement for the vibrating system [131]. This commonly used design configuration is a requisite to obtain accurate measurement of the resonant frequency (or period) of the vibrating flow pipe and its contents, which can then be applied to equation 2-25 to compute the fluid density. When an air-in-water mixture is contained within the flow tube, the drive coils have been reported to stall [141, 142] and have been unable to maintain flow tube oscillations due to high and rapidly fluctuating damping (up to three orders of magnitude higher than for single phase flows). Lastly, particles can build up inside the flow pipe when a vibrating densitometer is used in a horizontal orientation, resulting in change in the flow pipe mass and hence in the accuracy of the density measurement. This research work will therefore be aimed at improving upon some of the shortcomings of the vibrating densitometers mentioned in this section.

2.4 Research Aims of the present work

The primary aim of this research was to design and develop a novel, non-invasive densitometry system that could be used to accurately predict the mixture density in single phase and multiphase pipe flows without the need for a radioactive source. This instrument should (i) be low cost (ii) be non-invasive (iii) be of similar or better accuracy compared with existing densitometry systems and (iv) contain no radioactive source. This last requirement ensures that the system will not pose any health or safety hazards to personnel and the environment. The proposed densitometry system was also intended to offer improvements to some of the shortcomings of previous vibrating densitometers such as (i) stalling

of the meter oscillation due to increased damping of the flow and (ii) inaccurate density measurement in compressible and inhomogeneous multiphase flows.

2.5 Research methodology

The following work was identified as necessary to achieve the research aims:

1. To develop a novel mathematical model to predict the fluid mixture density in single phase and multiphase pipe flows using the mechanical vibration characteristics of a pipe and its contents.
2. To analytically validate the density prediction mathematical model.
3. To develop a novel signal processing technique for implementing the mathematical model for predicting mixture density developed in (1).
4. To design, construct and test a vibrating densitometry system. The physical density measurement system will include a flow pipe, an actuator, a force sensor, a displacement sensor, a current sensor and a temperature sensor. Careful calculations will be required to determine the specifications for the flow pipe, actuator, force sensor, and displacement sensor.
5. To calibrate the force sensor and displacement sensor.
6. To design and implement appropriate signal conditioning and processing circuits for the force sensor and displacement sensor. The circuits will be capable of removing noise interference in the signals and also to amplify the signal to the required level.
7. To design and develop a data acquisition and processing system using a National Instrument data acquisition card and LabVIEW software, to sample the output signals from the signal processing and conditioning circuits which can then be saved for further analysis.
8. To design and construct a bench test rig for static test investigations. The static tests will provide calibration data for dynamic flow loop tests, which will subsequently be used to evaluate the densitometry system.
9. To develop and implement a procedure for operating the vibrating densitometry system.

10. To perform static tests to determine the characteristics of the densitometry system using the bench test rig constructed in (8). The static tests will include bench experiments to validate the actuator specification, to determine the mass, stiffness constant and damping constant of the flow pipe used in the densitometry system and to determine system calibration constants. Further static tests will also be required to validate the signal processing techniques and to evaluate the frequency response characteristics of the densitometry system.
11. To perform static tests to investigate the measurement errors when the densitometry system is used to predict mixture density of a reference test mixture. Several test mixtures will be formulated for this purpose using water, vegetable oil, and solid particles. The measurement errors will be critically analysed and used to define optimal operating conditions for the densitometry system.
12. To design and develop a computer based control system for optimal operation of the densitometry system. The computer based control system will also include a means for computing the mixture density online.
13. To calibrate the reference measurement instrumentation on the dynamic flow loop at the University of Huddersfield. These include a DP sensor, a gravimetric measurement system, a turbine flow meter and an air flow rate meter.
14. To evaluate the capability of the densitometry system to give accurate density measurements in flows established in the dynamic flow loop at the University of Huddersfield. The density measurements obtained using the constructed densitometry system will be compared with density measurements obtained from the reference instrumentation. These tests will be conducted using various flows including ‘water only’, air-in-water and solids-in-water flows.
15. To investigate the capability of the constructed densitometry system to accurately predict mean in-situ volume fractions of the phases in two phase flows. These mean volume fraction measurements from the constructed densitometry system will again be compared with

measurements obtained from the reference instrumentation. These tests will be conducted using the same multiphase flow types as described in (14).

2.6 Thesis Overview

This section provides an overview of the thesis structure. Each chapter contained in this thesis describes a different aspect of the research work that has been conducted.

Chapter 3 This chapter presents a detailed description of the relevant background theories applicable to the current research work. These include; vibration theory of mechanical systems with mass, spring and damping elements; the theory of vibration of beams with 'fixed end' supports and the theory of the Discrete Fourier Transform (DFT) of a signal.

Chapter 4 This chapter describes the design and construction of the practical vibrating densitometry system, also referred to as VDMS in this thesis. The sub-sections describe the different developmental stages of the system. These include; the development of a mathematical model for predicting fluid density in single phase and multiphase pipe flows; design considerations and development of the specifications of the different components of the densitometry system, including the flow pipe, force actuator, force and displacement sensors, electrical current sensor and temperature sensor; design and implementation of the relevant signal processing circuits and the development of the data acquisition system.

Chapter 5 This chapter describes the different static tests that were conducted using the practical VDMS on a bespoke bench test rig that was designed and constructed. The results obtained from the static tests are also presented and discussed in this chapter. The static tests conducted included tests to validate the specification of the force actuator, to calibrate the force and displacement sensors and to determine the mass, stiffness constant and damping constant of the flow pipe. Other tests were conducted to determine the VDMS constant β and to investigate the agreement between the frequency response characteristics of the practical densitometry system and the theoretical model. An investigation which was

conducted to determine the capability of the VDMS to accurately predict the density of different test mixtures is also presented in this chapter and a discussion is presented of the measurement errors which were obtained. Lastly, the optimization of the VDMS operation is presented and the results obtained from using the optimized parameters of the densitometry system to predict the fluid density of the test mixtures are presented.

Chapter 6 This chapter presents a description of the experimental apparatus used in the current research. It describes the specification and flow measurement capability of the multiphase flow loop facility at the University of Huddersfield. Furthermore, the calibration procedures for the reference measurement instruments are also described in this chapter. These reference instruments include a differential pressure sensor, a turbine flow meter and a gravimetric flow measurement system. A technique for computing air flow rate measurements is also described. Lastly, the Fanning friction factor experimentally obtained for the flow loop working section is given.

Chapter 7 This chapter discusses the design and development of a computer based control system for implementing the optimized operation of the VDMS. This control system was implemented in LabVIEW and it includes program routines which allow the densitometry system data acquisition unit to acquire the force and displacement signals in real time; to compute an optimal frequency for the excitation signal that is generated and sent to the force actuator coils; and to compute the mixture density online.

Chapter 8 This chapter describes the flow loop experimental procedures and discusses the results obtained from using the practical VDMS and reference instruments to independently acquire density measurements in single phase (‘water only’) and two-phase (solids-in-water and air-in-water) vertically upward pipe flows. The predicted density measurements acquired from the practical VDMS are compared with density measurements obtained from using the reference instruments for different flow types of flow conditions. The

measurement errors obtained from the predicted density are also presented in this chapter and possible causes and sources of the errors are discussed. Possible solutions to reduce the density measurement errors from the VDMS are also suggested. The VDMS was also used to obtain mean phase volume fraction measurements in homogeneous solids-in-water and air-in-water vertical upward pipe flows. The results obtained from volume fraction measurements using the VDMS were also compared with volume fraction measurements obtained from the reference instruments. The measurement errors are discussed. Lastly, the effects of Coriolis forces on the measurement accuracy of the VDMS is discussed.

Chapter 9 This chapter presents the development of a modified mathematical model for predicting the mixture density for both compressible and incompressible multiphase mixtures. It further presents a comparison of the results of the frequency response characteristics obtained using the theoretical data from the density prediction models presented in chapter 4 and chapter 9 respectively, and the experimental data obtained from the practical densitometry system for air-in-water flows at different air volume fractions. Lastly, the predicted mixture densities for the air-in-water flow experiments were computed using the two density prediction models and the respective results obtained were compared with the reference density measurements and the errors were discussed in detail.

Chapter 10 This chapter presents the conclusions of the research work and summarises the aspects of the work that signify the author's contribution to knowledge of vibration densitometry measurement techniques. Recommendations for further work are also proposed in this chapter.

2.7 Summary

A range of existing methods that could conceivably be used or developed to address multiphase pipe flow mixture density measurement have been discussed in this chapter. The methods are discussed in terms of their fundamental principles of operation, design features, and shortcomings in providing

mixture density measurement. Furthermore, a critical discussion is given on the methodology chosen in the current research to address density measurement of flowing fluids. Lastly, a summary of the work packages undertaken in the program of research is presented.

Chapter 3

UNDERPINNING THEORY OF THE VIBRATING DENSITOMETRY SYSTEMS AND SIGNAL PROCESSING TECHNIQUES

3.1 Introduction

This chapter discusses the underpinning theory used in the development of a novel mathematical model for predicting mixture density in pipe flows. It also discusses the signal processing techniques used in implementing the mathematical model. The fundamental theory behind the development of the novel mathematical model was obtained from Newton's 2nd law of motion and Euler-Bernoulli beam theory. These fundamental theories were extended to describe the vibration characteristics of a mechanical system with mass, spring, and damping elements which is fixed at both of its ends. Once the mathematical model for predicting the density of a mixture was developed, a signal processing technique was required for practical implementation of the mathematical model. The signal processing technique was developed using the theory of the Discrete Fourier Transform.

3.2 Background theory of the vibrating densitometry system

The characteristics of the vibrating densitometry system can be described using a mechanical system with mass, spring and damping elements. The study of mechanical systems generally involves two important subjects, dynamics and vibration. The focus in this section will be on vibrating mechanical systems, which basically describe the oscillatory response to an excitation. The vibration of a mechanical system can be broadly categorised as follows; (i) free or forced vibration; (ii) harmonic or random vibration; (iii) damped or undamped vibration; and (iv) linear or non-linear vibration [143, 144]. A vibrating mechanical system where the external forcing excitation is an initial disturbance and the response dies out with time can be described as a freely vibrated system. Conversely, a vibratory mechanical system with a defined external excitation applied can be described as undergoing forced vibration. A vibratory mechanical system capable of dissipating energy until its response is completely attenuated can be described as a damped vibratory system. Most real systems will generally have some

form of damping that ensures the vibration amplitude diminishes with time. The elements in a vibrating mechanical system comprising of mass, spring and damping elements can be sub-divided into two groups, namely; energy (potential and kinetic) storage elements and energy dissipation elements. The mass and spring elements can be grouped as storage elements because they can store potential and kinetic energies, while the damping elements can be grouped as energy dissipation elements because they dissipate energy from the system. It is important to note that for a mechanical system to undergo vibration, it should have both potential and kinetic energy storage elements and these energies will be continually exchanged to maintain vibration. Similarly, a dissipation element is required to bring the system vibration to a stop [145].

The vibration response of a forced mechanical system with mass, spring and damping elements as applicable to the current research work will be described in this section. For such a system, the mathematical model describing the vibration characteristics can be developed using the Newtonian approach. Newton's second law can be explicitly applied to each element of the mechanical system to develop a set of equations that is used to describe its vibration characteristics. Generally, the response of a vibrating mechanical system to a forcing excitation will contain two components, a transient response and a steady state response. The transient response will be dependent on the system initial conditions and will fade away with time. Conversely, the steady state response will be dependent on the nature of the external forcing excitation applied to the system and will remain after the transient response has completely died out [146]. Analysis of the response of the forced vibratory mechanical system described above can be performed using either the time domain method or the frequency domain method and these methods can be related using Fourier Transforms. The preference of one analysis method over the other depends on factors such as the type of input forcing excitation, type of analytical model available, time duration of interest and quantities that needs to be determined.

3.2.1 Model of a Vibrating Mechanical System

As stated in the preceding section, the model of a simple vibrating mechanical system can be obtained using Newton's second law. The lumped parameter approach can be used to derive the model of such a system, where "lumped" implies that the mass of the system is assumed to be a concentrated mass acting at a single coordinate, also referred to as its degree of freedom. The degree of freedom of a vibrating body is the number of kinematically independent coordinates necessary to describe the complete motion of every element in the system. As mentioned previously, a vibratory mechanical system generally comprises inertia, stiffness and damping elements. For the vibrating mechanical system being considered, it is assumed to comprise one inertia, one stiffness and one damping element. Hence the system can be described using a single degree of freedom. If there were more than one inertia element in a vibratory system, then its characteristics could be described by using the appropriate degree of freedom corresponding to the number of inertial elements in the system. It should be noted at this point that only translation motion of the vibrating mechanical systems is considered in this section. The diagram of a simple mechanical vibratory system with one inertia element is shown figure 3-1. The input forcing function to the system is a harmonic function defined as $F(t)$.

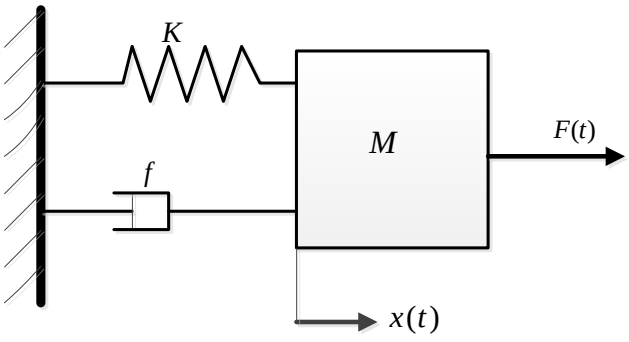

Figure 3-1: Diagram of a mechanical system with mass, spring and damping elements and having an input harmonic forcing excitation.

In figure 3-1, M represents the system mass, K is the stiffness constant of the spring element, f is the damping constant of the dissipative element, $F(t)$ is the time dependent harmonic forcing function and $x(t)$ is the resultant displacement of the system due to the forcing function. Since there is one inertia element in figure 3-1, the vibration kinematics is described using a single degree of freedom. If the

system mass is assumed to be a concentrated mass, then the force $F_m(t)$ exerted on the system due to its mass or inertia element is given by,

$$F_m(t) = M\ddot{x}(t) \quad \text{Equation 3-1}$$

where $\ddot{x}(t)$ is the system acceleration. Similarly, if the spring constant element is assumed to be linear, then the force exerted on the system by this element can be obtained using Hooke's law. This is given by,

$$F_s(t) = Kx(t) \quad \text{Equation 3-2}$$

where $F_s(t)$ is the force exerted on the system due to the spring element. The force exerted on the system due to the velocity of the dissipative element has a force-velocity relation given by,

$$F_d(t) = f\dot{x}(t) \quad \text{Equation 3-3}$$

where $F_d\ (t)$ is the force exerted on the system due to the damping element and $\dot{x}(t)$ is the system velocity. The free body diagram of the vibratory mechanical system when a harmonic forcing function F(t) is applied is shown in figure 3-2.

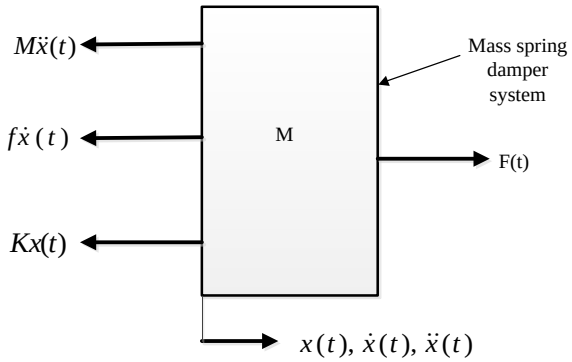

Figure 3-2: Free body diagram of the mass, spring damper system showing all forces acting on the single inertia element

The free body diagram shown in figure 3-2 can be used to obtain a general equation describing the vibration characteristics of the system. From Newton's second law, the resultant force acting on the vibratory system in the direction of its motion is given by,

$$F_m(t) = M\ddot{x}(t) \quad \text{Equation 3-4}$$

where $F_m(t)$ is the resultant force acting on the system mass in the direction of its motion (x axis). From the free body diagram given in figure 3-2, the resultant force is given by,

$$F_m(t) = F(t) - F_d(t) - F_s(t)$$ Equation 3-5

By combining equation 3-4 and equation 3-5 and simplifying, a second order differential equation that can be used to describe the response of the vibratory system to a forcing excitation is obtained as follows,

$$M\ddot{x}(t) + f\dot{x}(t) + Kx(t) = F(t)$$ Equation 3-6

The solution to equation 3-6 contains two parts, a transient solution and a steady state solution. The transient solution is mainly due to the free vibration response of the system when $F(t)$ equals zero and it is known to die out with time. When all transients have completely died out, the response of the system then contains only the steady state solution, which is due to the external forcing function $F(t)$. The resulting displacement of the system takes on the same frequency as the forcing function. For the vibratory system under consideration, the forcing function is assumed to be harmonic and is defined as follows,

$$F(t) = \mathbf{F}e^{j\omega t}$$ Equation 3-7

where **F** is a phasor representing the forcing function and ω is the frequency of the forcing function. Similarly, the displacement $x(t)$, velocity $\dot{x}(t)$ and acceleration $\ddot{x}(t)$ of the system are defined in term of the displacement phasor **X** by,

$$x(t) = \mathbf{X}e^{j\omega t}$$ Equation 3-8

$$\dot{x}(t) = j\omega\mathbf{X}e^{j\omega t}$$ Equation 3-9

$$\ddot{x}(t) = -\omega^2\mathbf{X}e^{j\omega t}$$ Equation 3-10

Substituting the expressions in equation 3-7 to equation 3-10 into equation 3-6 and simplifying gives,

$$(-\omega^2 M + j\omega f + K)\mathbf{X}e^{j\omega t} = \mathbf{F}e^{j\omega t}$$ Equation 3-11

Equation 3-11 can then be simplified and rearranged to complete the steps for converting the time dependent functions of the vibratory mechanical system given in equation 3-6 into the frequency dependent function given in equation 3-12.

$$\frac{\mathbf{X}}{\mathbf{F}} = \frac{1}{K - \omega^2 M + j\omega f}$$ Equation 3-12

Equation 3-12 is a complex expression that relates the resultant displacement phasor of the system to the phasor of the input forcing function in terms of the system parameters (M, f and K) and the forcing frequency ω. Additionally, equation 3-12 gives an important expression that can be used to generate the magnitude and phase Bode diagrams for a vibratory mechanical system, which is a useful tool to study its frequency response characteristics. Equation 3-12 can be used to generate the Bode diagrams for a fictitious second order vibratory mechanical system for a range of damping ratios within the interval $(0 \leq \zeta \leq 1)$, where $\zeta = f/2\sqrt{KM}$ as shown in figure 3-3.

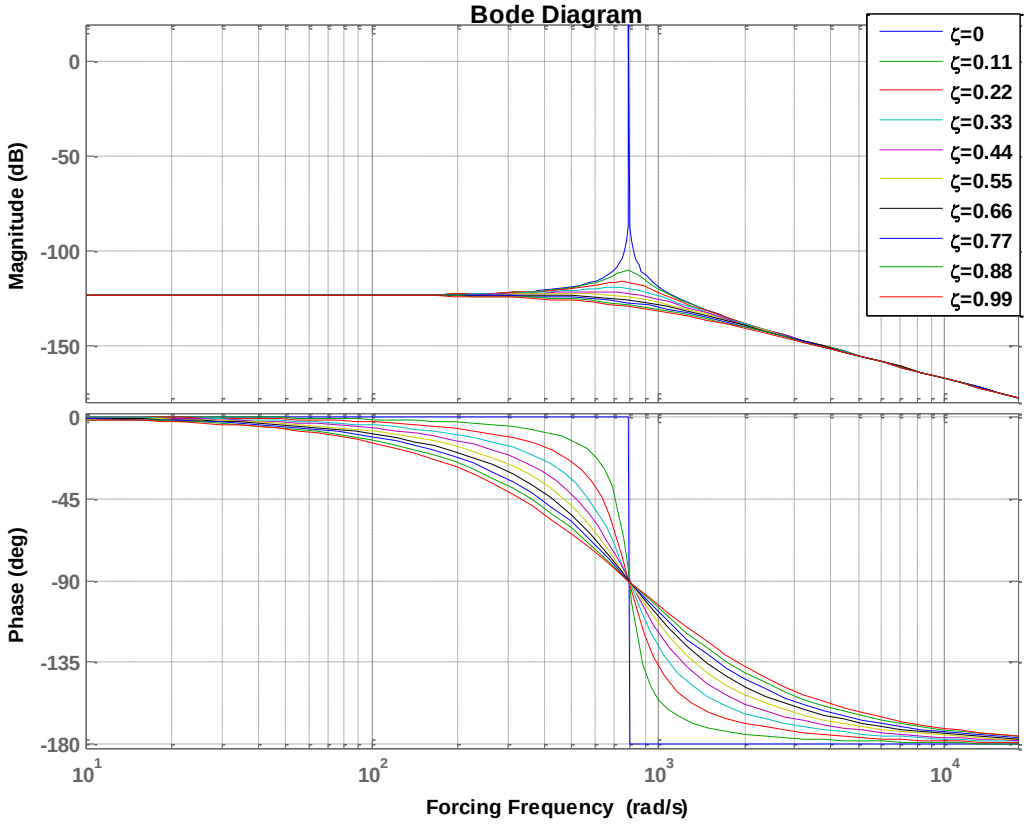

Figure 3-3:Typical magnitude ratio and phase angle plots for a second order mechanical vibratory system

3.3 Beam vibration theory

The theory of the transverse vibration of a beam fixed at both ends will be discussed in this section. Within the context of this thesis, this type of beam is interchangeably referred to as either an 'encastre' or 'fixed ends' beam. Euler-Bernoulli beam theory has been frequently used to describe the transverse vibration of beams. This theory first originated in the 18th century and was later modified by Timoshenko in 1921 [147]. The beam vibration theory provides a fundamental relationship between the transverse deflection y and distributed load per unit length q applied to a beam with constant cross section and material properties. This relationship is described by a fourth order differential equation given by,

$$\frac{d^4y}{dx^4} + \frac{q}{EI} = 0 \qquad \text{Equation 3-13}$$

where E is the elastic modulus, I is the second moment of area and x refers to a position along the beam. The solution to the fourth order differential equation can be obtained by integrating equation 3-13 four times and solving for the constants of integration. This is given by,

$$EIy = \frac{qx^4}{24} + \frac{C_1x^3}{6} + \frac{C_2x^2}{2} + C_3x + C_4 \qquad \text{Equation 3-14}$$

where C_1, C_2, C_3 and C_4 are the constants of integration. Next, the boundary conditions imposed on the beam by its supports can be used to determine the constants of integration. The first three modal shapes of a simply supported beam undergoing vibration are shown in figure 3-4.

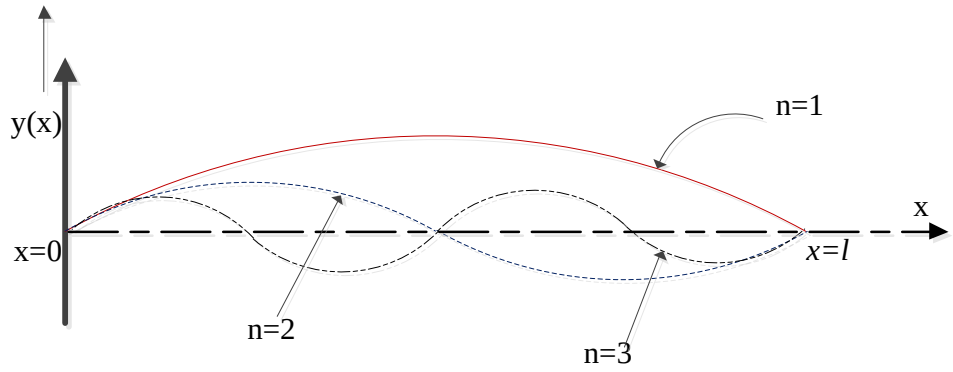

Figure 3-4: Diagram of the first three modal shapes of vibration for a simply supported beam

For a beam with 'fixed end' supports and with a distributed load, the boundary conditions are defined for the deflection and slope due to its fixed ends as *y(x)=0* at *x=0* or *x=l* and $\frac{dy(x)}{dx} = 0$ at *x=0* or *x=l*, where *l* is the length of the beam and *x* is the distance along the beam from one of its ends (see figure 3-4). These boundary conditions can then be applied to equation 3-14 to obtain the constants of integration. The solutions to equation 3-14 using the boundary conditions defined above are given as $C_1 = \frac{ql}{2}$, $C_2 = \frac{-ql^2}{12}$, and $C_3 = C_4 = 0$, and q and l are as defined previously. If the constants of integration obtained above are substituted into equation 3-14, a general expression describing the deflection of a beam with 'fixed end' supports due to its distributed weight is obtained as

$$y = \frac{qx^2}{24EI}(l - x)^2. \qquad \text{Equation 3-15}$$

It is common knowledge that a beam with fixed end supports will have its maximum deflection at the point where $x = \frac{l}{2}$, which coincides with its centre. Thus, the maximum deflection y_{mp} of a fixed end beam due to a uniformly distributed load applied at the centre will also be at the centre and it is given by

$$y_{mp} = \frac{ql^4}{384EI}. \qquad \text{Equation 3-16}$$

Additionally, the maximum static deflection of the beam due to its distributed weight *ql* is given by,

$$y_{mp} = \frac{ql}{K}$$ Equation 3-17

where K is the beam stiffness constant. It is important to state that q in equation 3-17 may be due to the weight per unit length of any uniformly distributed load on the beam as well as the weight per unit length of the beam itself (i.e. q is the weight per unit length of the beam plus load per unit length of material added to the beam). Equation 3-16 and equation 3-17 can then be combined and rearranged to obtain an expression for computing the stiffness constant of the beam. This is given by

$$K = \frac{384EI}{l^3}.$$ Equation 3-18

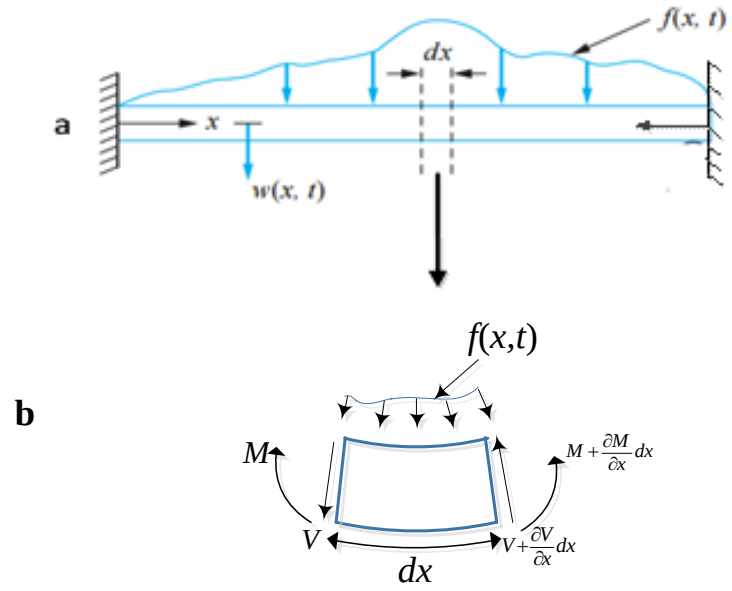

Figure 3-5: (a) Diagram of beam with 'fixed end' supports undergoing transverse vibration; (b) free body diagram of the differential element of the beam at an arbitrary time [143]

The fundamental frequency of vibration of an 'encastre' beam can be derived from the Euler-Bernoulli's beam theory [148]. Assuming the beam with fixed end supports shown in figure 3-5 (a) is homogeneous, isotropic, obeys Hooke's law and has a uniformly distributed mass M and length l, then the force required to cause a transverse displacement y of the beam from its equilibrium position at a distance x from one of its supports can be described by the equation of motion [149],

$$\frac{\partial^2}{\partial x^2}\left(EI\frac{\partial^2 y}{\partial x^2}\right) = -\frac{M}{l}\frac{\partial^2 y}{\partial t^2}$$ Equation 3-19

where $\frac{M}{l}$ is the mass per unit length of the beam, $\frac{\partial^2 y}{\partial t^2}$ is the acceleration of the beam in the transverse direction and $\frac{\partial^2}{\partial x^2}\left(EI\frac{\partial^2 y}{\partial x^2}\right)$ is the shear force acting on the beam. The solution to the equation of motion given in (3-19) is assumed to be of the form,

$$y = Y(x)\,sin(\omega_n t + \emptyset)$$ Equation 3-20

where ω_n is the fundamental frequency of the vibrating 'encastre' beam and $Y(x)$ is the amplitude of the transverse displacement at a distance *x* from one of the fixed end supports. By combining equation 3-19 and equation 3-20, the equation of motion of a vibrating beam with fix ends can be written as follows,

$$\left(\frac{\partial^4 Y(x)}{\partial x^4}\right) = \frac{M{\omega_n}^2}{EIl}Y(x)$$ Equation 3-21

Equation 3-21 is observed to be similar to the Euler-Bernoulli beam equation defined in equation 3-13. In order to determine the fundamental frequency of vibration $\omega_{n,1}$ of the beam with fixed ends, the solution to equation 3-21 will be required. For convenience and ease in solving equation 3-21, let

$$\propto^4 = \frac{M{\omega_{n,1}}^2}{EIl}.$$ Equation 3-22

By substituting equation 3-22 into equation 3-21, the Euler-Bernoulli beam equation for the beam with fixed end supports can be rewritten as,

$$\left(\frac{\partial^4 Y(x)}{\partial x^4}\right) = \propto^4 Y(x)$$ Equation 3-23

The general solution to equation 3-23 can be expressed in terms of trigonometric and hyperbolic functions and it is given by

$$Y(x) = C_1\,sin \propto l + C_2\,cos \propto l + C_3\,sinh \propto l + C_4\,cosh \propto l$$ Equation 3-24

The integration constants C_1, C_2, C_3 and C_4 can then be obtained by applying the homogeneous boundary conditions for a beam with fixed ends support as defined previously. Substituting the boundary conditions $Y(x) = 0$ at $x = 0$ or $x = l$ and $\frac{dY(x)}{dx} = 0$ at $x = 0$ or $x = l$ into equation 3-24 and simplifying gives,

$$cos(\propto l)\, cosh(\propto l) = 1 \qquad \text{Equation 3-25}$$

The equation given in 3-25 can be solved by plotting $\cosh(\propto l)$ against $\sec(\propto l)$. The first three consecutive roots of the plot are obtained as $\propto l = 4.73,\ 7.853$ and 10.996 respectively [149]. Since the frequency of vibration of the fixed end beam is a function of $\propto$, its fundamental frequency of vibration can be obtained using the first root obtained from the plot of $\cosh(\propto l)$ against $\sec(\propto l)$. This is given by,

$$\propto l = 4.73 \qquad \text{Equation 3-26}$$

$$\text{therefore, } \propto = \frac{4.73}{l} \qquad \text{Equation 3-27}$$

The fundamental frequency of vibration of the beam with fixed end supports undergoing transverse vibration can then be obtained by substituting equation 3-27 and equation 3-18 into equation 3-22 and simplifying the resulting expression. This is given by,

$$\omega_{n,1}{}^2 = \frac{K(4.73)^4}{384M} \qquad \text{Equation 3-28}$$

$$\omega_{n,1} = \beta\sqrt{\frac{K}{M}} \qquad \text{Equation 3-29}$$

where $\beta = 1.14$. The term β is a constant which relates the fundamental frequency of vibration $\omega_{n,1}$ of a beam with fixed end supports to K and M which are the stiffness constant and the total, uniformly distributed mass of the beam respectively. For a fixed end supported beam undergoing transverse motion, as shown in figure 3-5, the relationship given in equation 3-29 aptly describes the fundamental

frequency of the oscillatory motion. This important relationship will be applied to the equations of motion of the mass spring damper system investigated in this thesis..

3.4 Complex Discrete Fourier Transforms

The Discrete Fourier Transform abbreviated as DFT, is a powerful mathematical tool that has been in use over the years in numerous engineering applications to analyse measurement data. Most signals that occur in practical applications are analogue (continuous time) signals defined at all instants of time. These continuous time signals can be represented by a set of finite samples using a process known as discretization, enabling the DFT to be applied to continuous time signals. Unlike continuous time signals, discrete signals are only defined at discrete time intervals and this is known as the time domain representation of a discrete signal. The variation of the signal amplitude with time can be represented as a sequence of numbers given by,

$$x(t_r) = x_r, \qquad r = 0, 1, 2, 3, 4, \dots\dots\dots\dots \qquad \text{Equation 3-30}$$

where x_r is the rth term of the sequence, r is the index associated with this term and t_r is the discrete time and it is given by,

$$t_r = \frac{rT}{N} \qquad \text{Equation 3-31}$$

where T is the overall time period over which the signal is sampled and N is the total number of discrete samples taken over the time period. Alternatively, a discrete signal can be explicitly represented in terms of its frequency, known as the frequency domain representation. At each frequency, the amplitude and phase angle are required to completely represent the signal. The Discrete Fourier Transform technique enables the conversion of discrete signals between the time and frequency domains [150]. Although physical signals occurring in practical applications are real signals, it is often convenient to represent these real signals as a complex number. This offers a unique advantage in that it is easy and efficient to manipulate both the amplitude and phase properties of the signal at the same time. For a

discrete time signal $x(t_r)$ with N samples and a sampling period of T seconds, the Discrete Fourier Transform DFT equivalent, is described by a sequence of complex numbers $\mathbf{X}_\mathrm{k}$ defined by,

$$\mathbf{X}_\mathrm{k} = \frac{1}{N}\sum_{r=0}^{N-1} x_r e^{-j\left(\frac{2\pi rk}{N}\right)} \qquad \text{Equation 3-32}$$

For $k = 0, 1, 2, 3, \ldots\ldots\ldots\ldots\ldots\ldots, N-1$ and N is of the form, $N = 2^n$, where n is a positive integer. Alternatively, equation 3-32 can be written as,

$$\boldsymbol{X}_k = \frac{1}{N}\sum_{r=0}^{N-1} x_r \left[cos\left(\frac{2\pi rk}{N}\right) + j\, sin\left(\frac{2\pi rk}{N}\right)\right] \qquad \text{Equation 3-33}$$

If the real and imaginary components of $\mathbf{X}_\mathrm{k}$ are denoted as $\mathrm{Re}\{\mathbf{X}_\mathrm{k}\}$ and $\mathrm{Im}\{\mathbf{X}_\mathrm{k}\}$ respectively, then for values of k from 0 to $\mathrm{N}-1$, these components are given by,

$$Re\{\mathbf{X}_k\} = \frac{1}{N}\sum_{r=0}^{N-1} x_r \left[cos\left(\frac{2\pi rk}{N}\right)\right] \qquad \text{Equation 3-34}$$

$$Im\{\mathbf{X}_k\} = j\frac{1}{N}\sum_{r=0}^{N-1} x_r \left[sin\left(\frac{2\pi rk}{N}\right)\right]. \qquad \text{Equation 3-35}$$

The DFT is such a useful tool that it can be used to distinguish between various signal components at different frequencies. It has found great application in recovering low level deterministic signals buried in high amplitude random noise [151]. When dealing with DFTs, it is important to understand the phenomenon of aliasing in the process of discretizing a continuous signal. Shannon's sampling theorem provides a solution to this problem [152]. From Shannon's sampling theorem, unique values of $\mathbf{X}_k$ will exist from $0 \leq \frac{k}{T} \leq \frac{N}{2T}$ for the DFT defined in equation 3-32. It is therefore important that when dealing with DFTs, Shannon's sampling theorem is obeyed to ensure the accurate reconstruction of the properties of the time continuous signal from its samples without losing any information as a result of undersampling. In order to determine an appropriate sample number N to use in this work, that will ensure the properties of a continuous time signals can be accurately reconstructed using the DFT technique, an analysis was performed to reconstruct the properties of a deterministic continuous time

signal with random noise as defined in equation 3-36. In this analysis, different sample numbers N were used in the discretization of the continuous time signal.

$$x(t) = 3 + 2\,sin(2\pi 35t) + 6\,sin(2\pi 175t) + random\ noise \quad \text{Equation 3-36}$$

$x(t)$ is converted to an equivalent discrete time signal $x(t_r)$ using different sample number ($N = 2^n$) from n=9 to n=16, over a period T of 1 second. It should be stated that the signal sampling frequency f_s (where $f_s = \frac{N}{T}$) satisfies the Shannon's sampling criteria for all the values of N used in this investigation. MATLAB "FFT" algorithm was then used to compute the DFT of $x(t_r)$. The plots presented in figure 3-6 (a-c) shows the deterministic continuous time signal $x(t)$ and the real and imaginary parts of the DFT components of $x(t)$.

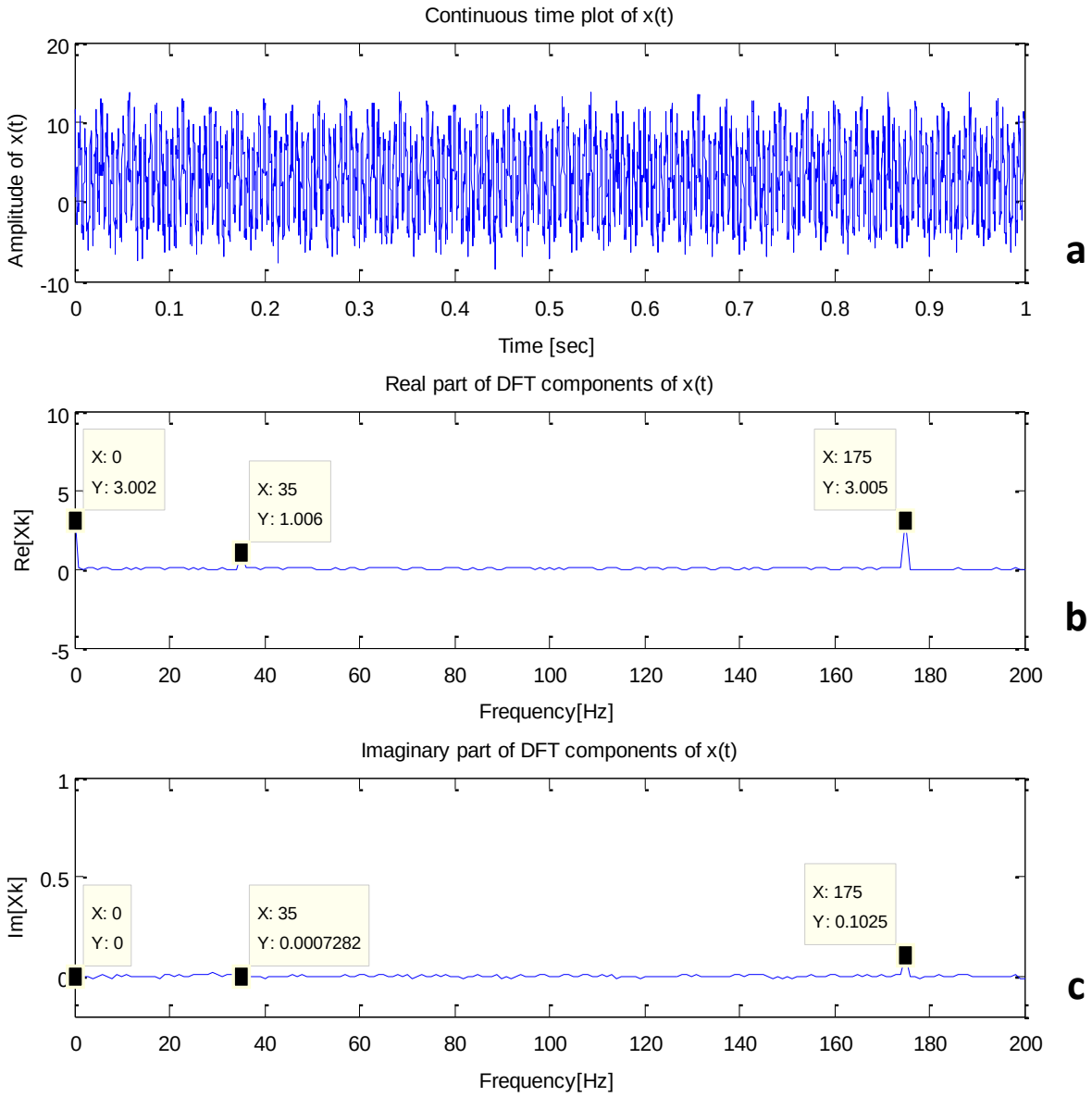

Figure 3-6: (a)Continuous time plot of x(t); (b) and (c) Plots of real and imaginary parts of DFT components of x(t)

Figure 3-6 (a-c) respectively show the continuous time plot of $x(t)$, the amplitudes of the real parts of the DFT components of $x(t)$ and the imaginary parts of the DFT components of $x(t)$. The advantage of the DFT technique becomes obvious from the plots shown in figure 3-6 (b) and (c). Firstly, the amplitude, phase and frequency properties of the individual signal components in $x(t)$ cannot be easily deduced from figure 3-6(a). However, with the DFT plots shown in figure 3-6 (b) and (c), the amplitude, phase and frequency information of the individual signals in $x(t)$ can be readily obtained from the

complex DFT plots by writing the respective DFT components of $x(t)$ in complex number form as $\mathbf{X}(\omega) = Re\{\mathbf{X}_k\} + Im\{\mathbf{X}_k\}$ and converting $\mathbf{X}(\omega)$ to its polar form. It is important to note that the amplitudes of the DFT components recovered in this way are only half of the actual amplitudes of the original signal component because the DFT plot shows frequencies from 0Hz to the Nyquist frequency. For the different values of N from 2^9 to 2^{16} used in this investigation, the amplitude, phase and frequency property of the individual signals in $x(t)$, recovered using the DFT technique, are compared with the original values defined in equation 3-36 and the relative percentage error is computed and presented in figure 3-7.

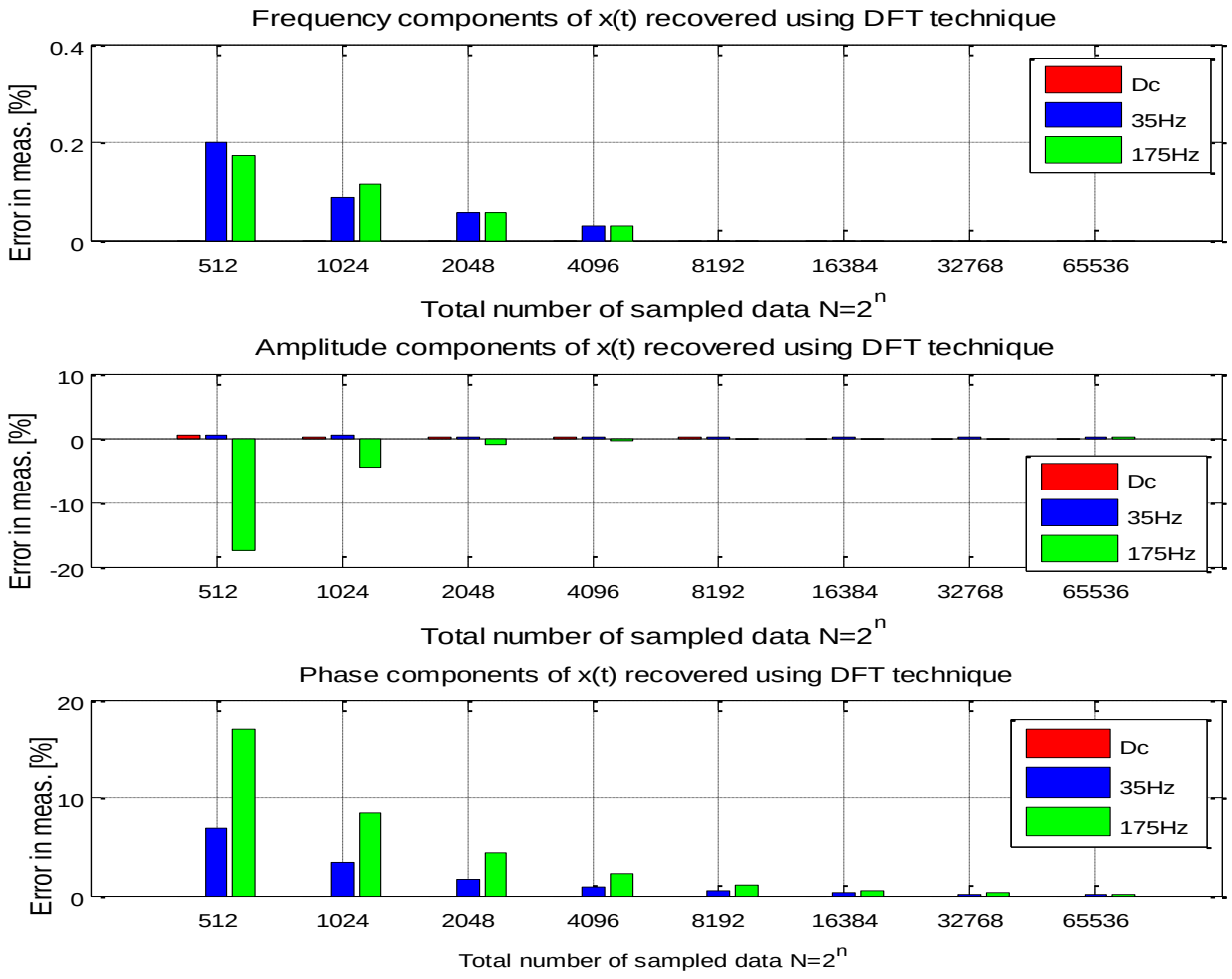

Figure 3-7(a-c): Measurement error in frequency, amplitude and phase components of x(t) recovered using DFT technique

The plots shown in figure 3-7 (a-c) respectively present the relative percentage error in the frequency, amplitude and phase of $x(t)$ recovered using the DFT technique. In figure 3-7 (a-c), the vertical axes represent the relative percentage difference between the frequency, amplitude and phase of $x(t)$ recovered using the DFT technique and the actual values defined in equation 3-36, while the horizontal axes represent the different number of sample data points N used in discretizing $x(t)$. The red, blue and green legend plots represent the DC component, 35Hz signal component and 175Hz signal component in $x(t)$ respectively. The results show that the error observed when the DFT technique was used to recover the frequency, amplitude and phase properties of $x(t)$ reduces progressively as the number of samples N used in the discretization of $x(t)$ was increased from 2^9 to 2^{16}. The least error in the recovered signal properties (frequency, amplitude and phase) was observed when the N was 2^{16}. Thus, in this research, $N = 2^{16}$ was used to discretize the continuous time signals which were measured. It is also important to state here that the NI data acquisition device used in this research had a data acquisition limit of 31.25ksamples/s for each analog input and this hardware limitation factor was also important in the decision to use 65536 ($N = 2^{16}$) data samples points in this research.

3.5 Summary

In this chapter, a mathematical model has been developed to describe the vibratory motion of a mechanical system comprising mass, spring and damping elements and having a harmonic forcing function as its input. The physical laws describing the force exerted by each element of the mechanical system were used to obtain an equation defining their contributing forces on the system. These expressions were then used to develop a general equation relating the forcing input and the displacement of the system in the frequency domain. Next, Euler-Bernoulli beam theorem was used to derive a mathematical relationship for the fundamental frequency of vibration of a beam with fixed end supports. This relationship, combined with the mathematical model for a vibratory mechanical system will be extended in chapter 4 to describe the vibratory motion of the vibrating densitometry system

developed in this research. Lastly, the theory of the complex DFT of a discrete time signal was presented and the results of an investigation to determine a suitable data sample number N when using the DFT technique was presented, which minimizes error in the recorded frequency, amplitude and phase of a sampled signal.

Chapter 4

DESIGN AND DEVELOPMENT OF THE VIBRATING DENSITY MEASUREMENT SYSTEM

4.1 Introduction

This chapter begins with a description of a novel mathematical model that was developed to predict the vibration characteristics of a mechanical system with mass, spring and damping elements and which was subsequently used to measure fluid density in single phase and multiphase pipe flows. The advantages of this model over existing models are also highlighted in this chapter. Furthermore, the design and development of a vibrating density measurement system (abbreviated to VDMS in all chapters of the thesis for convenience) is presented. The VDMS (see figure 4-3) consists of a measurement unit, a signal processing and conditioning unit and a data acquisition unit. The sub-components of the measurement unit include a straight length of pipe section with flexible corrugated bellows at both ends (referred to as the sensing pipe in this thesis), an electromechanical force actuator, a force sensor, a displacement measurement transducer, a signal generation unit to provide the required excitation signal to the force actuator and, finally, sensors for measuring the drive current and temperature. The signal conditioning and processing unit comprises of electronic circuits for converting the signals from the force sensor, displacement transducer, force actuator, current sensor, and temperature sensor into usable forms. These circuits were designed to give noise reduction and signal amplification. The data acquisition unit comprises of a 16 bit National Instrument data acquisition (DAQ) card and a computer with LabVIEW and MATLAB software.

4.2 Development of novel mathematical model for density prediction in pipe flow

The sensing pipe included in the measurement unit is an important component of the VDMS and its vibration characteristic, when a forcing is applied to it, was used to develop the novel mathematical model to predict the density of a mixture flowing through a pipe. As with most mechanical systems,

the sensing pipe used in this research has mass, spring and damping elements and its dynamic response can be accurately described by approximating the mathematical model to that of a mass spring damper system. The behaviour of such a dynamic system when subjected to a forcing excitation can be analysed either in the time domain or in the frequency domain and these domains can be related using Discrete Fourier Transforms as described in chapter 3. In this research, frequency domain analysis was preferred due to the nature of the input excitation (being sinusoidal) and the ease of analysis, it affords in the development of a signal processing technique for implementing the mathematical model on a practical system. It was shown in equation 3-12 that the force-displacement response of a mechanical system with mass, spring and damper elements undergoing vibration when subjected to a forcing excitation is given by,

$$\frac{\mathbf{X}}{\mathbf{F}} = \frac{1}{K - \omega^2 M + j\omega f} \qquad \text{Equation 3-12}$$

where **F** is the force phasor, f is the damping constant, K is the stiffness constant, M is the total mass and **X** is the displacement phasor of the mechanical system. A hypothetical undamped natural frequency ω_n of such a system can be obtained as follows,

$$\omega_n = \sqrt{\frac{K}{M}} \qquad \text{Equation 4-1}$$

Assuming that the sensing pipe used in the VDMS construction is fixed at both ends, then its hypothetical undamped natural frequency ω_n of vibration can be related to its actual fundamental frequency of vibration $\omega_{n,1}$ as shown in equation 3-29.

$$\omega_{n,1} = \beta\omega_n \qquad \text{Equation 3-29}$$

where β is a constant. It was therefore appropriate that equation 3-12 be modified to accurately describe the dynamic behaviour of the sensing pipe with 'fixed end' supports and subjected to a harmonic forcing excitation. Thus, by combining equation 3-12 and equation 3-29 and simplifying the resulting

expression, a modified model that can be used to accurately describe the force-displacement response of the sensing pipe with fixed ends is obtained as,

$$\frac{\boldsymbol{X}}{\boldsymbol{F}} = \frac{1}{-\omega^2 \widehat{M} + j\omega \hat{f} + K} \qquad \text{Equation 4-2}$$

where $\widehat{M}$ and $\hat{f}$ are the modified mass and modified damping constant of the sensing pipe, respectively, and these parameters are defined as,

$$\widehat{M} = \frac{M}{\beta^2} \qquad \text{Equation 4-3}$$

$$\hat{f} = \frac{f}{\beta} \qquad \text{Equation 4-4}$$

M and f are the actual mass and actual damping constant of the sensing pipe and β is the constant defined in equation 3-29. Note that in equation 3-12, only the system mass and damping constant are affected by frequency and are thus modified accordingly in equation 4-2. The mathematical model given in equation 4-2 was then modified and extended to develop a novel mathematical model that can be used to accurately describe the dynamic behaviour of the sensing pipe with fixed ends and any mixture contained within it. The mathematical model was developed from physical modelling of the dynamics of the sensing pipe and its contents. A key assumption made in the development of this model was that the total mass of the mechanical system is a lumped sum of the masses of the sensing pipe and its contents, hence its response can be described by using a single degree of freedom. Also from section 3.3, it was shown that the maximum transverse displacement of a beam with 'fixed end' supports due to a distributed load is at its centre. Hence, in this design, the forcing excitation was applied at the sensing pipe centre and the measured displacement response was also taken at the pipe centre. The diagram in figure 4-1 shows the physical model of the sensing pipe coupled to the mass of its contents within it.

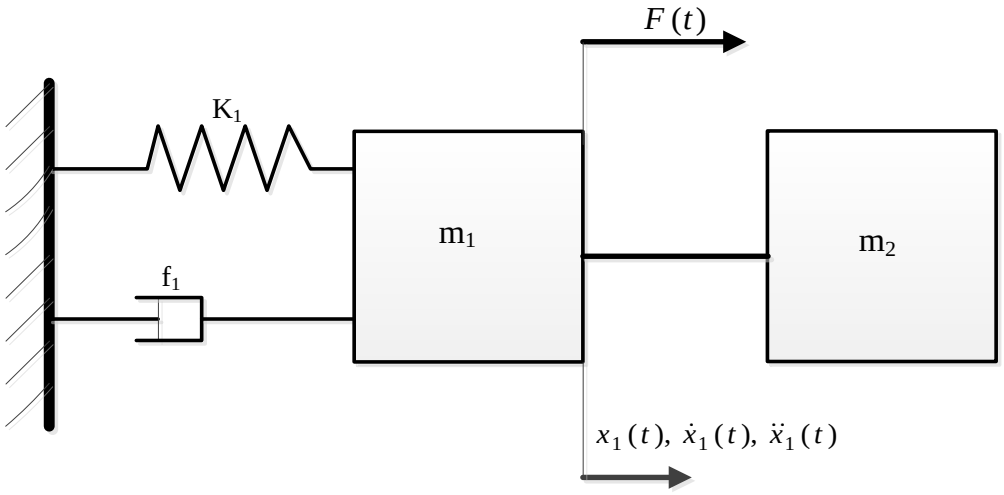

Figure 4-1: Model of sensing pipe and its contents having a single degree of freedom

The following definitions apply to the variables in the diagram shown in figure 4-1,

$$m_1 = \beta^2 \hat{m}_1$$ Equation 4-5

where m_1 is the true mass of the sensing pipe when empty, $\hat{m}_1$ is the modified mass of the sensing pipe when empty and β is referred to as the VDMS constant in this thesis. Similarly,

$$m_2 = \beta^2 \hat{m}_2$$ Equation 4-6

where m_2 is the true mass of the contents in the sensing pipe and $\hat{m}_2$ is the modified mass of the contents in the sensing pipe. Furthermore, the definitions for the actual damping constant f_1 of the sensing pipe is given as,

$$f_1 = \beta \hat{f}_1$$ Equation 4-7

where $\hat{f}_1$ is the modified damping constant of the sensing pipe. The free body diagram depicting the forces acting on the system when a harmonic forcing excitation is applied to the centre of the sensing pipe is shown in figure 4-2.

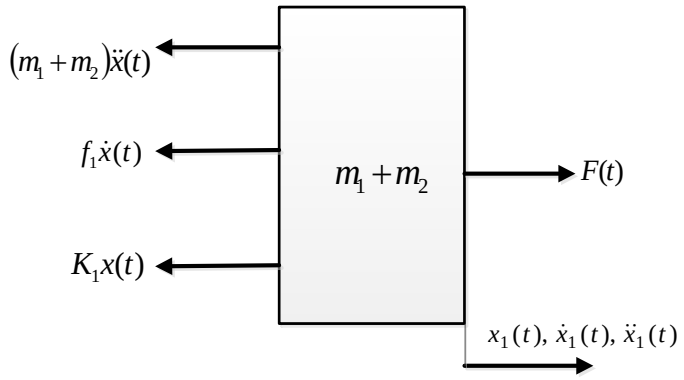

Figure 4-2: Free body diagram of VDMS with harmonic forcing excitation applied

In the free body diagram shown in figure 4-2, $\ddot{x}(t)$, $\dot{x}(t)$ and $x(t)$ respectively represent the acceleration, velocity and displacement of the mechanical system, whilst $F(t)$ represents the force applied. The total mass of the mechanical system is defined as the lump sum of the masses of the sensing pipe m_1 and its content m_2. Therefore, the equation of motion when a harmonic force excitation $F(t)$ is applied to the mechanical system (sensing pipe and its contents) can be described for each of its elements using the free body diagram in figure 4-2. This is given by,

$$(\hat{m}_1 + \hat{m}_2)\ddot{x}(t) + \hat{f}_1\dot{x}(t) + K_1x(t) = F(t) \qquad \text{Equation 4-8}$$

By substituting the phasor representation of the forcing excitation, displacement, velocity and acceleration given in equation 3-7 to equation 3-10 respectively into equation 4-8, the equation of motion of the mechanical system shown in figure 4-1 is represented in phasor form by,

$$(\hat{m}_1 + \hat{m}_2)\left(-\omega^2\mathbf{X}e^{j\omega t}\right) + j\omega\hat{f}_1\mathbf{X}e^{j\omega t} + K_1\mathbf{X}e^{j\omega t} = \mathbf{F}e^{j\omega t} \qquad \text{Equation 4-9}$$

Equation 4-9 can be simplified to give an expression that can be used to describe the dynamic response of the system shown in figure 4-1 when a forcing excitation is applied to its centre. This is given by,

$$\left[\{K_1 - \omega^2(\hat{m}_1 + \hat{m}_2)\} + j\omega\hat{f}_1\right]\mathbf{X} = \mathbf{F} \qquad \text{Equation 4-10}$$

From equation 4-10, the relationship between the displacement and force phasors at the centre of the system is given by,

$$\frac{\mathbf{X}}{\mathbf{F}} = \frac{1}{\left[\{K_1 - \omega^2(\hat{m}_1 + \hat{m}_2)\} + j\omega\hat{f}_1\right]}$$ Equation 4-11

In order to express equation 4-11 in a standard form, its complex conjugate is used to multiply the numerator and denominator terms. This gives the following,

$$\frac{\mathbf{X}}{\mathbf{F}} = \frac{\{K_1 - \omega^2(\hat{m}_1 + \hat{m}_2)\} - j\omega\hat{f}_1}{\{K_1 - \omega^2(\hat{m}_1 + \hat{m}_2)\}^2 + \left\{\omega\hat{f}_1\right\}^2}$$ Equation 4-12

Equation 4-12 is a complex function which is represented in the Cartesian form as shown below,

$$\boldsymbol{z} = a + jb$$ Equation 4-13

where a and jb are the real and imaginary parts of the complex function **z** respectively. In this derivation, the maximum force and displacement at the sensing pipe centre, and described in equation 4-12, are expressed in Euler form as follows,

$$\frac{\mathbf{X}}{\mathbf{F}} = \frac{|X_{max}(\omega)|}{|F_{max}(\omega)|}cos\,\theta(\omega) + j\frac{|X_{max}(\omega)|}{|F_{max}(\omega)|}sin\,\theta(\omega)$$ Equation 4-14

where $|X_{max}(\omega)|$ and $|F_{max}(\omega)|$ are the modulus of the maximum amplitude of the displacement and force respectively, $\theta(\omega)$ is the phase difference between the displacement and force and ω is the forcing frequency. $\frac{|X_{max}(\omega)|}{|F_{max}(\omega)|}cos\,\theta(\omega)$ is referred to as the in-phase component of the system response whilst $\frac{|X_{max}(\omega)|}{|F_{max}(\omega)|}sin\,\theta(\omega)$ is the out-of-phase component of the system response. By comparing equation 4-12 and equation 4-14, an alternative expression can be derived for the in-phase and out-of-phase components of the system response in terms of the system properties K_1, $\hat{m}_1, \hat{m}_2$, $\hat{f}_1$ and ω. These are obtained as follows,

$$\frac{|X_{max}(\omega)|}{|F_{max}(\omega)|}cos\,\theta(\omega) = \frac{K_1 - \omega^2(\hat{m}_1 + \hat{m}_2)}{\{K_1 - \omega^2(\hat{m}_1 + \hat{m}_2)\}^2 + \left\{\omega\hat{f}_1\right\}^2}$$ Equation 4-15

$$\frac{|X_{max}(\omega)|}{|F_{max}(\omega)|}sin\,\theta(\omega) = \frac{-\omega\hat{f}_1}{\{K_1 - \omega^2(\hat{m}_1 + \hat{m}_2)\}^2 + \left\{\omega\hat{f}_1\right\}^2}$$ Equation 4-16

where $|X_{max}(\omega)|$, $|F_{max}(\omega)|$ and $\theta(\omega)$ can be obtained from the DFTs of the measured force and displacement signals. Two measurement parameters $\hat{a}$ and $\hat{b}$ are defined using the in-phase and out-of-phase components of the system response. These are given by,

$$\hat{a}(\omega) = \frac{\frac{|X_{max}(\omega)|}{|F_{max}(\omega)|} cos\,\theta(\omega)}{\frac{|X_{max}(\omega)|}{|F_{max}(\omega)|} sin\,\theta\,(\omega)} = \cot\theta(\omega) \qquad \text{Equation 4-17}$$

$$\hat{b}(\omega) = \frac{|X_{max}(\omega)|}{|F_{max}(\omega)|} cos\,\theta(\omega). \qquad \text{Equation 4-18}$$

Also, equivalent expressions can be obtained for $\hat{a}$ and $\hat{b}$ in terms of the system properties by substituting equation 4-15 and equation 4-16 into equation 4-17 and equation 4-18 respectively. These are given by,

$$\hat{a}(\omega) = \frac{\left\{\{\omega^2(\hat{m}_1 + \hat{m}_2)\} - K_1\right\}}{\left(\omega\hat{f}_1\right)} \qquad \text{Equation 4-19}$$

$$\hat{b}(\omega) = \frac{K_1 - \omega^2(\hat{m}_1 + \hat{m}_2)}{\{K_1 - \omega^2(\hat{m}_1 + \hat{m}_2)\}^2 + \left\{\omega\hat{f}_1\right\}^2}. \qquad \text{Equation 4-20}$$

Equation 4-19 and equation 4-20 give the theoretical expression for computing the measurement parameters $\hat{a}$ and $\hat{b}$ in terms of the system properties K_1, $\hat{f}_1$, $\hat{m}_1$, $\hat{m}_2$ and ω. In order to develop a mathematical model that can be used to obtain the mass m_2 of the contents of the sensing pipe, equation 4-19 and equation 4-20 can be combined and rearranged to make $\hat{m}_2$ the subject of formula. But firstly, equation 4-19 is rearranged to make $\omega\hat{f}_1$ the subject of formula and squaring the resulting expression gives,

$$\left(\omega\hat{f}_1\right)^2 = \frac{\{K_1 - \omega^2(\hat{m}_1 + \hat{m}_2)\}^2}{\hat{a}^2(\omega)}. \qquad \text{Equation 4-21}$$

Equation 4-20 and equation 4-21 can then be combined and simplified to obtain a single expression relating the measurement parameters $\hat{a}$ and $\hat{b}$ and the system properties $K_1, \hat{m}_1, \hat{m}_2$ and ω. This is obtained as,

$$\hat{b}(\omega) = \frac{1}{\left[\{K_1 - \omega^2(\hat{m}_1 + \hat{m}_2)\}\left(1 + \frac{1}{\hat{a}^2(\omega)}\right)\right]}. \quad \text{Equation 4-22}$$

The mass of the contents of the sensing pipe can then be obtained by rearranging the expression in equation 4-22 to make $\hat{m}_2$ the subject of formula. The sequence of algebraic operations used to obtain $\hat{m}_2$ is shown by the following set of equations. Since the parameters $\hat{a}$ and $\hat{b}$ can be obtained from measurement from the VDMS operation, equation 4-22 is simplified to give,

$$\frac{1}{\hat{b}(\omega)\left(1 + \frac{1}{\hat{a}^2(\omega)}\right)} = \{K_1 - \omega^2(\hat{m}_1 + \hat{m}_2)\}. \quad \text{Equation 4-23}$$

Also, since the sensing pipe stiffness constant K_1 can be determined by bench testing, equation 4-23 is further simplified as given below,

$$K_1 - \frac{1}{\hat{b}(\omega)\left(1 + \frac{1}{\hat{a}^2(\omega)}\right)} = \{-\omega^2(\hat{m}_1 + \hat{m}_2)\}. \quad \text{Equation 4-24}$$

A similar argument applies to the frequency ω of the forcing excitation which can be obtained from measurement. Equation 4-25 is simplified as follows

$$\hat{m}_1 + \hat{m}_2 = \frac{1}{\omega^2}\left\{K_1 - \frac{1}{\hat{b}(\omega)\left(1 + \frac{1}{\hat{a}^2(\omega)}\right)}\right\}. \quad \text{Equation 4-25}$$

Equation 4-25 gives an expression that can be used to obtain the total modified mass of the sensing pipe and its contents. The modified mass of the contents of the sensing pipe can then be obtained by subtracting the modified mass of the sensing pipe from equation 4-25. This is given by

$$\hat{m}_2 = \left[\frac{1}{\omega^2}\left\{K_1 - \frac{1}{\hat{b}(\omega)\left(1 + \frac{1}{\hat{a}^2(\omega)}\right)}\right\} - \hat{m}_1\right]. \quad \text{Equation 4-26}$$

By substituting equation 4-26 into equation 4-6, the true mass of the contents of the sensing pipe can be computed as follows,

$$m_2 = \beta^2 \left\{ \left[\frac{1}{\omega^2} \left(K_1 - \frac{1}{\hat{b}(\omega)\left(1 + \frac{1}{\hat{a}^2(\omega)}\right)} \right) - \hat{m}_1 \right] \right\}. \quad \text{Equation 4-27}$$

The mathematical model derived in equation 4-27 gives the expression for computing the actual mass m_2 of the sensing pipe contents in terms of the sensing pipe stiffness constant K_1, its modified mass $\hat{m}_1$ when empty, the frequency ω of the forcing excitation , the defined measurement parameters $\hat{a}$ and $\hat{b}$ and the VDMS constant β. For convenience, the term containing the defined measurement parameters $\hat{a}$ and $\hat{b}$ in equation 4-27 shall be represented by a single variable called lambda λ, where lambda is defined as,

$$\lambda(\omega) = \frac{1}{\hat{b}(\omega)\left(1 + \frac{1}{\hat{a}^2(\omega)}\right)}. \quad \text{Equation 4-28}$$

The mathematical expression for computing the mass m_2 of the mixture contained within the sensing pipe can therefore be rewritten as,

$$m_2 = \beta^2 \left\{ \frac{1}{\omega^2} \{K_1 - \lambda(\omega)\} - \hat{m}_1 \right\} \quad \text{Equation 4-29}$$

where $\lambda(\omega)$ and ω are obtained from measurements from the VDMS. Finally, the predicted density ρ_m of the sensing pipe contents can be obtained as follows,

$$\rho_m = \frac{m_2}{V_{pipe}} \quad \text{Equation 4-30}$$

where the mass m_2 of the sensing pipe contents is obtained using equation 4-29 and V_{pipe} is the fixed volume of the sensing pipe. The model shows that provided $\hat{m}_1$, K_1 and β are known, then the density of the pipe contents can be obtained by measurement of λ and ω. The predictive mathematical model given in equation 4-29 represents a novel contribution of this work and it was used in this research to compute the mass of the contents of the sensing pipe from which density measurements were calculated. The above model formed the basis from which the new density system was developed. The advantages of the novel density model are presented in section 4.2.1.

It is important to mention here that the accuracy of the model given in equation 4-29 is dependent on the assumption that the mass of the sensing pipe and its contents are considered as a lumped mass $(m_1 + m_2)$ and their motion can be described using a single degree of freedom. Hence, for incompressible flows e.g. liquid only, liquid-liquid flows and solids-liquid flows the model is expected to give accurate density prediction of the flowing fluid. This accuracy may be reduced if the model is used to predict density in compressible flows, e.g. gas-liquid flows. The mathematical expressions developed in equation 4-29 and equation 4-30 were used in this research work to predict the density in both single phase and multiphase pipe flows.

4.2.1 Advantages of the novel mathematical model for predicting density in pipe flows

The novel mathematical model given in equation 4-29 has the following advantages when compared with existing models for determining density in a vibratory densitometer.

1) The model allows for the system to be operated over a wider frequency range of choice by forcing the sensing pipe to vibrate at that frequency, unlike previous density prediction models which require that the densitometry system must be operated at its resonant frequency to obtain accurate measurement.

2) The measured density of the sensing pipe contents is obtained using the measurement parameters $\hat{a}$ and $\hat{b}$ and the forcing frequency ω (which could be a frequency other than its resonant frequency) obtained from the measured force and dispalcement.

3) The damping characteristics of the contents of the sensing pipe are duly accounted for by the measurement parameters $\hat{a}$ and $\hat{b}$.

4) Since the frequency ω of the forcing is known, the value of ω in equation 4-29 can be accurately determined.

4.3 Design and construction of vibrating density measurement system (VDMS)

This section describes the design and construction of the vibrating density measurement system VDMS. As stated in the introductory section of this chapter, the VDMS consisted of a measurement/sensing unit, a signal conditioning and processing unit and a data acquisition unit. The measurement unit includes a straight length of pipe with corrugated bellows at both ends of the pipe, an electromechanical force actuator, a force sensor, a displacement sensor, a temperature sensor, a current sensing circuit and a system to generate the excitation signal to the actuator coils. The signal conditioning and processing unit include the associated electronic circuits required to attenuate signal noise and amplify the respective signals from the force sensor, displacement sensor, temperature sensor and current sensing circuit to a required level. The data acquisition unit includes the hardware and software used to acquire the required signals from the associated signal conditioning circuitry. A diagram of the VDMS sub-units is shown in

figure 4-3.

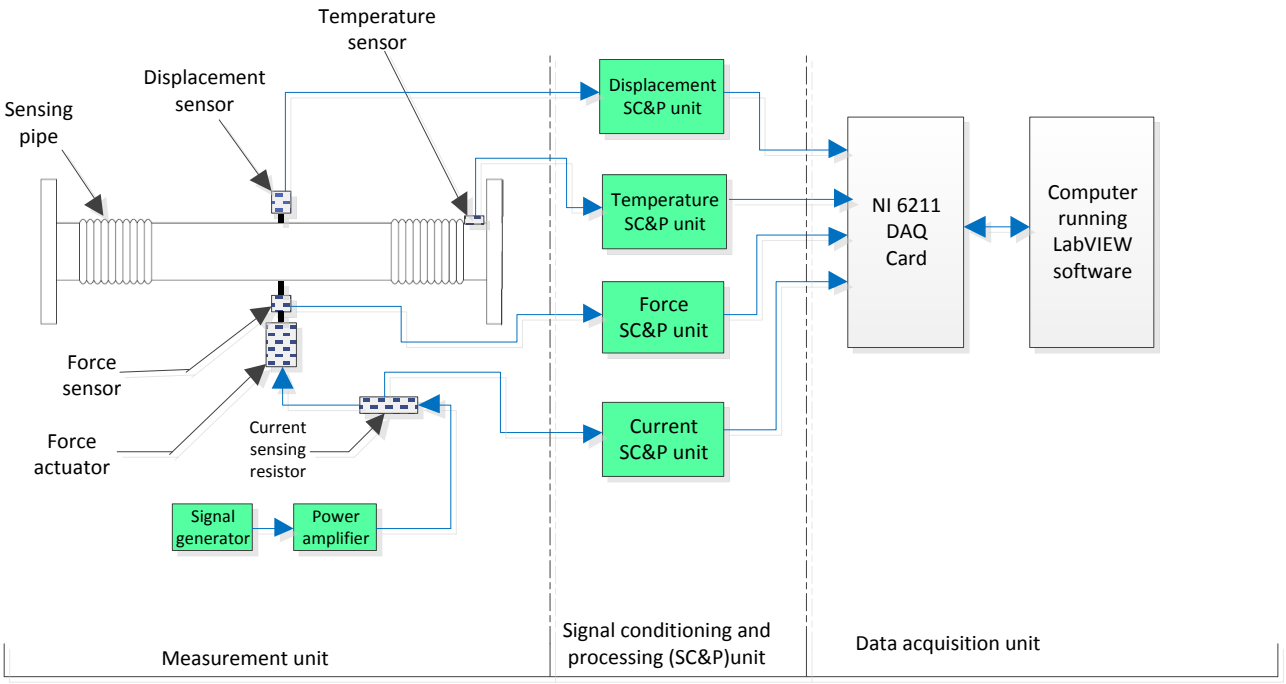

Figure 4-3: Block diagram of the VDMS subunits

4.3.1 Mechanical design and construction of sensing pipe

The sensing pipe is an important component of the VDMS measurement unit. When developing the novel mathematical model given in equation 4-29, it was assumed that the dynamic behaviour of the sensing pipe and its contents can be accurately described as a mechanical system with mass, spring and damping elements. Hence, it was assumed that the sensing pipe used for the VDMS also had mass, spring and damping properties. Since the magnitude of the displacement response associated with the VDMS is influenced by the sensing pipe stiffness, it was important that the sensing pipe used in the VDMS measurement unit was adequately flexible to ensure that the vibration amplitude was large enough to be detected by the displacement sensor. An extensive theoretical analysis was made using Euler-Bernoulli beam theory, described in section 3.3, to determine appropriate pipe dimensions required to give a desired displacement at the centre of the sensing pipe. The dimensions obtained were then used to develop a three dimensional (3D) model of the sensing pipe using Solidworks software [153]. Solidworks finite element analysis was then used to optimize the specifications for the sensing pipe such as, its length, thickness, number of corrugated bellows and bellows pitch, to ensure that measurable deflections could be obtained at the sensing pipe centre when undergoing excitation by the force actuator described in section 4.3.2. The sensing pipe was constructed from 316L stainless steel and has an internal diameter of 78mm, which corresponds to the internal diameter of the working section of the flow loop at the University of Huddersfield which was used in the current research. From equation 3-16, it will be recalled that the transverse deflection at the centre of a pipe with fixed ends due to its weight was shown to be dependent on its length and second moment of area. Thus, in order to obtain a measurable transverse deflection at the sensing pipe centre, its length and wall thickness were respectively made as long and as thin as was permissible by pipe manufacturing limitations. The maximum pressure that the sensing pipe could withstand before buckling was used to determine the smallest wall thickness allowable. In addition, the cost of the pipe material and ease of welding the material were other factors that were considered. A stainless steel sheet with a thickness of 1mm was

used to construct the sensing pipe. Two flexible bellows were welded at 50mm from both ends of the sensing pipe. The bellows each have ten corrugations with a pitch and height of 9.4mm and 2.4mm respectively. The maximum working pressure of the bellows is 10bar, which is higher than the maximum working pressure of the flow loop at the University of Huddersfield. The total length of the sensing pipe is 600mm. BS4505 stainless steel flanges were welded to both ends of the sensing pipe to provide rigid and water tight connection of the VDMS to the flow loop. One advantage of this design is that the corrugated bellows included in the sensing pipe construction helped to increase its flexibility, thereby ensuring that a greater deflection could be achieved for a given force applied and hence resulting in an increase in the measurement sensitivity. Other advantages of this design are that it is non-intrusive and the sensing pipe material is relatively inexpensive and readily available. The choice of stainless steel also guarantees that the sensing pipe is relatively immune to corrosion.

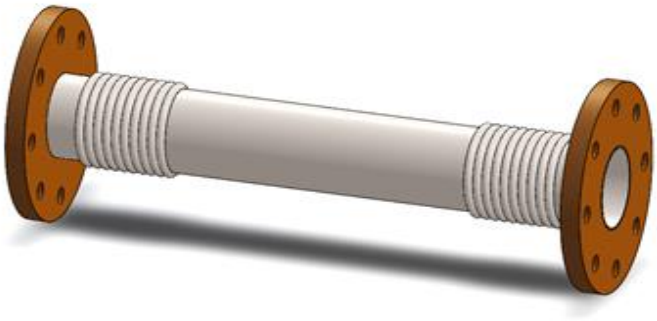

Figure 4-4: 3D model of sensing pipe designed using Solidworks software

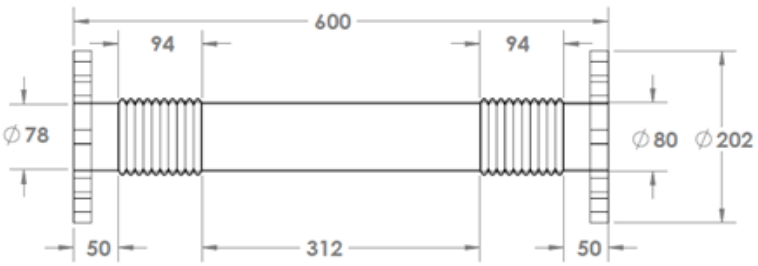

All dimensions are in mm

Figure 4-5: Diagram of sensing pipe showing its dimension specifications

Figure 4-4 and figure 4-5 respectively show a 3D model and the dimension specifications of the sensing pipe. Once the sensing pipe had been designed to specification and constructed, it became necessary to determine the specifications of the ancillary sensors included in the measurement unit of the VDMS as discussed in sections 4.3.2 and 4.3.3.

4.3.2 Specification of force actuator

A force actuator was required to generate the force needed to mechanically excite the sensing pipe. The type of actuator selected for this research was dependent on a number of factors including the principle of operation, suitability to the model developed and cost. Having carried out extensive research based on the selection criteria mentioned above a "voice coil" type electromagnetic force actuator [154] was selected. This actuator consists of a moving coil assembly with incorporated shaft contained within an immovable permanent magnet assembly as depicted in figure 4-6.

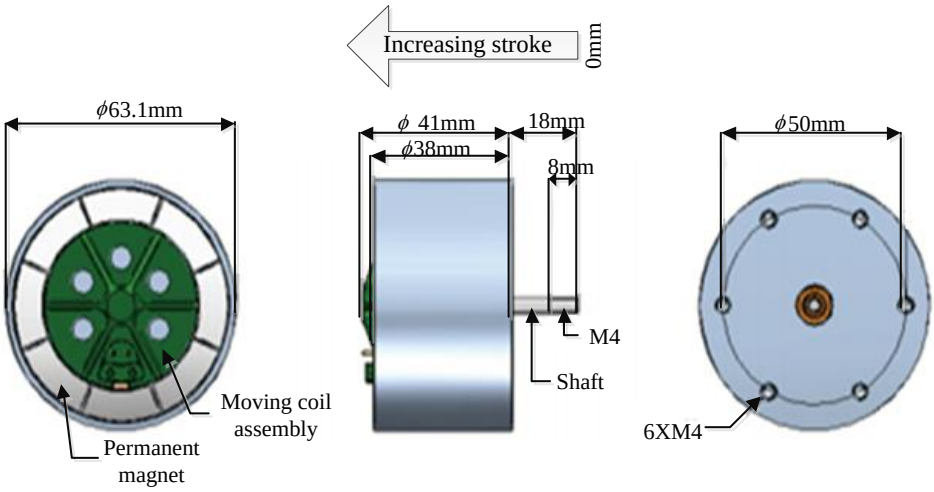

Figure 4-6: Picture of the voice coil actuator showing its parts and dimensions[155]

The operation of the electromagnetic force actuator is based on the Lorentz force principle whereby a current is passed through a moving coil assembly contained within an immovable permanent magnet assembly. The interaction of the magnetic field generated by the current with the magnetic field of the permanent magnet will cause a force to act upon the moving coil assembly. This force can be defined by,

$$F(t) = I(t)k_{vca} \qquad \text{Equation 4-31}$$

where $F(t)$ is the force generated, $I(t)$ is the current applied and k_{vca} is a constant of proportionality for the force actuator and it is defined by,

$$k_{vca} = BLN \qquad \text{Equation 4-32}$$

where B is the magnetic flux density generated by the fixed permanent magnet, N is the number of turns of the coil windings and L is the effective length of the moving coil in the magnetic field. Since the permanent magnet flux density is fixed, the direction of the linear displacement of the moving coil assembly depends solely on the direction of the current flowing through the coils. An advantage of 'voice coil' actuators (VCA) over solenoids and other types of force actuator is that they have a linear force-current relationship, which makes control of the applied force easier to achieve by directly controlling the current applied to the moving coil assembly. Other advantages are short stroke, bi-directional linear actuation and low hysteresis. The force specification of the voice coil actuator can be estimated from the force-displacement relationship of a vibratory mechanical system. The force required to displace a vibratory mechanical system is given by [156],

$$|F| = |X|K\left\{\left(1-\frac{\omega}{\omega_n}\right)^2 + \left(2\zeta\frac{\omega}{\omega_n}\right)^2\right\}^{0.5} \qquad \text{Equation 4-33}$$

where $|F|$ is the magnitude of the applied force from the voice coil actuator, $|X|$ is the magnitude of the system displacement, K is the system stiffness constant, ζ is the system damping ratio, ω_n is the system undamped natural frequency and ω is the frequency of force applied to the system. In order to obtain an estimate of the force magnitude required to displace the sensing pipe by 10microns at different forcing frequencies, a plot of applied force versus forcing frequency was generated using equation 4-33.

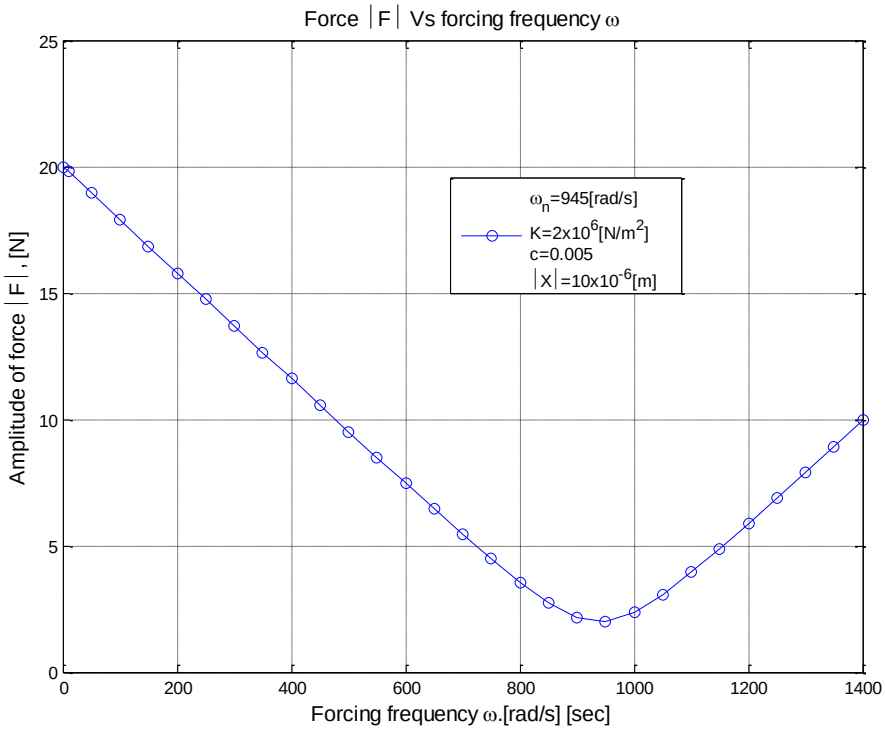

Figure 4-7:Force versus forcing frequency plot for a vibrating mechanical system for known values of K, c, x and ω_n

The maximum amplitude of the vibration of the sensing pipe was chosen as 10microns in this analysis because of the accuracy, range, sensitivity and cost of available displacement sensors capable of measuring such magnitudes of displacement. The stiffness constant K was set as $2 \times 10^6 \mathrm{N/m}$. This value was intentionally made 35% greater than the sensing pipe stiffness constant (see section 5.3.2). The main reason for using this greater stiffness constant in the analysis described here was to ensure that the force actuator capacity is large enough to give a measurable vibration amplitude of the sensing pipe when it is mechanically excited. From figure 4-7, it is seen that the force required to cause the sensing pipe to vibrate with a maximum amplitude of 10microns, for the values of K, ζ and ω_n used, is a maximum when the frequency of the forcing excitation is zero and this force decreases to a minimum when the forcing frequency equals the resonant frequency of the vibrating mechanical system. From figure 4-7, a force with a maximum amplitude of 22N would be required to cause the vibratory mechanical system to vibrate with an displacement amplitude of 10microns when a dc forcing function is applied to the actuator. At the system resonant frequency however, the force amplitude

required to produce a displacement amplitude of 10microns is just above 2N. Consequently, a VM6340 Voice Coil Actuator (VCA) was purchased from Geeplus Europe [157] for this research. For convenience, this actuator will be referred to as VCA in further sections of this thesis. The VCA purchased is capable of generating a peak force of 31N at 100% excitation signal duty cycle (ED) (see figure 4-8), where ED as used here refers to the percentage duration when the actuator excitation signal is "on" during one period. The force-stroke displacement characteristic of the VCA is presented in figure 4-8. This diagram shows that if the VCA is operated at 100% excitation signal duty cycle (ED), the force-displacement characteristic will be linear (i.e. the force generated by the actuator will be proportional to the current applied) when the displacement of the stroke of the moving coil assembly is less than 2.5mm. The VCA was operated within this specification in this research. However, if the VCA is operated at 25% and 10% duty cycle respectively, it can generate forces up to 65N and 105N.

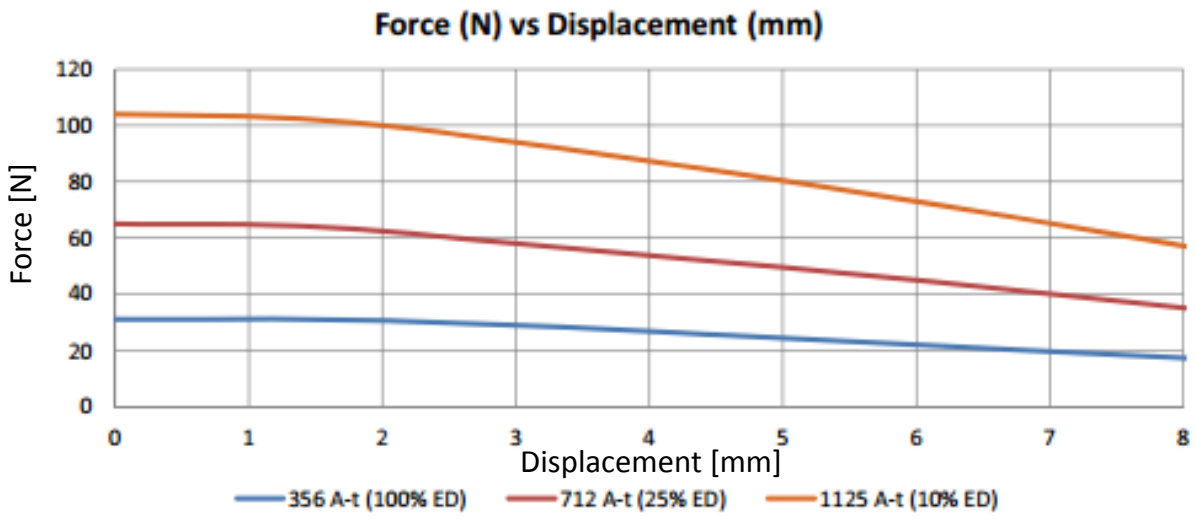

Figure 4-8: Force versus displacement plot of VM6340 voice coil actuator[155]

Since the density prediction model given in equation 4-29 is in the frequency domain, it was also important to understand how the VCA excitation signal frequency affects its force stroke displacement relationship. From the investigations conducted, it was observed that when the VCA moving coil was excited, the stroke of the moving shaft increased with an increase in the frequency of the excitation signal. However, a mechanical stop could be used to limit the stroke of the moving coil assembly

without it affecting the magnitude of the force generated. Thus, provided the stroke of the moving coil assembly was limited to less than 2.5mm using a mechanical stop, the VCA could be operated at any frequency of choice. In this research, the stroke of the VCA moving coil assembly was limited to 2.5mm using a bespoke "soft" mechanical stop.

Figure 4-9: (a) and (b) Bespoke "soft" mechanical stop used to limit VCA shaft stroke

4.3.3 Specification of force sensor

A force sensor was used to measure the force generated from the VCA, thus providing the force data necessary for the density prediction model given in equation 4-29. The choice of force sensor was based on the required force measurement range, sensor specification, measurement accuracy and cost. A strain gauge type load cell was obtained for this purpose which was capable of measuring both compressive and tensile forces. It has M4 threads on both faces that could be used to attach the sensor to the measurement setup. This load cell was purchased from LCM Systems limited and a picture of it is shown in figure 4-10.

Figure 4-10: Picture of tension and compression load cell [158]

Typically, a compression and tension load cell consists of four strain gauges connected in a Wheatstone bridge configuration, which are bonded onto a central sensing area of the load cell structure. The Wheatstone bridge is an electrical equivalent of two parallel voltage divider circuits.

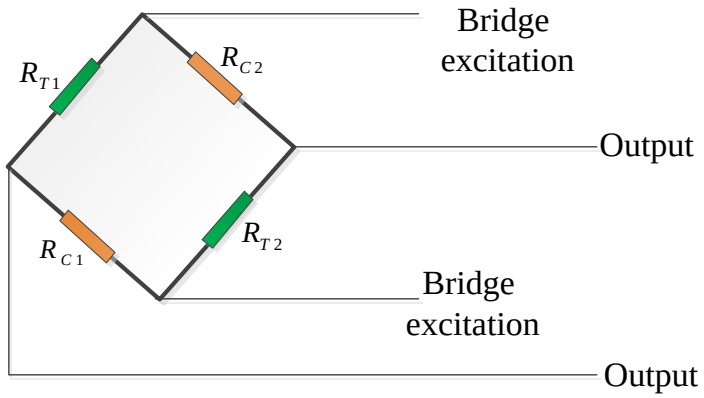

Figure 4-11: Load cell tension and compression strain gauges configured in a Wheatstone bridge circuit

Figure 4-11 is a diagram of a tension and compression load cell comprising of four strain gauges connected in a Wheatstone bridge configuration. The two strain gauges labelled R_{T1} and R_{C1} form one voltage divider circuit of the bridge, while the other two strain gauges R_{C2} and R_{T2} form the other voltage divider circuit. The completed Wheatstone bridge requires a stable dc voltage supply to excite the circuit. The excitation voltage usually varies from 5Vdc to 10Vdc but is typically 10Vdc. The output voltage V_o of the Wheatstone bridge circuit is measured between the middle nodes of the two voltage divider circuits and is given by,

$$V_o = \left(\frac{R_{T2}}{R_{T2} + R_{C2}} - \frac{R_{C1}}{R_{T1} + R_{C1)}}\right) V_{exc} \qquad \text{Equation 4-34}$$

where R_{T1} and R_{T2} are the resistances of the strain gauges in tension, R_{C1} and R_{C2} are the resistances of the strain gauges in compression and V_{exc} is the Wheatstone bridge circuit DC excitation voltage. When a force is applied to the bonded strain gauges on the load cell a resistance change takes place which causes the Wheatstone bridge circuit to become unbalanced. This action provides an output signal that is linearly proportional to the force applied. The output signal is typically a few millivolts and requires amplification before it can be read. The signal amplification and processing circuitry for

the load cell is discussed in section 4.3.4. Since the maximum force required to displace the sensing pipe by 10microns was estimated as approximately 20N, a load cell with a safe load limit of 100N and a non-linearity error of $\pm 0.25\%$ of rated load capacity was selected. The reason for selecting this rating was to avoid damage to the load cell due to normal overloading and/or shock loading. Further information on the load cell is contained in the data sheet included in Appendix D.

4.3.4 Load cell signal conditioning and processing circuitry

The load cell works by converting a force acting on the strain gauges into an equivalent electrical signal. The output signal from the load cell is an electrical signal in millivolts and may have electrical noise embedded in it. It was therefore important to remove the noise embedded in the load cell signal and to amplify its magnitude to the required level. The specification for the load cell signal conditioning and processing circuit was obtained from LCM System's limited [158] for this research. The load cell conditioning circuit provided voltage excitation for the strain gauge bridge as well as strain sensing and amplification. The circuit comprises a bridge voltage excitation circuit, strain sensing and amplification circuit, filter circuit, span and zero offset adjustment circuits.

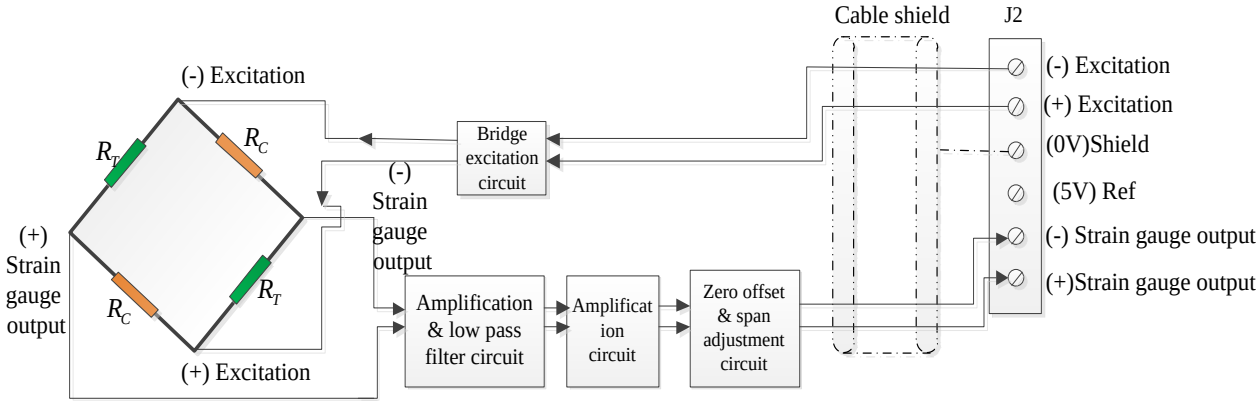

Figure 4-12: Block diagram of load cell signal conditioning and processing circuitry

From figure 4-12, the strain gauge bridge is provided with a constant voltage excitation of 10Vdc from a precision voltage regulator when the strain excitation wires from the load cell are connected to the points labelled "$(+)$ excitation" and "$(-)$ excitation" on the J2 screw terminal block. When a force is applied to the load cell, the bridge resistances change and a very small voltage in the millivolt range is

sensed across the outputs of the strain gauge bridge. The output from the strain gauge bridge is amplified in a two stage procedure. Firstly an instrumentation amplifier, with appropriate sensitivity and common mode rejection ratio (CMMR) and having a fixed gain is used to amplify the voltage signal to a level where it can be accurately measured. The amplified output is then passed through a low pass filter to improve the output signal quality in noisy environments. The cut-off frequency of the filter can be set using a potentiometer. The output signal from the low pass filter is further amplified using an instrumentation amplifier with adjustable gain. The span and zero of the output signal from the instrument amplifier can be adjusted as required using the relevant potentiometers. See Appendix D for the load cell and signal conditioning circuit data sheets.

4.3.5 Calibration of the load cell and associated signal conditioning and processing circuit.

Since the density prediction model given in equation 4-29 requires the measured force data from the VDMS to compute the terms $\hat{a}$ and $\hat{b}$, it was crucial that the measured force data obtained from the load cell was highly reliable and accurate. For this reason, the calibration of the load cell and associated signal conditioning and processing circuit used in this research were outsourced to LCM Systems Limited. The load cell and signal conditioning and processing circuit were calibrated using a BS EN ISO 7500-1 certified calibration setup that is traceable to the United Kingdom Accreditation Service (UKAS). The result of the calibration performed by LCM Systems Limited, using five calibration points, is shown in figure 4-13.

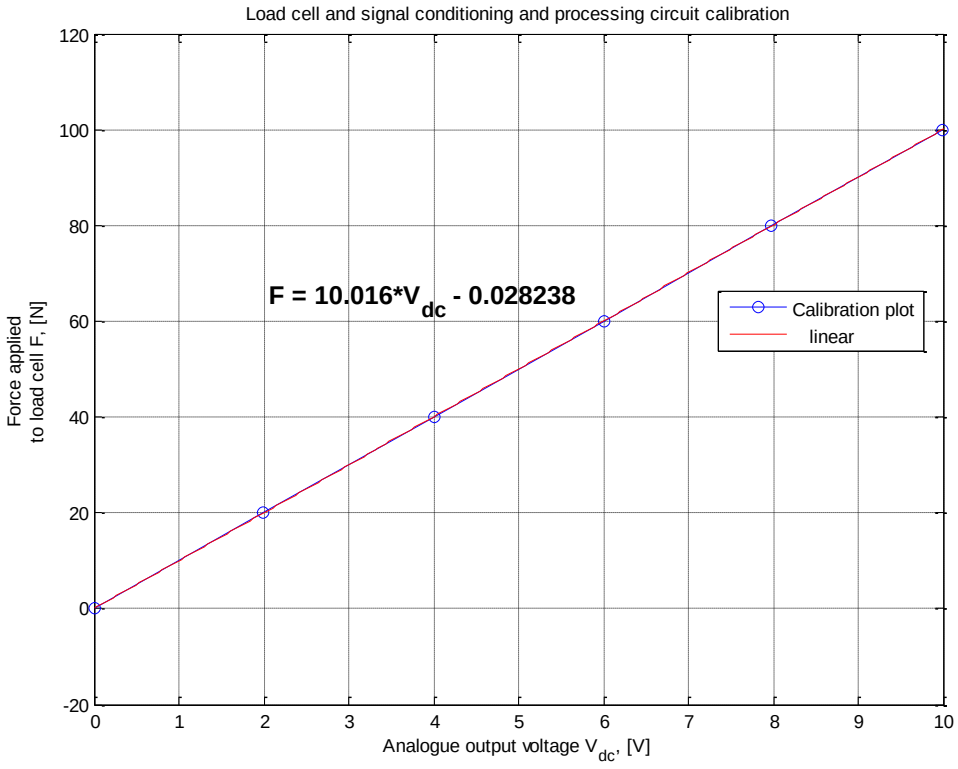

Figure 4-13: Calibration plot of load cell and signal conditioning and processing circuit

From the plot shown in figure 4-13, it can be seen that the force voltage relationship of the load cell and signal conditioning and processing circuit was linear for an applied force range from 0-100N. A calibration equation relating the force sensed by the load cell to the output voltage from the signal conditioning circuit was found from the line of best fit as,

$$F = 10.016V_{dc} - 0.028238 \qquad \text{Equation 4-35}$$

where F is the force measured and V_{dc} is the analogue output voltage measured from the load cell signal conditioning and processing circuit. This equation was used to compute the measured force in all the results presented in chapter 5, chapter 8 and chapter 9 of this thesis.

4.3.6 Specification of displacement sensor

A displacement sensor was required to measure the displacement of the sensing pipe at its centre and to provide displacement measurement data to the density prediction model given in equation 4-29. In order to select a suitable displacement sensor for use with the VDMS several factors were considered. These factors included the required measurement range of the sensor, its accuracy, principle of

operation and cost. A linear variable displacement transducer (abbreviated to LVDT) was selected for the VDMS because it is capable of measuring displacements as small as a few millionths of an inch. Additionally, there is no physical contact across the transducer sensing element, but rather it relies on electromagnetic coupling, which means clean data, infinite resolution and a very long life [159]. Typically, an LVDT is an electromechanical device that comprises of 3 coils - a primary coil and two symmetrically wound secondary coils connected in "opposite series" as shown in figure 4-14.

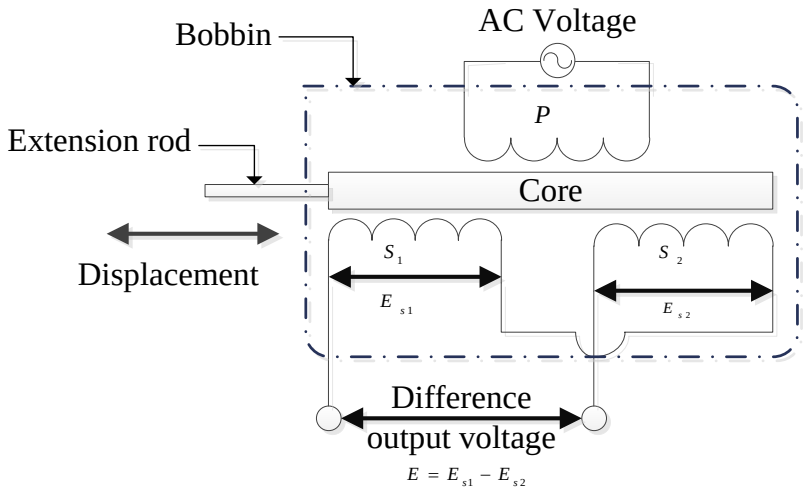

Figure 4-14: Conventional circuit connection of the linear variable differential transducer (LVDT)

The primary coil is designated P and the secondary coils are designated S_1 and S_2 respectively. A free moving cylindrical magnetic core is fitted within the bobbin and passes through the centre of the coil assembly providing a path for the magnetic flux linking the coils. One end of the magnetic core is usually fitted to an extension rod, which emerges from one end of the cylindrical bobbin and is attached to a component, the displacement of which is to be measured (see figure 4-14). Electrical connections to the primary and secondary coils are normally made using screened multi-core cables emerging from the side of the casing of the bobbin. This transducer uses the linear variable differential transformer (LVDT) principle to measure linear displacement from an electrical signal containing phase information (for direction) and amplitude information (for distance). If the primary coil of the LVDT is energised with a sinusoidal voltage of constant magnitude, the magnetic flux developed in the primary coil is coupled to the secondary coils S_1 and S_2 by the magnetic core and thereby induces

sinusoidal voltages in the secondary coils. The operation of the LVDT will now be described with respect to the position of the magnetic core from its reference position (also known as null point). The diagram shown in figure 4-15(a-c) is used to illustrate the main points.

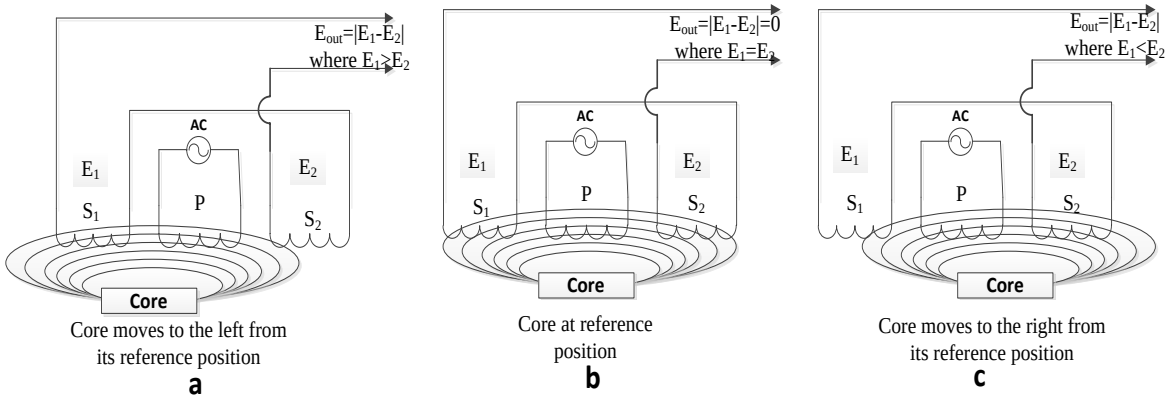

Figure 4-15: Position of LVDT magnetic core relative to its null point and the resultant differential induced voltages in the secondary coils [160]

If the movement of the magnetic core is to the left from the reference position (see figure 4-15 (a)), the flux coupled to S_1 will be more than S_2, likewise the induced voltages and the magnitude of the output E_{out} will be $|E_1 - E_2|$ where $E_1 > E_2$. The phase angle of E_{out} relative to the voltage in the primary coil will be $180°$ (see figure 4-16). Alternatively, if the magnetic core moves towards the right from the reference position (see figure 4-15 (c)), the magnitude of the output E_{out} will be $|E_1 - E_2|$ where $E_1 < E_2$ and the phase angle between E_{out} and the voltage in the primary coil will now be $0°$ (see figure 4-16). At its reference position (see figure 4-15 (b)), the phase angle between E_{out} and the voltage in the primary coil will be $90°$ and the magnitude of E_{out} will be zero since $E_1 = E_2$. This is expected since the secondary coils are symmetrical, but connected in series opposition. When the magnetic core moves away from its null position as shown in figure 4-15 (a and c), there is an increase in the magnetic flux coupled to the secondary coil in the direction of the core movement and a decrease in the magnetic flux in the other secondary coil away from the core movement. In all three scenarios described above, the magnitude of the differential induced voltage E_{out} across the LVDT secondary

coils can be interpreted to indicate displacement from the reference null position, and the phase of E_{out} indicates the direction of the displacement [160].

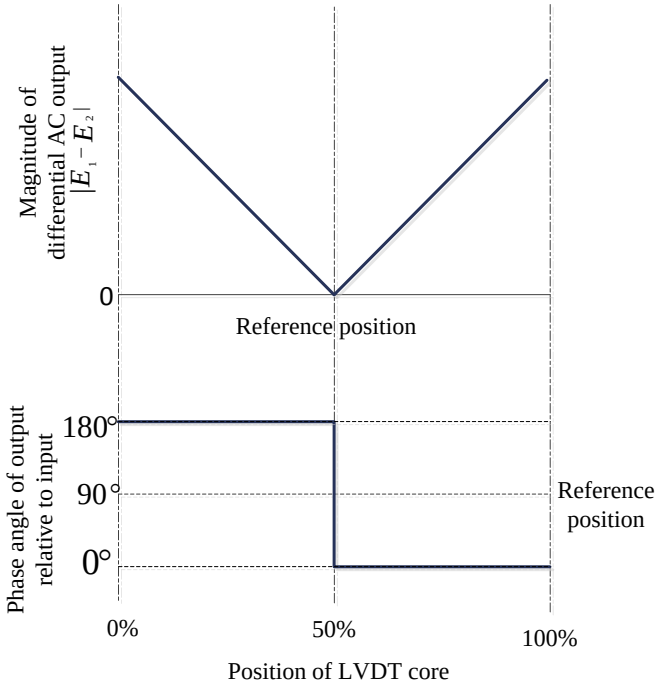

Figure 4-16: Magnitude and phase output of conventional LVDT versus core displacement

The diagram in figure 4-16 shows the variation of the magnitude and phase of the LVDT output as the distance travelled by the magnetic core goes from 0% to 100%, where 50% indicates the reference position of the core. With LVDTs, the magnitude and phase of the output relative to the excitation phase respectively enable the signal processing electronics to determine the distance and direction travelled by the magnetic core with respect to its reference point. An LVDT was purchased for this research from RDPE electronics [159]. The LVDT has a measurement range of ± 0.5mm and a non-linearity error of $\pm 0.25\%$ of the full scale measurement. More details on the specification of the LVDT used in this research are provided in the data sheet shown in Appendix C.

4.3.7 LVDT signal conditioning and processing circuitry

Recall from section 4.3.6, the LVDT has been described as an electromechanical transducer whose input is the mechanical displacement of the transducer magnetic core, and the output is a differential voltage in the transducer secondary coils, proportional to the position of the magnetic core from its

reference position. A signal processing circuit was therefore required to determine the distance and direction travelled by the LVDT magnetic core from its reference position. An electronic circuit capable of providing the aforementioned signal processing function for the LVDT was obtained from RDPE. The design and operation of this circuit is described below.

The signal conditioning and processing circuitry of the LVDT consists of a sine wave oscillator and power amplifier circuit, a demodulator circuit, a filter circuit and an output amplifier circuit. The sine wave oscillator circuit generates a low distortion sine wave signal with a frequency of 5kHz and a constant amplitude of 1Vrms. This signal is used to drive the primary coil of the transducer via the power amplifier. Once the primary coil is excited, the AC signal is electrically coupled to the secondary coils by the magnetic core and induces voltages in the secondary coils. The demodulator circuit is used to determine the difference between the voltages induced in the secondary coils. The output from the LVDT secondary coils consists of a differential sine wave voltage whose magnitude and phase give the magnetic core position as described above. The filter circuits and amplifier circuits are used to remove signal noise and to amplify the magnitude of the differential voltage to the required level [159].

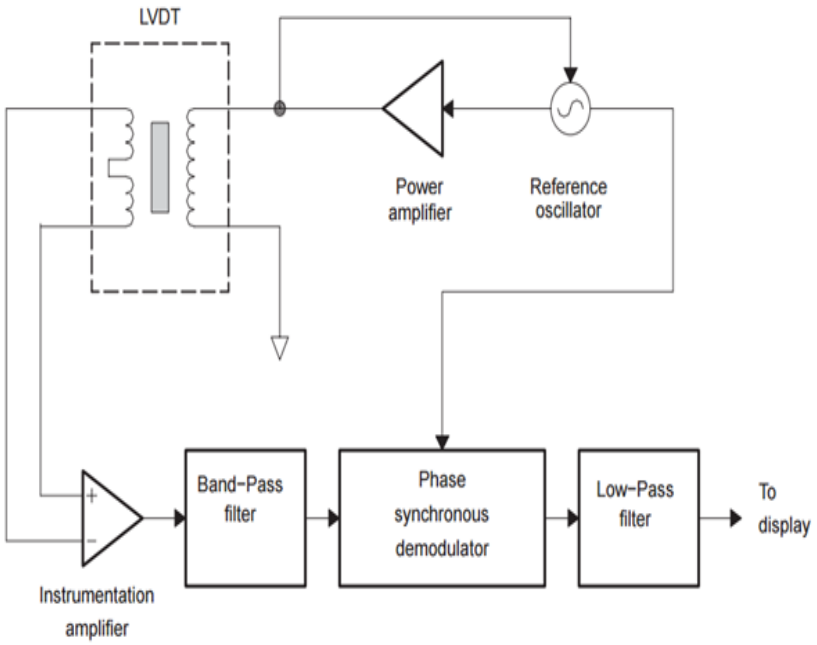

Figure 4-17: Block diagram of the LVDT signal conditioning circuitry [159]

4.3.8 Calibration of LVDT and associated signal conditioning and processing circuit

In order to ensure the accuracy of the displacement data used in the research presented in this thesis, it was required that the LVDT and associated signal conditioning circuitry were calibrated using equipment traceable to the United Kingdom Accreditation Service (UKAS) [161]. The LVDT and signal conditioning and processing circuit were calibrated by RDPE electronics using a two-point calibration method. The calibration equipment used was traceable to National Physical Laboratory (NPL) standards and it was used to measure the analogue output from the signal conditioning and processing circuit when the LVDT was displaced to two positions corresponding to ±0.5mm from its zero point (i.e. when the magnetic core was displaced 0.5mm in each direction from the reference point).

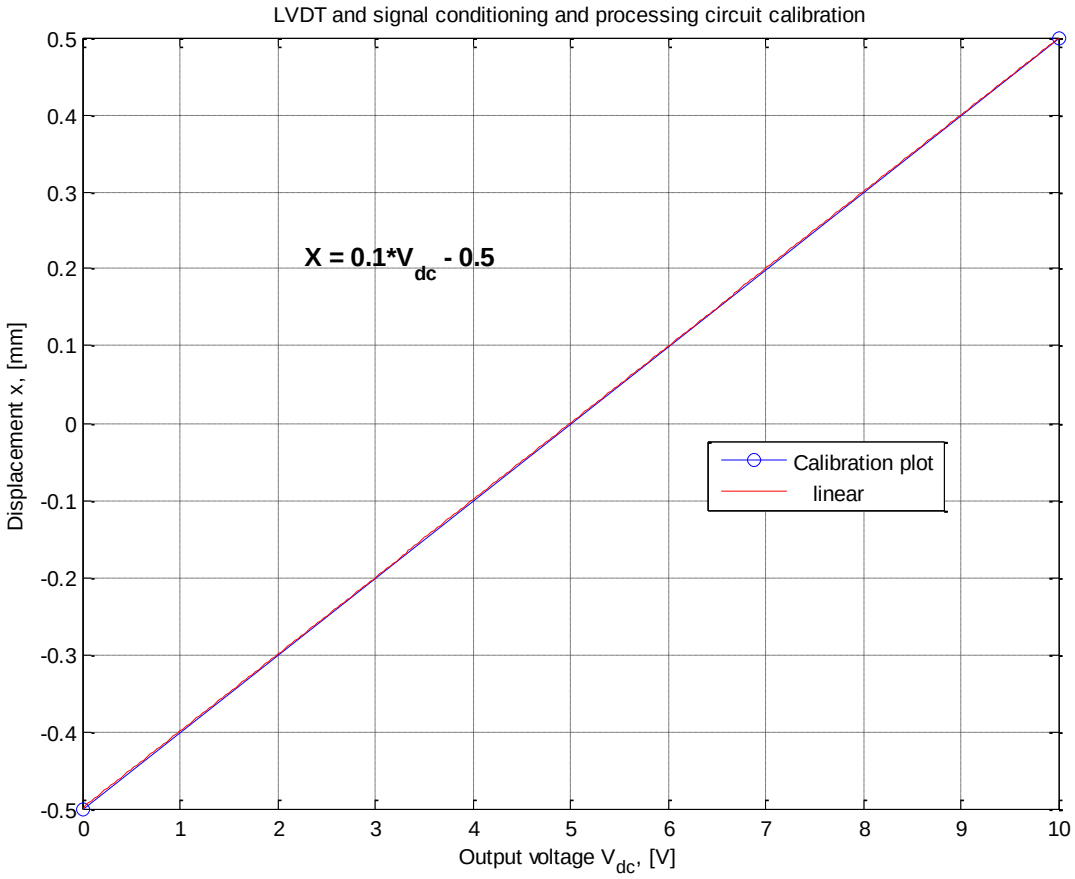

Figure 4-18: Calibration plot of LVDT and signal conditioning circuitry

Figure 4-18 shows the relationship between the magnetic core movement from its reference point and the analogue output voltage from the LVDT signal conditioning and processing circuit. The line of best fit was used to generate a calibration equation for the LVDT and signal conditioning and processing circuit and this is given by,

$$x = 0.1V_{dc} - 0.5 \qquad \text{Equation 4-36}$$

where *x* is the displacement in mm of the LVDT core and V_{dc} is the analogue output voltage from the LVDT signal conditioning and processing circuit. This equation was used to compute the measured displacement in all of the results presented in chapter 5, chapter 8 and chapter 9 of this thesis.

4.3.9 Force actuator drive current measurement circuitry

A force actuator drive current measurement circuit was used to ensure that the current flowing through the coils of the VCA was within safe operating limits and also to prevent overheating of its coils. The current measurement circuit is a network of resistance elements with a differential amplifier with precisely defined gain and is used to measure the current flowing through the coils of the voice coil actuator. A high side current sensing technique was employed in the design of the current measurement circuit. In a high side current sensing circuit, a current sensing precision resistor was connected in series between the actuator voltage excitation source V_{exc} and the actuator coil windings as shown in figure 4-19. The voltage across the sensing resistor R_s was connected to the differential inputs of an amplifier with a predefined gain that was set using the feedback resistor R_g. The output V_{op} from the instrument amplifier was then connected to a data acquisition device. The switch was used to start/stop the flow of current through the VCA coils and the fuse served to protect the VCA coils from damage due to current surge. This configuration has the advantage that the load is connected directly to the ground and the current is monitored directly from the source. It is also immune to ground noise.

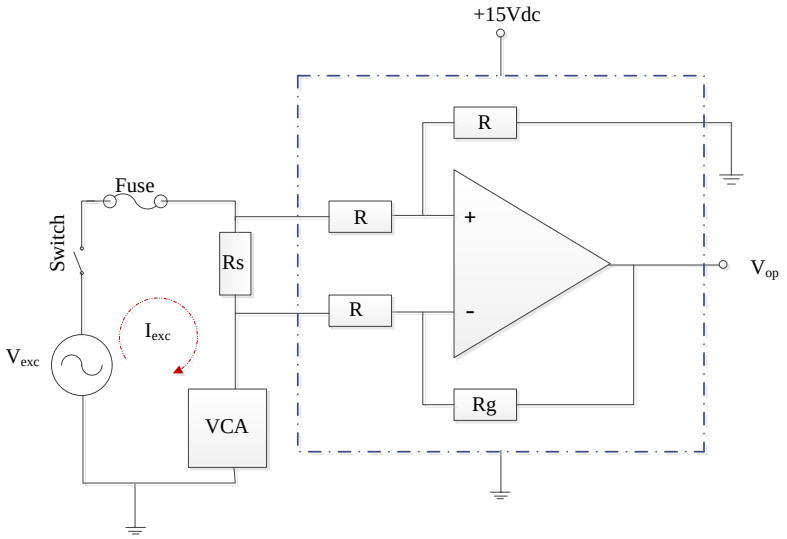

Figure 4-19: Schematic of VCA signal excitation and current sensing circuit

The output voltage V_{op} and reference resistance R_s were then used to compute the current in the VCA coils (see equation 5-6) which in turn was used for monitoring purposes to ensure the VCA coil was within safe limits during use.

4.3.10 Temperature sensor signal conditioning and processing circuitry

A temperature sensor was required to measure the sensing pipe temperature so that any changes in its stiffness constant due to temperature variation could be appropriately compensated. The type of temperature sensor selected for this research was dependent on a number of factors, including the principle of operation, sensitivity and cost. A surface mount platinum resistance temperature PRT sensor was obtained for this research. It has a fast response time and a measurement range of $-50℃$ to $+150℃$. The PRT sensor excitation and signal conditioning and processing circuit, shown in figure 4-20, was designed using the INA326 chipset from Texas Instrument. The temperature sensor signal conditioning and processing circuit provides an excitation voltage to the PRT sensor and generates an output voltage V_o that is proportional to the resistance change in the PRT sensor. The resistance change is related to the change in temperature sensed. The gain of the circuit is set using a single precision resistor R_g while C_{filter} and R_{filter} are used to set the -3dB frequency of the filter.

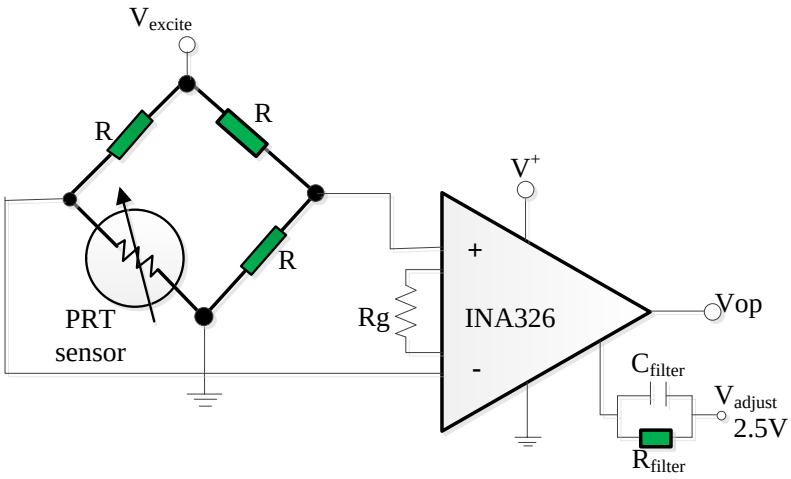

Figure 4-20: Schematic of PRT sensor signal excitation and processing circuit

The output voltage V_{op} from the circuit was then used to compute the temperature of the sensing pipe which was required to compensate for any changes to the pipe stiffness constant due to temperature variation.

4.3.11 Calibration of the PRT sensor and associated signal conditioning and processing circuit

A calibration equation used to compute the pipe temperature from the output voltage from the PRT sensor signal conditioning and processing circuit was obtained by calibrating the PRT sensor and associated signal conditioning and processing circuit. The temperature of a sample of water was varied by heating and for each measurement point, the water temperature was measured as well as the output voltage from the circuit in figure 4-20.

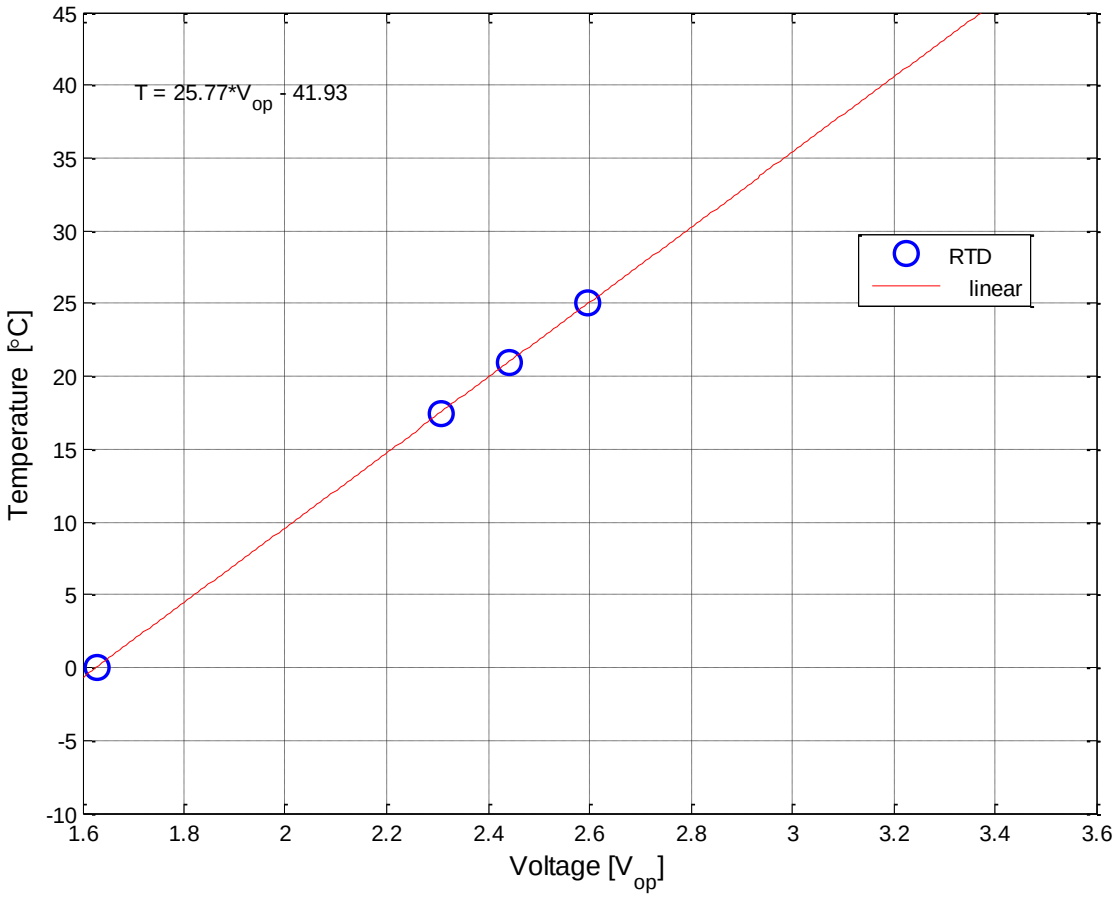

Figure 4-21: Calibration plot of PRT sensor and signal conditioning circuitry

Figure 4-21 shows the relationship between the measured temperature and the analogue output voltage from the PRT sensor signal conditioning and processing circuit. The line of best fit was used to generate a calibration equation for the PRT sensor and signal conditioning and processing circuit and this is given by,

$$T = 25.77V_{op} - 41.93 \qquad \text{Equation 4-37}$$

where T is the temperature measured in degree Celsius by the PRT and V_{op} is the analogue output voltage from the PRT sensor signal conditioning and processing circuit.

4.4 VDMS data acquisition system

A data acquisition system was developed for the VDMS using a National Instruments data acquisition card and LabVIEW software. A NI USB 6211 data acquisition card was used to digitize the analogue

output signals from the respective signal conditioning circuits. The NI USB 6211 DAQ card has 16 analogue input channels, 2 analogue output channels, 4 digital output channels, and 2 "thirty two bit" counters. The NI USB 6211 DAQ card features a USB 2.0 for powering its internal circuitry and for data transfer. It has an ADC resolution of 16 bits and a maximum sample rate of 250kS/s for all the analogue input channels. The maximum input voltage range per channel is ± 10V. The minimum voltage V_{min} that can be resolved using the NI USB 6211 DAQ card is given by,

$$V_{min} = \frac{V_{+V} - V_{-V}}{2^n} \qquad \text{Equation 4-38}$$

where V_{+V} and V_{-V} are the upper and lower limits respectively, of the input voltage signal range and n is the ADC resolution of the data acquisition card. Thus, for the NI USB 6211 DAQ card with an input voltage span of 20V and a resolution of 16bits, the minimum input voltage that can be measured is 305μV. The smallest voltage signal from the signal conditioning circuits described in sections 4.3.4, 4.3.7, 4.3.9 and 4.3.10 was approximately 0.1V. The sampling frequency of the A/D subsystems was selected such that it obeys the Nyquist sampling criterion. The maximum frequency of the excitation signal to the VCA was capped at 170Hz, a few Hertz above the resonant frequency of the sensing pipe when empty. During the earlier bench test experiments, a sampling frequency of 5kHz was first selected for the USB 6211 DAQ card. The data acquisition setting was configured to acquire a total of 2^{16} sampled data points *N* in one period *T*. The sampling frequency was later reduced to 2.5kHz to improve the resolution of the Fast Fourier Transform (FFT) of the sampled signals (see section 5.10.1). The resolution of the FFT of a sampled signal is given by,

$$df = \frac{f_s}{N} \qquad \text{Equation 4-39}$$

where df is the frequency resolution of the FFT, N is the total number of sampled data points used to calculate the FFT and f_s is the sampling frequency. The Fast Fourier Transform of the sampled data was required to compute the complex DFT of the measured force and displacement signals at the

VDMS forcing frequency. The complex DFTs of the measured force and displacement signals were used in the implementation of the signal processing technique, which is described in section 4.5.

4.5 VDMS Signal processing scheme

In order to implement the novel mathematical technique for predicting density as given in equation 4-29, a signal processing technique was required to compute the measurement parameters $\hat{a}$ and $\hat{b}$ and ω defined in the density prediction model. Since the model was developed in the frequency domain, it was imperative that the signal processing scheme for the VDMS was developed in line with the mathematical model to provide a means for obtaining $\hat{a}$, $\hat{b}$ and ω. The signal processing scheme was developed using the Discrete Fourier Transform (DFT) technique. The signal processing scheme was first implemented offline during the early stages of the research and was later implemented online. This section will focus on the offline implementation of the signal processing scheme while the online implementation will be discussed in detail in chapter 7.

The force and displacement signals from the load cell and LVDT were discretized and saved to a computer using the data acquisition system and acquisition settings described in section 4.4. The discretized displacement and force signals are voltage signals that can be converted to their respective displacement and force quantities in metres and Newtons, respectively, using the relevant calibration equations given in sections 4.3.5 and 4.3.8. The complex DFTs of the displacement and force signals can then be obtained using a MATLAB program developed using the MATLAB Fast Fourier Transform "FFT" function given in Appendix A. The complex DFTs are then used to compute the frequency, peak magnitude of the force and displacement signals and the phase difference between the displacement signal and the force signal, which are then used to compute the parameters $\hat{a}$ and $\hat{b}$ according to equation 4-17 and equation 4-18. The flow chart describing the sequence of the MATLAB instructions to compute the complex DFTs of the measured force and displacement signals is shown in figure 4-22.

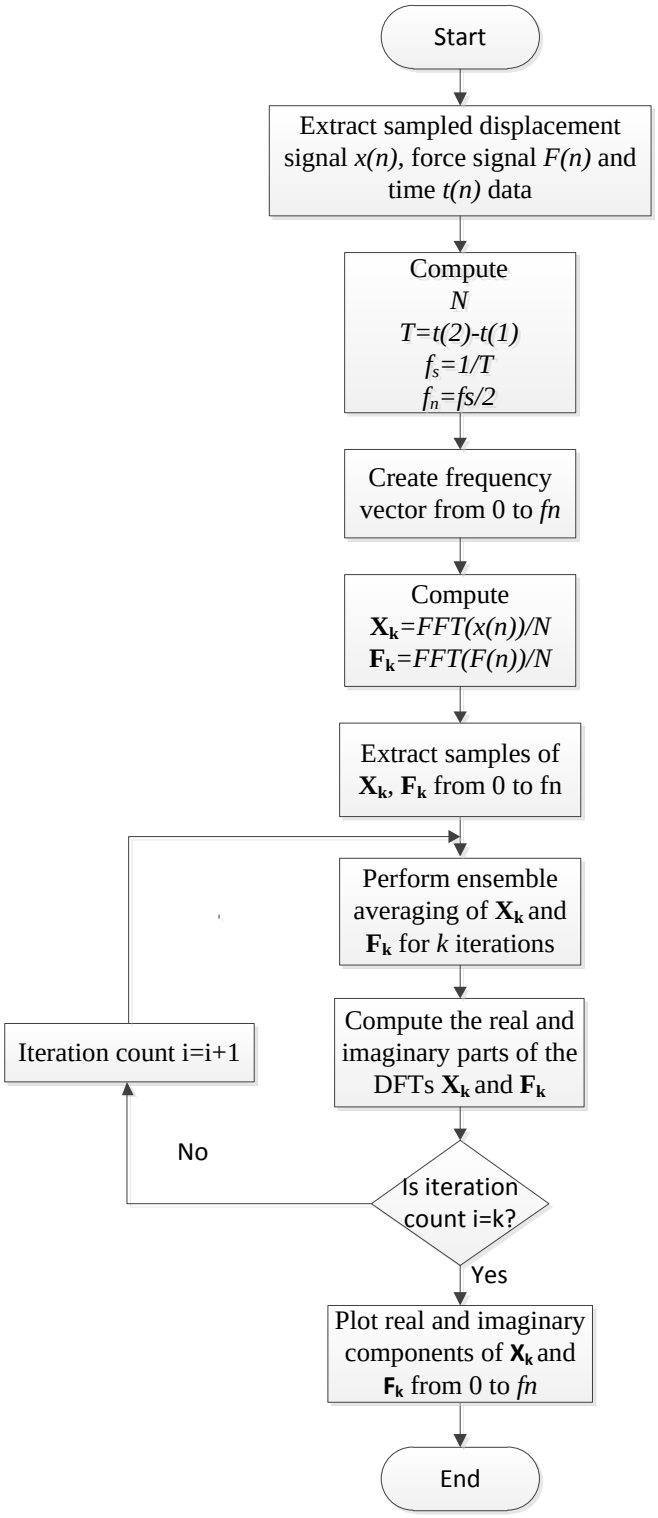

Figure 4-22: Flow chart of MATLAB instructions to compute complex DFT of sampled force and displacement signals

For a sampled force signal and displacement signal obtained using the data acquisition system described in section 4.4, the complex DFTs of the discrete time displacement and force signals $x(n)$ and $F(n)$ are given by,

$$\mathbf{X}_\mathrm{k} = [X_k]_{Re} + j[X_k]_{Im} \quad \text{Equation 4-40}$$

$$\mathbf{F}_\mathrm{k} = [F_k]_{Re} + j[F_k]_{Im} \quad \text{Equation 4-41}$$

where $\mathbf{X}_\mathrm{k}$ and $\mathbf{F}_\mathrm{k}$ are phasors respectively representing the complex DFTs of $x(n)$ and $F(n)$, k is the DFT index, $[X_k]_{Re}$ and $[F_k]_{Re}$ are the amplitudes of the real components of the DFTs of $x(n)$ and $F(n)$ respectively and $[X_k]_{Im}$ and $[F_k]_{Im}$ are the amplitudes of the imaginary components of the DFTs of $x(n)$ and $F(n)$ respectively. The DFT frequency ω_k is defined as,

$$\omega_k = \frac{2\pi k}{T} \quad \text{Equation 4-42}$$

where T is the period of the sampled signals $x(n)$ and $F(n)$. The plots in figure 4-23 (a-d) represent the real and imaginary components of the DFTs of a displacement and force signal obtained from the VDMS using the data acquisition system described in section 4.4.

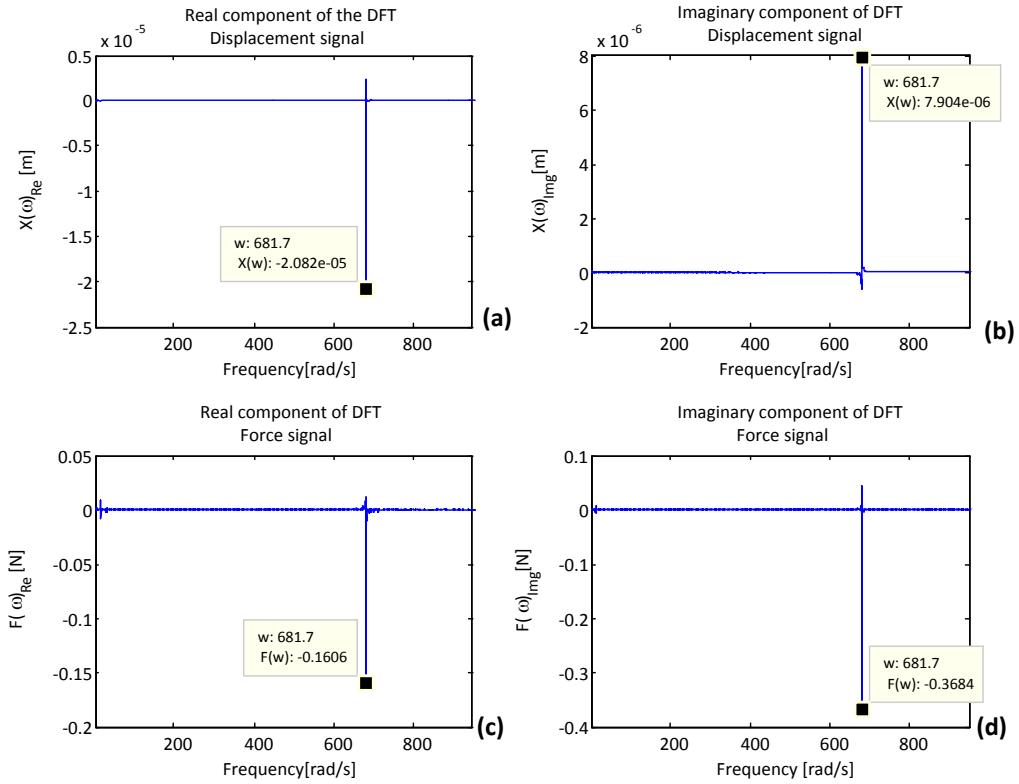

Figure 4-23: complex DFT of sampled displacement and force signals

Figure 4-23(a) and (b) shows the amplitude of the real and imaginary components of the complex DFT of the sampled displacement signal $x(n)$ and figure 4-23(c) and (d) shows the amplitude of the real and

imaginary components of the complex DFT of the sampled force signal $F(n)$. In the plots shown in figure 4-23 (a-d), $\omega_k = 681.7 rad/\text{s}$ which represents the VDMS excitation frequency. Thus, the DFTs of the displacement and force signals presented in the form shown in figure 4-23 (a-d) can be expressed mathematically as given in equation 4-40 and equation 4-41. Using these equations representing the respective DFT components, the magnitude and phase of both the displacement and force signals can then be computed at the relevant VDMS operating frequency as follows,

$$|X_{max}(\omega_k)| = \{([X_k]_{Re})^2 + ([X_k]_{Im})^2\}^{0.5} \quad \text{Equation 4-43}$$

$$\theta_x(\omega_k) = tan^{-1}\left[\frac{[X_k]_{Re}}{[X_k]_{Im}}\right] \quad \text{Equation 4-44}$$

where ω_k is the VDMS operating frequency and $|X_{max}(\omega_k)|$ and $\theta_x(\omega_k)$ are the magnitude of the peak amplitude and corresponding phase of $x(n)$ respectively. Similarly, the peak magnitude $|F_{max}(\omega_k)|$ and corresponding phase $\theta_F(\omega_k)$ of the sampled force signal $F(n)$ are given by,

$$|F_{max}(\omega_k)| = \{([F_k]_{Re})^2 + ([F_k]_{Im})^2\}^{0.5} \quad \text{Equation 4-45}$$

$$\theta_F(\omega_k) = tan^{-1}\left(\frac{[F_k]_{Im}}{[F_k]_{Re}}\right) \quad \text{Equation 4-46}$$

The measurement parameters $\hat{a}$ and $\hat{b}$ defined in equation 4-17 and equation 4-18 can then be computed using equation 4-35 to equation 4-38 as follows,

$$\hat{a}(\omega_k) = \frac{\left\{\frac{|X_{max}(\omega_k)|}{|F_{max}(\omega_k)|}\cos\theta(\omega_k)\right\}}{\left\{\frac{|X_{max}(\omega_k)|}{|F_{max}(\omega_k)|}\sin\theta(\omega_k)\right\}} = \cot\theta(\omega_k) \quad \text{Equation 4-47}$$

$$\hat{b}(\omega_k) = \frac{|X_{max}(\omega_k)|}{|F_{max}(\omega_k)|}\cos\theta(\omega_k) \quad \text{Equation 4-48}$$

where $\theta(\omega_k)$ is the phase difference between the displacement signal and the force signal and is obtained as follows,

$$\theta(\omega_k) = \theta_x(\omega_k) - \theta_F(\omega_k). \quad \text{Equation 4-49}$$

The magnitude ratio Mr of the system is defined as,

$$Mr(\omega_k) = \frac{|X_{max}(\omega_k)|}{|F_{max}(\omega_k)|}$$ Equation 4-50

Note that $\theta(\omega_k)$ should be in the range $-\pi < \theta(\omega_k) < \pi$. Once the measurement parameters $\hat{a}(\omega_k)$, $\hat{b}(\omega_k)$ and ω_k are obtained, the density of a mixture flowing through a pipe can then be computed using the density prediction model defined in equation 4-29 and equation 4-30.

4.6 Summary

A novel mathematical model to predict the density of a mixture flowing through a pipe has been developed from fundamental principles. In addition, the design and construction of a physical, vibrating density measurement system (VDMS) have also been described in this chapter. The constructed VDMS features three subunits; (i) a measurement unit comprising a sensing pipe, a voice coil actuator, a load cell, a LVDT, a current sensor and a temperature sensor; (ii) signal conditioning units for the load cell, LVDT, force actuator drive current detection and temperature sensor which were used to remove noise embedded in the respective signals and to amplify their amplitudes to the require level and (iii) a data acquisition system developed using a NI USB6211 DAQ card and LabVIEW software. The design decisions made in the selection of the force actuator and sensors used, their principles of operation and specifications as well as the calibration of these sensors were also presented in this chapter. Lastly, a signal processing technique to implement the novel mathematical model for density prediction was developed using the Discrete Fourier Transforms of the sampled displacement and force signals.

Chapter 5

BENCH TESTS ON THE VIBRATING DENSITY MEASUREMENT SYSTEM (VDMS)

5.1 Introduction

Firstly, this chapter describes the design and construction of a bench test rig that was used in this research. It further describes the bench tests that were carried out in the design and construction of the VDMS as well as a discussion of the results that were obtained from the tests. The bench tests discussed in this chapter include; tests to determine the sensing pipe stiffness constant K_1, empty mass m_1 and damping constant f_1; tests to validate the displacement pattern of the sensing pipe when a force is applied to its centre and the voice coil actuator (VCA) specifications (force constant, coil resistance and coil inductance). Further bench tests described in this chapter include bench tests to determine the value of the VDMS constant "β" (see section 5.8.1) and to investigate the frequency response characteristics of the VDMS using different test mixtures. Once the practical vibratory densitometry system and signal processing techniques were developed, a series of experiments were conducted to investigate the relative accuracy of the VDMS when used to predict the mixture density of standard 'test mixtures' that were formulated for this purpose. The results obtained from these experiments were discussed and used to define optimal operating conditions for the VDMS.

5.2 Design and construction of bench test rig for VDMS characterization

During the design and development of the VDMS, a bench test rig was required to investigate the characteristics of its sub-units before it was used in a flow loop. The bench test rig provided features akin to the flow loop, which allowed the characteristics of the constructed VDMS to be investigated. The bench test rig had features that enabled the sensing pipe to be firmly fixed at both ends and also for centrally positioning the VCA, load cell and LVDT on the sensing pipe. Solidworks software was first used to design a 3D model of the bench test rig as shown in figure 5-1, before it was then constructed. It is important to state here that the constructed bench test rig was crucial to the success of

the research because it was used to provide useful data such as pipe spring constant K_1, damping constant f_1 and VDMS constant β which were required in the novel model developed in Equation 4-29 to compute the mass of the contents of the sensing pipe and hence its density.

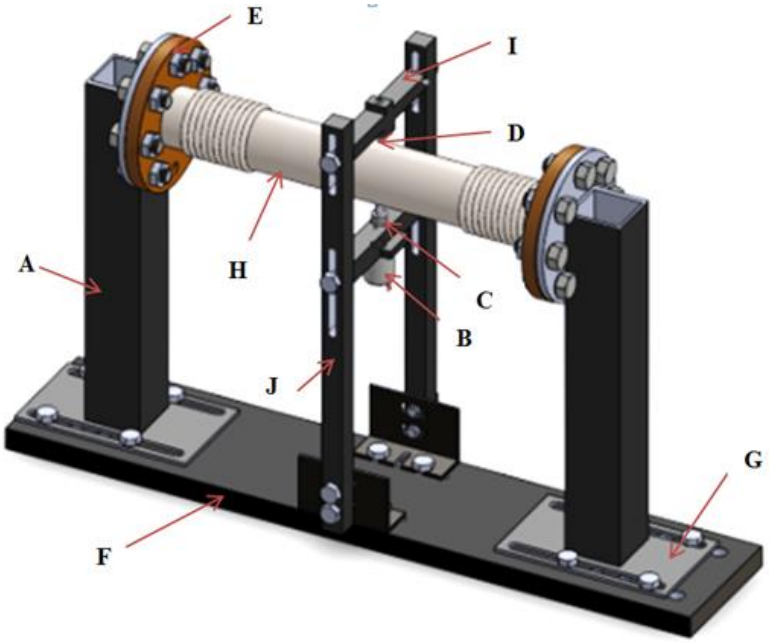

Figure 5-1:Solidwork 3D model of the bench test rig with VDMS

***A**: Steel supports **B**:VCA **C**:load cell **D**:LVDT **E**:stainless steel flanges **F**:test rig base **G:** steel frame base plates **H**: sensing pipe **I:** bespoke sensor holder **J**: support framework*

The test rig has two steel supports (A) with dimensions 80mm X 80mm X 500mm each. Standard BS304 stainless steel flanges (E) were centrally welded to the top end of the steel supports and flat steel base plates (G) with through groove slots and having dimensions of 250mm X 150mm X 16mm were welded to the bottom of each support. The standard BS304 flanges were to provide a means for firmly connecting the sensing pipe to the test rig using M12 bolts and nuts and the groove slots were to ensure the distance between the steel supports were adjustable and could fit the length of the sensing pipe and any gasket(s) used between the flange connections. Also, an additional flat steel plate with dimensions 1000mm X 250mm X 20mm was used to construct the base of the test rig (F). The steel plate had threaded M12 holes at its ends and centre to provide a means for vertically fastening the steel supports

labelled “A” and “J”, in figure 5-1, to the test rig base. The bases of these steel supports were fastened to the test rig in a vertical orientation using M12 nuts. The test rig support framework “J” and bespoke sensor holders “I” were used to centrally position the VCA, load cell and LVDT assembly onto the sensing pipe. The support framework (J) comprises two square section steel bars with dimensions 30mmX30mX600mm and positioned on either side of the sensing pipe and connected to the two bespoke sensor holders “I” to form a rigid unit. At the base of the support framework are two angle bars with M12 groove slots which are used to firmly fasten the assembled “J” and “I” unit to the test rig base (G) using M12 bolts and nuts. The bespoke sensor holders “I” were carefully designed so the VCA, load cell and LVDT could be properly fitted to the support framework in a central position of the sensing pipe. Once the VCA was fitted onto the bespoke sensor holder “I”, the moving coil shaft of the VCA was then connected to the load cell on one end using a bespoke stringer with M4 threads (see figure 5-2). On the other end, the load cell was connected to a second bespoke stringer that was welded to the centre of the sensing pipe using an M4 bolt and nut. The bench test rig could either be used in a vertical or horizontal orientation.

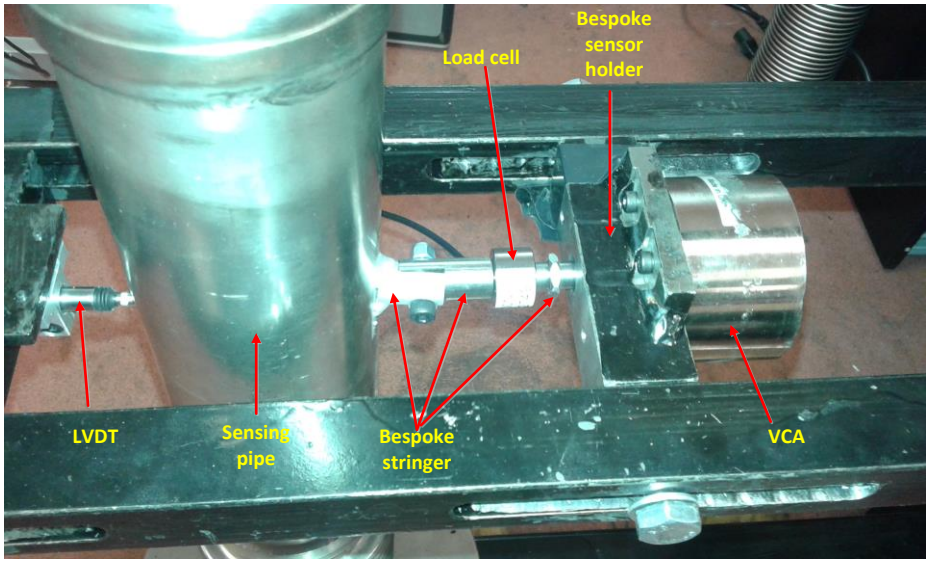

Figure 5-2:Picture of the bespoke sensor holders and stringers used to centrally position and connect the load cell, LVDT and VCA to the sensing pipe

Figure 5-2 shows a picture of the bespoke sensor holders and stringers used to centrally position and connect the load cell, LVDT and VCA to the sensing pipe. Once the bench test rig had been designed and constructed, the measurement unit, signal conditioning unit and data acquisition unit were all assembled to form the overall vibratory densitometry system. The data acquisition unit was configured using the settings discussed in section 4.4. The outputs from the electronic circuits associated with the LVDT, load cell, current sensor and temperature sensor were all connected to the NI USB6211 analogue input ports. Corresponding virtual channels were created using LabVIEW to acquire the measurement signals. The data acquisition settings were configured using the specifications discussed in section 4.5.

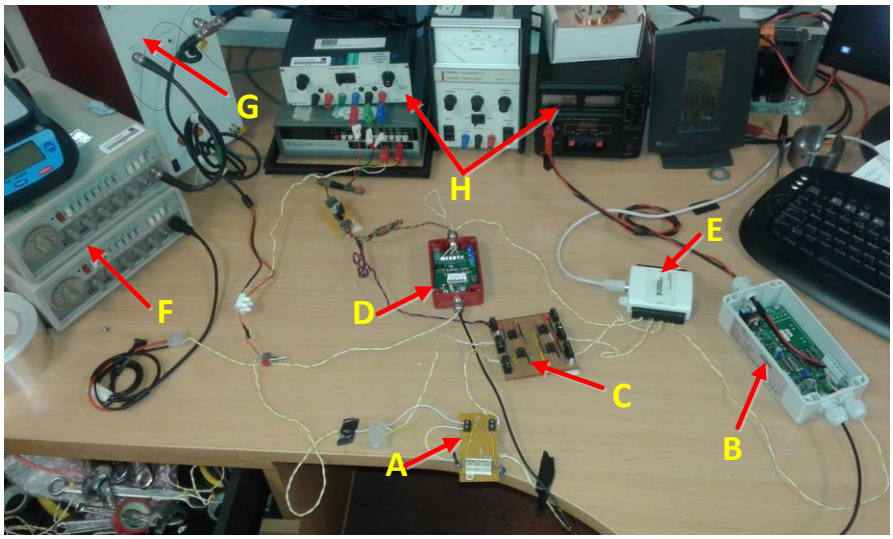

A:Current sensing circuit
B:Load cell signal conditioning circuit
C:PRT sensor signal conditioning circuit
D:LVDT signal conditioning circuit
E:NI DAQ card
F:Signal generator
G:Power amplifier
H:dc power supply

Figure 5-3:Picture of signal conditioning units and data acquisition card

5.3 Bench test to determine stiffness constant K_1 of sensing pipe

From the novel mathematical model for predicting fluid density given in equation 4-29, it is seen that the sensing pipe stiffness constant is one of the variables required to predict the density of the contents of the pipe. It was therefore necessary to accurately determine the sensing pipe stiffness constant K_1. The pipe stiffness constant is a physical property that describes its resistance to deformation when a force is applied to it and was determined using experimentation based on Hooke's law. A separate validation test was also performed using Solidworks FEA. The aim of the validation tests was to ensure

the value of the stiffness constant obtained for the sensing pipe and used in the density prediction mathematical model was the most accurate obtainable from the measurement instruments available.

5.3.1 Testing procedure

The experimental method designed to determine the sensing pipe stiffness constant K_1 was based on the fundamentals of Hooke's law. The experimental set-up includes the bench test rig, the sensing pipe, a set of standard slotted mass blocks of different masses and a ZEISYS coordinate measurement machine (CMM). The bench test rig was used to firmly connect the sensing pipe in a horizontal position and the slotted mass blocks were used to apply known weights to the centre of the sensing pipe (see figure 5-4). The ZEISYS CMM was used to measure and record the displacement at the sensing pipe centre when different weights were applied. The ZEISYS CMM used for this purpose had been calibrated using equipment traceable to the UKAS. The ZEISYS CMM has very low measurement uncertainty of $1\mu m$. It enables computer aided measurement runs, has a vibration free mechanical structure and has high rigidity. It is also equipped with automatic recording and data processing units [162]. The sensing pipe was then firmly fixed at both of its ends to the bench test rig and carefully placed on the ZEISYS CMM worktable so as not to cause any damage. The VDMS setup was manually aligned with the mutually perpendicular X, Y and Z axes of the CMM before it was firmly secured to its position using a CMM clamping kit.

In this experiment, the ZEISYS CMM was firstly used to measure the reference position of the sensing pipe when no weight was applied. Next, the mass hanger was connected to the centre of the sensing using a jubilee clip (see figure 5-4). Once the mass hanger was fixed at the centre of the sensing pipe, five different weights were added to the mass hanger using the set of mass blocks (see "A" in figure 5-4) and for each weight added, the resultant displacement of the sensing pipe from its reference position was measured and recorded using the ZEISYS CMM. The sensing pipe resultant displacement

measurements were repeated five times, for each weight applied to the pipe centre, to reduce variability in the measurement result.

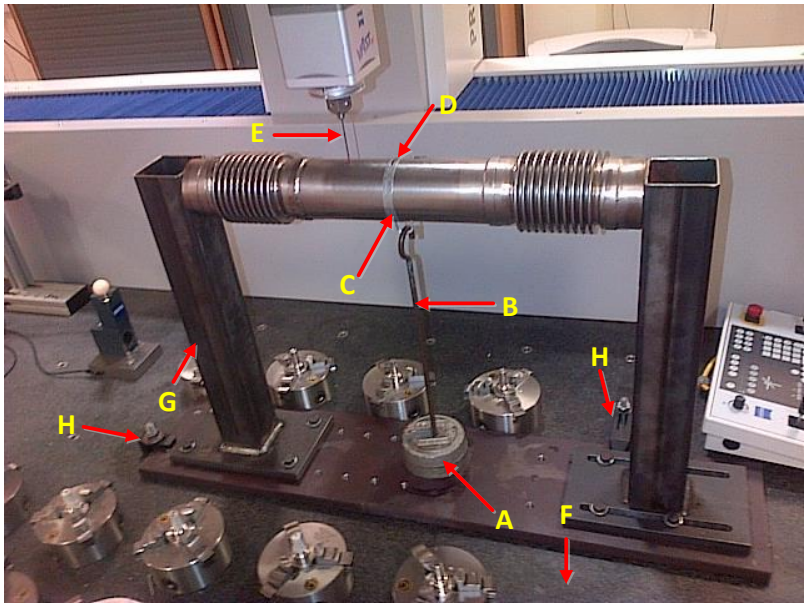

Figure 5-4: Experimental set up to measure sensing pipe stiffness constant

5.3.2 Results of the experimental testing to determine the stiffness constant K_1

For each experiment run, the total weight applied to the sensing pipe centre was computed by adding the weights of the mass hanger, the jubilee clip and the set of mass blocks on the hanger respectively. The total weights were obtained by multiplying the total masses by acceleration due to gravity g, where g was taken as 9.8m/s^2. The random errors associated with the measurement of the resultant displacement were minimized by taking the average of the five displacement measurements for each weight added. Using Hooke's law, the curve relating the force applied (total weight) to the sensing pipe and the resulting average displacement was used to compute the sensing pipe stiffness constant K_1 using the expression below,

$$F = K_1 x \qquad \text{Equation 5-1}$$

where F is the force applied (total weight) at the sensing pipe centre and x is the resultant average displacement at the pipe centre. Note that the five sets of displacement and weight data were taken at different times and for all the experiments undertaken the sensing pipe was always in its elastic region. Also, the temperature of the CMM room where the experiment was conducted was tightly controlled at 20℃.

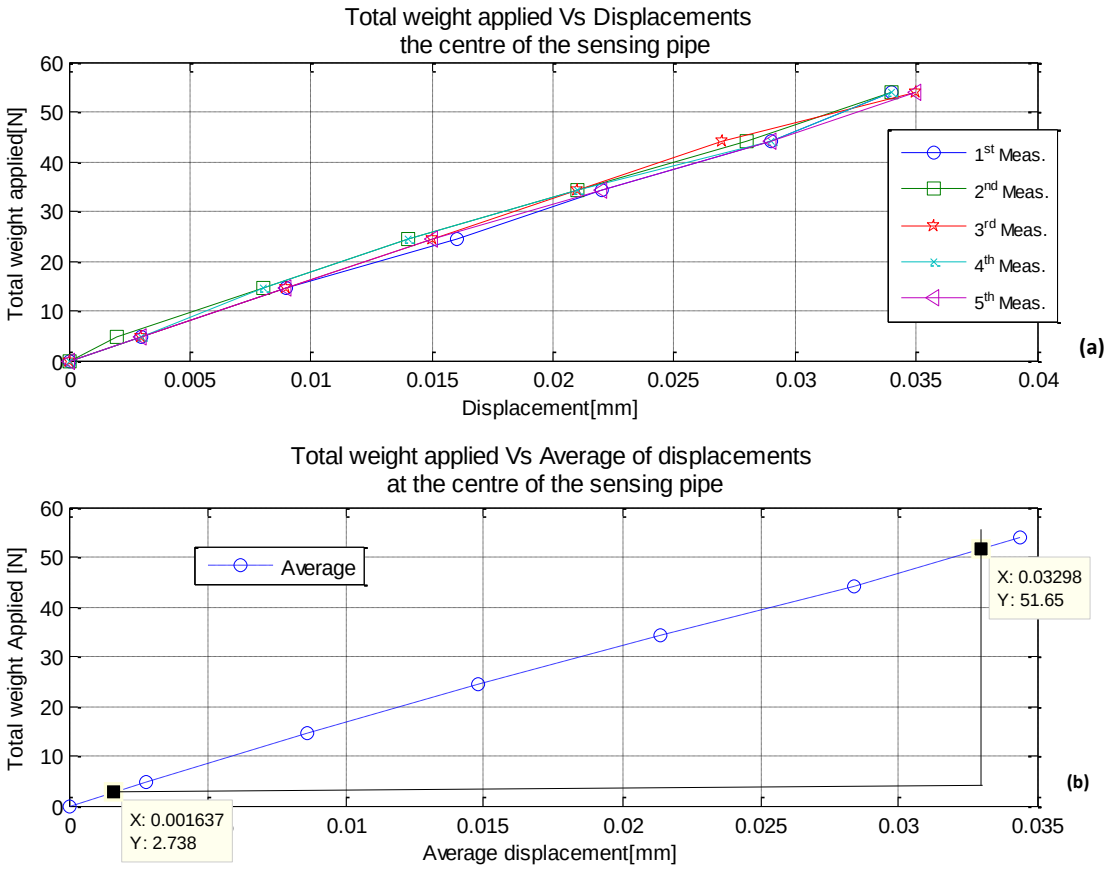

Figure 5-5(a):Plots of applied weights against displacements at the centre of the sensing pipe, (b) Plot of applied weights against average displacements at the centre of the sensing pipe

Figure 5-5(a) shows the total weight applied versus resulting displacement curve at the sensing pipe centre for the five different displacement measurements using each weight. Figure 5-5(b) shows the plot of the total weight applied against average displacement at the sensing pipe centre. The vertical axes represent the total weight applied to the sensing pipe centre in Newtons N and the horizontal axes represents the average displacements at the sensing pipe centre in millimetres mm. The sensing pipe

stiffness constant K_1 was obtained from the slope of the plot in figure 5-5(b) as $1.55 \times 10^6 \mathrm{N/m}$. The Solidworks FEA was used to validate the results obtained from these experiments to determine the sensing pipe stiffness constant K_1. Solidworks finite element analysis (FEA) method was used to discretize the sensing pipe 3D model into beam elements and linear stress analysis was used to determine the displacement response of the model due to the effect of applied forces. The sensing pipe 3D model shown in figure 4-4 was evaluated in Solidworks under static mode. The sequence outlined below was followed to perform the linear static analysis using Solidworks [163];-

- A static study was created in Solidworks window using the property manager by right clicking the simulation study tab to create a new simulation study.
- The material of the sensing pipe was selected as 316L stainless steel by right clicking on apply/edit material on the simulation study tree and selecting the appropriate material.
- The sensing pipe model was restricted at both of its ends to ensure movement only in the direction of the Z-axis when a force was applied to the centre of the sensing pipe in the direction of the Z-axis. This was achieved by right clicking on the fixture icon in the simulation tree and defining the model restraint.
- An external vertical point load of 1N was applied to the sensing pipe centre by right clicking on the load icon in the simulation study tree and selecting the type of load and magnitude to apply to the model.
- An "intricate mesh" was then created for the model before running the simulation.
- The result of the sensing pipe displacement was obtained from the result icon on the simulation tree.

The force and displacement results from Solidswork FEA were also applied to equation 5-1 to compute the sensing pipe stiffness constant K_1. This was obtained as $1.50 \times 10^6 \mathrm{N/m}$ and it compares closely with the result obtained from Figure 5-5 (b). However, further experiments and analysis were performed using different 'test mixtures' contained in the sensing pipe (see section 5.8) to define an

optimal value for the VDMS constant β for which good agreement exists between the experimental frequency response and theoretical frequency response curves of the VDMS. The optimal value of the sensing pipe stiffness constant K_1 for which the optimal VDMS constant β was defined was obtained as $1.45 \times 10^6 \mathrm{N/m}$ and this value was used in the experimental results presented in chapter 5, chapter 8 and chapter 9 of this thesis.

5.4 Bench test to determine mass m_1 of empty sensing pipe

From the novel mathematical model given in equation 4-29, the sensing pipe mass, designated as m_1 in this thesis was required to predict the density of the contents of the pipe. It was therefore necessary to accurately determine the sensing pipe mass, when empty, that will be used in the density prediction model.

5.4.1 Testing procedure

The sensing pipe mass when empty and without the flanges welded was obtained from a simple measurement using a precision digital mass scale with an accuracy of ± 0.01Kg. The empty sensing pipe was placed on the mass scale and its mass was read off from the digital readout of the scale. This measurement was repeated five times to minimize the influence of random errors on the measured mass.

5.4.2 Results of the testing

The mass of the empty sensing pipe was computed from the average of the measurements taken. This was obtained as 2.24kg at 20.5℃. Also, from the results of further experiments and analysis performed to define an optimal value for the VDMS constant β (see section 5.8), the value of the empty pipe mass for which the optimal value for the VDMS constant β was defined was obtained as 2.20kg and this value was used in the experimental results presented in chapter 5, chapter 8 and chapter 9 of this thesis.

5.5 Bench test to determine the sensing pipe damping constant f_1

A transient response test was used to determine the damping properties of the sensing pipe when it was empty. Although this was not directly required in the novel mathematical model given in equation 4-29, it was used to compute the theoretical frequency response of the system and also for the development of the mathematical model for the computer based control system (see section 7.3.1).

5.5.1 Testing procedure

The damping ratio ζ of the sensing pipe was determined by the step testing technique. A step change in a force, of known magnitude, was applied to the sensing pipe and the resulting displacement of the sensing pipe was then recorded. The transient properties of the recorded displacement response of the pipe were then used to compute the damping ratio for the sensing pipe.

5.5.2 Results of the testing

The sensing pipe displacement in response to the application of a step change in the applied force was plotted as shown below.

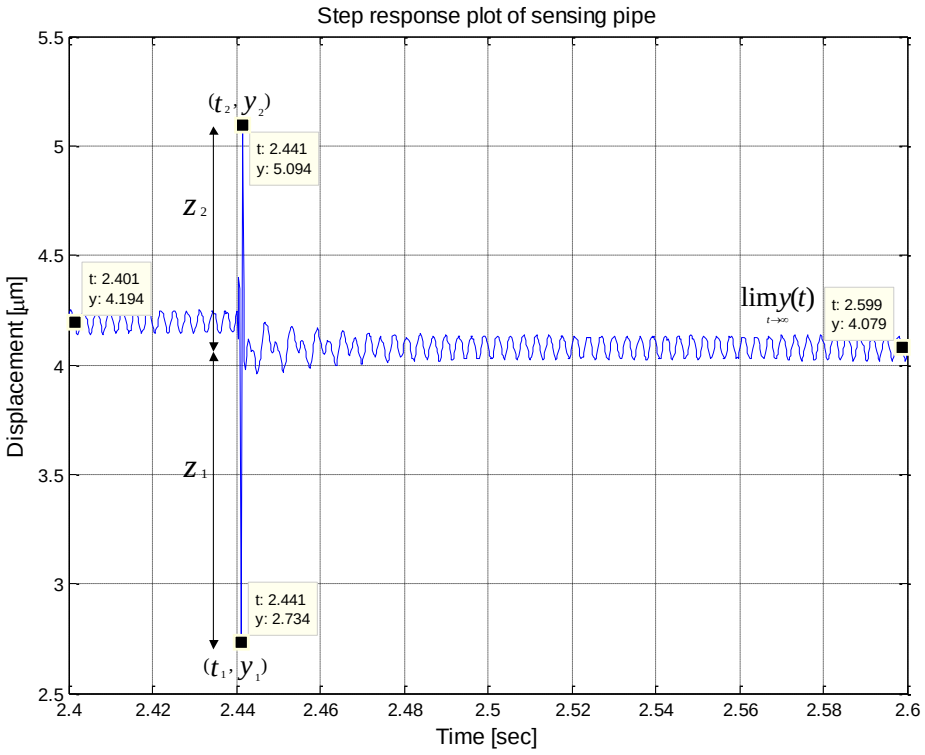

Figure 5-6: Step response plot of sensing pipe

From figure 5-6, z_1 and z_2 represent the magnitude of the first overshoot and first undershoot respectively, and are obtained using the expressions below,

$$z_1 = y_1(t_1) - \lim_{t\to\infty} y(t_\infty) \qquad \text{Equation 5-2}$$

$$z_2 = \lim_{t\to\infty} y(t_\infty) - y_2(t_2) \qquad \text{Equation 5-3}$$

where $y_1(t_1)$ and $y_2(t_2)$ are the sensing pipe displacement at time t_1 and t_2 respectively and $\lim_{t\to\infty} y(t_\infty)$ is the final value of the sensing pipe displacement in the direction of the applied force. The magnitude of the first overshoot z_1 in figure 5-6 is negative because the direction of the force applied to the sensing pipe was vertically downward. The magnitudes of the first overshoot z_1 and first undershoot z_2 were then used to compute the damping ratio ζ using the expression,

$$\zeta = \sqrt{\frac{\ln\left(\frac{z_1}{z_2}\right)^2}{\ln\left(\frac{z_1}{z_2}\right)^2 + \pi^2}} \qquad \text{Equation 5-4}$$

Finally, the damping ratio ζ was obtained as 0.005 and this value was used to compute the sensing pipe damping constant f_1 as 18.05kgs^{-1} using the expression,

$$f_1 = 2\zeta\sqrt{K_1 m_1} \qquad \text{Equation 5-5}$$

5.6 Bench test to investigate the displacement pattern of the sensing pipe with fixed end supports and a static load applied at the centre

A major assumption in the development of the novel mathematical model for predicting density in single phase and multiphase pipe flows was that the sensing pipe is fixed at both ends, and thus, it is expected to take up a displacement pattern similar to a 'fixed end' beam with a point load applied to its centre [164]. From section 3.3, it was shown that when a force is applied to the centre of a 'fixed end' horizontal beam, the maximum transverse displacement would be located at its centre point. It was therefore necessary to verify that for the sensing pipe used in this work, its displacement to an applied load will be at a maximum at the pipe centre and zero at the supports.

5.6.1 Testing procedure

The experimental setup used in this investigation was similar to the setup described in section 5.3.1 to determine the sensing pipe stiffness constant. The CMM scanning head was programmed to obtain displacement measurements across the span of the sensing pipe at predefined spatial locations. Once the setup was readied, with no weight applied on the mass hanger attached to the sensing pipe, the CMM was used to take a number of measurements at the defined points across the span of the sensing pipe. These measurements obtained were used as references to calculate the true displacement of the sensing pipe at the predefined spatial locations when weights were applied. Different sets of mass blocks were added to the mass hanger at the sensing pipe centre and, for each set of mass blocks added, the CMM scanning head was used to measure and record the displacement of the sensing pipe across its span at the predefined measurement points. This experiment was repeated twice and the average of the two sets of measurement was taken to reduce the random errors in the measurement.

5.6.2 Results of the testing

The true displacement of the sensing pipe at each reference point, when a known weight was applied at the pipe centre was calculated by subtracting the displacement obtained when no weight was applied to the sensing pipe from the displacement when a known weight was applied. The plots of the true displacement of the sensing pipe across its span for various applied weights are presented in figure 5-7.

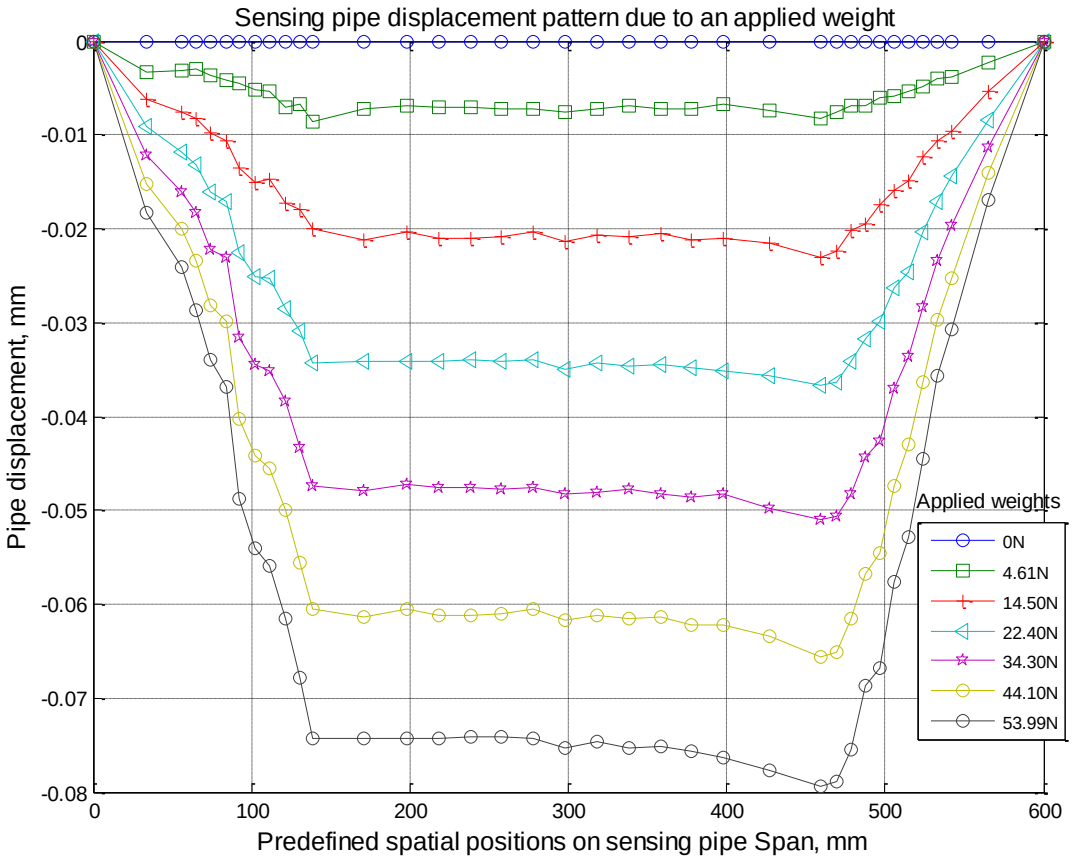

Figure 5-7: Displacement pattern of the sensing pipe when weight blocks are applied

The vertical axis of the plot in figure 5-7 represents the true displacement of the sensing pipe from a reference positions when different known weights were applied at its centre and the horizontal axis represents the predefined spatial positions on sensing pipe span. The legend plot represents the different weights applied to the sensing pipe centre. From the results shown in figure 5-7, the displacement pattern when a static load was applied to the centre of the sensing pipe fixed at both ends agrees closely with the theoretical prediction by Timoshenko [164]. For the experiments where the weights applied to the sensing pipe centre were less than 34.30N, the displacement pattern of the sensing pipe was observed to be symmetrical about its centre. The displacements were observed to be maximum between 145mm and 455mm. The influence of the bellows at each end of the sensing pipe can be seen by investigating the displacement patterns between 51mm to 144mm and 456mm and 549mm on the sensing pipe span, which corresponds to the positions of the bellows. The maximum displacement at

the pipe centre can be seen to be mainly due to the displacement from the bellows. It is important to point out that when weights greater than 34.30N were applied to the centre of the sensing pipe, one of the bellows (at measurement point 460mm) appeared to deflect more than the other. This may be due to an imperfect weld seam between the straight pipe spool and the bellows at 460mm.

5.7 Static tests to investigate voice coil actuator (VCA) specifications

Several tests were conducted to validate the specifications of the VCA that were quoted by the manufacturers before it was used and to better understand its operation. Electrically, the VCA is like a single phase motor with resistive and inductive properties. The tests carried out on the VCA were to determine its force constant k_{vca}, coil winding resistance R_{vca}, coil winding inductance L_{vca}, and rise time τ_{vca}. The moving coil assembly of the VCA comprises of 258 turns of 0.25mm copper wire wound on a 43mm diameter circular bobbin. The coil was wound in 6 layers on the bobbin and has a mass of 24g. The maximum safe operating temperature of the VCA coil is 130℃. The coil windings are terminated on two adjacent pins on the circular bobbin. The moving coil assembly has a shaft fixed to the bobbin on one end and on the other end, it has an M4 thread. The M4 thread served as a means for connecting the VCA to the sensing pipe via the bespoke stringers and load cell (see figure 5-2). Two thin, stranded, insulated copper wires were connected to the coil termination pins. These wires were used to apply an excitation current to the VCA coils. It is important to state at this point that the manufacturers of the VCA basically have two options of coil windings, the standard coil option and the short coil option. The short coil option designated as VM6340S-250 was selected for this research because of the following advantages it has over the standard coil option. The short coil option has a moving coil that is usually longer than the working airgap of the VCA, which allows a linear force to be generated while the moving coil and permanent magnet overlap. This ensures a more efficient interaction between the fields generated by the VCA moving coil assembly and the permanent magnet.

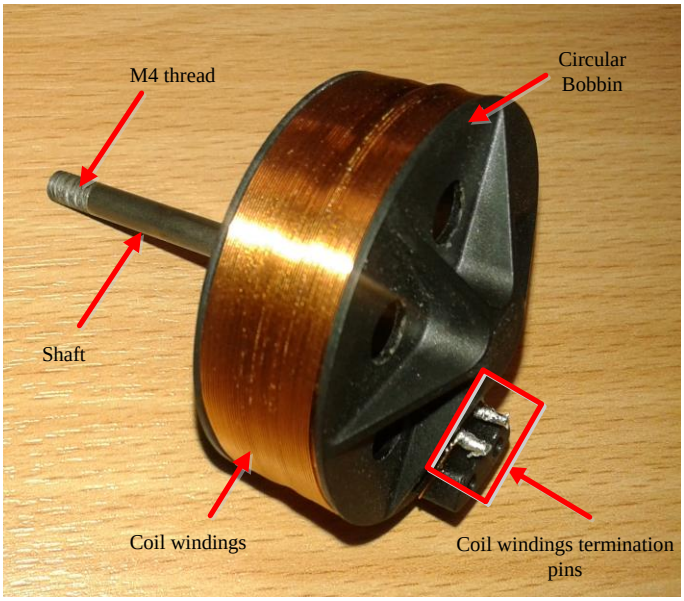

Figure 5-8: Picture of VCA moving coil assembly

5.7.1 VCA Coil resistance

In this research, the VCA coil winding resistance R_{vca} was required to compute the current flowing in the coil using equation 5-6. The coil current was crucial in ensuring the actuator was always operated within its safe limit. The VCA coil winding resistance R_{vca} was also required for a Simulink model of the VDMS described in section 7.3.1. The nominal resistance of the VCA was obtained by simply measuring the resistance of the coil winding at 20.5℃, using a precision Fluke digital multimeter as described below.

5.7.1.1 Testing procedure

A high precision Fluke digital multimeter was used for this purpose. Firstly, the actuator coil winding was completely isolated before the two test leads of the Fluke meter were connected to the two terminal pins of the VCA coil assembly shown in figure 5-8. It should be stated here that care was taken to ensure good contact was made between the test leads and the terminal pins on the VCA moving coil assembly and that the meter was set to auto-range measurement mode to ensure the resistance measurement was made with the best resolution obtainable.

5.7.1.2 Results of the testing

The measured resistance of the coil winding was obtained from the multimeter display as 11.64Ω. This value was used to calculate the VCA coil current and was used in the mathematical model of the VCA used in the design of a computer based control system for ensuring optimal operation of the VDMS (see section 7.3.1).

5.7.2 VCA Coil inductance

Measurement of the VCA coil inductance was necessary to obtain the model parameters required to develop the VCA mathematical model used in the design of the computer based VDMS control system described in section 7.3.1. The VCA coil inductance was measured using an Agilent LCR meter and was validated from experimentation using a series LR electrical circuit.

5.7.2.1 Testing procedure

The inductance of the VCA coil was measured using an Agilent LCR meter. The moving coil assembly was isolated before measurement and the two test leads from the LCR meter were connected to the coil terminal pins of the VCA moving coil assembly. The LCR meter was appropriately configured before measurements were read off the meter display. The measured inductance of the VCA coil was obtained as 9.70mH.

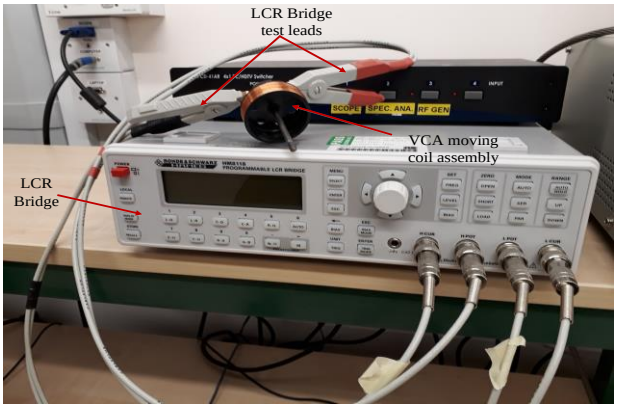

Figure 5-9: Picture of Agilent LCR bridge and VCA moving coil assembly used to measure its inductance

A simple test using a series LR electrical circuit was also used to compute the inductance of the VCA coil and to validate the inductance measurement obtained from using the Agilent LCR meter. The series LR electrical circuit comprises the VCA coil windings in series with a 1Ω precision resistor and an AC signal excitation source as depicted in figure 5-10. An SPST switch was used to control the time interval the excitation current was applied to the LR circuit and a fuse served as a protection from unsafe currents flowing through the VCA coil windings.

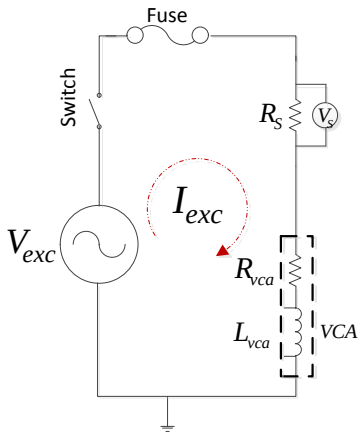

Figure 5-10: Schematic of series LR circuit used to measure coil winding inductance of VCA

An AC signal with peak amplitude V_{exc} and frequency f was applied to the series LR circuit. The voltage dropped across a 1Ω precision resistor R_s was measured using a voltmeter and this voltage was used to compute the current flowing through the LR circuit. The current through the precision resistor also represents the current flowing through the VCA coil windings since they are connected in series and it is given by,

$$I_{exc} = \frac{V_s}{R_s} \qquad \text{Equation 5-6}$$

where V_s is the peak magnitude of the voltage dropped across the 1Ω precision resistor, R_s is the resistance value of the precision resistor and I_{exc} is the peak amplitude of the current flowing through the LR circuit. The inductance of the coil winding was then calculated using the equation,

$$L_{vca} = \frac{\left(\left(\frac{V_{exc}}{I_{exc}}\right)^2 - {R_t}^2\right)^{0.5}}{2\pi f}$$ Equation 5-7

where L_{vca} is the inductance of the VCA winding, R_t is the total resistance of the VCA coil winding R_{vca} (see section 5.7.1) and the 1Ω precision resistor R_s in series. The experiment was repeated using different input excitations with varying amplitudes but the same frequency of 200.8Hz. For each experiment, the voltage drop across the 1Ω precision resistor was measured and recorded.

5.7.2.2 Results of the testing

The inductance of the VCA coil winding obtained from the Agilent LCR bridge meter display was 9.70mH. Also from the validation tests conducted, the inductance of the VCA for the different tests conducted was computed using equation 5-6 and equation 5-7. The input voltage to the LR circuit, the corresponding voltage dropped across the precision resistor and the calculated inductance of the VCA coil winding are presented in Table 5-1.

Table 5-1: Measurement results obtained from experiment to calculate the inductance of VCA coil winding

Test Number	**Input AC voltage to series LR circuit** (Vexc)	**Voltage** Vs **measured across precision resistor**	**Calculated Inductance** Lvca **of VCA coil windings**
	[V]	**[V]**	**[H]**
1	0.70	3.96E-02	9.81E-03
2	0.90	5.06E-02	1.00E-02
3	1.09	6.12E-02	9.96E-03
4	1.32	7.40E-02	1.01E-02
5	1.66	9.19E-02	1.02E-02
6	2.20	1.20E-01	1.05E-02

The average of the VCA coil inductance was computed from table 5-1 as 10.09mH using the inductances obtained from the six different tests conducted. The values agree closely with the measured inductance obtained using the LCR meter.

5.7.3 VCA force constant

In this research work, knowledge of the VCA force constant was required to develop the mathematical model that was used to develop the computer based VDMS control system described in section 7.3.1. Although the force constant for the VCA was provided in the data sheet, it was necessary to validate this constant by experimentation. The VCA force constant designated as k_{vca} in this thesis, is a factor which, when multiplied by the coil excitation current gives the peak force generated under 100% duty cycle excitation conditions. The VCA force constant k_{vca} is defined as the ratio between the force generated by the VCA in Newton (N) and the current applied to the VCA coil windings in amperes (A). The force generated by the VCA can be described using Lorentz's law and from equation 4-31 can be expressed as,

$$F = k_{vca} I_{exc} \qquad \text{Equation 5-8}$$

where I_{exc} is the peak current applied to the VCA coil windings. By combining equation 5-1 and equation 5-8, a relationship can be established for computing the VCA force constant k_{vca} in terms of the sensing pipe stiffness constant K_1, the peak current applied to the VCA coil winding I_{exc} and the resultant displacement x of the sensing pipe from a reference position. This is given by,

$$k_{vca} = \frac{K_1 x}{I_{exc}} \qquad \text{Equation 5-9}$$

5.7.3.1 Testing procedure and static test results

An experimental setup comprising the series LR electrical circuit described in section 5.8.1 and the constructed VDMS was used to determine the VCA force constant k_{vca}. The sensing pipe was firmly fixed at both ends to the test rig, with the VCA and LVDT centrally positioned in a vertical orientation on opposite sides of the sensing pipe. A dc voltage supply was used to provide current in the series LR circuit. When the switch shown in figure 5-10 was closed, the dc voltage supply to the LR circuit underwent a step change from 0 to V_{exc} and current flowed through the VCA coil winding. This action caused the VCA to generate a force that was applied to the sensing pipe centre and the sensing pipe

was consequently displaced from its reference position due to the step change in force applied. The pipe displacement x and voltage drop V_s across a precision resistor were measured using the LVDT and the voltage meter respectively. The test was repeated using different values of V_{exc} shown in table 5-2.

5.7.3.2 Results of the testing

For the different values of dc voltage supply V_{exc} used to excite the LR circuit in this experiment, the voltage drop V_s across the precision resistor, the initial pipe displacement x_i and final pipe displacement x_f are presented in Table 5-2. The change in the pipe displacement x due to the step change in force applied, in the direction of the applied force, was computed as the difference between x_i and x_f. The negative sign indicates that the force was applied downward and the pipe displacement was in the direction of the applied force which was also downward. For each value of V_{exc} used in this experiment, the VCA coil current was obtained as per equation 5-6 and equation 5-9 was then used to compute k_{vca} and these values are shown in table 5-2.

Table 5-2: Measurements to obtain VCA force constant

Test Number	Dc voltage to VCA coil Vexc	Voltage drop across precision resistor Vs	Pipe reference position	Pipe final position	Change in pipe position in direction of applied force	Current in VCA coil	force constant Kvca
	V	V	m	m	m	A	N/A
Test 1	4.778	0.3954	3.49E-04	3.45E-04	-4.20E-06	0.3351	-19.43
Test 2	4.002	0.3319	3.49E-04	3.46E-04	-3.50E-06	0.2813	-19.29
Test 3	4.776	0.3974	3.49E-04	3.45E-04	-4.20E-06	0.3368	-19.33
Test 4	6.300	0.5199	3.49E-04	3.44E-04	-5.40E-06	0.4406	-19.00
Test 5	9.231	0.7289	3.49E-04	3.41E-04	-8.00E-06	0.6177	-20.07

The VCA force constant k_{vca} used in this work was then computed from the average of the results above as 19.42N/A.

5.8 Bench test to determine the VDMS frequency response characteristics and constant β

From equation 4-29, it is seen that the mathematical model for predicting density in single phase and multiphase pipe flows is a function of the operating frequency ω of the VDMS, the sensing pipe

stiffness constant K_1, the VDMS constant β and a measurement variable λ that is obtained from $\hat{a}$ and $\hat{b}$ (see equation 4-17, equation 4-18 and equation 4-28). All of these variables except K_1 are frequency dependent. It was therefore important to investigate the frequency response characteristics of the practical VDMS system in order to understand how closely the experimental frequency response acquired from the practical VDMS agreed with the frequency response of a theoretical model of the system. An experiment was undertaken to investigate the frequency response of the practical VDMS at different operating frequencies from 0rad/s up to 1000rad/s. This frequency range covered frequencies from dc up to the fundamental frequency of vibration of the VDMS when it was empty. This experiment also provided the data to determine the VDMS constant β as defined in equation 3-29.

The frequency response theorem was used to compute the magnitude ratio and phase difference information using the theoretical model and these data were obtained from the modulus and argument of the complex function describing the behaviour of the VDMS that was given in equation 4-14. The expressions to compute the theoretical magnitude ratio and phase difference data respectively are given by,

$$Mr(\omega) = 20\log_{10}\frac{1}{\sqrt{[K_1 - \omega^2(\hat{m}_1 + \hat{m}_2)]^2 + \left[\omega\hat{f}_1\right]^2}} \qquad \text{Equation 5-10}$$

$$\theta(\omega) = \tan^{-1}\left(\frac{\omega\hat{f}_1}{[K_1 - \omega^2(\hat{\mathrm{m}}_1 + \hat{\mathrm{m}}_2)]}\right) \qquad \text{Equation 5-11}$$

where Mr is the magnitude ratio in decibels, θ is the phase difference between the pipe displacement and applied force in degrees, ω is the VDMS operating frequency in rad/s and K_1 is the sensing pipe stiffness constant in N/m. The variables $\hat{m}_1$, $\hat{m}_2$ and $\hat{f}_1$ have been defined in equation 4-5 to equation 4-7 and they represent the modified mass of the empty pipe, the modified mass of the contents of the pipe and the pipe modified damping constant respectively. The actual pipe mass m_1 when empty, the actual pipe damping constant f_1 and pipe stiffness constant K_1 are all constants that have been determined from bench tests conducted. Several test mixtures were then formulated using (i) spherical

plastic balls which represented a solid phase and (ii) water and vegetable oil which represented liquid phases. The spherical plastic balls used had a diameter of 4mm and a density of 1340kg/m^3 while the density of vegetable oil and water were 920kg/m^3 and 998.6kg/m^3 respectively, at 20.5℃. Each test mixture was prepared by carefully measuring predetermined amounts of the test substances (spherical solid balls, water or vegetable oil) to form liquid only, solids-liquid and liquid-liquid mixtures. A graduated measuring cup with a known mass was used to collect a predetermined quantity of each test substance which was weighed using a mass scale. The compositions and properties of the different test mixtures prepared are shown in table 5-3.

Table 5-3: Composition and properties of test mixtures used in the bench testing experiments

Test mixture (S/No)	Test mixture name	Composition of test mixtures in sensing pipe	Actual mass of VDMS (m_1+m_2) [Kg]	Density of test mixture [kg/m^3]
TM-1	Test mixture 1	Sensing pipe(2.2kg)+v.oil only(2.57kg)	4.770	919.84
TM-2	Test mixture 2	Sensing pipe(2.2kg)+water(1.39kg) +v.oil(1.30kg)	4.889	962.43
TM-3	Test mixture 3	Sensing pipe(2.2kg)+water(2.36kg) +v.oil(0.35kg)	4.909	969.62
TM-4	Test mixture 4	Sensing pipe(2.2kg)+water(1.80kg) +v.oil(0.92kg)	4.917	972.27
TM-5	Test mixture 5	Sensing pipe(2.2kg)+water only(2.79kg)	4.990	998.58
TM-6	Test mixture 6	Sensing pipe(2.2kg)+water(2.70kg) +solids(0.16kg)	5.053	1021.13
TM-7	Test mixture 7	Sensing pipe(2.2kg)+water(2.37kg) +solids(0.57kg)	5.139	1051.94

From Table 5-3, the mass of each test mixture was obtained by subtracting the total mass of the measuring cup and the test mixture from the mass of the empty measuring cup for each test sample. The total mass of the VDMS was obtained by adding the mass of the empty sensing pipe to that of the relevant test mixture. The pipe stiffness constant and damping constant were obtained from the bench test results in section 5.3.2 and 5.5.2. Lastly, the reference density measurement in this investigation was obtained from the mass of the relevant test mixture and the fixed internal volume of the sensing pipe. The internal volume of the pipe $V_{pipe}$was computed using the volume formula for a hollow cylinder and applying the dimensions of the sensing pipe given in figure 4-5. This was obtained as

$2.8 \times 10^{-3} m^3$ and this value was used to compute the results presented in section 5.8.2, 5.9.2, chapter 8 and chapter 9 of this thesis.

From equation 5-10 and equation 5-11, it is clear that the VDMS constant β must be determined so that the modified masses of the sensing pipe $\hat{m}_1$ and its contents $\hat{m}_2$ and the modfiied damping constant $\hat{f}_1$ can be determined from the actual masses m_1 and m_2 and the actual damping constant f_1. Thus, the VDMS constant β enables the theoretical variation of magnitude ratio and phase difference with frequency to be computed (using equation 5-10 and equation 5-11) for the different test mixtures given in table 5-3.

5.8.1 Testing procedure to determine the VDMS constant β

The constant β relates the fundamental frequency of vibration of the VDMS to its total mass m_1+m_2 and stiffness constant K_1 (see equation 3-29). From section 3.3, it was shown that the VDMS constant β can be determined analytically for a pipe with simple geometry. However, due to the complex geometry of the sensing pipe, as a result of the flexible bellows, and given the need to use an accurate value of β in the density prediction model, it became necessary for an experimental test to be conducted to obtain the best value of β for the VDMS and its support structure when undergoing vibration. The frequency range used in this investigation was such that the frequency response of the VDMS could be investigated from dc to a few rad/s beyond its fundamental resonant frequency for all of the test mixtures considered. Several frequency measurement points were selected within this frequency range and the theoretical and experimental frequency responses were compared for all of the test mixtures. The procedure used to determine the experimental frequency response of the VDMS will be described first, and that for the theoretical frequency response will be described afterwards. “Test mixture 2” will be used here to illustrate the different steps taken to obtain the frequency response data. “Test mixture 2” comprises a mixture of water and vegetable oil. To prepare this test mixture, two measuring cups were used to obtain 1.4litres of water and 1.2litres of vegetable oil respectively. The mass of each measuring cup and its contents was then measured using a mass scale and recorded afterwards. The

bench test rig was positioned in a vertical orientation as shown in figure 5-11. The flanges at the bottom end of the sensing pipe and test rig frame were fastened together using bolts and nuts, while the top flange of the test rig frame was removed to provide access for pouring the test mixture into the sensing pipe.

Figure 5-11: Picture of the sensing pipe connected to bench test rig

Once the test mixture was available, it was carefully poured into the sensing pipe and the top flange of the test rig frame was fastened to the sensing pipe and the test rig base. Care was taken to ensure the VCA, load cell and LVDT assembly were properly aligned at the sensing pipe centre. Once the setup was completed, an excitation signal of constant amplitude and frequency was applied to the VCA. The force applied to the sensing pipe midpoint from the VCA and the resulting displacement of the sensing pipe midpoint were then measured and recorded using the load cell and LVDT and their associated signal conditioning circuits. For each experiment conducted to investigate the VDMS frequency response for a given test mixture, the amplitude of the VCA excitation signal was kept constant while the frequency was varied between 0rad/s and 760rad/s at predetermined frequency points. For each frequency point where a measurement was taken in the experiment, the force and displacement signals

were measured and then saved to a computer. For each test mixture used in this experiment, five different measurements were taken at each frequency point. Once the force and displacement signals had been saved to a computer, their respective DFTs were obtained in the form given in equation 4-35 and equation 4-36. These DFT components were then used to compute the magnitude of the peak amplitude and corresponding phase of the displacement and force signals using equation 4-43 to equation 4-46. The magnitude ratio Mr and corresponding phase difference θ at a given frequency (VDMS operating frequency ω_k) were then obtained using equation 4-49 and equation 4-50 respectively. The theoretical frequency response information of the VDMS was obtained using equation 5-10 and equation 5-11 where the modified total mass $\hat{m}_1 + \hat{m}_2$ and modified damping constant $\hat{f}_1$ were respectively obtained from,

$$\hat{m}_1 + \hat{m}_2 = \frac{m_1 + m_2}{\beta^2} \qquad \text{Equation 5-12}$$

$$\hat{f}_1 = \frac{f_1}{\beta}. \qquad \text{Equation 5-13}$$

5.8.2 Results of the testing

From the expressions given in equation 5-10, equation 5-11, equation 5-12 and equation 5-13, it is apparent that the value of the VDMS constant β must be known in order to compute the theoretical frequency response of the VDMS. The value of β for a fixed end beam with simple geometry obtained in section 3.3 was used as an initial value, in an iteration technique, to determine the actual VDMS constant required to compute the VDMS theoretical frequency response. Since the initial value for β was obtained for a fixed end beam with simple geometry, the iterative optimization technique was used to determine a more accurate value of β for the VDMS which ensured the magnitude ratio and phase difference data obtained from the experiments agreed with the theoretical frequency response. The iterative technique uses Microsoft Excel solver [165] to obtain a single value for β that gave the "best fit" between the experimental and theoretical magnitude ratio and phase difference responses for each test mixture. Microsoft Excel solver is an iterative tool used to find optimal solutions for all kinds of

decision problems subject to various constraints. It works by adjusting the values in decision variable cells to satisfy the limits defined in constraint cells and to produce the results desired in the objective cells. The constraint used in the present study was to require equal magnitude ratio and phase difference values for the theoretical and experimental results across the range of frequencies investigated. The decision variable cell was selected as the cell with the value of the VDMS constant β. The initial value of this cell was set to 1.14 which corresponds to the theoretical value obtained in section 3.3. For each of the test mixtures given in table 5-3, Microsoft Excel solver was used to find a single optimal value for the constant β giving the best fit between the experimental and theoretical magnitude ratio and phase difference data. The results for β obtained for the seven test mixtures investigated are shown in table 5-4.

Table 5-4: VDMS constant obtained for the different test mixtures

Test mixture (S/No)	Test mixture name	Components of test Mixture	VDMS constant β
TM-1	Test mixture 1	Sensing pipe(2.2kg)+v.oil only(2.57kg)	1.2878
TM-2	Test mixture 2	Sensing pipe(2.2kg)+water(1.39kg) +v.oil(1.30kg)	1.2874
TM-3	Test mixture 3	Sensing pipe(2.2kg)+water(2.36kg) +v.oil(0.35kg)	1.2897
TM-4	Test mixture 4	Sensing pipe(2.2kg)+water(1.80kg) +v.oil(0.92kg)	1.2839
TM-5	Test mixture 5	Sensing pipe(2.2kg)+water only(2.79kg)	1.2805
TM-6	Test mixture 6	Sensing pipe(2.2kg)+water(2.70kg) +solids(0.16kg)	1.2826
TM-7	Test mixture 7	Sensing pipe(2.2kg)+water(2.37kg) +solids(0.57kg)	1.2824

From the results in

table 5-4, it can be observed that test mixtures containing similar substances have values of β which are close to each other. It was considered plausible that β may be affected by the mass distribution of the pipe contents and so it was therefore instructive to group the different test mixtures according to the similarity of the phases of the constituent substances in the mixture. The test mixtures were put in two groups, namely; liquid-liquid test mixtures and solids-liquid test mixtures. The liquid-liquid group

includes the test mixtures comprising of only one or two liquids, and the solids-liquid group includes the test mixtures comprising of solid balls and liquid. These groups are presented in table 5-5.

Table 5-5: Test mixture groups and average value of VDMS constant

Test mixture groups	Test mixture number (TM)	Average value of VDMS constant β
Liquid-Liquid	1,2,3,4,5	1.2863
Solids-Liquid	6,7	1.2825

A single value of β for the liquid-liquid group was obtained as 1.2863 from the average of the values of β shown for test mixtures 1-5 in

table 5-4. Similarly, a single value of β for the solids-liquid test mixture group was obtained as 1.2825 from the average of the values of β for test mixtures 6 and 7. Since the mass distribution of an incompressible test mixtures is expected to be approximately uniform, and given that the two groups of test mixtures used in the current investigation are incompressible, it was decided that a single value for the VDMS constant β should be used in this research. The single value of β chosen for the VDMS was 1.2844 and it was obtained from the average value of β for the two groups of test mixtures given in table 5-5. This value of the VDMS constant β gave the best agreement between the experimental and theoretical frequency response curves for the two groups of test mixtures considered. This value of β was used in section 5.9 to investigate the capability of the novel mathematical model and signal processing technique to predict the density of a mixture contained in the sensing pipe.

Once this single value of β had been obtained, the resultant theoretical magnitude ratio and phase difference frequency responses were generated for the seven test mixtures and compared with the experimental frequency response for the same mixtures. These plots demonstrate the good matches between the theoretical model and the experimental results. The plots of the magnitude ratio and phase difference plots for the seven test mixtures investigated are shown in figure 5-12 to figure 5-18.

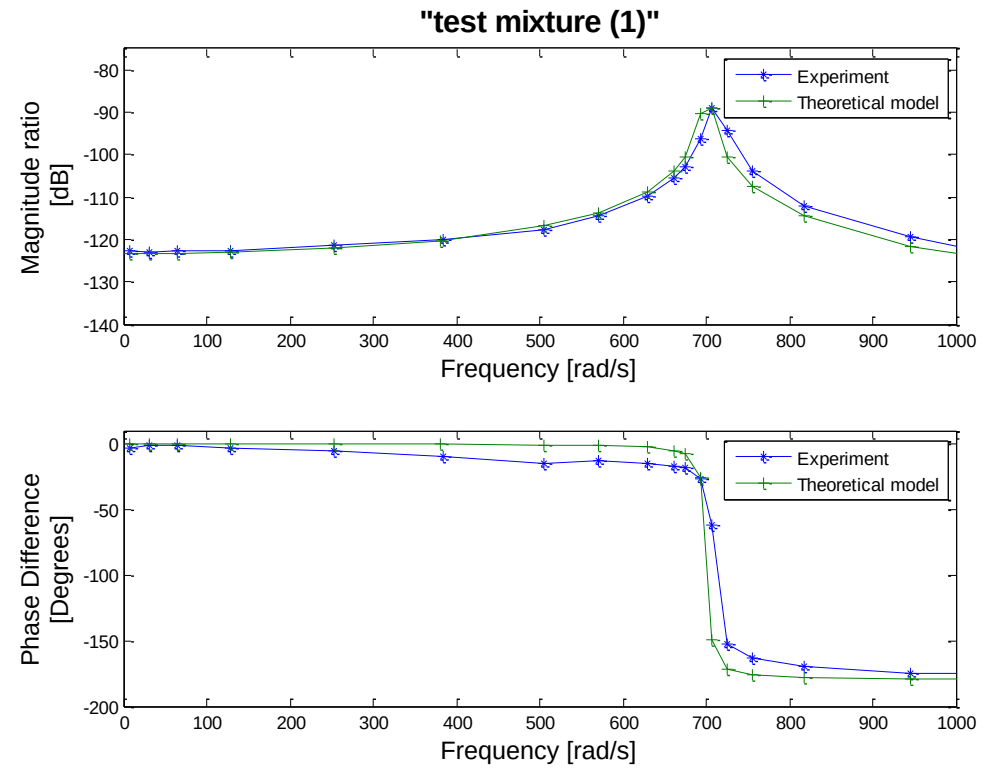

Figure 5-12: Experimental and theoretical frequency response plots for test mixture (1)

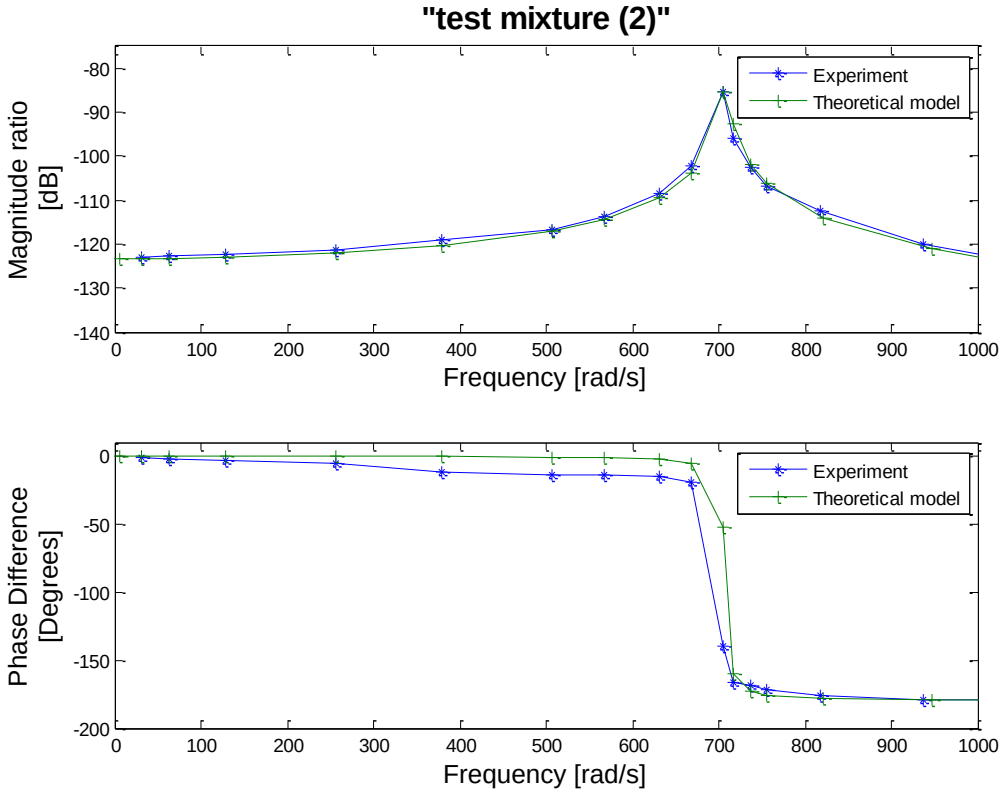

Figure 5-13: Experimental and theoretical frequency response plots for test mixture (2)

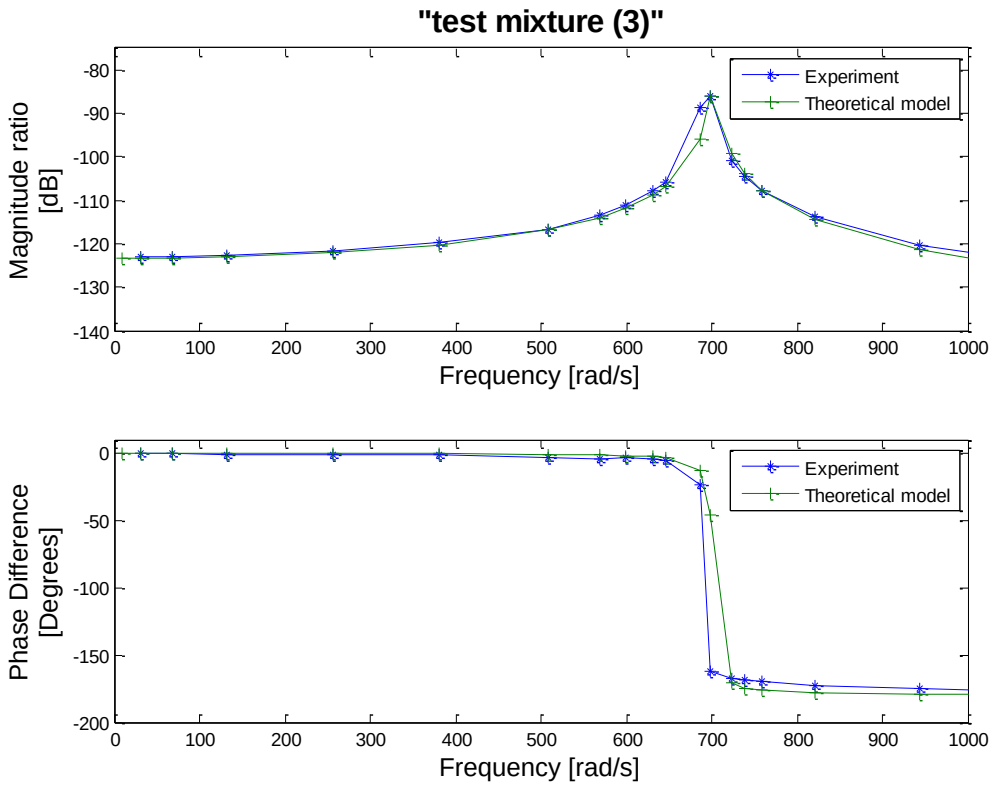

Figure 5-14: Experimental and theoretical frequency response plots for test mixture (3)

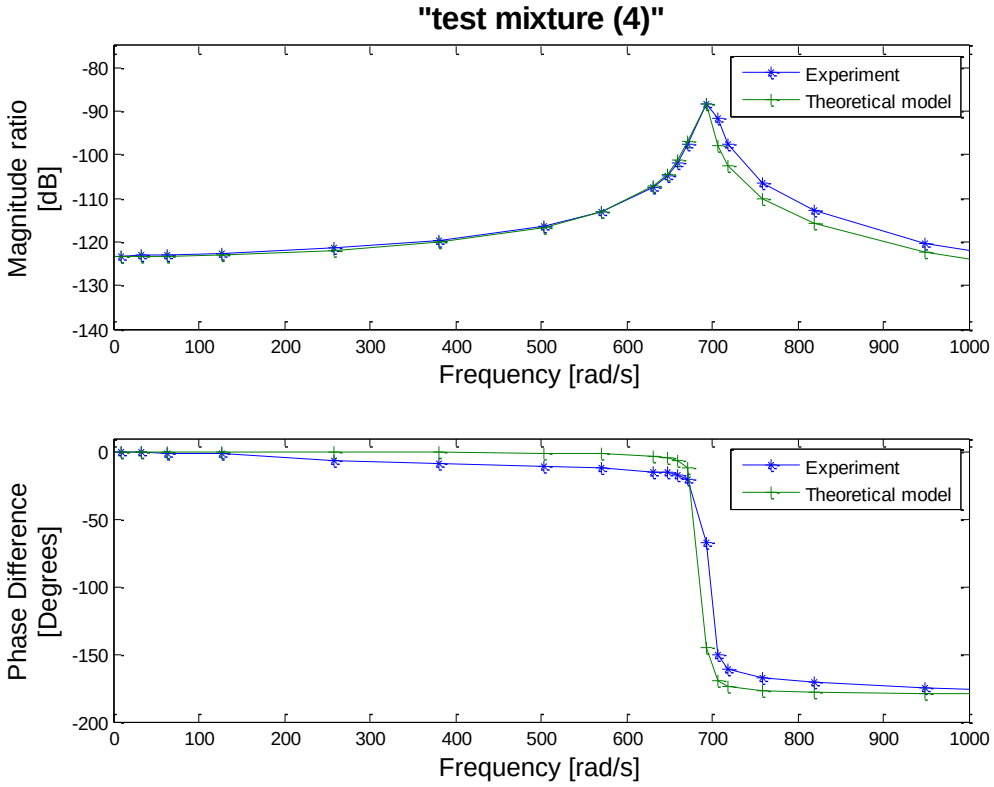

Figure 5-15: Experimental and theoretical frequency response plots for test mixture (4)

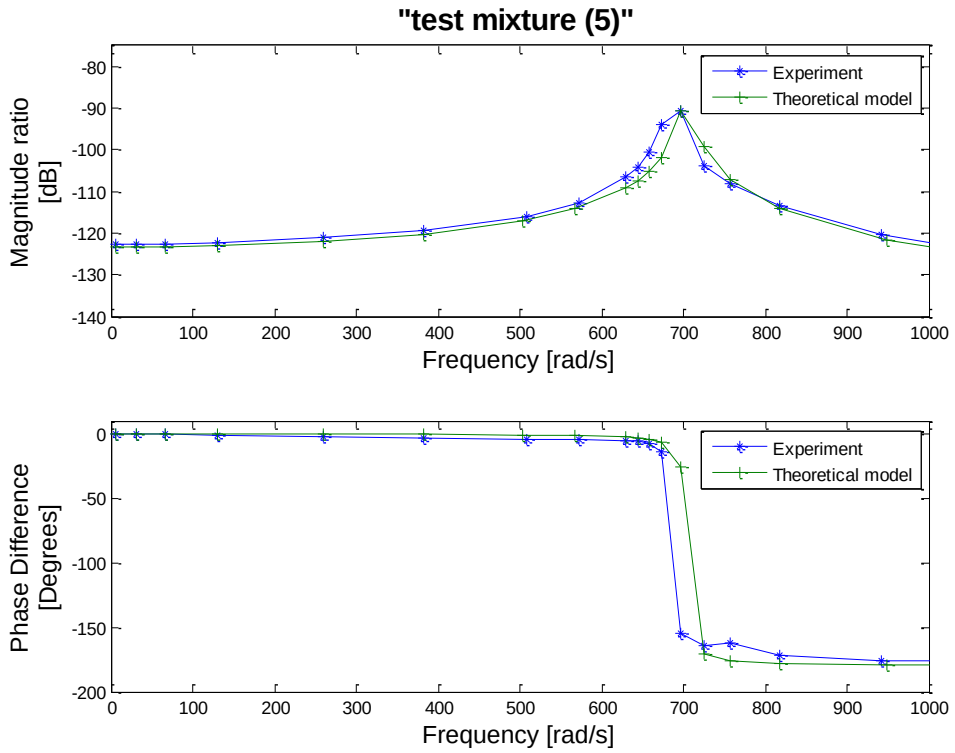

Figure 5-16:Experimental and theoretical frequency response plots for test mixture (5)

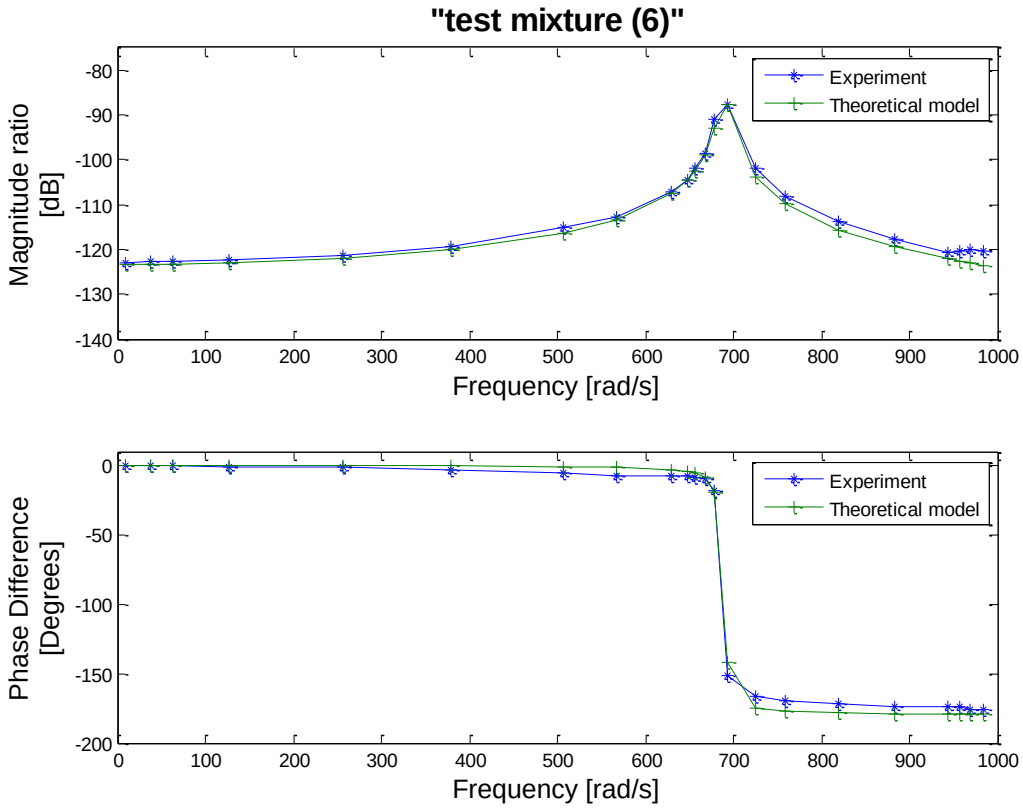

Figure 5-17:Experimental and theoretical frequency response plots for test mixture (6)

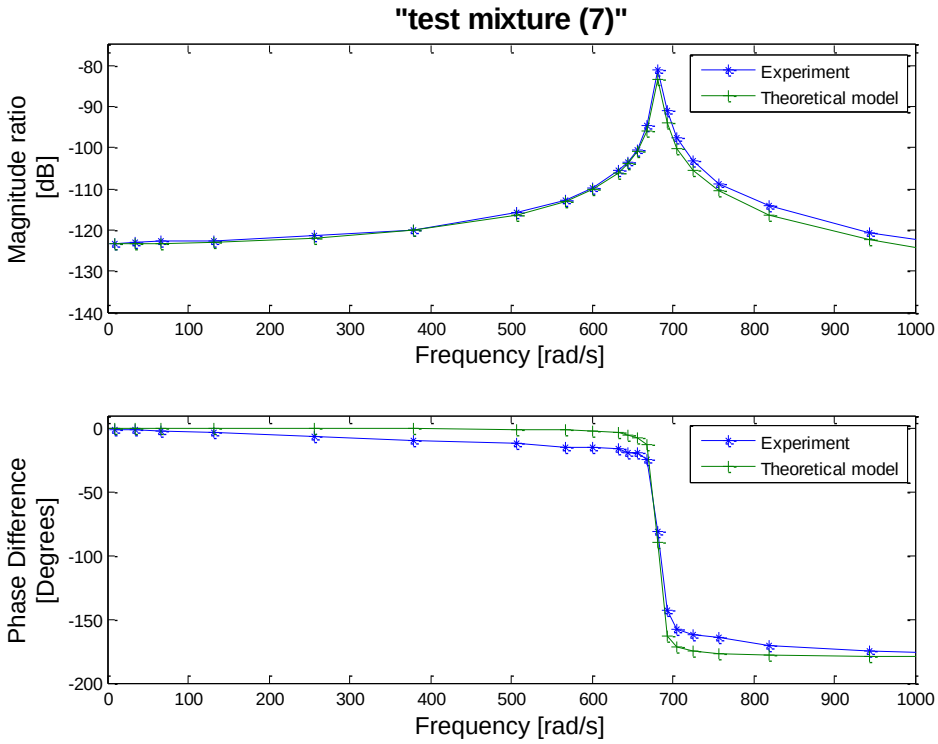

Figure 5-18: Experimental and theoretical frequency response plots for test mixture (7)

For the plots shown in figure 5-12 to figure 5-18, the green curves represent the theoretical frequency response characteristics of the VDMS, while the blue curves represent the experimental frequency response characteristics of the VDMS. The vertical axes represent either the magnitude ratio in decibels or the phase difference in degrees obtained as described in section 5.8 and the horizontal axes represent the frequency of excitation of the VDMS. From the results shown in figure 5-12 to figure 5-18, the magnitude ratio and phase difference plots for the experiments and theoretical model closely overlay each other over the frequency range investigated for all test mixtures. For the different test mixtures investigated more measurement points are required around the resonant frequency region of the VDMS to accurately describe the behaviour of the phase angle $\theta(\omega)$ which changes rapidly close to the resonance frequency. Furthermore, the agreement between the theoretical and experimental frequency responses appears to deviate as the operating frequency is increased beyond the resonant frequency. This increasing deviation between the theoretical and experimental response curves may be due to higher vibration modes of the VDMS at higher operating frequencies. For this reason, it was decided

that further investigation on the operation of the VDMS would be restricted to frequencies up to its first resonant frequency. The results in figure 5-12 to figure 5-18 have shown that a single value for the constant β describes the vibration characteristics of the VDMS system with a good degree of accuracy. This single value of β will subsequently be used in the novel mathematical model developed in equation 4-29 for predicting the density of a pipe flow.

5.9 Bench tests to investigate the accuracy of the constructed VDMS, novel mathematical model and signal processing technique when used to predict the density in pipe flows

Once the VDMS constant β had been determined and the theoretical and experimental frequency response characteristics of the VDMS had been confirmed to be in good agreement, it was then necessary to investigate the capability of the physical VDMS, in conjunction with the novel mathematical model and relevant signal processing techniques, of giving accurate density measurements when used in pipe flows.

5.9.1 Test conditions investigated

An experiment to investigate the accuracy of the physical VDMS was designed using the test mixtures described in table 5-3. From the frequency response plots presented in figure 5-12 to figure 5-18, it was seen that, as the operating frequency of the VDMS was increased closer to its resonant frequency for each test mixture, the force required to cause a measurable displacement of the sensing pipe decreased. Since a smaller force will be required to displace the pipe at frequencies close to its resonant frequency, the decision was taken to reduce the operating frequency range of the VDMS in this experiment from 0-1000rad/s to 500rad/s to 760rad/s. The bench test rig was set up in a vertical orientation and the operating procedure described in section 5.9.2 was used to operate the VDMS. Several predetermined frequency measurement points were selected within the measurement frequency range. For each test mixture, the VDMS was operated at each predetermined frequency point and the force applied to the sensing pipe midpoint and resulting displacement were simultaneously measured and recorded using the load cell and LVDT, their respective signal conditioning units and the data acquisition unit. For

each frequency point used in the experiment, five different measurements were obtained to reduce random errors in the predicted density measurements as described in section 5.9.2.

5.9.2 Predicted density measurements obtained using constructed VDMS, novel mathematical model and signal processing technique

The predicted densities of the test mixtures were computed for each frequency investigated using the signal processing technique described in section 4.5, which involves (i) calculating the terms $\hat{a}$ and $\hat{b}$ (see equation 4-17 and equation 4-18), from the force and displacement measurements, (ii) finding the mass m_2 of the contents of the sensing pipe using equation 4-29 and finally (iii) computing ρ_m using equation 4-30. For each test mixture investigated, the density measurement error at each frequency measurement point was computed by comparing the predicted density obtained from the VDMS with the reference density of the relevant test mixture. The density measurement error for the j[th] frequency measurement point was obtained as follows,

$$e_{tm,j} = \frac{\bar{\rho}_{tm,m,j} - \rho_{tm,ref}}{\rho_{tm,ref}} \times 100 \qquad \text{Equation 5-14}$$

where j is an index denoting the j[th] frequency measurement, $\rho_{tm,ref}$ is the reference density of a relevant test mixture and $\bar{\rho}_{tm,m,j}$ is the mean density (averaged of 5 measurement points) prediction from the VDMS for a given text mixture at the j[th] frequency and it is given by,

$$\bar{\rho}_{tm,m,j} = \frac{1}{5}\sum_{i=1}^{5} \rho_{tm,m,j,i} \qquad \text{Equation 5-15}$$

where $\rho_{tm,m,j,i}$ is the i[th] density prediction obtained from the VDMS at the j[th] frequency measurement point for a given text mixture. This information was then used to compute a mean percentage error $\bar{e}_{tm}$ and a standard deviation term S_{tm} for the percentage errors associated with each test mixture.These were obtained as follows,

$$\bar{e}_{tm} = \frac{1}{N}\sum_{j=1}^{N} e_{tm,j} \qquad \text{Equation 5-16}$$

$$S_{tm} = \sqrt{\frac{1}{N}\sum_{j=1}^{N}\left(e_{tm,j} - \bar{e}_{tm}\right)^2}$$ Equation 5-17

where $\bar{e}_{tm}$ is the mean error in the predicted densities for a given test mixture, S_{tm} is the standard deviation of these errors and N is the total number of frequency measurement points used for each test mixture. The plots of the density measurement errors versus frequency for the seven test mixtures are shown in figure 5-19.

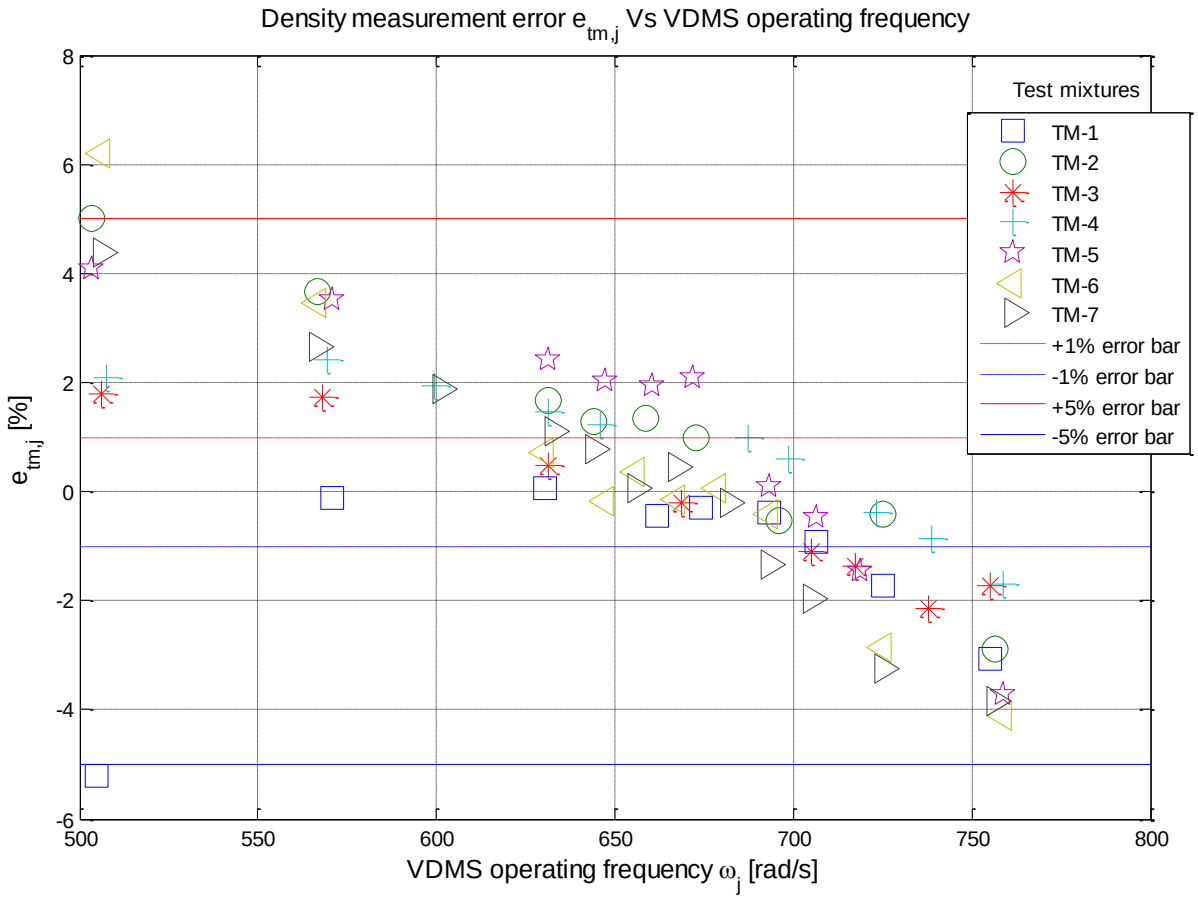

Figure 5-19: Plots of relative errors $e_{tm,j}$ in predicted density measurements for the seven test mixtures given in table 5-3

The plots presented in figure 5-19 show the variation of the percentage relative errors $e_{tm,j}$ in the predicted densities when the VDMS operating frequency was varied between 500rad/s and 760rad/s. The curves with red and blue dashed line markers represent $\pm 1\%$ error bars respectively. Similarly, the plots with red and blue continuous line markers represent $\pm 5\%$ error bars respectively. Furthermore, the data on the horizontal axis represents the VDMS operating frequency and the data on

the vertical axis represents the percentage relative error $e_{tm,j}$ in predicted density obtained for a given frequency measurement point and were computed using equation 5-14. The standard deviation of the errors S_{tm} provides a good measure of the random scatter in the density measurements whilst the method for computing $\bar{e}_{tm}$ is better for showing up "systematic offset errors" in the density measurements. Values for $\bar{e}_{tm}$ and S_{tm} for each test mixture investigated are presented in table 5-6.

Table 5-6: Means errors and standard deviation of errors in predicted density for the test mixtures investigated

Test mixture (S/No)	Test mixture name	Components of test Mixture	Mean error $\bar{e}_{tm}$ [%]	Standard deviation S_{tm} of errors [%]	Resonant frequency of test mixture [rad/s]
TM-1	Test mixture 1	Sensing pipe(2.2kg)+v.oil only(2.57kg)	-0.57%	0.60%	711.25
TM-2	Test mixture 2	Sensing pipe(2.2kg)+water(1.39kg) +v.oil(1.30kg)	1.11%	1.41%	702.32
TM-3	Test mixture 3	Sensing pipe(2.2kg)+water(2.36kg) +v.oil(0.35kg)	-0.13%	1.26%	702.14
TM-4	Test mixture 4	Sensing pipe(2.2kg)+water(1.80kg) +v.oil(0.92kg)	1.15%	0.92%	698.41
TM-5	Test mixture 5	Sensing pipe(2.2kg)+water only(2.79kg)	1.24%	1.69%	691.45
TM-6	Test mixture 6	Sensing pipe(2.2kg)+water(2.70kg) +solids(0.16kg)	0.10%	1.73%	688.25
TM-7	Test mixture 7	Sensing pipe(2.2kg)+water(2.37kg) +solids(0.57kg)	-0.01%	1.79%	682.36

5.9.3 Discussion of measurement results and measurement errors when using the physical VDMS to predict mixture density

Before discussing the density prediction results and the measurement errors obtained for the different test mixtures investigated, it is important to state here that the single value for the VDMS constant β obtained in section 5.8.1 was applied in the novel mathematical model to compute the predicted density and the expression in equation 5-18 was used to compute the resonant frequency for all the test mixtures.

$$\omega_{n,1} = \beta \sqrt{\frac{K_1}{m_1 + m_2}}$$ Equation 5-18

From the results shown in figure 5-19, the relative error $e_{tm,j}$ in the predicted density for all test mixtures in the frequency range investigated are within $\pm 5\%$ for the vast majority of the measurements taken. A careful analysis of the trend in the errors presented in figure 5-19, shows that as the VDMS operating frequency was increased towards the resonant frequency for the relevant test mixtures (see table 5-6), the errors associated with the predicted density were seen to reduce considerably. When the VDMS operating frequency was between 670rad/s and 715 rad/s, $e_{tm,j}$ was within $\pm 1\%$ of the reference density for 90% of the measurements taken. This result highlighted the need to define an optimal operating frequency range for the VDMS. It is worth mentioning that a theoretical analysis of the density prediction model using the system parameters obtained from the bench tests described above and computing $\hat{a}$ and $\hat{b}$ respectively using equation 4-19 and equation 4-20 showed that the model could be used to compute density in a pipe flow at any frequency of choice. However, the physical limitations imposed by the sensitivity and accuracy of the displacement sensor associated with the VDMS can restrict the range of frequency for which measureable displacements can be obtained and thence the VDMS operating frequency range.

From the results presented in table 5-6, the mean errors $\bar{e}_{tm}$ in the predicted densities for all the test mixtures used in the investigation are less than $\pm 0.57\%$ with the exceptions of test mixtures 2, 4 and 5 while the standard deviations S_{tm} of the errors for all the test mixtures are less than 1.8%. For all seven test mixtures investigated, the overall mean $\bar{e}_{tm,t}$ of the errors in the predicted densities is found to be 0.41%. It is immediately obvious from these results that the density measurement has a positive offset and a significant scatter exists in the measurement results, hence the need to reduce the measurement errors $e_{tm,j}$ associated with predicting the mixture density. Further investigations were thus conducted to determine optimal parameters for operating the VDMS to reduce these measurement errors.

5.10 Minimizing the error $e_{tm,j}$ in the predicted density obtained using the VDMS

Given the large scatter observed in the predicted density results shown in figure 5-19, it became imperative to optimize the operation of the VDMS to obtain more satisfactory density measurements. From the novel mathematical model developed in equation 4-29 for predicting density in pipe flows, the measurement errors associated with $\rho_{tm,m,j,i}$ could possibly be from one or more of the following sources; (i) error in the value of the VDMS constant β, (ii) error in the measurement of the VDMS operating frequency ω (iii) errors associated with the force and displacement measurement. In order to minimize the error in the predicted density, the three possible sources of errors were investigated. Firstly, an optimal value for the VDMS constant β_{opt} was defined using the overall mean $\bar{e}_{tm,t}$ of the errors for all measurements taken using the seven test mixtures. The overall mean $\bar{e}_{tm,t}$ of the errors was obtained as follows,

$$\bar{e}_{tm,t} = \frac{1}{7N}\sum_{p=1}^{7}\sum_{j=1}^{N} e_{tm,j} \qquad \text{Equation 5-19}$$

where $\bar{e}_{tm,t}$ is the overall mean error for all 7 test mixtures investigated across all measured frequency points for each test mixture, N is the total number of frequency measurement points for each test mixture and $e_{tm,j}$ is the relative error at the jth frequency point for the pth test mixture. The value of $\bar{e}_{tm,t}$ was found to be 0.41%. Since the predicted density is proportional to the square of the VDMS constant β, the value of $\bar{e}_{tm,t}$ can be minimized by reducing β by the factor given in equation 5-20,

$$b_x = \left(1 + \frac{\bar{e}_{tm,t}}{100}\right)^{-0.5} \qquad \text{Equation 5-20}$$

where b_x is the VDMS constant optimization factor. The optimal VDMS constant β_{opt} was then obtained using the expression,

$$\beta_{opt} = b_x\beta \qquad \text{Equation 5-21}$$

The optimal value for the VDMS constant β_{opt} was obtained as 1.2819. This new value for the VDMS constant β_{opt} when applied to the novel mathematical model will give the smallest mean error in the predicted density. Secondly, analyses were also carried out to investigate the optimal operating frequency for which the density measurement errors could be minimized. From the results represented in figure 5-19, it is clearly seen that as the VDMS operating frequency moves closer to the resonant frequency of the relevant test mixture, the errors associated with the predicted density decrease. The measurement errors are observed to be within the $\pm 1\%$ error bars when the VDMS was operated between 660-715 rad/s. This frequency range corresponds to the resonant frequency range for the test mixtures investigated (see table 5-6). Thus, additional error reduction could be achieved by selecting a more limited operating frequency range for the VDMS where it is expected that the displacement of the pipe could be accurately measured. Thirdly, it was also found possible to minimize the measurement errors by increasing the resolution of the measured VDMS operating frequency ω when taking the DFT of the measured force and displacement signals, by reducing the sampling frequency of the data acquisition unit. In order to ensure the sampling frequency used in this investigation still conformed to Shannon's sampling criterion, the data acquisition sampling frequency f_s was reduced by 50% from 5kHz to 2.5kHz and this reduction in the data sampling frequency resulted in an increase in the resolution of the measured operating frequency changing from 0.08rad/s to 0.04rad/s. An extensive investigation was therefore carried out to understand and quantify, where possible, the measurement errors associated with using the load cell and LVDT to obtain force and displacement measurements. From equation 4-19 and equation 4-20, if an incompressible mixture is contained within the sensing pipe, then the theoretical equivalent of the term $\lambda(\omega)$ defined in equation 4-28 is given by,

$$\lambda(\omega) = K_1 - (\hat{m}_1 + \hat{m}_2)\omega^2 \qquad \text{Equation 5-22}$$

where K_1 is the sensing pipe stiffness constant, $\hat{m}_1$ is sensing pipe modified mass when empty defined in equation 4-5, $\hat{m}_2$ is the modified mass of the contents of the pipe defined in equation 4-6 and ω is

the VDMS operating frequency. By operating the VDMS at the resonant frequency associated with a given test mixture, the operating frequency ω becomes equal to $\omega_{n,1}$ (see equation 3-29). Therefore, the theoretical value of λ also referred to as λ_{opt} can be found by substituting equation 3-29 and equation 5-18 into equation 5-22. This value of λ_{opt} was found to be zero. Since the experimental value for λ for all the measurements taken was obtained using $\hat{a}$ and $\hat{b}$ and these parameters were computed using the DFTs of the measured force and displacement signals using equation 4-47 and equation 4-48, minimizing $\lambda(\omega)$ minimizes the influence of measurement errors in $\hat{a}$ and $\hat{b}$, the predicted value of m_2 and hence $\rho_{tm,m,j,i}$. It was therefore instructive to understand how the errors associated with the measurement of the applied force and pipe displacement at different VDMS operating frequencies relates to $\lambda(\omega)$, the predicted value of m_2 and hence $\rho_{tm,m,j,i}$. The plot of $\lambda(\omega)$ against the VDMS operating frequency ω is shown for all seven test mixture in figure 5-20.

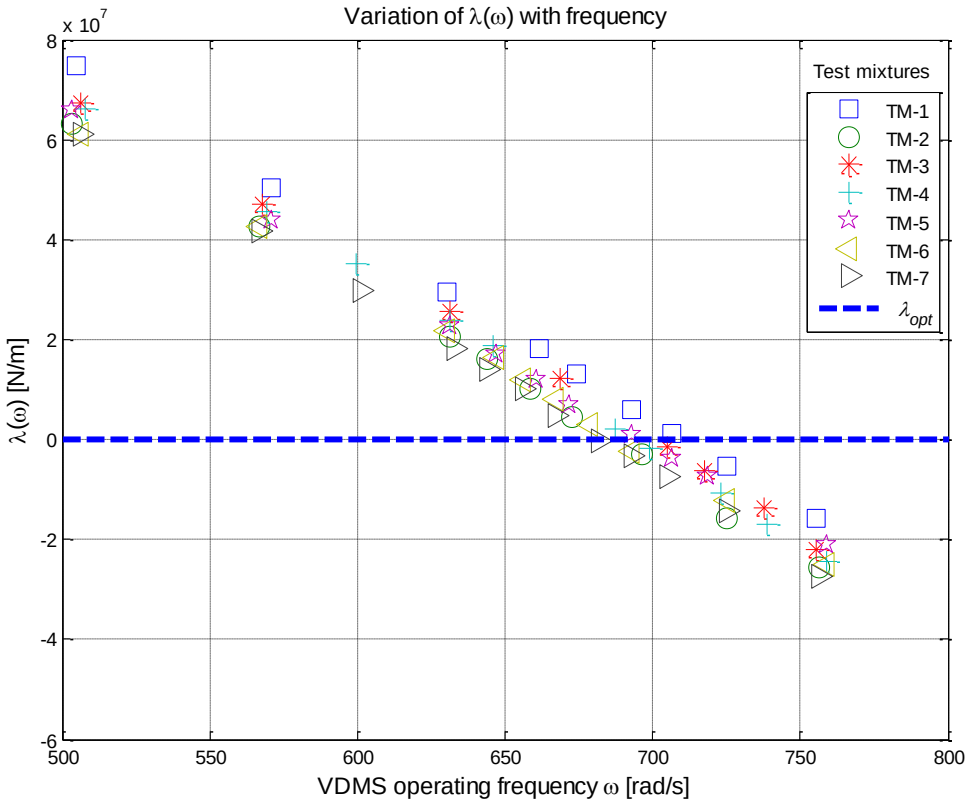

Figure 5-20: Plot of variation of $\lambda(\omega)$ value with VDMS operating frequency

Figure 5-20 shows the variation of $\lambda(\omega)$ with the VDMS operating frequency ω. The data on the vertical axis represents the $\lambda(\omega)$ obtained using equation 4-28 while the data on the horizontal axis represents the VDMS operating frequency. The different test mixtures investigated are represented by different symbols and colours. The curve with blue dashed line marker represents the theoretical value of the λ which was obtained using equation 5-22. The result in figure 5-20 shows that for the experimental data the parameter $\lambda(\omega)$ reduces rapidly with increasing operating frequency. When ω lies between 660rad/s to 715rad/s, which extends across the resonant frequency for all the test mixtures investigated, $\lambda(\omega)$ is seen to be close to zero. From figure 5-19, it is seen that the measurement errors $e_{tm,j}$ associated with the predicted density are smallest when the VDMS operating frequency ω was between 660rad/s to 715rad/s. Thus, by choosing operating frequencies where $\lambda(\omega) \cong 0$, measurement errors associated with the load cell and LVDT and modelling errors associated with the system damping will be minimized and so the density measurement will be more accurate. The frequency range where $\lambda(\omega) \cong 0$ was defined as the optimal frequency f_{opt} range for operating the VDMS. Further analysis was thus required to investigate the density measurement errors using the optimal parameters.

5.10.1 Results of VDMS Optimization

Using the defined optimal operating parameters f_{opt}, β_{opt} and a data sampling frequency f_s obtained from section 5.10, the measurement errors in the predicted density were computed for the test mixtures described in table 5-3. These are presented in figure 5-21.

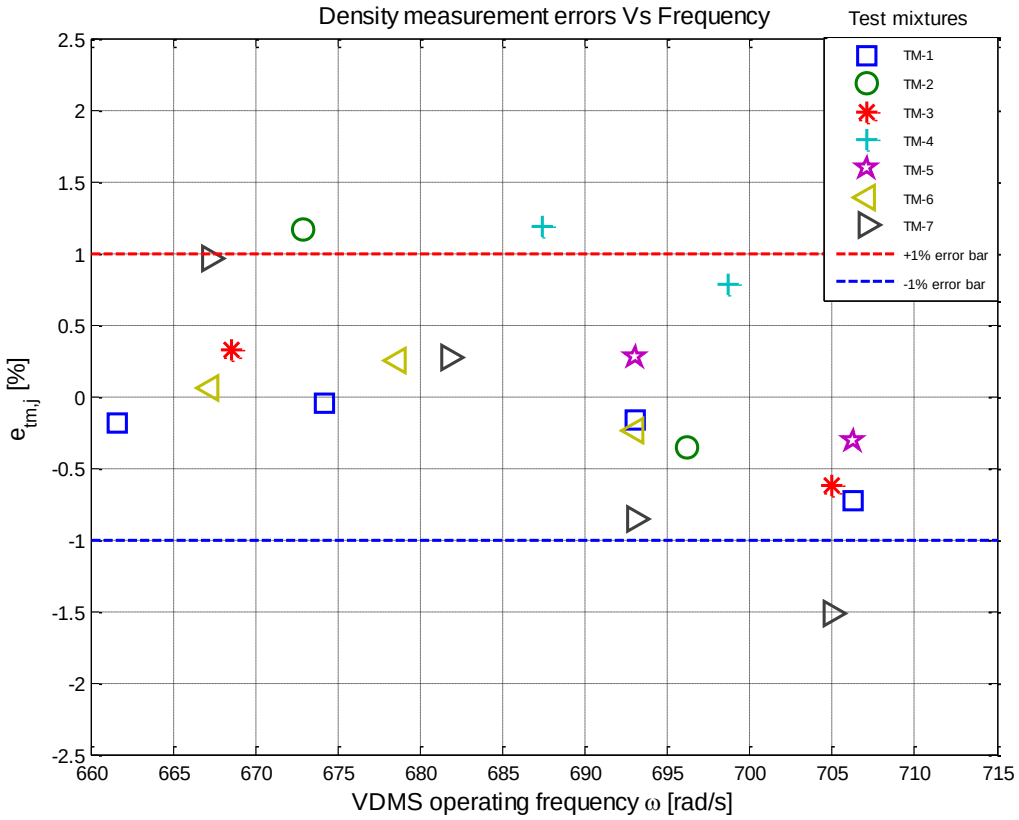

Figure 5-21:Density measurement errors for VDMS optimal operating condition

The plot in figure 5-21 shows the measurement errors in the predicted density when the VDMS was operated using the optimal conditions (f_{opt}, β_{opt} and f_s) described in section 5.10. For the plots in figure 5-21, the vertical axis represents the density measurement error computed using equation 5-14, while the horizontal axis represents the optimal operating frequency range of the VDMS. The different test conditions are represented by different symbols and colours on the plot. The plots with red and blue dashed line represent $\pm 1\%$ error bars. It is clearly seen from the results that the measurement errors were consistently within $\pm 1\%$ for over 90% of the measurements taken. The mean error $\bar{e}_{tm}$ and standard deviation S_{tm} of the errors in $\rho_{tm,m,j,i}$ were then computed using equation 5-16 and equation 5-17 and are shown in table 5-7.

Table 5-7: Mean error and standard deviation of measurement errors when VDMS was operated using the defined optimal parameters f_{opt}, β_{opt} and f_s

Test mixture (S/No)	Test mixture name	Components of test Mixture	Mean error $\bar{e}_{tm}$ [%]	Standard deviation S_{tm} of errors [%]
TM-1	Test mixture 1	Sensing pipe(2.2kg)+v.oil only(2.57kg)	-0.24%	0.62%
TM-2	Test mixture 2	Sensing pipe(2.2kg)+water(1.39kg) +v.oil(1.30kg)	0.82%	0.99%
TM-3	Test mixture 3	Sensing pipe(2.2kg)+water(2.36kg) +v.oil(0.35kg)	-0.41%	0.20%
TM-4	Test mixture 4	Sensing pipe(2.2kg)+water(1.80kg) +v.oil(0.92kg)	0.87%	0.74%
TM-5	Test mixture 5	Sensing pipe(2.2kg)+water only(2.79kg)	-0.14%	0.79%
TM-6	Test mixture 6	Sensing pipe(2.2kg)+water(2.70kg) +solids(0.16kg)	-0.36%	1.38%
TM-7	Test mixture 7	Sensing pipe(2.2kg)+water(2.37kg) +solids(0.57kg)	-0.58%	1.44%

Once the errors were computed for the experiments to determine the test mixtures densities using the optimized VDMS operating conditions, it was then instructive to compare the results obtained from the normal and optimized VDMS operation. The mean $\bar{e}_{tm}$ of the error and the standard deviations S_{tm} of the errors for the results presented in table 5-6 and table 5-7 are plotted on a bar chart for the seven test mixtures as shown in figure 5-22 (a) and (b) respectively.

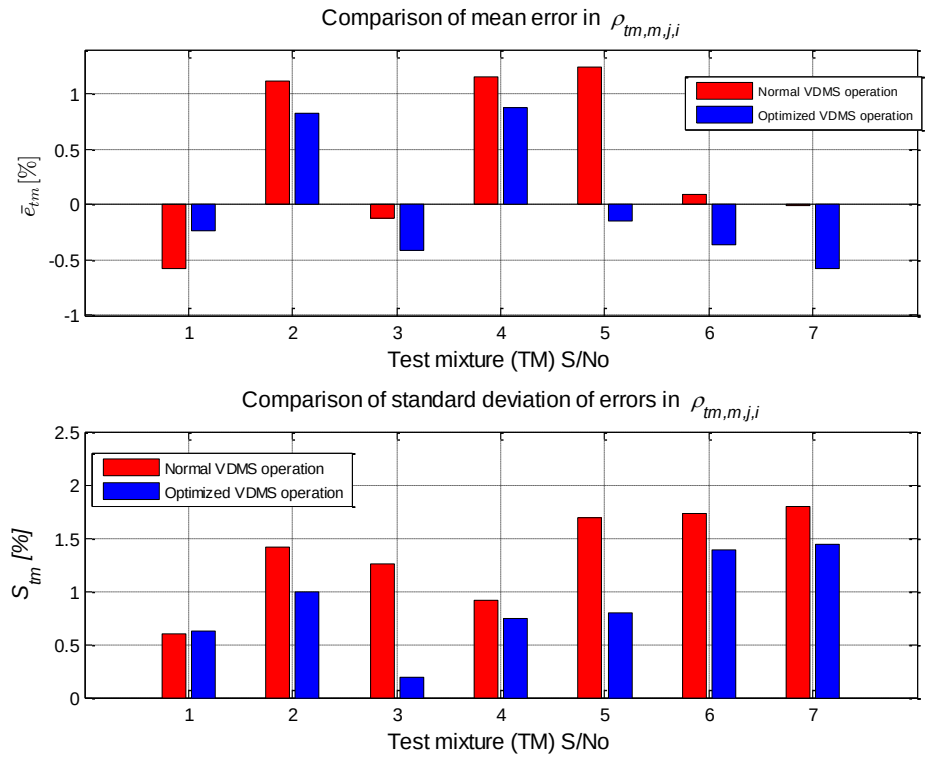

Figure 5-22:(a) Comparison of mean measurement error in predicted density (b) Comparison of mean of standard deviations of measurement errors in predicted density

The bar chart in figure 5-22(a) shows the comparison between the mean $\bar{e}_{tm}$ of the errors in the predicted densities for each test mixture used in the investigation when the VDMS was operated using the parameters obtained from the bench tests and the defined optimized operating condition. These different operating conditions are indicated by different colours as shown in the legend. Similarly, figure 5-22(b) shows the comparison between the standard deviations S_{tm} of the errors in $\rho_{tm,m,j,i}$ for each test mixture used in the investigation at the different VDMS operating conditions. From figure 5-22(a), it is seen that the mean error of the errors in $\rho_{tm,m,j,i}$ when the VDMS was operated using the optimized parameters are less than $\pm 1\%$ for the test mixtures 1,2 and 4. Figure 5-22(b) shows reduction in the standard deviation of the errors in the experiments where the optimized operating conditions were used. The results also show that the maximum values of the mean error $\bar{e}_{tm}$ and standard deviation S_{tm} of the errors obtained when the VDMS was used to predict the density of the respective test mixtures using the normal and optimized operating conditions are reduced from 1.24% and 1.79% to

0.87% and 1.44% respectively. Again, by operating the VDMS using the optimal values of f_{opt}, β_{opt} and f_s for all seven test mixtures used in this investigation, it was possible to reduce the overall mean error $\bar{e}_{tm,t}$ and overall standard deviation $S_{tm,t}$ of the errors from 0.41% and 1.51% to −0.01% and 1.07% respectively. From the results obtained, it can be concluded that use of the optimal conditions produces an improvement in the density measurement accuracy obtained when using the VDMS.

5.11 Summary

The design and construction of the novel vibratory densitometry system have been described in this chapter. Firstly, the construction of a bespoke bench test rig used in the research work was described. The several bench tests that were conducted to determine the mass m_1, spring stiffness K_1 and damping properties f_1 of the sensing pipe have been described in sections 5.3 to 5.5. These sections also include discussion of the results from the bench tests to determine m_1, K_1 and f_1. Furthermore, the results of an investigation to validate the displacement pattern of the sensing pipe with 'fixed end' supports when a load was applied to its centre were described in section 5.6. The results of the bench tests conducted to validate the VCA coil resistance R_{vca}, coil inductance L_{vca} and force constant k_{vca} specifications were presented in section 5.7. An experiment to determine the frequency response characteristics of the constructed VDMS was also described in section 5.8 and the result obtained was used to determine an initial value for the VDMS constant β. The initial value for β was then used to predict the mixture density of some test mixtures. The density measurement errors relative to the reference were computed, analysed and used to define optimal operating conditions (operating frequency range f_{opt}, optimal VDMS constant β_{opt} and data sampling frequency f_s) for the VDMS which will ensure the measurement errors were minimized. Lastly, the VDMS was used to predict the mixture density of seven test mixtures using the defined optimal operating conditions for the VDMS and the results presented in section 5.10.1 shows significant improvement in density measurement accuracy.

Chapter 6

FLOW APPARATUS AND ITS CALIBRATION

6.1 Introduction

Having obtained satisfactory results from the bench testing described in section 5.10, the next stage was to investigate the capability of the constructed VDMS and the associated mathematical model and signal processing techniques, to accurately predict the density of a mixture when used in dynamic flows. A multiphase flow loop with reference measurement instruments sited at the University of Huddersfield was used for this purpose. This chapter will describe the characteristics of the multiphase flow loop, the functions of the reference flow measurement instrumentation used with it and the calibration procedures for these reference instruments. It will also describe several techniques developed to provide reference measurements for the mean solids volume fraction, mean gas volume fraction and gas volumetric flow rate. These reference measurement techniques were adapted from some of the existing works by Lucas et al [166]. Experiments undertaken to determine the Fanning pipe frictional factor will also be described.

6.2 The multiphase flow loop facility at the University of Huddersfield

An existing multiphase flow loop facility at the University of Huddersfield [14] was used to establish a number of flow conditions that were used in the current investigation. This facility is capable of producing different types of vertical or inclined upward flows, namely; single phase 'water only' flows; solids-in-water flows, with water as the continuous phase and spherical solid balls as the dispersed phase; and air-in-water flows, with water as the continuous phase and air as the dispersed phase. The auxiliary measurement instruments used on the flow loop provide the following reference measurements; (i) water volumetric flow rate $Q_{w,ref}$ (ii) solids volumetric flow rate $Q_{s,ref}$ (iii) air volumetric flow rate $Q_{a,ref}$ (iv) solids volume fraction $\alpha_{s,ref}$ (v) air volume fraction $\alpha_{a,ref}$ and (vi) differential pressure ΔP across a one metre pipe length in the working section of the flow loop. The

flow loop working section refers to that part of the flow loop where the flow property measurements are taken, and it has an internal diameter of 80mm and a vertical length of approximately 3m. As mentioned in the introductory part of this section, the flow loop can be oriented to provide upward flows which are either vertical or inclined at an angle θ from the vertical. For the current investigation, the flow loop was always oriented to give upward vertical flows only. This was because of the challenges and risk involved in inclining the working section of the flow loop with the VDMS installed. A picture and schematic diagram of the multiphase flow loop facility that was used are shown in figure 6-1and

figure 6-2.

Figure 6-1: Picture of the Multiphase flow loop facility used in this research

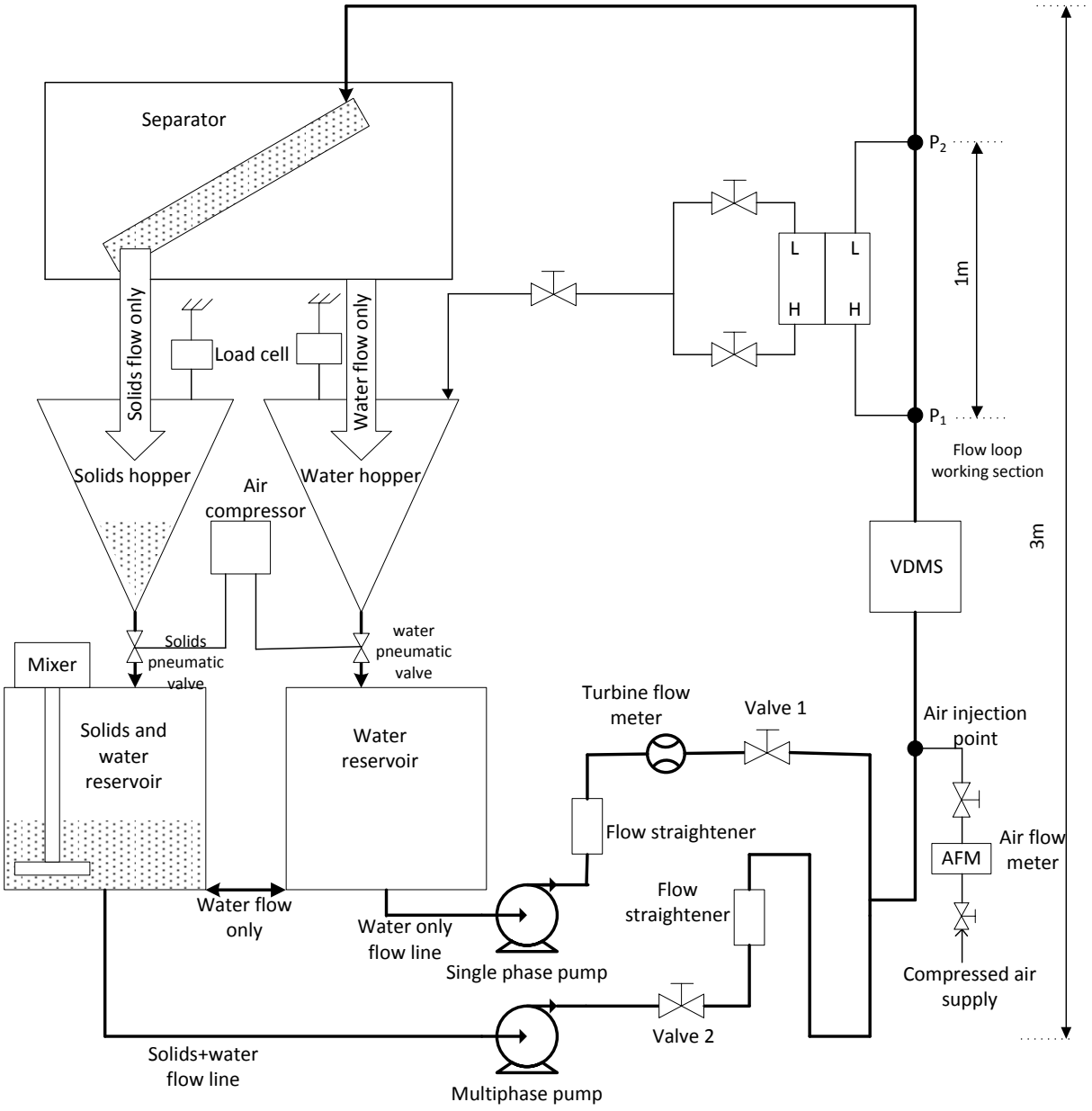

Figure 6-2: Schematic diagram of the Multiphase flow loop used in this research

Figure 6-2 is a schematic of the flow loop facility used in this research showing the reference flow measurement instruments, reservoirs, pumps, control valves ,the separator unit and the installed VDMS. Also, figure 6-1 shows the picture of the flow loop facility with the VDMS and associated supports installed in the flow loop working section. In order to simplify the schematic diagram

presented, the power supply and control units for the water pump and solids pump have not been included. The operation of the flow loop will now be explained in the following paragraphs.

In order to generate 'water only' flows, a 240V ac single phase, in-line centrifugal pump which is connected to the water reservoir is used. As a precaution to ensure the pressure head is sufficient to convey water from the water reservoir through the flow loop, valve 2 (see figure 6-2) is kept closed. Also, valve 1 is kept open before turning on the water pump. Once the water pump is turned on, it pumps water through the working section of the flow loop and back to the water reservoir, via the separator and hopper system. The flow rate of water through the working section can be varied manually by adjusting valve 1 (see figure 6-2). Also, an in-line turbine meter is used to measure the flow rate of water through the working section. For 'water only' flows, the flow loop can generate water flow rates up to 17.5m^3/hr.

The flow loop can also be used to generate solids-in-water flows, where water forms the continuous phase and spherical plastic balls forms the dispersed solids phase. The spherical plastic balls have a diameter of 4mm and a density of 1340kg/m^3. A multiphase pump is used either as a standalone pump, or in conjunction with the water pump, to pump the solids-water mixtures. To achieve high solids volume fractions, the multiphase pump is used as a standalone pump to convey solids-water mixtures from the solids-water reservoir. A 1kW stirrer mounted in the solids-water reservoir is used to ensure a homogenous solids-water mixture is maintained, which is then pumped to the working section of the flow loop. The total flow rate of the mixture in the working section of the flow loop can be varied by using a variable frequency drive (VFD) control unit to control the speed of the multiphase pump. In order to generate solids-in-water flows with low solids volume fraction, the multiphase pump is used in conjunction with the single phase water pump to pump a solids-water mixture from one reservoir and water only from the other reservoir. Both reservoirs are interconnected to allow water to flow between the reservoirs, but grilles (see figure 6-2) are used to prevent solids from flowing into the water reservoir. When both pumps are used to generate solids-in-water flows, the total flow rate and the

volume fraction of the solids in the working section can be varied by adjusting the speed of the multiphase pump using the VFD control unit and by manually adjusting “valve 1”. The solids-in-water mixture is circulated through the working section, then into the separator where it is separated into its respective phases, which are then returned to their respective reservoirs via the conical stainless steel hopper system. The separator consists of a tank containing a rectangular cross-section chute of stainless steel mesh, with baffles positioned at intervals along the chute to reduce the mixture flow velocity and consequently improve the efficiency of the separation.

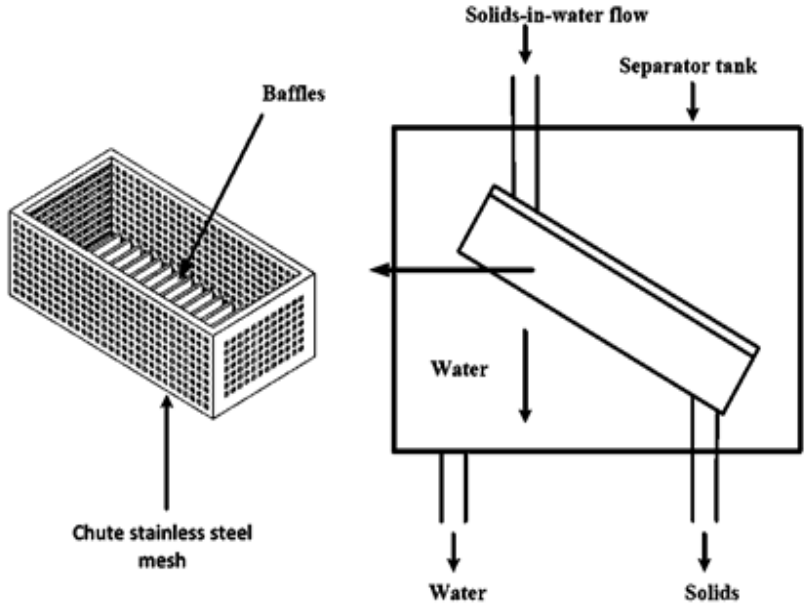

Figure 6-3: Diagram of the stainless steel mesh separator [1]

Pneumatically actuated ball valves are installed in-line at the base of the hoppers. Each hopper is suspended on a load cell and when the ball valves are closed, the system can be used to perform independent batch measurements of the rate of increase of mass of both the solids and water phases as shown in figure 6-4.

A Yokogawa EJA 110A differential pressure (DP) sensor installed across a one metre length of the flow loop working section is used to provide a differential pressure measurement across this length of working section. An air purging system connected to the DP sensor ensures that no air is trapped in the DP sensor measurement lines. This helps to eliminate errors in the measured differential pressure.

The flow loop can also be used to generate bubbly air-in-water flows, where water forms the continuous phase and air forms the dispersed phase. In order to generate air-in-water flows, the single phase water pump is used to pump water through the flow loop while air is introduced into the base of the working section of the flow loop using a compressed air supply (see figure 6-2). The air supply line has a manually controlled ball valve which is used to regulate the flow of air. A thermal mass flow meter is also connected in-line in the air supply line and is used to measure the mass flow rate of air into the working section of the flow loop. The total flow rate of the air-water mixture can also be varied by either adjusting "valve 1" to change the water flow rate or by adjusting the air valve or air pressure regulator to change the air flow rate.

6.3 Reference measurement devices

The reference measurement instruments used on the flow loop provided the relevant reference measurements for the experiments and included (i) a gravimetric measurement system, (ii) a differential pressure DP sensor, (iii) a thermal mass flow meter, and (iv) a turbine flow meter. Their operation and calibration will be discussed in the following sections.

6.4 The gravimetric flow measurement system

The gravimetric flow measurement system was used in this research to provide reference measurements for the solids volumetric flow rate $Q_{s,ref}$ and the water volumetric flow rate $Q_{w,ref}$ in solids-in-water flows. It comprises of two stainless steel hoppers suspended on load cells, two pneumatically actuated valves installed at the bases of the hoppers, a signal processing unit and a data acquisition unit connected to a flow measurement computer. The load cell signal processing circuitry and the control circuit for the pneumatic control valves are interfaced to the flow measurement computer. A QuickBasic 4.5 program, running on the flow measurement computer, was specifically written to control the operation of the pneumatic control valves and to obtain mass measurement readings of the contents of the hoppers from the respective load cells when the pneumatic valves were closed.

Figure 6-4:Picture of the gravimetric flow measurement system

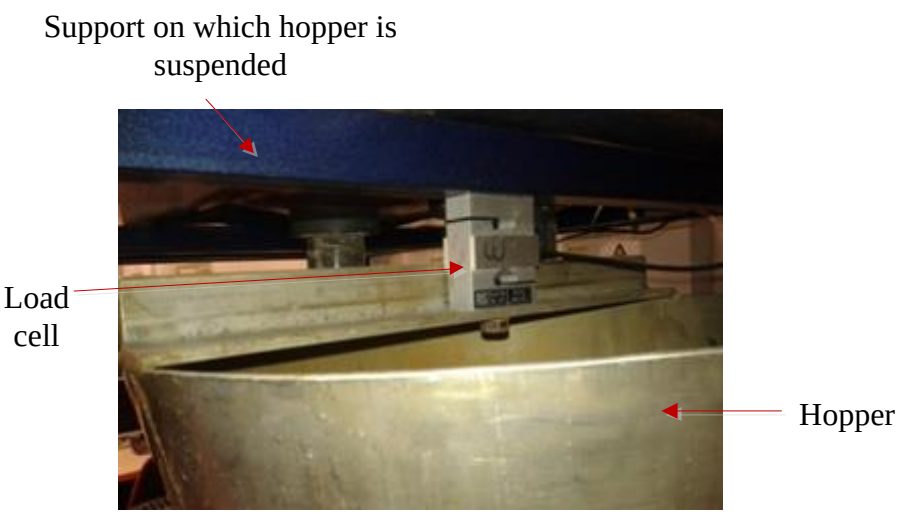

Figure 6-5: Picture of the one of the hoppers suspended from a load cell

Figure 6-4 shows a picture of the gravimetric measurement system, whilst figure 6-5 shows a picture of one of the hoppers suspended from a load cell. When a solids-water mixture was pumped through the working section of the flow loop, the separator was used to separate the mixture into its solids and liquid phases which then entered into their respective hoppers (see figure 6-2). The QuickBasic program was used to automatically determine the reference solids volumetric flow rate $Q_{s,ref}$ and water volumetric flow rate $Q_{w,ref}$ as described below. In order to obtain the reference measurements $Q_{s,ref}$ and $Q_{w,ref}$, the QuickBasic program was used to close the pneumatic control valves and the time interval Δt taken to fill a given hopper with a predetermined

mass M_i was recorded. Using these measurements, the mass flow rate $\dot{M}_i$ of the relevant phase was calculated as follows,

$$\dot{M}_i = \frac{M_i}{\Delta t} \qquad \text{Equation 6-1}$$

The reference volumetric flow rate $Q_{i,ref}$ of the ith phase in the mixture was then obtained from the measured mass flow rate $\dot{M}_i$ given by equation 6-1 and the relevant phase density ρ_i as follows,

$$Q_{i,ref} = \frac{\dot{M}_i}{\rho_i} \qquad \text{Equation 6-2}$$

where the subscript i can be either "s" or "w" representing solids and water phase respectively, $Q_{i,ref}$ is the reference volumetric flow rate of the ith phase, $\dot{M}_i$ is the measured mass flow rate of the ith phase and ρ_i is the density of the ith phase.

6.4.1 Calibration of gravimetric flow measurement system

Before using the gravimetric flow measurement system to obtain reference water and solids volumetric flow rate measurements, it was important that the system was calibrated. As a precautionary measure, to ensure accurate measurements were obtained, the flow loop was always left to attain a steady flow condition before obtaining measurements. From equation 6-1 and equation 6-2, it is clearly seen that once the density of each measured phase is known, the volumetric flow rate of the phases can be obtained from their mass flow rate measurements. Hence, it was important to calibrate the load cells and signal conditioning circuits connected to the hoppers to ensure they gave accurate mass flow rate measurements. The calibration of the load cells ensured that an accurate relationship was established between the measured voltage from each load cell signal conditioning circuit and the mass in the respective hopper.

The load cells were calibrated using a QuickBasic program to close the pneumatic valves and a graduated measuring cup was then used to add known masses of water into both the solid and water hoppers independently. For each hopper system, the mass of water added was increased in

steps of 2kg over the full range of the load cell span, which was 0kg to 40kg, and the output voltages from the load cell signal conditioning circuits were then recorded. This process was repeated three times to ensure repeatability and accuracy of the measurements obtained. The average of the measured output voltages from the load cell signal conditioning circuits and corresponding masses were taken and are presented in figure 6-6 which shows a plot of the mass of water added to each hopper against the output voltages from the respective load cell signal conditioning circuits. In figure 6-6, the plot with green circular markers represent the calibration data obtained for the solids hopper system, while the plot with blue square markers represent the calibration data obtained for the water hopper system.

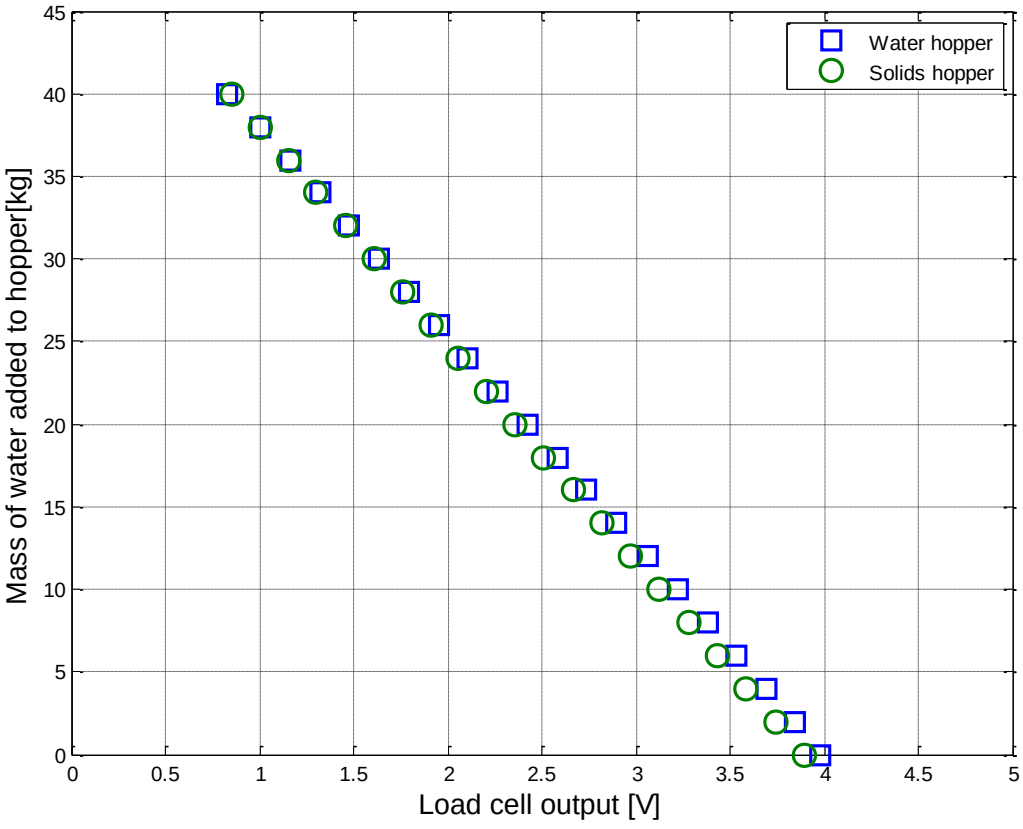

Figure 6-6: Calibration plots for solids and water hopper systems

The results in figure 6-6 shows excellent linear relationships between the mass of water added to the hoppers and the relevant output voltages from the load cell circuits. Linear regression was

then used to obtain a first order equation relating the mass of water added to each hopper to the corresponding output voltage from the load cell of that hopper. These relationships were obtained as follows

$$M_s = -12.7V_s + 50.7 \quad \text{Equation 6-3}$$

$$M_w = -13.1V_w + 51.1 \quad \text{Equation 6-4}$$

where M_s is the mass of water added to solids hopper, V_s is the output voltage from the load cell signal conditioning circuit connected to the solids hopper, M_w is the mass of water added to water hopper and V_w is the output voltage from the load cell signal conditioning circuit connected to the water hopper. These equations were then integrated into the QuickBasic program for computing $Q_{s,ref}$ and $Q_{w,ref}$. It is important to state here that the gravimetric measurement system was set up in such a way that the measured masses M_w and M_s of material inside the solids and water hopper were not affected by the masses of the empty hoppers or the masses of the pneumatic valves.

6.4.2 Operation of the gravimetric flow measurement system

This section describes the process of operating the gravimetric flow measurement system. Once the QuickBasic program to calculate $Q_{s,ref}$ and $Q_{w,ref}$ is started, a program prompt requests the user to enter the lower mass limit and upper mass limit for both the water hopper and the solids hopper. For each measurement cycle, the pneumatic control valves are closed and the time taken for the mass in each hopper to increase from the lower mass limit to the upper mass limits is recorded. The upper mass limit represents the total mass that is collected in a given hopper before the pneumatic control valve reopens. The total mass of water M_w and solids M_s collected in the respective hoppers within a given time are computed using the expressions,

$$M_w = M_{w_{(U)}} - M_{w_{(L)}} \quad \text{Equation 6-5}$$

$$M_s = M_{s_{(U)}} - M_{s_{(L)}} \quad \text{Equation 6-6}$$

where $M_{w_{(U)}}$ is the upper mass limit of water in the water hopper and $M_{w_{(L)}}$ is the lower mass limit of water in water hopper. $M_{s_{(U)}}$ is the upper mass limit of solids in the solids hopper and $M_{s_{(L)}}$ is the lower mass limit of solids in the solids hopper. The mass flow rate of the water phase $\dot{M}_w$ and of the solids phase $\dot{M}_s$ can then be computed using equation 6-7 and equation 6-8. These are given as follows,

$$\dot{M}_w = \frac{M_{w_{(U)}} - M_{w_{(L)}}}{\Delta t_w} \qquad \text{Equation 6-7}$$

$$\dot{M}_s = \frac{M_{s_{(U)}} - M_{s_{(L)}}}{\Delta t_s} \qquad \text{Equation 6-8}$$

where Δt_w and Δt_s are the time intervals taken to acquire the predetermined masses M_w and M_s of water and solids respectively. Furthermore, the reference water volumetric flow rate $Q_{w,ref}$ and solids volumetric flow rate $Q_{s,ref}$ can then be computed using the expressions,

$$Q_{w,ref} = \frac{\dot{M}_w}{\rho_w} \qquad \text{Equation 6-9}$$

$$Q_{s,ref} = \frac{\dot{M}_s}{\rho_s} \qquad \text{Equation 6-10}$$

where ρ_w and ρ_s are the densities of the water phase and the solids phase respectively. Previous work by Cory [14] has shown that the separator design is not perfectly efficient in separating the solids-water mixtures. During separation wet solids particles entering the solids hopper introduce a small quantity of water into the solids hopper. This causes the load cell connected to the solids hopper to slightly overestimate the mass of solids contained in the hopper. If not compensated for, this introduces a measurement error to the reference solids volumetric flow rate $Q_{s,ref}$. Since the volume of water in the water hopper is significantly greater than the volume of water entering the solids hopper the resultant error in the measured mass of water has negligible effect on the estimated water volumetric flow rate $Q_{w,ref}$. However, by accounting for the water entering the

solids hopper, a more accurate estimate of $Q_{s,ref}$ can be obtained. Cory [14] and Muhamedsalih [1] have independently obtained an empirical correction factor q_x to compensate for errors in the reference solids volumetric flow rate measurements $Q_{s,ref}$. q_x was measured to be 0.962 and so the corrected solids volumetric flow rate $Q_{s,c,ref}$ is given by,

$$Q_{s,c,ref} = q_x \, Q_{s,ref} \qquad \text{Equation 6-11}$$

6.5 Differential Pressure sensor

A Yokogawa EJA 110A differential pressure DP sensor was installed across a one meter axial length of the flow loop working section to obtain a differential pressure measurement. This differential pressure measurement could be used, dependent upon the specific application, to compute either (i) the reference solids volume fraction $\alpha_{s,ref}$ or (ii) reference air volume fraction $\alpha_{a,ref}$ or (iii) the friction factor f_F associated with the flow through the working section. A schematic representation of the differential pressure sensor installed in the flow loop is shown in figure 6-7.

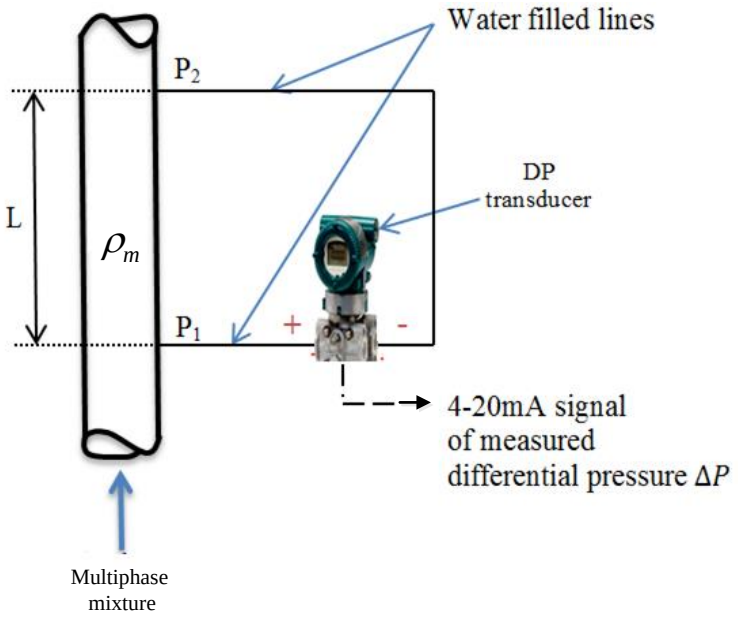

Figure 6-7: Schematic of DP sensor connection on flow loop

Figure 6-8: Picture of Yokogawa DP sensor installed in flow loop.

In the diagram shown in figure 6-7, P_1 and P_2 represents the static pressure at the upstream and downstream pressure tappings respectively, and L is the vertical distance between the pressure tappings. The distance L was carefully measured as one metre. The DP sensor has high side and low side pressure lines which are connected to the working section and which were completely filled with water during the experiments. The pressure lines were also connected to a purging system (see figure 6-2) to remove any air trapped in the lines which could cause the DP sensor to give inaccurate differential pressure measurements. As a precautionary measure, to ensure air wasn't trapped in the pressure lines before taking differential pressure measurements from the DP sensor, the pressure lines were always flushed with water from the purging system at the start of each experiment. The Yokogawa EJA 110A differential pressure sensor used in this research has a measurement range of 0-40 inches water gauge. The 4-20mA output signal from the DP sensor transmitter was converted to an equivalent 1-5Vdc signal using a current to voltage converter circuit. The current to voltage converter circuit schematic diagram is shown in figure 6-9.

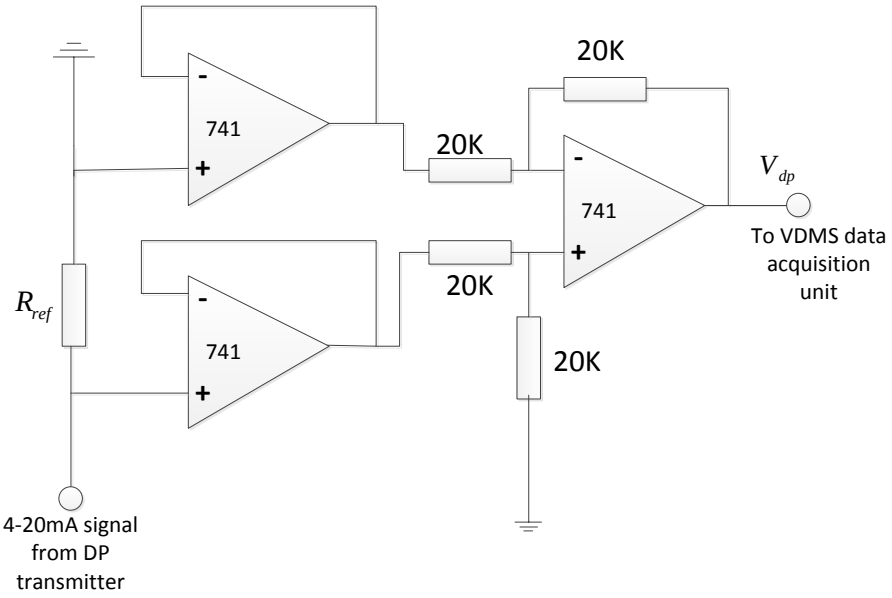

Figure 6-9: Schematic of DP transmitter current to voltage converter circuit

From the schematic shown in figure 6-9, the 4-20mA signal from the DP transducer is connected to a 250Ω, $\pm 0.1\%$ high precision resistor, which is connected across two buffer amplifiers. The outputs from the buffer amplifiers are connected to the VDMS data acquisition unit via a unity gain differential amplifier circuit.

By considering the water filled pressure lines of the DP sensor connection shown in figure 6-7, the differential pressure ΔP measured by the DP sensor for all types of flow is given by,

$$\Delta P = P_1 - (P_2 + \rho_w g L) \qquad \text{Equation 6-12}$$

where P_1 and P_2 are the static pressures at the upstream and downstream pressure tappings and are connected to the "+" and "-" pressure ports of the DP sensor respectively (see figure 6-7), ρ_w is the water density, g is acceleration due to gravity, 9.81ms^{-2} and L is the axial length between the upstream and downstream pressure tappings. If a steady multiphase mixture flows through the working section, the pressure difference P_1 - P_2 between the upstream and downstream tappings is given by,

$$P_1 - P_2 = (\rho_{mix} g L + F_m) \qquad \text{Equation 6-13}$$

where ρ_{mix} is the mean density of the multiphase mixture and F_m is the pressure loss due to fluid friction between the pressure tappings. Equation 6-12 and equation 6-13 can be combined to obtain a simplified expression for the differential pressure ΔP measured by the DP cell. This is given by,

$$\Delta P = gL(\rho_{mix} - \rho_w) + F_m \qquad \text{Equation 6-14}$$

If the flow through the working section is assumed to be solids-in-water flow, then the relationship between the mixture density ρ_{mix} and the solids volume fraction α_s is given by [9],

$$\rho_{mix} = \alpha_s \rho_s + (1 - \alpha_s)\rho_w \qquad \text{Equation 6-15}$$

where ρ_s is the solids density. Provided that $\rho_s > \rho_w$, an expression to compute the reference solids volume fraction $\alpha_{s,ref}$ of the solids-water mixture can be obtained by combining equation 6-14 and equation 6-15 as follows,

$$\alpha_{s,ref} = \frac{\Delta P - F_m}{gL(\rho_{s,ref} - \rho_{w,ref})} \qquad \text{Equation 6-16}$$

From equation 6-16, it becomes immediately obvious that, if the densities of the solid and liquid phases are known, then the solids volume fraction in a two phase solids-in-water flows can be computed from the differential pressure ΔP measured by the DP cell and from calculating the frictional pressure loss F_m along the pipe length L. This equation was used to provide reference solids volume fraction $\alpha_{s,ref}$ measurements in the current investigation. Additionally, an expression to determine the reference mixture density $\rho_{sw,ref}$ in solids-in-water flows can be obtained by combining equation 6-15 and equation 6-16 as follows,

$$\rho_{sw,ref} = \rho_{w,ref} + \frac{\Delta P - F_m}{gL} \qquad \text{Equation 6-17}$$

Equation 6-17 was used to provide reference measurements of the mixture density $\rho_{sw,ref}$ in solids-in water flows.

Assuming the flow through the working section is air-in-water flow, then the connections of the DP sensor pressure lines in the working section (see figure 6-7) will be reversed, in order to correctly estimate the frictional pressure loss F_m (i.e. the low "-" pressure port is connected to the upstream tapping and the high "+" pressure port is connected to the downstream pressure tapping in the flow loop working section). The differential pressure measured by the DP sensor is now given by,

$$\Delta P = P_2 + \rho_w g L - P_1 \qquad \text{Equation 6-18}$$

When a steady air-in-water mixture flows through the working section, the pressure difference P_1-P_2 between the upstream and downstream tappings is as defined in equation 6-13. Also, for air-in-water flows, the relationship between the mixture density ρ_{mix} and the air volume fraction α_a is approximated by [9],

$$\rho_{mix} = \alpha_a \rho_a + (1 - \alpha_g)\rho_w \qquad \text{Equation 6-19}$$

Since $\rho_w \gg \rho_a$, equation 6-19 can be simplified by ignoring ρ_a because it is negligible. Thus, the relationship between the mixture density and air volume fraction is given by,

$$\rho_{mix} = (1 - \alpha_a)\rho_w \qquad \text{Equation 6-20}$$

By combining equation 6-13, equation 6-18 and equation 6-20, an expression to compute the reference air volume fraction $\alpha_{a,ref}$ in air-in-water flows is obtained as follows,

$$\alpha_{a,ref} = \frac{\Delta P + F_m}{\rho_{w,ref} g L} \qquad \text{Equation 6-21}$$

Furthermore, a reference mixture density $\rho_{aw,ref}$ measurement in air-in-water flows can be obtained by combining equation 6-20 and equation 6-16. This is given by,

$$\rho_{aw,ref} = \rho_{w,ref} - \frac{\Delta P + F_m}{g L} \qquad \text{Equation 6-22}$$

Equation 6-21 and equation 6-22 were used to provide reference measurements of the air volume fraction $\alpha_{a,ref}$ and the air-in-water mixture density $\rho_{aw,ref}$ respectively in the current work.

6.5.1 Calibration of the Differential Pressure sensor

In section 6.5, it was shown that the differential pressure ΔP measured across an axial length L of the working section is required to compute reference volume fractions and mixture densities in multiphase flows. Hence, it was important to calibrate the DP sensor and its current to voltage converter circuit before use. A bespoke calibration test rig was constructed for this purpose. The calibration rig includes a carefully graduated flow pipe with two pressure tappings one metre apart. From the original calibration certificate provided for the Yokogawa EJA 110A DP transducer, the pressure measurement range was from 0-40 inches of H_2O (equivalent to 0-100cm of H_2O). The pressure lines of the DP transducer were then connected to the pressure tappings on the graduated flow pipe and were filled with water. In order to calibrate the DP sensor and its current to voltage converter circuit, water was added to the flow pipe in increments of 10cm. At each water level, the output voltage from the current to voltage converter circuit was recorded. A calibration plot for the differential pressure ΔP across the DP sensor versus the output voltage from the current to voltage converter circuit was then produced as shown in figure 6-10.

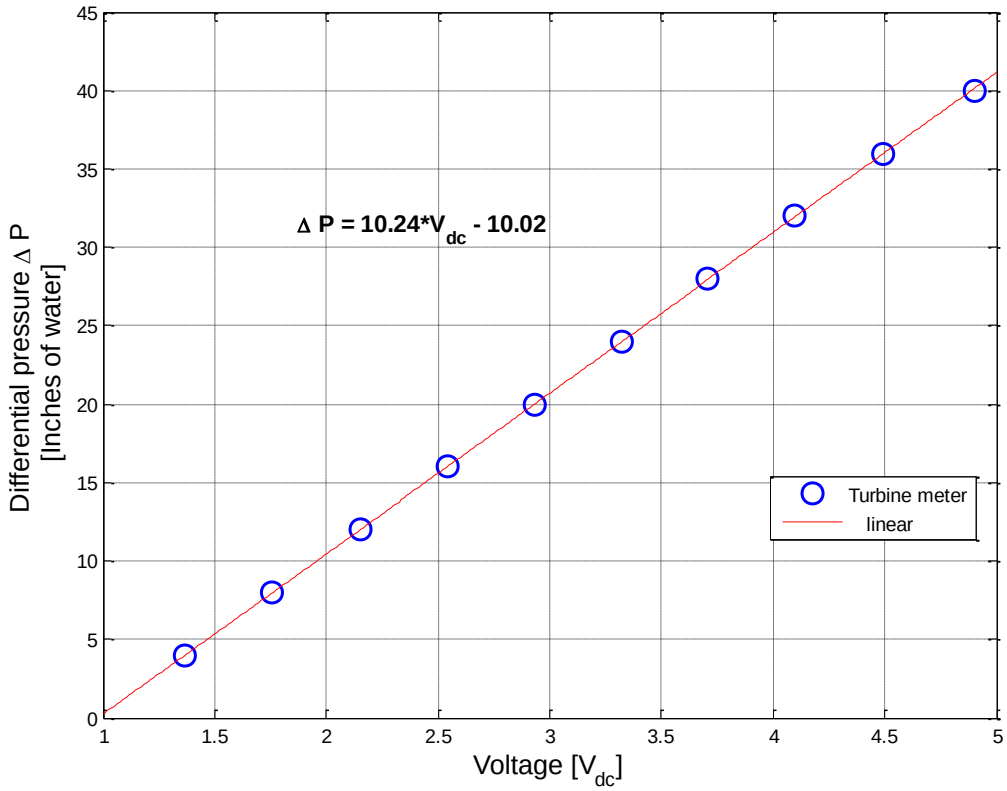

Figure 6-10: DP transducer calibration plot

The vertical axis of the plot in figure 6-10 represents the differential pressure ΔP across the DP cell in inches of water and the horizontal axis represents the output voltage from the DP transducer's current to voltage converter circuit. The calibration plot shows a linear relationship between ΔP and the output voltage. Linear regression was used to obtain the best fit for the calibration plot. Using this calibration equation ΔP can then be obtained in Pascal as follows,

$$\Delta P = 249.174\{10.24V_{dp} - 10.023\} \qquad \text{Equation 6-23}$$

where ΔP is the differential pressure in Pa and V_{dp} is the measured output voltage from the current to voltage converter circuit. Equation 6-23 was used to compute the measured differential pressure ΔP from the DP transducer in the current work.

6.6 Turbine flow meter

An "Able" [167] turbine meter was installed in-line between the single phase water pump and the manually controlled ball valve ("valve 1" in

figure 6-2) and was used to provide the reference water volumetric flow rate $Q_{w,ref}$ in single phase "water only" and air-in-water flow experiments. The reference water volumetric flow rate $Q_{w,ref}$ measurement was obtained from the output frequency of the turbine flow meter rotor with the aid of a frequency counter. $Q_{w,ref}$ is given by,

$$Q_{w,ref} = K_t f_t \qquad \text{Equation 6-24}$$

where K_t is the meter constant for the turbine flow meter and f_t is the turbine meter output frequency.

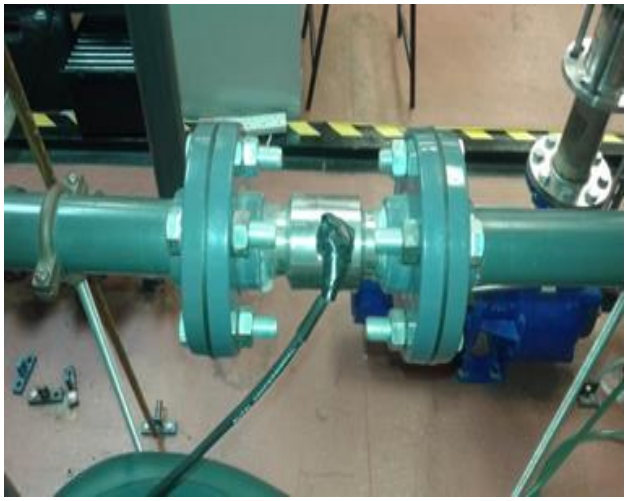

Figure 6-11: Picture of the "Able" turbine flow meter installed in-line in the flow loop

6.6.1 Calibration of turbine flow meter

Given that turbine flow meters are generally susceptible to wear with usage, which increases measurement inaccuracies, it was expedient that the turbine flow meter installed in the flow loop was recalibrated before it was used and the calibration results compared against the manufacturer's factory calibration results. The turbine flow meter was calibrated by comparing the water volumetric flow rate measurements obtained from the turbine meter against the water volumetric

flow rate measurement obtained from the gravimetric flow measurement system, in the "water only" flow condition.

In order to calibrate the turbine flow meter, the volumetric flow rate of water in the working section of the flow loop was varied over its range, using the manual flow valve (see valve 1 in figure 6-2) For each water flow rate selected, the frequency of the turbine meter rotor was measured using a frequency counter. In addition, the gravimetric measurement system was used to simultaneously measure the volumetric flow rate of water in the working section of the flow loop. The measurements obtained were then used to generate a plot of the water volumetric flow rate $Q_{w,ref}$ obtained from the gravimetric flow measurement system versus the measured frequency f_t of the turbine meter rotor. This plot is shown in figure 6-12.

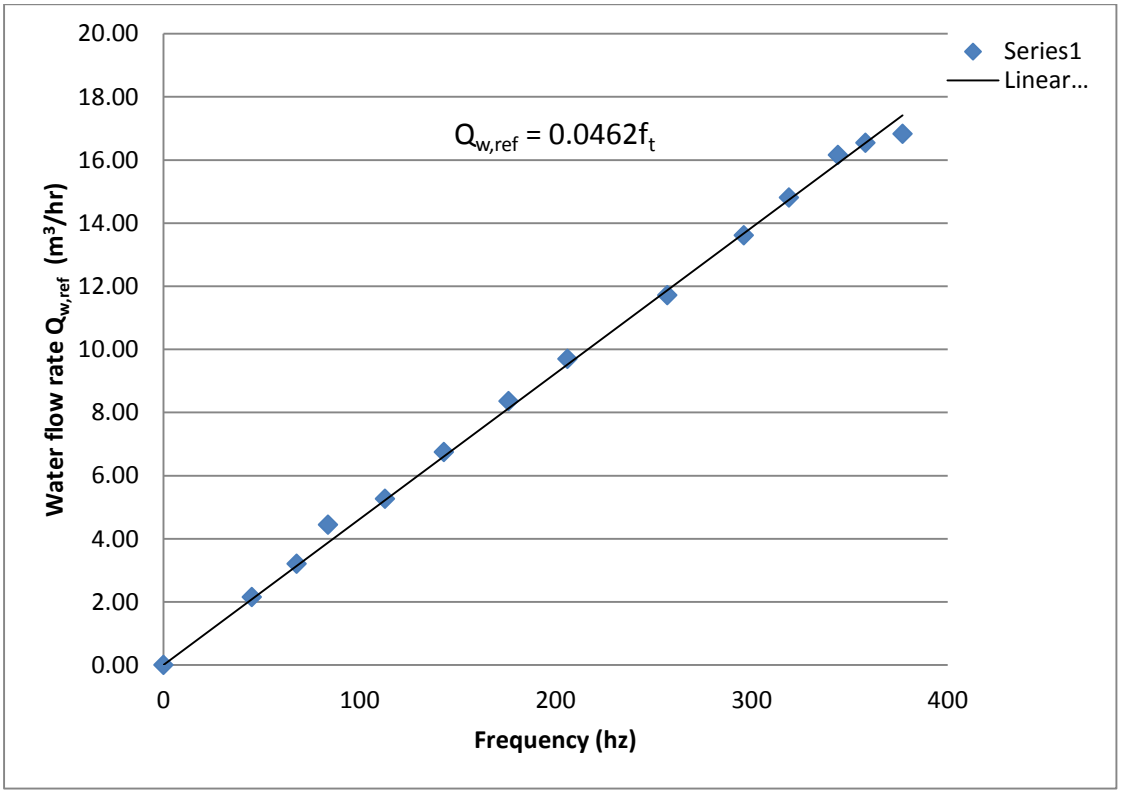

Figure 6-12: Turbine flow meter calibration plot

In figure 6-12, the vertical axis represents the measured water flow rate $Q_{w,ref}$ in m^3hr^{-1}, and was obtained using the gravimetric system described in section 6.4, while the horizontal axis represents the measured output frequency of the turbine flow meter rotor in Hz. The results presented in figure

6-12 shows a good linear relationship between the measured volumetric flow rate and measured output frequency. The meter factor k_t of the turbine meter can be obtained from the slope of the plot in figure 6-12 using linear regression and it was found to be $0.0462\mathrm{m}^3\mathrm{h}^{-1}\mathrm{Hz}^{-1}$ over the flow range from $2\mathrm{m}^3\mathrm{hr}^{-1}$ to $17.5\mathrm{m}^3\mathrm{hr}^{-1}$. Therefore, the equation used in the present study to determine volumetric flow rate using the turbine flow meter is given by,

$$Q_{w,ref} = 0.0462 f_t \qquad \text{Equation 6-25}$$

The meter factor k_t obtained in the calibration experiment described above agrees perfectly with that provided by the manufacturer in the factory calibration certificate. This result shows that the meter factor was unchanged from its factory calibration value.

6.7 Air flow measurement

An air flow meter was required to measure the volumetric flow rate at which air flowed in the working section of the flow loop in the air-in-water flow experiments. A thermal mass flow meter had originally been installed in the air supply line for this purpose, but had developed a fault and could not be repaired. An alternative method was therefore developed to measure the volumetric air flow rate by using the measured differential pressure in the working section of the flow loop.

6.7.1 Volumetric Air flow rate computation method

In air-in-water two phase flows where water forms the continuous phase and air the dispersed phase, the homogeneous mixture velocity u_h (also known as the mixture superficial velocity) is given by,

$$u_h = \frac{Q_w + Q_a}{A} \qquad \text{Equation 6-26}$$

where Q_w is the volumetric flow rate of water, Q_a is the volumetric flow rate of air and A is the cross sectional area of the flow loop working section. If the air flow rate is initially assumed to be zero, (i.e. the flow comprises of water only), then equation 6-26 can be used to compute an approximate value for u_h. Furthermore, an initial estimate of the frictional pressure loss F_m in the

flow can be obtained as described in section 6.8. In equation 6-21, it has been shown that the air volume fraction of the air-in-water mixture can be obtained using the measured frictional pressure loss F_m in the flow and the differential pressure ΔP measured across a one metre axial length L of the flow pipe as follows,

$$\alpha_a = \frac{\Delta P + F_m}{\rho_w g L} \qquad \text{Equation 6-27}$$

where ρ_w is the water density, and g is acceleration due to gravity (9.81m^2/s). Next, the velocity u_w of water can be determined once an initial estimate of the air volume fraction α_a is known. u_w is obtained as follows,

$$u_w = \frac{Q_w}{(1-\alpha_a)A} \qquad \text{Equation 6-28}$$

where Q_w is the water volumetric flow rate obtained using the turbine flow meter. Baz-Rodriguez et al [168] have shown that for air-in-water bubbly flows, such as those used in the present study, where the bubble size has a diameter of 10mm or less, the air slip velocity u_{sp} is approximately 0.25m/s. If the air-in-water flow is assumed to be a bubbly flow, then the slip value obtained by Baz-Rodriguez et al can be applied. Using this slip velocity u_{sp}, an initial estimate of the air velocity u_a can be made as follows,

$$u_a = u_w + u_{sp} \qquad \text{Equation 6-29}$$

Equation 6-29 and equation 6-27 can then be combined to obtain an initial estimate of the air volumetric flow rate Q_a as follows,

$$Q_a = u_a(\alpha_a)A \qquad \text{Equation 6-30}$$

The value of Q_a obtained can then be input into equation 6-26 as a new value for the air volumetric flow rate (since Q_a was initially assumed to be zero) and the sequence for calculating Q_a, given above, is repeated until the air volumetric flow rate value obtained after successive iteration does not change (see figure 6-13). The process for calculating the air volumetric flow rate is shown in

the flow chart in figure 6-13. This technique was used to estimate the air volumetric flow rate $Q_{a,ref}$ in this research.

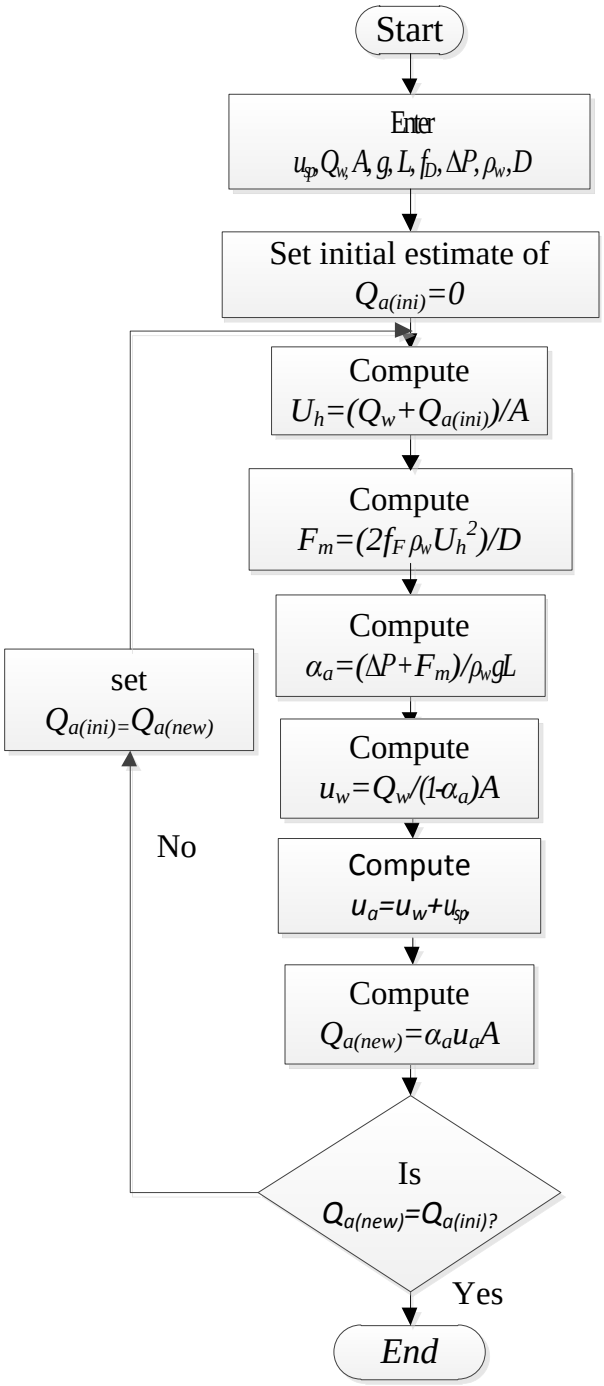

Figure 6-13: Flow chart showing the procedure for computing the reference air volumetric flow rate

6.8 Friction factor calculation for flow loop

To determine the frictional pressure loss F_m in a multiphase pipe flow, the appropriate friction factor is required. Two of the commonly used friction factors are the Darcy and Fanning friction factors which are related by,

$$f_D = 4f_F \qquad \text{Equation 6-31}$$

where f_D is the Darcy friction factor and f_F is the Fanning friction factor [169]. These factors can be used interchangeably by applying equation 6-31. The Fanning friction factor was used in the current study to compute the frictional pressure loss F_m in the vertically upward pipe flows that were investigated. With reference to [169], F_m is given by

$$F_m = \frac{2f_F L\rho_w(u_h)^2}{D} \qquad \text{Equation 6-32}$$

where f_F is the Fanning friction factor which in the present study is obtained from experiments, ρ_w is the water density, D is the flow pipe diameter, L is axial length between the upstream and downstream pressure tappings and u_h is a relevant velocity. In single phase "water only" flows, u_h is the water velocity and in multiphase flows, u_h is the homogeneous mixture velocity (also known as the mixture superficial velocity). In the current investigation, an experiment was conducted to determine the Fanning friction factor f_F for the flow loop working section. The experimental set-up to determine the friction factor was performed using water only flows, the DP transducer described previously in section 6.5 was used to measure the differential pressure over a fixed pipe length and the water flow rate $Q_{w,ref}$ was measured using the turbine meter described previously in section 6.6. The DP sensor connections in this experiment are shown in figure 6-14.

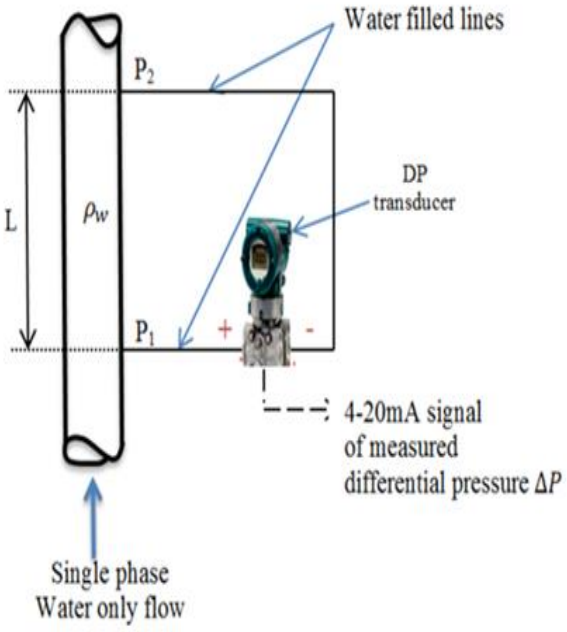

Figure 6-14: DP sensor connections for "water only" flow

From figure 6-14, the differential pressure ΔP measured by the DP sensor is given by,

$$\Delta P = P_2 - P_1 \qquad \text{Equation 6-33}$$

where P_1 and P_2 respectively are the static pressures at the upstream and downstream pressure tapping in the working section. Also, the differential pressure drop $P_1 - P_2$ across a length L in the flow pipe is given by,

$$P_1 - P_2 = F_m \qquad \text{Equation 6-34}$$

By combining equation 6-33 and equation 6-34, the frictional pressure loss in single phase "water only" flow is obtained as,

$$F_m = \Delta P \qquad \text{Equation 6-35}$$

Equation 6-32 and equation 6-35 can then be combined and simplified to obtain an expression to determine the Fanning friction factor as follows.

$$f_F = \frac{D\Delta P}{2L\rho_w(u_w)^2} \qquad \text{Equation 6-36}$$

where u_w is the velocity of the water, and it is given by

$$u_w = \frac{Q_{w,ref}}{A}$$ Equation 6-37

In order to compute the Fanning friction factor f_F over a range of values of u_w, the flow rate of water in the working section was varied using "valve 1" (see

figure 6-2). For different valve positions, starting from when the valve was fully closed to when it was fully opened, the volumetric flow rate of water $Q_{w,ref}$ and the differential pressure ΔP measured across a one meter length of the working section of the flow loop were measured. Equation 6-36 and equation 6-37 were then used to compute f_F. In order to show the relationship between the friction factor and the water velocity, a simplified Moody diagram was generated as shown in figure 6-15. Note that in conventional Moody diagrams, f_F is normally plotted against Reynolds number Re. However, for the purpose of the present study it was more convenient to plot f_F against flow velocity.

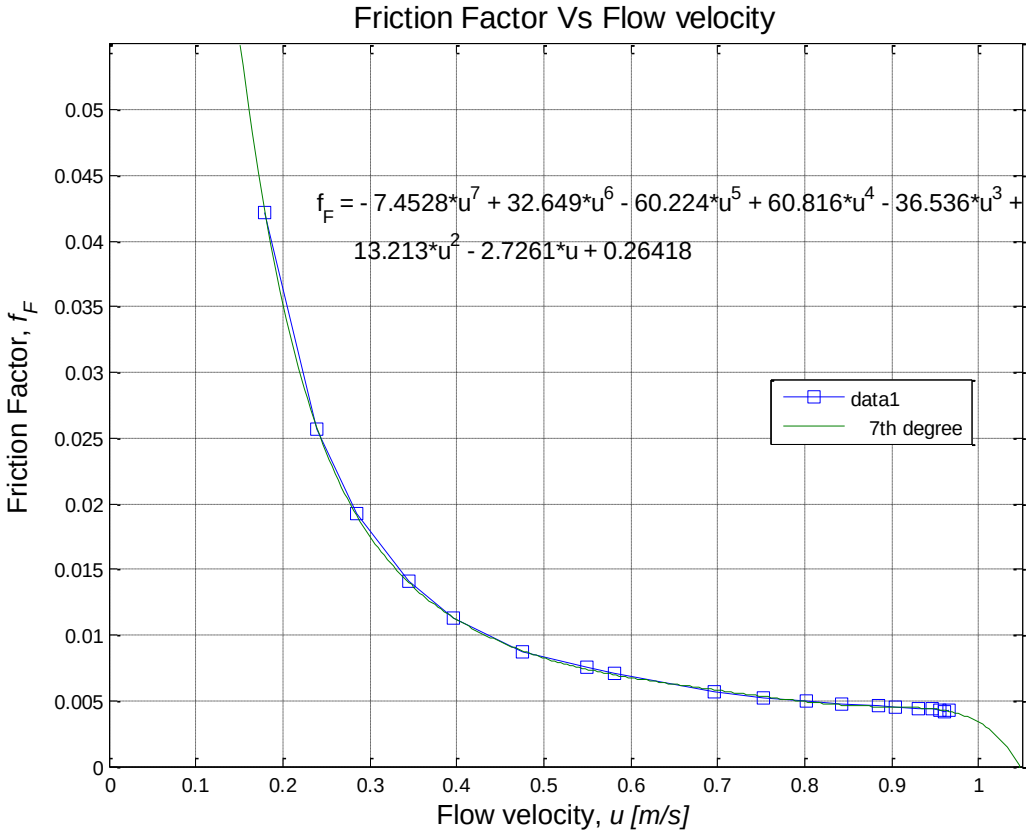

Figure 6-15: Friction factor plot for single phase water only flow

The vertical axis represents the Fanning friction factor computed using equation 6-36. The horizontal axis represents the flow velocity in the working section and it was computed using equation 6-37. Note, with reference to equation 6-32, that when computing the frictional pressure loss F_m for multiphase flows, the horizontal axis in figure 6-15 is taken as referring to the homogeneous mixture velocity u_h given in equation 6-26. From figure 6-15, a seventh order polynomial was fitted onto the plot for friction factor against flow velocity. This is given by,

$$f_F = -7.45u^7 + 32.65u^6 - 60.22u^5 + 60.82u^4 - 36.54u^3 + 13.21u^2 - 2.73u + 0.26 \quad \text{Equation 6-38}$$

where u is the flow velocity. Equation 6-38 was used to compute the Fanning friction factor in the current research. For two phase solids-in-water flows, the frictional pressure loss is obtained from,

$$F_m = \frac{2f_F L \rho_w (u_{h(sw)})^2}{D} \quad \text{Equation 6-39}$$

where f_F is calculated from equation 6-38 using the homogenous mixture velocity $u_{h(sw)}$ given by,

$$u_{h(sw)} = \frac{Q_{w,ref} + Q_{s,ref}}{A} \quad \text{Equation 6-40}$$

and where $Q_{w,ref}$ and $Q_{s,ref}$ are the water and solids volumetric flow rates obtained from the reference instruments (see section 6.4). Similarly, the frictional pressure loss in air-water flow is given by,

$$F_m = \frac{2f_F L \rho_w (u_{h(aw)})^2}{D} \quad \text{Equation 6-41}$$

where f_F is again computed from equation 6-38 using the homogenous mixture velocity $u_{h(aw)}$ given by,

$$u_{h(aw)} = \frac{Q_{w,ref} + Q_{a,ref}}{A} \quad \text{Equation 6-42}$$

where $Q_{w,ref}$ and $Q_{a,ref}$ are water and air volumetric flow rate measurements obtained using the turbine meter (see section 6.6) and the air flow rate computation method (see section 6.7.1).

6.9 Summary

This chapter has provided a description of the flow measurement capability of the flow loop facility located at the University of Huddersfield. The different flow measurement instruments used in the flow loop include (i) a gravimetric flow measurement system which was used to provide reference water and solids volumetric flow rate measurements in solids-water flows, (ii) a turbine flow meter used to provide reference water volumetric flow rate measurement in single phase "water only" and air-in-water flows, and (iii) a differential pressure sensor to provide differential pressure measurements across a fixed length of the working section. The flow measurement instruments were calibrated before being used in this research and the calibration procedures and results have been discussed in detail in section 6.4.1 to 6.7.1. Furthermore, techniques were developed, using the instrumentation in the flow loop, to provide reference measurements of the solids volume fraction $\alpha_{s,ref}$ (see section 6.5), air volume fraction $\alpha_{a,ref}$ (see section 6.5) and air volumetric flow rate $Q_{a,ref}$(see section 6.7.1). These measurements ($\alpha_{s,ref}, \alpha_{a,ref}$ and $Q_{a,ref}$) required knowledge of the appropriate Fanning pipe frictional factor f_F and experiments were undertaken to determine f_F as described in section 6.8.

Chapter 7

DESIGN AND DEVELOPMENT OF A PC BASED CONTROL SYSTEM FOR THE VIBRATING DENSITY MEASUREMENT SYSTEM (VDMS)

7.1 Introduction

In chapter 4 and chapter 5 of this thesis, the design and construction of the VDMS has been described alongside relevant bench tests conducted to determine the system characteristics. The results of the testing were used to define optimal operating conditions for the VDMS. The main conclusions drawn from the VDMS optimization (see section 5.10.1) will be restated here to clarify the purpose of this chapter. In section 5.10.1, it was found that the density measurement errors associated with the VDMS were minimized when it was operated at its optimal frequency range (i.e. frequencies closest to its relevant resonant frequency). When the VDMS was operated in this frequency range, the parameter lambda λ defined in equation 4-28 was found to become approximately zero. Because λ is obtained from $\hat{a}$ and $\hat{b}$ its accuracy is dependent upon errors associated with the measurements of force and displacement (see equation 4-17 and equation 4-18). Therefore, as λ tends to zero, the influence of these measurement errors is minimized. Consequently, it was shown that the errors associated with the predicted density of the test mixtures, given in table 5-3, were minimized. This chapter will focus on describing the design and implementation of a computer based control system for the VDMS that ensures the system can be operated close to its optimal frequency and will therefore ensure that measurement errors associated with the predicted density are minimized. The computer based VDMS control system will also be able to provide online computation of the predicted density and to save measurement data for further analysis where needed. The computer based VDMS control system developed includes the following subsystems (i) a frequency control system to determine the VDMS optimal operating frequency (ii) a VCA excitation unit to generate an appropriate excitation signal that is sent to the VCA, (iii) a data acquisition unit to obtain the force and the displacement measurements

from the VDMS and (iv) a signal processing unit to implement the technique for computing fluid density online (see section 4.5). The computer control system also includes a user control and display interface. The subsystems of the computer based control system for the VDMS will be described in the following sections.

7.2 Development of computer based signal generator for the VCA coil excitation

A computer based signal generator was required to generate an appropriate excitation signal to the VCA coil windings. This subsystem includes a computer running a LabVIEW program to generate the required excitation signal that is sent to the VCA and a power amplifier to provide the current needed to drive the VCA coils. The LabVIEW program uses the "simulate signal" express VI [170] to generate a sinusoidal signal with constant amplitude and zero phase and offset properties (see figure 7-1). The rate at which the generated signal is written to the buffer of the data acquisition unit can also be defined in the property window of this VI (see figure 7-1). The output of the frequency controlled system described in section 7.3 is connected to the frequency property terminal of the "simulate signal" express VI via the "toggle switch" and "average" function blocks. The "toggle switch" function block provided an alternative means to manually define the frequency to the "simulate signal" express VI using an input text box (see Appendix F figure 1).

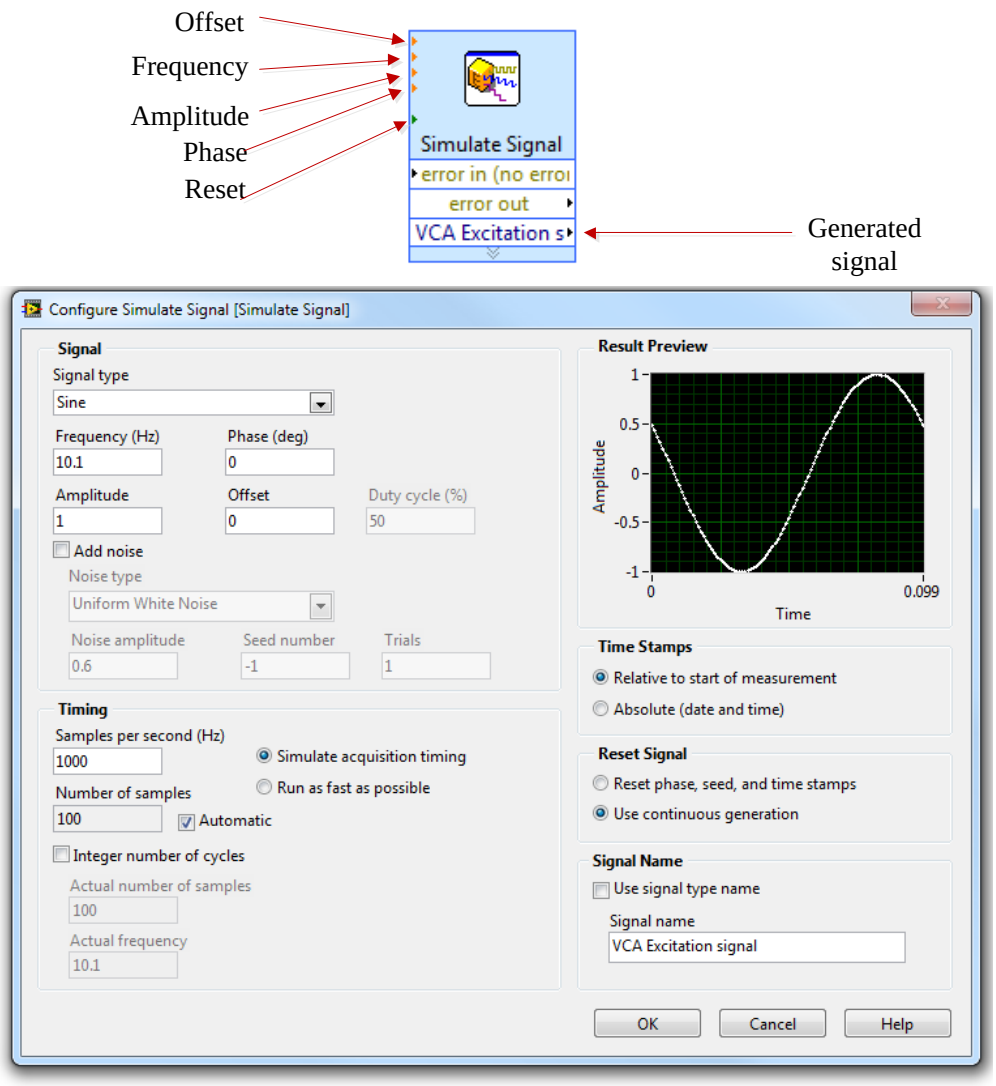

Figure 7-1: Picture of LabVIEW "simulate signal" express VI property window

The output from the "simulate signal" express VI is connected to a LabVIEW "DAQmx analog output" function block. This function block was configured to output a sinusoidal signal that is generated via an analog output channel of the NI-USB6211 DAQ card. The NI-USB6211 was connected to a computer which had LabVIEW and MATLAB software installed on it. Twisted, sheathed copper wire was used to connect the signal generated from the analogue output channel of the NI-USB6211 DAQ card to the terminals of the VCA coil winding (see figure 5-8) via a power amplifier. The block diagram of the computer based signal generator unit for the VCA excitation is shown in figure 7-2.

Figure 7-2: Block diagram of computer based signal generator for VCA excitation

This system represents a major development from the earlier method used for exciting the VCA coil winding which is shown in figure 4-3. The excitation signal to the VCA coil winding was now generated and automatically controlled using a computer running a LabVIEW program rather than a signal generator.

7.3 Development of computer based frequency control system for VDMS excitation

In order to ensure that the VDMS was operated at its optimal frequency when used to predict density in pipe flows, a frequency control system was required for the VCA excitation. The frequency control system was needed to automatically compute the VDMS optimal operating frequency using the measured force and displacement signals obtained from the VDMS for a given flow. There were two options that could be used to implement the frequency control system, namely, a hardware option (i.e. using a microcontroller and the associated hardware) or a software option (i.e. using an appropriate software). The software option was selected because it was relatively easy to implement and offers flexibility in making quick changes to the design. LabVIEW software was chosen for the frequency control system development due to the authors expertise and availability of a software license.

From section 5.10.1, it was shown that to ensure the VDMS is optimally operated, $\hat{a}$ obtained using equation 4-17 should tend to zero because this means that the term lambda λ also tends to zero. Consequently, $\hat{a}$ was used as the control variable in the design of the frequency control system. The block diagram of the frequency control loop is shown in figure 7-3.

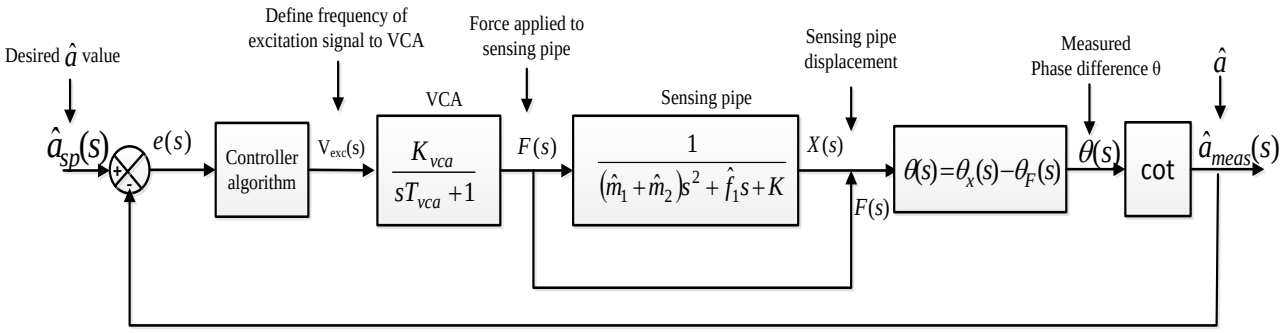

Figure 7-3: Block diagram of VCA excitation frequency control loop

In figure 7-3, the error $e(t)$ in the frequency control system is defined as follows,

$$e(t) = \hat{a}_{sp}(t) - \hat{a}_{meas}(t) \qquad \text{Equation 7-1}$$

where $\hat{a}_{sp}(t)$ and $\hat{a}_{meas}(t)$ are the process set point and controlled variable respectively. $\hat{a}_{meas}$ is obtained using equation 4-47, $\hat{a}_{sp}$ is the desired set point and is set equal to zero. Note that when $\hat{a}_{meas} = 0$, this corresponds to a phase difference between the displacement and force of $-90°$ and it is related to equation 4-17.

The error signal e(t) forms the input to the controller and the controller output $V_{exc}(t)$ is defined by,

$$V_{exc}(t) = \{K_c(t)e(t)\} + K_{bias} \qquad \text{Equation 7-2}$$

where K_{bias} is the controller bias (the output of the controller when the error is zero) and $K_c(t)$ is defined by,

$$K_c(t) = \left\{ K_p + \frac{1}{T_i}\int_0^t dt \right\} \qquad \text{Equation 7-3}$$

where K_p and T_i are the proportional gain and integral time of the controller respectively. The controller output signal, with the appropriate frequency as set by the controller algorithm, is then sent to the VCA. Note that the controller output signal provides the signal to the frequency terminal of the "simulate signal" express VI shown in figure 7-1. Note also that in this frequency control

system, the force and displacement measurements obtained from the VDMS are used to compute $\hat{a}_{meas}$ using equation 4-47. See Appendix F, figure 2 for the LabVIEW program for the frequency control system.

7.3.1 Development of the mathematical model for the open loop VDMS excitation signal frequency control system

This section describes the development of the mathematical model for the open loop frequency control system. The open loop control system comprises of the VCA, the sensing pipe and the force and displacement sensors and the technique for obtaining $\hat{a}$. In order to design an appropriate controller for the closed loop frequency control system, the overall open loop transfer function of the system was required. The transfer function of the VCA was obtained from its equivalent LR electrical circuit shown in figure 5-10. From basic electrical circuit theorem, the relationship between the input voltage $V_{exc}(t)$ and the VCA coil current $I_{exc}(t)$ is given by,

$$V_{exc}(t) = I_{exc}(t)R_{vca} + L_{vca}\frac{dI_{exc}(t)}{dt} \qquad \text{Equation 7-4}$$

where R_{vca} and L_{vca} are the resistance and inductance of the VCA coil winding respectively and $\frac{dI_{exc}(t)}{dt}$ is the rate of change of the coil excitation current with time. When $t = 0$, no current initially flows through the LR electrical circuit (i.e. $I_{exc}(0) = 0$), and the Laplace Transform technique can be used to obtain the transfer function relating the coil excitation current and its input voltage as follows,

$$\frac{\mathrm{I_{exc}}(s)}{\mathrm{V_{exc}}(s)} = \frac{\frac{1}{R_{vca}}}{s\left(\frac{L_{vca}}{R_{vca}}\right) + 1} \qquad \text{Equation 7-5}$$

where s is the Laplace operator and $\mathrm{I_{exc}}(s)$ and $\mathrm{V_{exc}}(s)$ are the Laplace Transforms of the coil excitation current and input voltage respectively. Furthermore, the force generated by the VCA used in this research, is described using Lorentz principle and it has been defined in equation 4-31.

Thus, by substituting equation 4-31 into equation 7-5 a relationship between the input voltage to the VCA coil windings and the force generated is obtained as;

$$\mathrm{G_{vca}}(s) = \frac{\mathrm{F}(s)}{\mathrm{V_{exc}}(s)} = \frac{\frac{k_{vca}}{R_{vca}}}{s\left(\frac{L_{vca}}{R_{vca}}\right) + 1} \qquad \text{Equation 7-6}$$

where $\mathrm{G_{vca}}(s)$ is the transfer function of the VCA, F(s) is the Laplace Transform of the force generated and k_{vca} is the VCA force constant. A time constant T_{vca} and a steady state gain K_{vca} for the VCA can be defined from equation 7-6 as follows,

$$T_{vca} = \frac{L_{vca}}{R_{vca}} \qquad \text{Equation 7-7}$$

$$K_{vca} = \frac{k_{vca}}{R_{vca}} \qquad \text{Equation 7-8}$$

Since the excitation signal to the VCA is a sinusoidal signal with a constant amplitude V_{exc} and a frequency ω that is defined by the controller, the Laplace Transform of the force generated by the VCA is obtained from equation 7-6 as,

$$\mathrm{F}(s) = \left(\frac{\omega V_{exc}}{s^2 + \omega^2}\right)\left(\frac{K_{vca}}{sT_{vca} + 1}\right) \qquad \text{Equation 7-9}$$

Furthermore, the mathematical model describing the characteristics of the sensing pipe and its contents (previously given in equation 4-8) is used to obtain its transfer function $\mathrm{G_{s-pipe}}(s)$ as,

$$\mathrm{G_{s-pipe}}(s) = \frac{\mathrm{X(s)}}{\mathrm{F(s)}} = \frac{1}{\left[\{\hat{m}_1 + \hat{m}_2\}s^2 + s\hat{f}_1 + K_1\right]} \qquad \text{Equation 7-10}$$

where X(s) is the Laplace Transform of the sensing pipe displacement, K_1 is the sensing pipe stiffness constant, $\hat{f}_1$ is the system modified damping constant and $\hat{m}_1$ and $\hat{m}_2$ are the modified masses of the sensing pipe and its contents respectively (see equation 4-5 and equation 4-6). The Laplace Transform of the sensing pipe displacement is obtained from equation 7-9 and equation 7-10 as follows,

$$\mathrm{X}(s) = \left(\frac{\omega V_{exc}}{s^2 + \omega^2}\right)\left(\frac{K_{vca}}{sT_{vca} + 1}\right)\left(\frac{1}{\{\hat{m}_1 + \hat{m}_2\}s^2 + s\hat{f}_1 + K_1}\right)$$ Equation 7-11

The values of $\hat{m}_1$, $\hat{m}_2$, $\hat{f}_1$, K_1, L_{vca} and R_{vca} were obtained from the bench testing described in chapter 5. The Laplace Transforms of the displacement X(s) and force F(s) are then used to obtain their respective phases $\theta_x(s)$ and $\theta_F(s)$ which are required to compute the phase difference $\theta(s)$ between the displacement and the force signals (see equation 4-49) and is given by,

$$\mathrm{G}_\theta(s) = \frac{\theta(s)}{X(s)F(s)} = \theta_x(s) - \theta_F(s)$$ Equation 7-12

$\theta_x(s)$ is the Laplace Transform of the phase of the displacement signal X(s) defined in equation 7-11 and $\theta_F(s)$ is the Laplace Transform of the phase of the force signal F(s) defined in equation 7-9. Lastly, the transfer function $\mathrm{G}_{\hat{a}}(s)$ relating the Laplace Transform of the process control variable $\hat{a}_{meas}(s)$ and $\theta(s)$ is given by,

$$G_{\hat{a}}(s) = \frac{\hat{a}_{meas}(s)}{\theta(s)} = cot(s)$$ Equation 7-13

where cot is the cotangent function. The open loop frequency control system can thus be represented as shown in

figure 7-4 below.

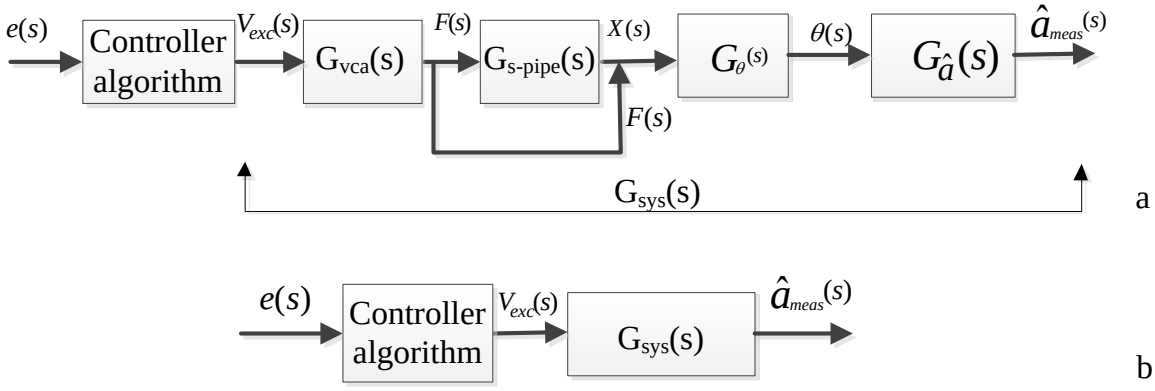

Figure 7-4: (a)Block diagram showing the sub-systems of the frequency control system (b) Block diagram open loop frequency control system

The open loop transfer function $G_{ol}(s)$ of the frequency control system can then be defined by combining the subsystems in figure 7-4(b). This is given by,

$$G_{ol}(s) = K_c(s)G_{sys}(s) \quad \text{Equation 7-14}$$

where $G_{sys}(s)$ (see figure 7-4(a)) is defined as follows,

$$G_{sys}(s) = G_{vca}(s)G_{s-pipe}(s)G_{\theta}(s)G_{\hat{a}}(s) \quad \text{Equation 7-15}$$

7.3.2 Design of controller for the closed loop frequency control system for VDMS operation

Once the mathematical model for the open loop system was developed, it was then necessary to determine appropriate gains for the controller that will ensure the closed loop frequency control system is stable and gives an appropriate response to changes in its set point input. The choice of proportional plus integral control was to ensure the tightest control possible for the closed loop frequency control system, although, error within $\pm 1\%$ of the desired operating frequency of the VDMS was permissible since the VDMS operating frequency would still remain within the identified optimal operating frequency range. The system properties obtained from the bench testing described in chapter 5 and "Test mixture 2" data given in table 5-3 were used in the theoretical analysis to investigate the characteristics of the closed loop frequency control system. MATLAB "pidtool" [171] was used in the selection of appropriate controller parameters for the closed loop frequency control system. The MATLAB "pidtool" function is an interactive graphical user interface GUI tool for PID controller design. The control system configuration used by the PID Tuner is shown below.

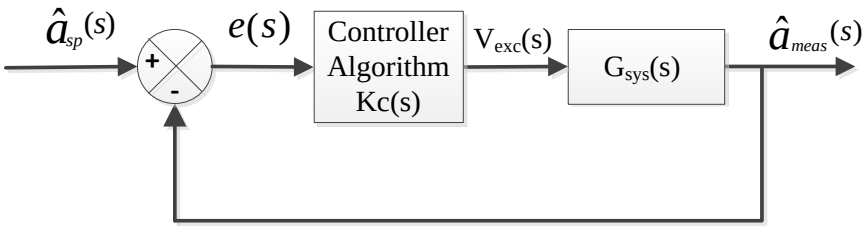

Figure 7-5: Diagram of the VDMS frequency control system

The MATLAB "pidtoool" uses the transfer function $G_{ol}(s)$ defined in equation 7-15 to determine appropriate controller parameters for which the closed loop response meets specific design requirements of stability and fast response time. The PID tuner dialogue box was used to select desired output response characteristics for the closed loop frequency control system when its input undergoes a step change.

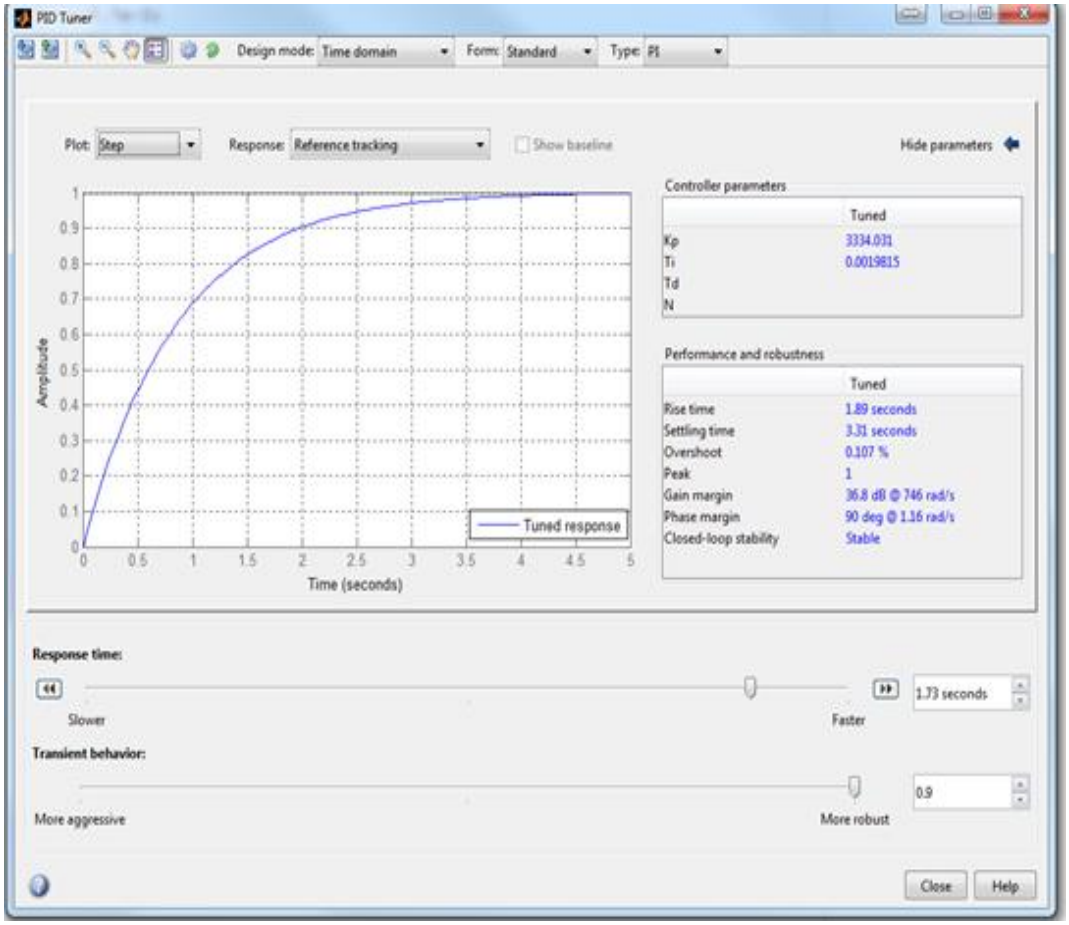

Figure 7-6: Step response of closed loop frequency control system

From figure 7-6, it is apparent that the system will achieve a steady response for controller proportional gain K_p and integral time T_i of 3334.01 and $2msec$ respectively. The response time and settling time of the closed loop system response were also obtained as 1.73seconds and 3.31seconds respectively which were considered good for this application. These parameters gives the critically damped response for the system for which its output response is fastest and has no oscillations. The diagram in figure 7-7 shows that the gain and phase margins of the closed loop

system were obtained as 36.8dB and 90° respectively. This indicates that the closed loop system is robust and will not easily become unstable for these controller parameters.

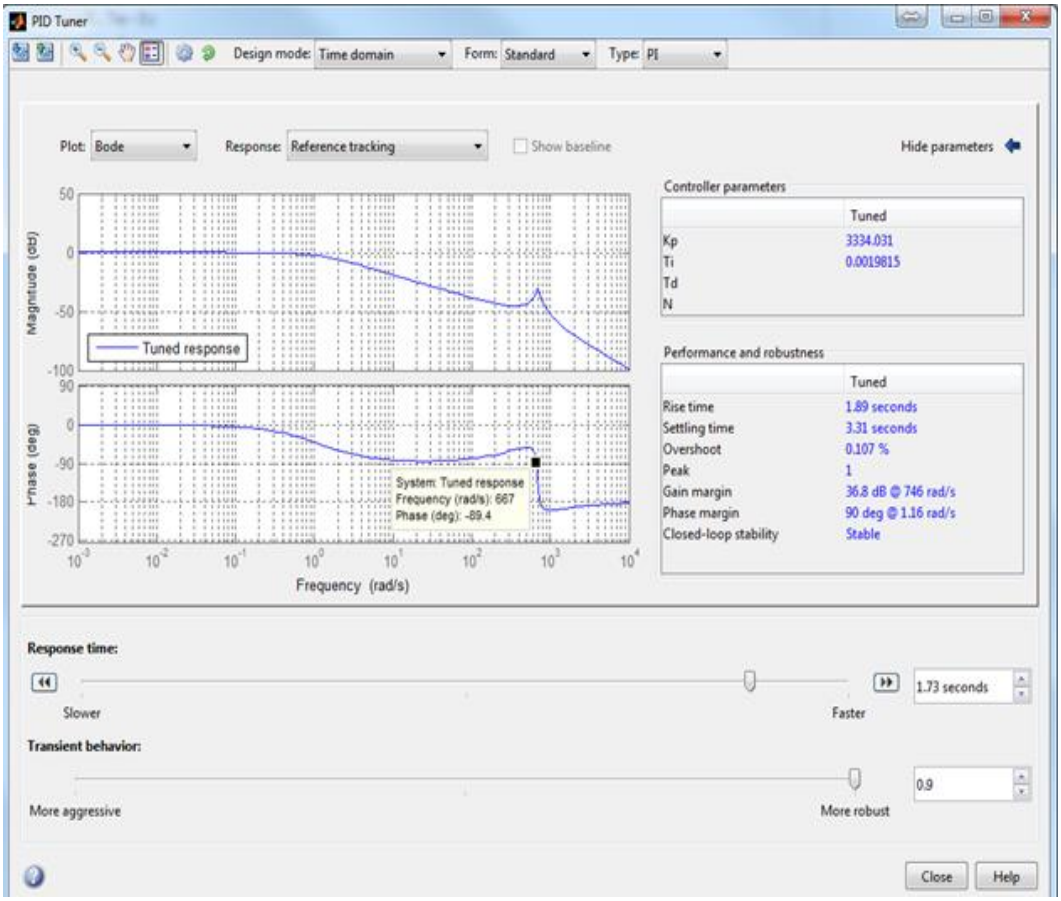

Figure 7-7: Bode plot of frequency control system

The phase of the output response is approximately -90° when the frequency of the system is 667rad/s. It is worth mentioning here that the PI controller used in the frequency control system had an autotune function to automatically determine appropriate controller parameters that ensured the system response meets the above design specifications.

7.4 Implementation of the data acquisition unit for the PC based control system for the VDMS operation

In order to implement the computer based control system for the VDMS, a modification of the data acquisition unit described in section 4.4 was required. The data acquisition unit comprises of a National Instrument DAQ card (NI-USB6211) which has sixteen analogue inputs (16-bit,

250kS/s) and two analogue outputs operated via LabVIEW and MATLAB software. The LabVIEW software allows seamless integration with nearly any hardware from any vendor [172] and in this research it was integrated to operate with a number of measurement sensors. The data acquisition unit was used to provide an interface between the measurement sensors and the computer. The electrical output signals from the DP sensor current to voltage converter circuit, voltage outputs of signal conditioning circuits for the force, displacement and temperature sensors and VCA coil current monitoring circuit were connected to five analogue inputs $AI_1 \rightarrow AI_5$ respectively of the NI DAQ device. The excitation signal to the VCA coil windings was generated in LabVIEW and sent through the analogue output channel AO_0 to the VCA coils. The schematic of the connections between the signal conditioning circuits and DAQ unit is shown in figure 7-8.

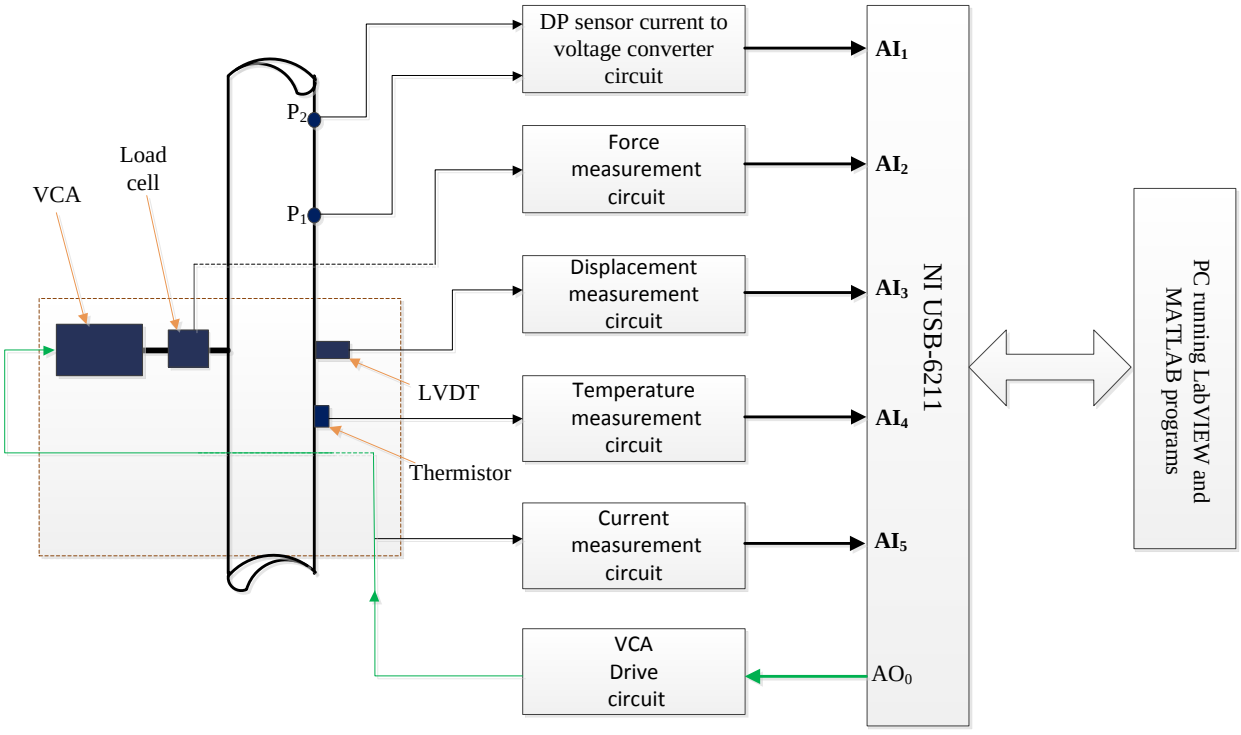

Figure 7-8: Schematic of computer based VDMS control system

7.5 Development of LabVIEW routines for computer based control system for VDMS operation.

In order to implement the computer based control system for the VDMS operation, several routines were developed in LabVIEW. These included routines (i) to acquire measurements from the respective sensors, (ii) to generate the VCA excitation signal, (iii) to implement the frequency control system for the VCA excitation signal and (iv) to implement the signal processing technique online. The different routines developed are discussed in the following sub-sections.

7.5.1 Data acquisition routine

The data acquisition routine was used to acquire the physical signals from the respective sensors via the NI DAQ card. A "DAQ assistant" function block was used to acquire the analogue measurement signals from the respective signal conditioning circuits. The DAQ assistant analogue input channels $\mathrm{AI}_1 \rightarrow \mathrm{AI}_5$ were configured to measure the DP signal, force signal, displacement signal, temperature signal and current signal respectively. The "DAQ assistant" acquisition mode was configured to acquire 2^{16} data samples N at a rate f_s of 2.5kHz for each measurement cycle, where a cycle is defined as $\frac{N}{f_s}$. These data sampling specifications ensured that the number of samples acquired in a cycle was sufficient to correctly describe the properties of the measured signals. The terminals for the NI DAQ card virtual channels were also grounded using the reference single ended (RSE) mode, which allowed the signal measurements to be made with respect to the system ground. The flow chart of data acquisition routine is shown in figure 7-9.

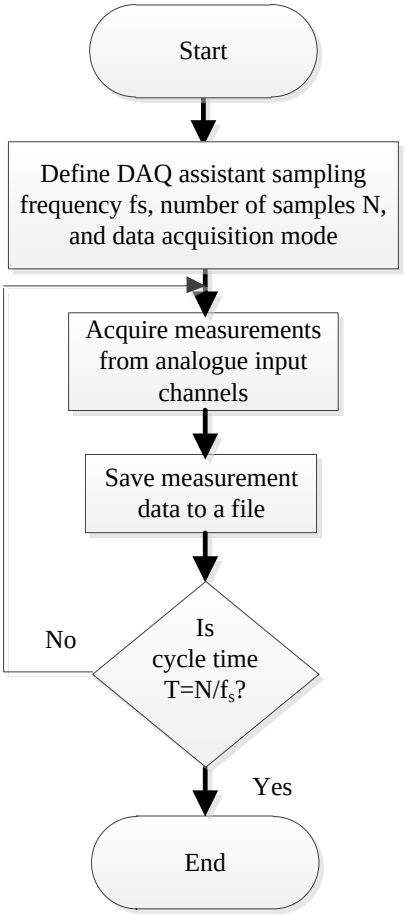

Figure 7-9: Flow chart for data acquisition routine.

7.5.2 VCA excitation signal generation routines

The VCA excitation signal generation routine was used to generate and control a sinusoidal signal with a constant amplitude, zero phase angle and offset, and has its frequency automatically set by the output from the frequency control system described in section 7.5.3. The output from the controller is determined by the algorithm defined in equation 7-2. This routine was performed using two separate parallel "while loops" to take advantage of the multi-tasking capability of LabVIEW software. The "while loops" were programmed to execute simultaneously and so it was possible to generate a signal to excite the VCA and take measurements simultaneously using the data acquisition routine.

Three key LabVIEW function blocks were used in the development of the VCA excitation signal generation routine. These were the "simulate signal", "DAQmx create virtual channel" and

"DAQmx write (VI)" function blocks. The "simulate signal" function block was used to generate a sinusoidal signal. The signal generated had its frequency set using the controller output from the frequency control system. The "simulate signal" function block was also used to set the rate at which the signal generated was written to the buffer of the analogue output channel and the number of samples to write. "DAQmx create virtual channel (VI)" was used to create an analogue output virtual channel to output the sinusoidal signal generated, while the "DAQmx write" function block was used to write the signal generated from the "simulate signal"function block to the virtual analogue output channel created. The "DAQmx create virtual channel (VI)" analogue output channel AO_0 was then configured to output the generated excitation signal in continuous mode. The "DAQmx create virtual channel" function block was also configured to regenerate samples that were previously generated so as to ensure that a continuous output was achieved without LabVIEW having to continuously write new data to the buffer. This was achieved by reusing the data already written to the buffer. The flow chart in figure 7-10 shows the principal stages of the VCA excitation signal routine.

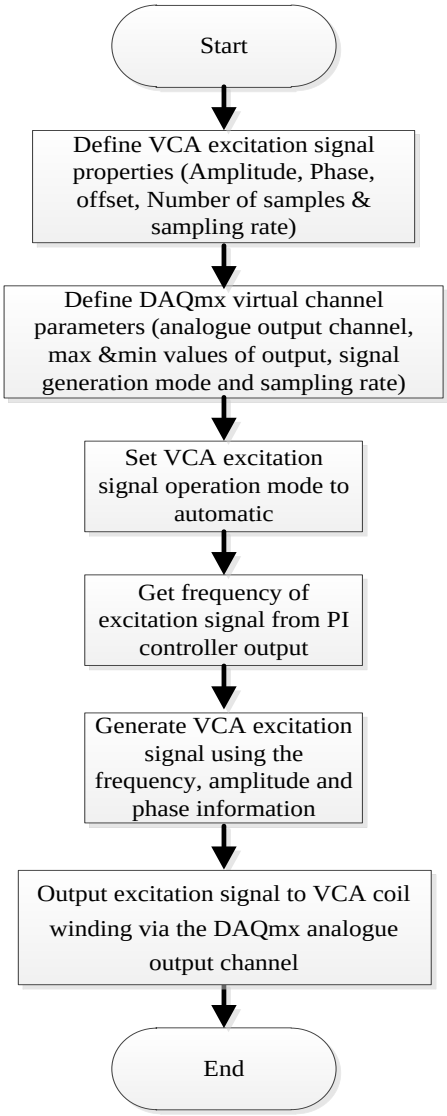

Figure 7-10: Flow chart of VCA excitation signal generation routine

The flow chart in figure 7-10 shows the flow diagram of the LabVIEW program that was used to generate the VCA excitation signal. Firstly, the properties (amplitude, offset, phase angle, number of samples and sampling rate) of the VCA excitation signal are defined in the "simulate signal" express VI. Also the properties (output channel name, maximum and minimum permissible signal amplitude, generation mode and sampling frequency) of the analogue output channel are defined using the DAQmx virtual channel properties. The operation mode is then set to "automatic" to allow the system to automatically compute the value of the VCA excitation signal frequency using

the frequency control system described in section 7.5.3. The generated signal is then sent to the VCA coils from the analogue output channel via a power amplifier.

7.5.3 Frequency control system routine

The frequency control system was a novel and important element required to achieve the overall objective of developing a computer based control system for the VDMS operation. A "proportional plus integral" control strategy was used to implement the closed loop control of the VDMS excitation frequency. The control action was implemented using an inbuilt LabVIEW "proportional plus integral" (PI) controller with an autotune function for optimal gain selection. In order to design the frequency control system, reference was made to the result obtained in section 5.10 for optimizing operation of the VDMS. It was shown that when the VDMS was operated at its optimal frequency, the phase difference between the displacement signal and force signal was $-90°$ and consequently, the measurement parameters $\hat{a}$ and λ tend to zero. At the optimal operating frequency, the measurement errors associated with using the VDMS to predict fluid density were minimized. Therefore, the purpose of the closed loop frequency control system was to ensure the VDMS could be automatically operated close to its optimal frequency for many different types of flow condition. From the Bode plot of the frequency control system shown in figure 7-7, the phase of the output response was $-90°$ when the frequency was 667rad/s. This frequency was then used to set the controller gain bias K_{bias} and it determined the output from the controller when the error was zero.

The frequency control system was implemented in a parallel "while loop" in the LabVIEW program environment. The measured value of $\hat{a}_{meas}$ was connected to the process controlled variable (PV) terminal of the PI controller, while the set point input terminal was set to zero using a numeric input box. The controller has an in-built autotune function which was used to automatically determine optimal values for the proportional gain K_p and the integral time T_i for each different flow condition. A "timer" function block was also used to set the sampling time of

the PI controller. The output from the PI controller was connected to a “select” function block via a “range” function block. The “range” function block limits the output from the controller to a specified range. This action was to avoid damage to the VCA coil winding due to proportional kick from the controller. The “select” function block was used to implement an option to either manually define the frequency of the VCA excitation signal or for it to be computed automatically using the frequency control system. This option extended the range of usability of the program, so that it could be used to operate the VDMS at frequencies outside the optimal range as the research needs might require. The controller output was then passed through an “average” function block that computes the moving average of the frequency value before it was connected to the frequency terminal of the “simulate signal” function block. The excitation signal generated was then sent to the VCA coil winding via a power amplifier.

7.5.4 Online signal processing routines

This section describes the implementation of a LabVIEW program to perform the appropriate signal processing techniques online. A MATLAB script running in the LabVIEW program environment was used to implement the signal processing technique. The measured signals (differential pressure, current, temperature, force and displacement) from the “DAQ assistant” were time dependent signals that were clustered as an array and thus needed to be separated into their respective signals. A LabVIEW “index array” function block was used to obtain the respective signals from the array cluster. Since the force signal and the displacement signal obtained using the “DAQ assistant” were voltage signals, it was important that these signals were converted to their equivalent values in Newtons and meters respectively, using the relevant calibration equations give in equation 4-35 and equation 4-36. Once the force and displacement signals had been converted, it was then necessary to change these signals from the time domain to the frequency domain. This was because the signal processing technique was implemented in the frequency domain. A “dual channel spectral measurement” function block was used for this

purpose. This function block has two input terminals designated as “X” and “Y” and can be used to generate magnitude and phase frequency responses of the inputs at two output terminals. This function block produces the respective DFTs of the force signal and displacement signal which are then used to calculate the magnitude ratio and phase difference (as shown in figure 7-11). One output terminal provides the magnitude frequency response which is calculated and displayed as a spectrum showing the magnitude ratio of the inputs (Y/X), in decibels, against the excitation signal frequency in Hz. The other output terminal provides the phase frequency response which is also calculated and displayed as a spectrum showing the phase difference between the inputs Y and X, in radians, against excitation signal frequency in Hz. In order to configure the “dual channel spectral measurement” function block, the force and displacement signals were respectively connected to the X input and Y input of this function block. The magnitude and phase output spectra were then connected to a “get XY value” function block which was configured to return the value of the magnitude and phase difference of the system response at the excitation signal frequency. The data value to return was determined by,

$$D_k = \frac{k}{f_s} \times f_{(exc)k} \qquad \text{Equation 7-16}$$

where k is the DFT index of the magnitude and phase data to return from the data spectrum, D_k are the magnitude and phase data returned at k, f_s is data sampling frequency and $f_{(exc)k}$ is the VCA excitation signal frequency also returned at k. The measured phase difference θ_k returned was connected to a “case select” function block. This function block applies a defined trigonometry condition to ensure that θ_k lies in the range of $-\pi \leq \theta_k \leq \pi$. The measured magnitude ratio Mr_k, phase difference θ_k and VCA excitation frequency $f_{(exc)k}$ were connected as inputs to the MATLAB script running in the LabVIEW programming environment. The measured peak force, the peak displacement, the phase difference between measured displacement and force signals and the VCA excitation frequency were then declared as input variables to the MATLAB script. In

addition, the VDMS constant β, the sensing pipe mass m_1, stiffness constant K_1 and sensing pipe volume V_{pipe} were defined as fixed variables in the MATLAB script. The equations to obtain $\hat{a}$, $\hat{b}$, m_2 and ρ_m given in equation 4-47, equation 4-48, equation 4-29 and equation 4-30 respectively were then implemented in the MATLAB script. The computed density of the flow was then connected to an "average" function block to obtain a moving average of the predicted density value, and hence to eliminate random measurement errors. A reference density measurement was defined in the MATLAB script for single phase water only flows, while the differential pressure measurement techniques described in section 6.5 were used to obtain reference density measurements for solids-in-water flows and air-in-water flows. A flow chart of the LabVIEW routine to compute the predicted fluid mixture density in real time is shown in figure 7-11.

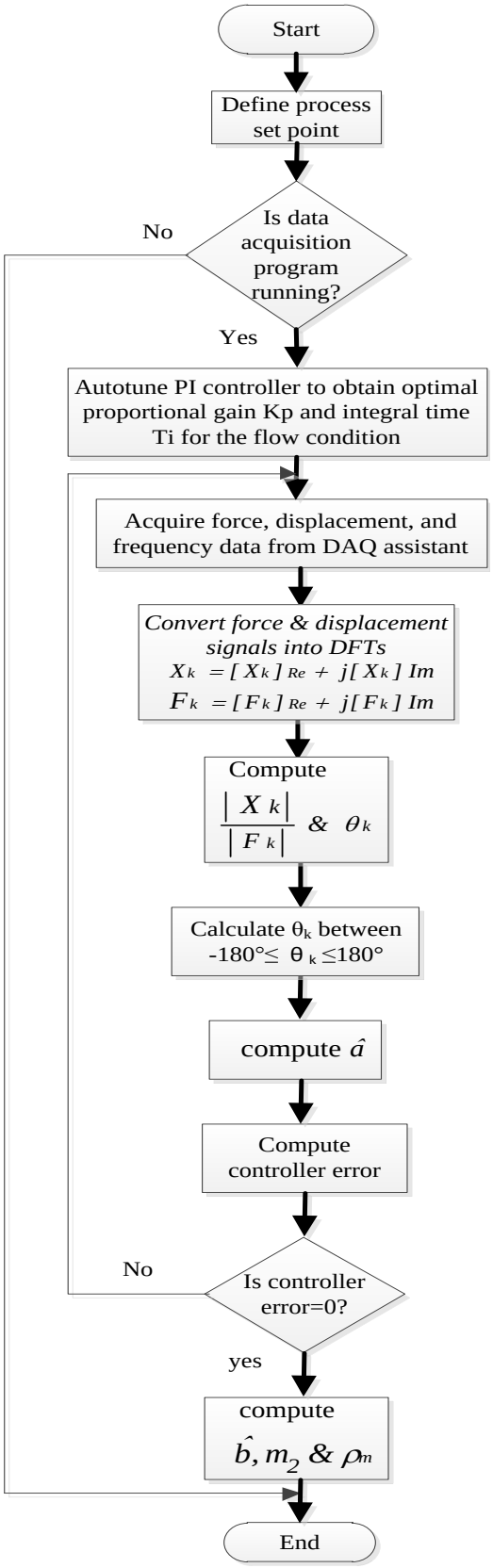

Figure 7-11: Flow chart of LabVIEW routine to obtain online density measurement of a flow using the VDMS

The sequence of operation of the density computation routine is described here. Firstly, the program was started and the set point input $\hat{a}_{sp}$ of the frequency control system was defined as zero. The controller autotune function was used to define the proportional gain and integral time for the flow condition for which density measurements were to be taken. Once the controller had been automatically tuned, the measured force and displacement signals, obtained using the data acquisition routine, were converted to their respective Discrete Fourier Transforms DFTs. These DFTs were then used to compute the operating frequency $f_{(exc)k}$ of the VDMS and the magnitude ratio Mr_k and the phase difference θ_k values between the displacement signal and the force signal. The phase difference was then used to compute the process variable $\hat{a}_{meas}$ which was continuously fed back to be compared with the set point input $\hat{a}_{sp}$ of the controller. An error signal was then computed using equation 7-1 and when this error was within $\pm 1\%$ of $\hat{a}_{sp}$, the online signal processing routine computed the term $\hat{b}$, the mass of the contents of the sensing pipe m_2, the predicted density ρ_m and a density measurement error e defined in equation 8-2. The accuracy of the computer based VDMS was tested using air-in-water flows and the results are presented and discussed in section 8.6 and 8.7. The routines developed and the user interactive interface for the computer based VDMS control system are shown in Appendix F.

7.6 Summary

A computer based control system for the VDMS has been described in this chapter. The control system comprises a measurement unit, signal conditioning and data acquisition unit and signal generation, frequency control and density measurement LabVIEW routines. A unique feature of this system is that the frequency of the excitation signal to the VCA coil winding was generated using a frequency control system implemented in LabVIEW. The frequency control system uses a "proportional plus integral" controller to determine an optimal operating frequency for the excitation signal sent to the VCA coil winding. The frequency control system ensured that the

phase difference of the displacement signal was always approximately -90° with respect to the force signal, thereby minimizing the influence of measurement errors on the predicted fluid density. The measured force and displacement signals were also used to compute the process measurement variable $\hat{a}$ for the frequency control system. After online signal processing, the force and displacement signals were then used to provide online density prediction of the flow through the sensing pipe.

Chapter 8

EXPERIMENTAL RESULTS OBTAINED USING THE VDMS TO MEASURE THE DENSITY OF FLOWING FLUIDS AND DISCUSSION OF THE RESULTS

8.1 Introduction

Once the VDMS was designed and constructed and satisfactory results were obtained from the bench tests conducted to determine its properties and performance, the next stage of this research work was to investigate its capability to provide accurate density measurements when used in single phase and multiphase flows. This chapter gives a description of the experimental procedures used in the dynamic flow investigations to obtain both density and phase volume fraction measurements for different flow conditions. It also presents a discussion of the measurement results obtained. The types of flow and flow conditions considered in this investigation were determined by the capability of the flow rig used. These include "water only", "solids-in-water" and "air-in-water" vertically upward flows. Reference density and mean phase volume fraction measurements were also obtained using the reference instruments previously described in chapter 6. The percentage relative errors in the predicted densities and mean phase volume fractions of the flows were computed using the measurements acquired from the VDMS and the reference instruments. Furthermore, statistical analysis of the measurement errors is presented and discussed and the likely source(s) of the errors are also discussed. It is important to mention at this point that for all of the investigations conducted, the VDMS was installed vertically in the flow loop working section (see figure 6-1). Lastly, the effect of the Coriolis force on the accuracy of the measured density obtained using the VDMS is discussed.

8.2 Density measurement results obtained using reference instruments for "water only" vertically upward flows

A reference density of water $\rho_{w,ref}$ was obtained for this research work using a sample of water from the flow loop reservoir. The experiment to determine $\rho_{w,ref}$ was conducted under controlled laboratory conditions using the sample of water collected from the flow loop and carefully regulating its temperature using ice, an electric heater and a stirrer. Once the temperature of the water sample was steady at 20℃, it was carefully and quickly transferred into a standard 50mL conical flask using a pipette. An analytical balance, with measurements traceable to the United Kingdom Accreditation Services (UKAS), was first used to measure the mass of the standard 50mL conical flask when empty and then when it was filled with the sample of water from the flow loop. The respective masses recorded are given in table 8-1.

Table 8-1: Measured masses standard conical flask at 20℃

Measurement description	Measured mass [g]	Measured temperature [°C]
Standard 50mL conical flask-empty	44.8364	20.00
Standard 50mL conical flask-filled with water from the flow loop	94.7127	20.00
Mass of water added to the standard 50mL conical flask	49.8763	

The reference density of water contained in the flow loop at a temperature of 20℃ was obtained as 997.526kg/m^3 using the expression,

$$\rho_{w,ref} = \frac{M_{50mL}}{V_{50mL}}$$ Equation 8-1

where M_{50mL} is the mass of water added to the standard 50mL conical flask and V_{50mL} is the volume of the standard conical flask. This value of $\rho_{w,ref}$ obtained was used as the reference density of water in the dynamic flow experiment results presented in chapter 8 and chapter 9.

8.3 Predicted density measurements obtained using the VDMS in "water only" vertically upward pipe flows

Firstly, the density measurement capability of the constructed VDMS was investigated using single phase, "water only" flows because the flow behaviour is simple and its dynamics and characteristics are well understood. In this investigation, the single-phase centrifugal pump (see figure 6-2) was used to pump water from the water reservoir through the working section of the flow loop. The manually operated flow control valve, designated as "valve 1" in figure 6-2 was used to vary the water volumetric flow rate in the working section to achieve flows with different water volumetric flow rates. For each water flow rate used in this investigation, the vertically upward, "water only" flow was circulated round the flow loop for 10 minutes allowing the flow to stabilise. This also ensured that the temperature of the flow remained uniform when VDMS measurements were taken. Once steady flow conditions were achieved, the VDMS was excited using the setup shown in figure 4-3 and this setup included a signal generator and a power amplifier that was used to send a sinusoidal excitation signal to the VCA coil winding. The amplitude of the excitation signal sent to the VCA was kept constant and was chosen such that it prevented the VCA coil winding from overheating.

Given that the optimal VDMS operating frequency ω_{opt} in "water only" flow, which is crucial to ensure the errors associated with the VDMS when used to predict density are minimized, was initially unknown, the first task in this investigation was to determine ω_{opt}. The frequency response characteristics obtained for "water only" test mixture (see figure 5-16) was used to select a range of appropriate frequencies, close to its resonant frequency, to operate the VDMS. From

figure 5-16, this frequency range was selected as between 677rad/s and 688rad/s. The results obtained from operating the VDMS between this frequency range were then used to select an optimal VDMS operating frequency that ensured the density measurement errors were minimized. Next, the data acquisition unit was used to measure the force applied to the sensing pipe centre and the resultant displacement at the sensing pipe centre. The sensing pipe temperature and the VCA coil current were also measured. The data acquisition unit was also used to save the measurements obtained to a file and each measurement was acquired for a period of 26.21seconds ($\frac{N}{f_s}$ see section 4.4). The saved measurements were then used to provide an offline computation of the flow density using the signal processing technique described in section 4.5 and the density prediction model given in equation 4-29 and equation 4-30.

8.3.1 Flow conditions generated when the VDMS was used to measure density in "water only" vertically upward pipe flows at operating frequencies between 677rad/s and 688rad/s

Once the VDMS operating frequency range was selected, different "water only" flow conditions were generated for use in the investigation to determine ω_{opt}. The flow conditions investigated varied from no flow, when the flow control valve was fully shut, to maximum flow, when the flow control valve was fully open. The water volumetric flow rate $Q_{w,ref}$ through the working section of the flow loop was measured using a turbine flow meter.

Table 8-2: Flow conditions generated for "water only" vertically upward flows when the VDMS was operated between 677rad/s-688rad/s.

Flow condition number, n	Flow condition name	Water flow rate $Q_{w,ref}$ [m^3/hr]	VDMS operating frequency range [rad/s]
1	FC_w-1	0.00	677-688
2	FC_w-2	3.49	
3	FC_w-3	8.21	
4	FC_w-4	11.70	
5	FC_w-5	15.72	

For each of the flow condition given in table 8-2, the VDMS was operated at predetermined frequency points over the selected frequency range (677rad/s-688rad/s), which was expected to be within 1% of the resonant frequency for "water only" flows. An average of four measurements was taken at each the VDMS operating frequency point used in a given flow condition, and these measurements were used to compute the flow density. The density measurement results obtained from the investigation to determine ω_{opt} for "water only" flows are presented and discussed in section 8.3.2.

8.3.2 Density measurement results obtained using the VDMS in "water only" vertically upward flows at operating frequencies between 677rad/s-688rad/s

This section presents a discussion of the density measurement results that were obtained using the VDMS in "water only" vertically upward flows for operating frequencies between 677rad/s-688rad/s. For each of the flow conditions listed in table 8-2, the measured force and displacement signals obtained from the relevant sensors provided the force, displacement and frequency data used in the signal processing technique described in section 4.5 to compute the flow density. For each density measurement taken at an operating frequency used in a given flow condition, the respective force and displacement data were used to compute the magnitude ratio Mr and the phase difference θ of the VDMS response, which in turn were used to compute the density measurement

parameters $\hat{a}$, $\hat{b}$ and λ (see section 4.5). These parameters were used to compute the predicted density $\rho_{w,m,n,i}$ of the "water only" flow at the ith operating frequency for the nth flow condition. Since the objective of this investigation was to determine an optimal VDMS operating frequency ω_{opt} that will enable accurate density measurements to be taken using the VDMS, only the measurement results that were needed for this purpose are presented. These measurements include $\rho_{w,m,n,i}$, λ, $\hat{a}$, θ and Mr and they are shown in figure 8-1 to figure 8-5 respectively.

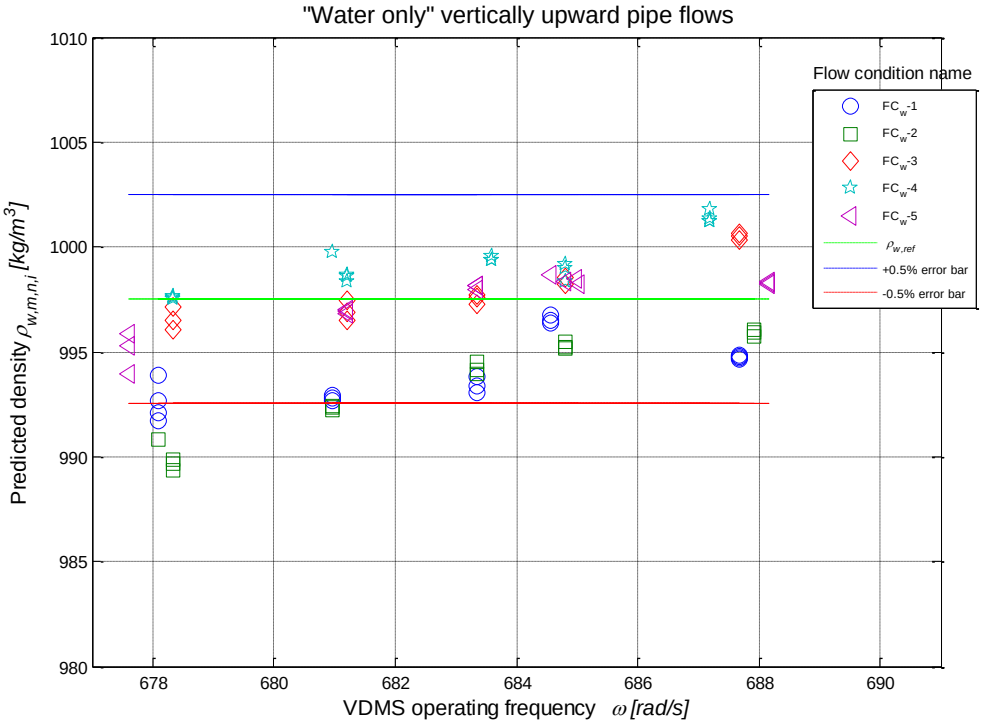

Figure 8-1: Predicted density versus operating frequency plots for different water flow rates obtained using the VDMS in "water only" vertically upward pipe flows

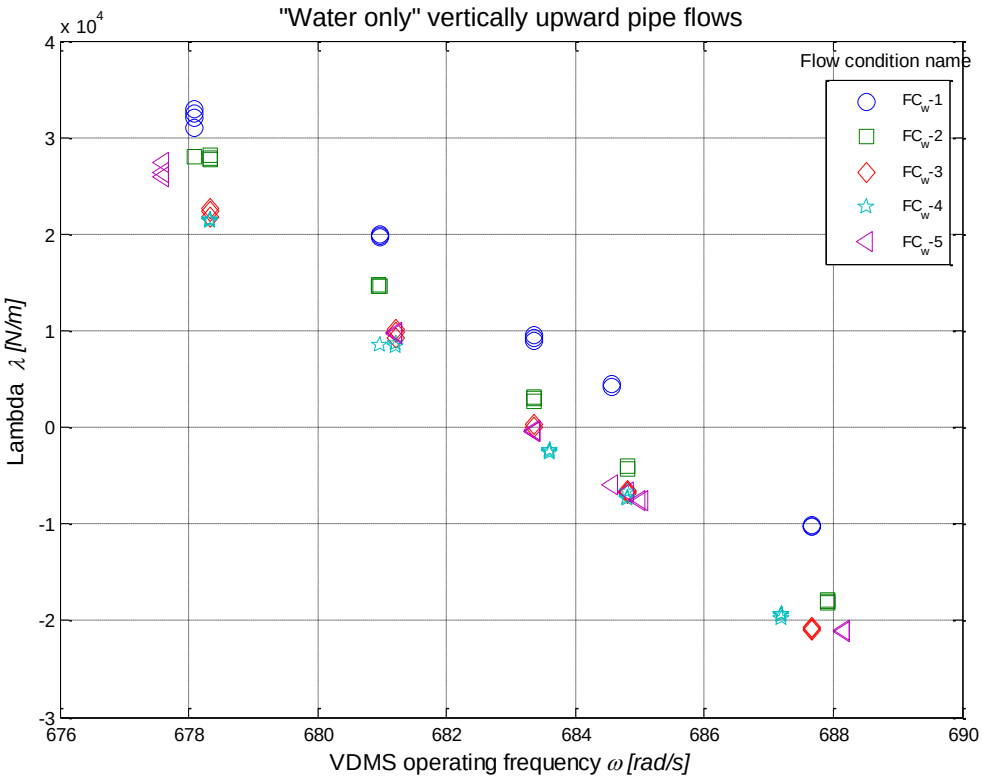

Figure 8-2: λ versus operating frequency plots for different water flow rates using the VDMS is used in "water only" vertically upward pipe flows

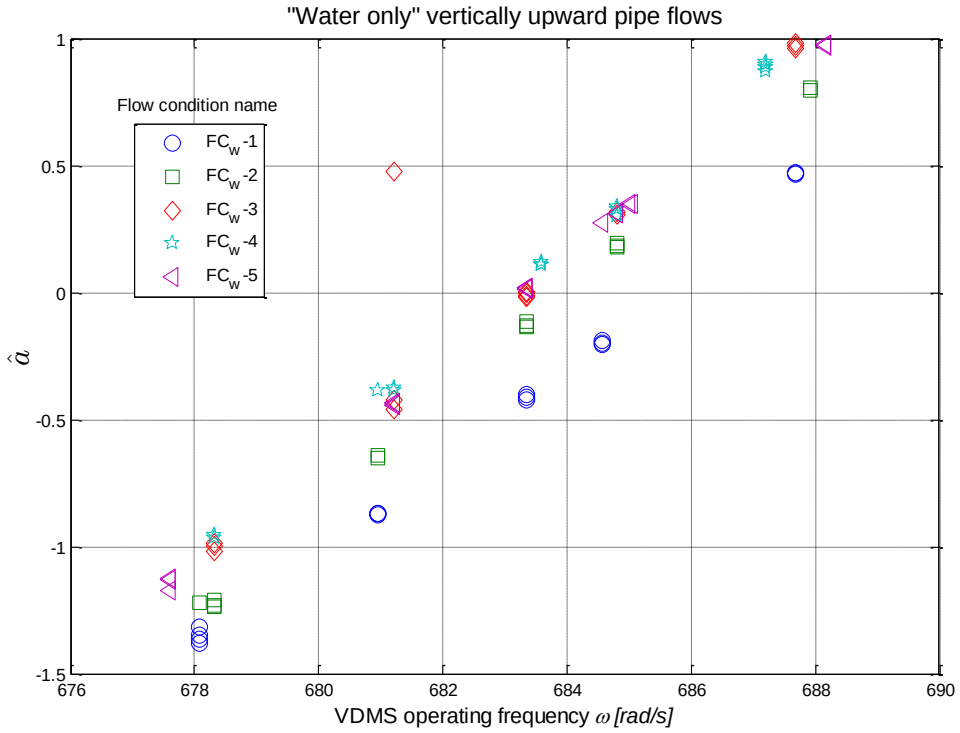

Figure 8-3: â versus operating frequency for different water flow rates using the VDMS in "water only" vertically upward pipe flows

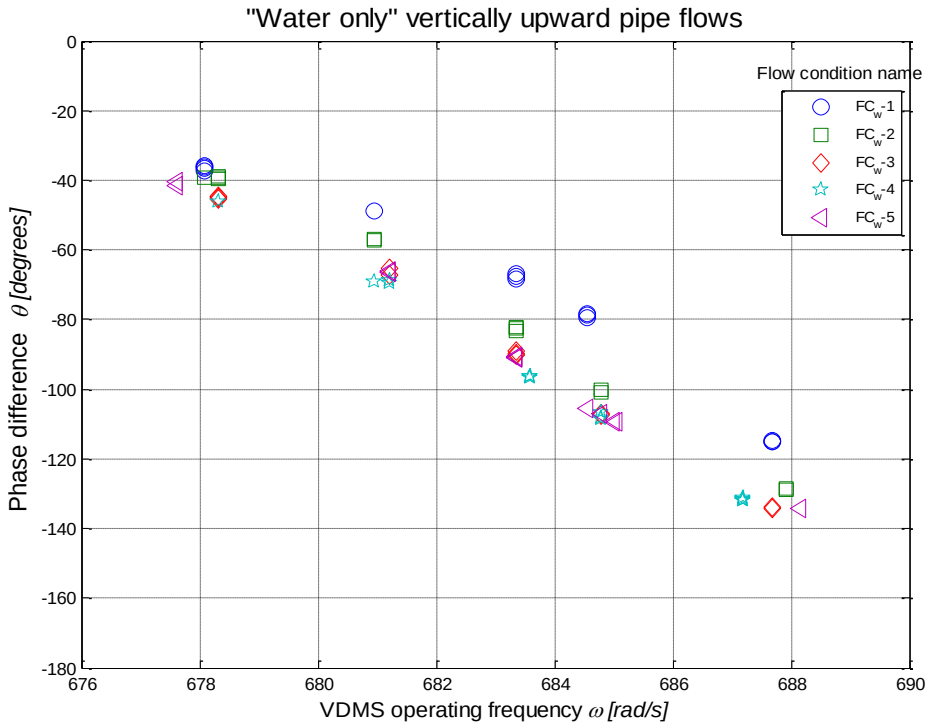

Figure 8-4: Phase difference θ versus operating frequency for different water flow rates using the VDMS in "water only" vertically upward pipe flows

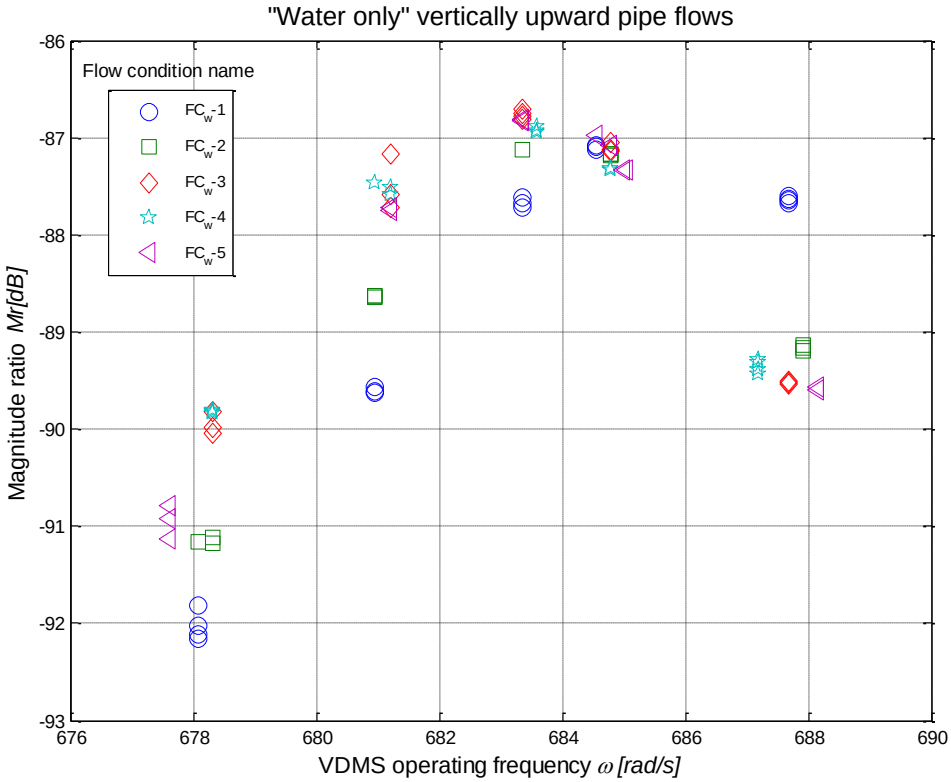

Figure 8-5: Magnitude ratio Mr versus operating frequency for different water flow rates using the VDMS in "water only" vertically upward pipe flows

In all of the plots shown in figure 8-1 to figure 8-5, the different water flow rates $Q_{w,ref}$ used in the investigation have been represented by different plot colours and symbols as shown in the legend. The predicted densities shown in figure 8-1 for "water only" vertical upward pipe flow were computed using equation 4-29 and equation 4-30 and the measured ω and λ values. In figure 8-2, the lambda λ values shown were computed using equation 4-28 and the measured $\hat{a}$ and $\hat{b}$ values. Figure 8-3 shows the variation of the measured value of $\hat{a}$, computed using equation 4-47, with operating frequency. The values of θ shown in figure 8-4 were obtained using equation 4-49 and the respective phase angle obtained from the displacement and force phasors whilst the values of Mr shown in figure 8-5 were obtained using equation 4-50 and the respective magnitudes of the displacement and force phasors.

The results shown in figure 8-2 to figure 8-5 for λ, $\hat{a}$, θ and Mr respectively, were used to select an optimal VDMS operating frequency ω_{opt} in "water only" dynamic flows that ensured the phase difference θ between the displacement and force signal was approximately -90°. The value of ω_{opt} selected also ensured that $\hat{a}$ and λ were close to zero and that the errors associated with the density measurements obtained using the VDMS in "water only" flows were minimized. Since θ and Mr were used in this research work to compute $\hat{a}$, λ and $\rho_{w,m,n,i}$ respectively, their results will be discussed first. From figure 8-4 and figure 8-5, it is apparent that the phase difference θ of the VDMS response is closest to -90° and the magnitude ratio Mr is maximum when the VDMS operating frequency ω was between 683rad/s and 685rad/s and these results suggested that the resonant frequency of the "water only" flow was in this frequency range. Consequently, the values for λ and $\hat{a}$ shown in figure 8-2 and figure 8-3 respectively tend to zero in the same frequency range (683rad/s-685rad/s). From the results obtained in section 5.10.1, it was conceivable in this investigation that the errors associated with using the VDMS to obtain density measurements in "water only" flows would be minimized at operating frequencies between 683rad/s and 685rad/s.

Qualitatively, it is apparent from the results in figure 8-1 that $\rho_{w,m,n,i}$ obtained for the different flow conditions were consistently within $\pm 0.5\%$ of the reference density and were also tightly clustered when ω was between 681rad/s and 685rad/s for the different flow conditions. However, when ω was between 677rad/s and 680rad/s, $\rho_{w,m,n,i}$ is observed to have a relatively larger scatter and is outside the $\pm 0.5\%$ error band for FC_w-1 ($0m^3/hr$) and FC_w-2 ($3.49m^3/hr$). At ω between 683rad/s and 685rad/s, which corresponds to the frequency range where θ was approximately -90° and λ and $\hat{a}$ tend to zero, $\rho_{w,m,n,i}$ was closest to the reference density for all of the flow conditions investigated. Hence the optimal VDMS operating frequency ω_{opt} was computed from the average of this frequency range (683rad/s and 685rad/s) as 684rad/s. Further investigations were then conducted using ω_{opt} and a different set of flow conditions which considered a wider range of water volumetric flow rates. These flow conditions are listed in table 8-3.

8.3.3 Density measurement results obtained when the VDMS was operated at the optimal operating frequency ω_{opt} in "water only" vertically upward pipe flows

In this investigation, a wider range of water flow rates was considered in order to understand how changes to the water flow rate affected the predicted densities $\rho_{w,m,n,i}$ obtained using the VDMS at its optimal frequency ω_{opt}. The different water flow rates used in this investigation are listed in table 8-3 and for each water flow rate, the VDMS was operated at $\omega_{opt} = 684\text{rad/s}$.

Table 8-3: Flow conditions used in "water only" vertically upward flows experiments when VDMS was operated at its optimal frequency

Flow condition number n	Flow condition name	Water flow rate $Q_{w,ref}$ [m^3/hr]	Optimal VDMS operating frequency ω_{opt} [rad/s]
6	FC_w-6	0.0	684
7	FC_w-7	1.4	
8	FC_w-8	2.6	
9	FC_w-9	4.5	
10	FC_w-10	5.9	
11	FC_w-11	7.0	
12	FC_w-12	8.2	
13	FC_w-13	9.4	
14	FC_w-14	10.7	
15	FC_w-15	12.6	
16	FC_w-16	14.2	
17	FC_w-17	15.2	
18	FC_w-18	16.8	

For each of the flow conditions used in this investigation, an average of five different sets of measurements was taken using the data acquisition unit. Again, the signal processing technique described in section 4.5 was used to compute the magnitude ratio Mr and phase difference θ of the VDMS response and thence the measurement parameters $\hat{a}$ and λ and the predicted density $\rho_{w,m,n,i}$ of the "water only" flow. These measurement results are presented in figure 8-6 to figure 8-10 respectively.

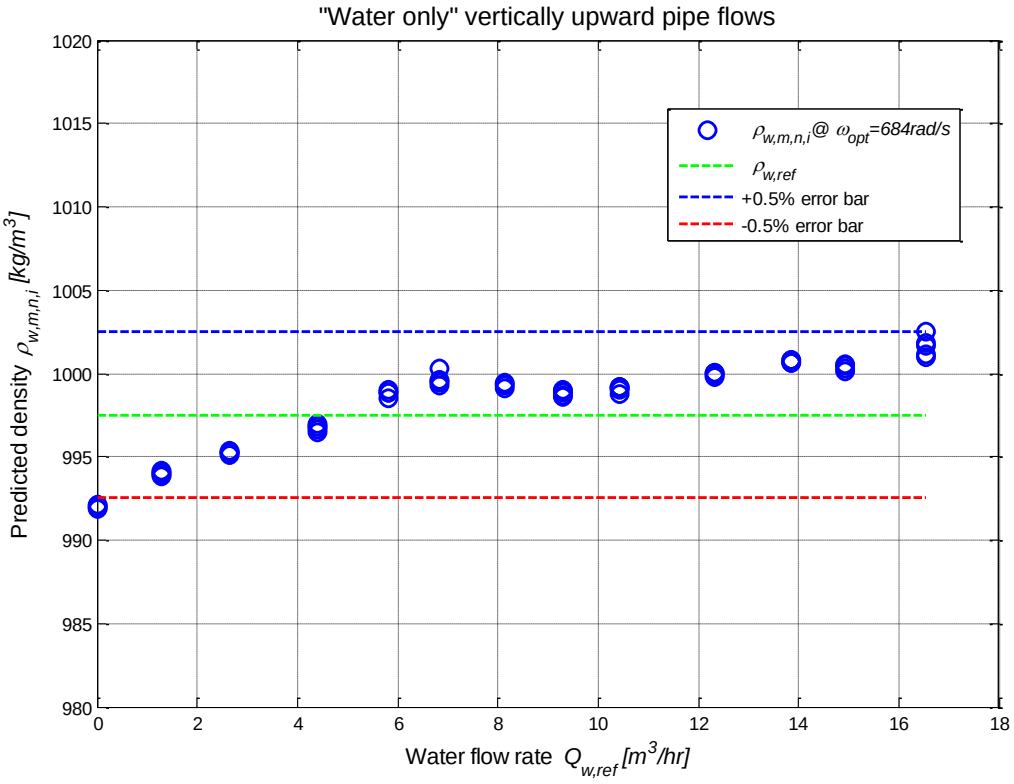

Figure 8-6: Predicted water density versus reference water volumetric flow rate when the VDMS was operated at its optimal frequency in "water only" vertically upward pipe flows

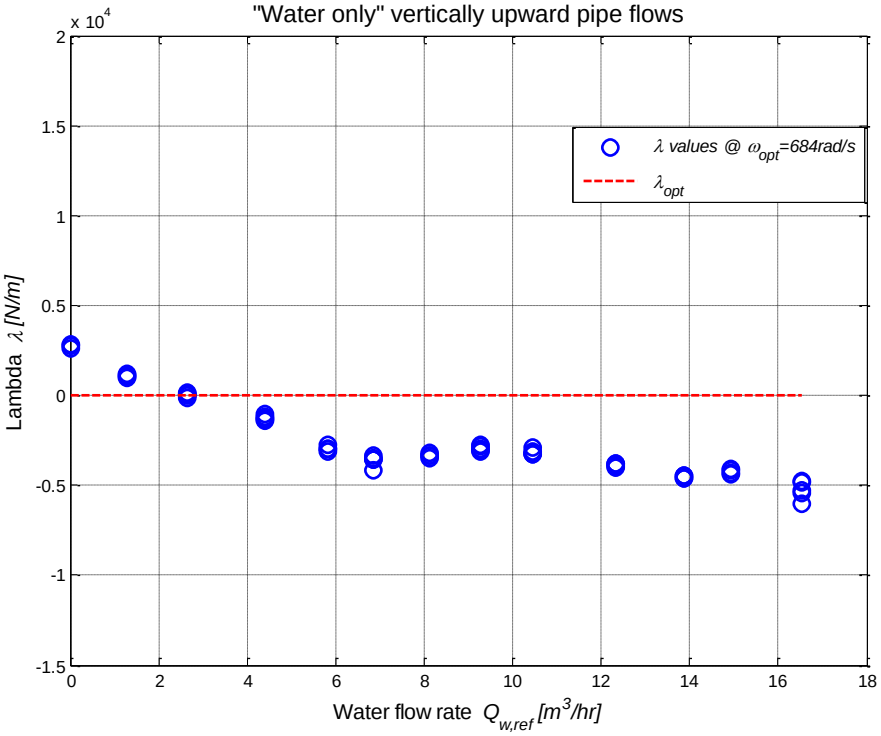

Figure 8-7: λ versus reference water volumetric flow rate when the VDMS was operated at its optimal frequency in "water only" vertically upward pipe flows

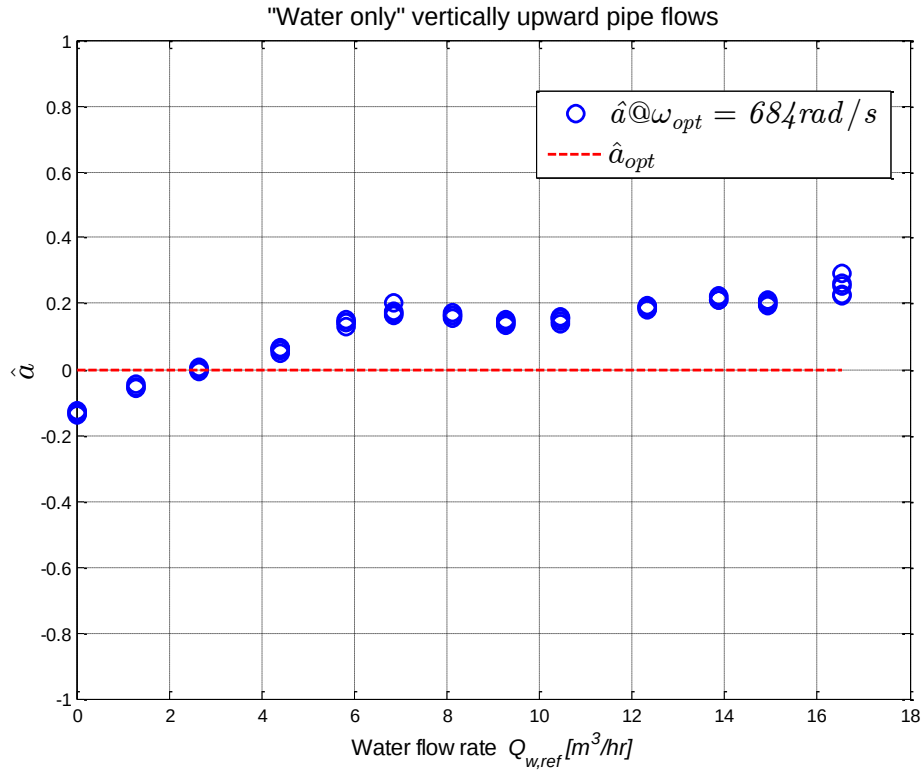

Figure 8-8: â versus reference water volumetric flow rate when the VDMS was operated at its optimal frequency in "water only" vertically upward pipe flows

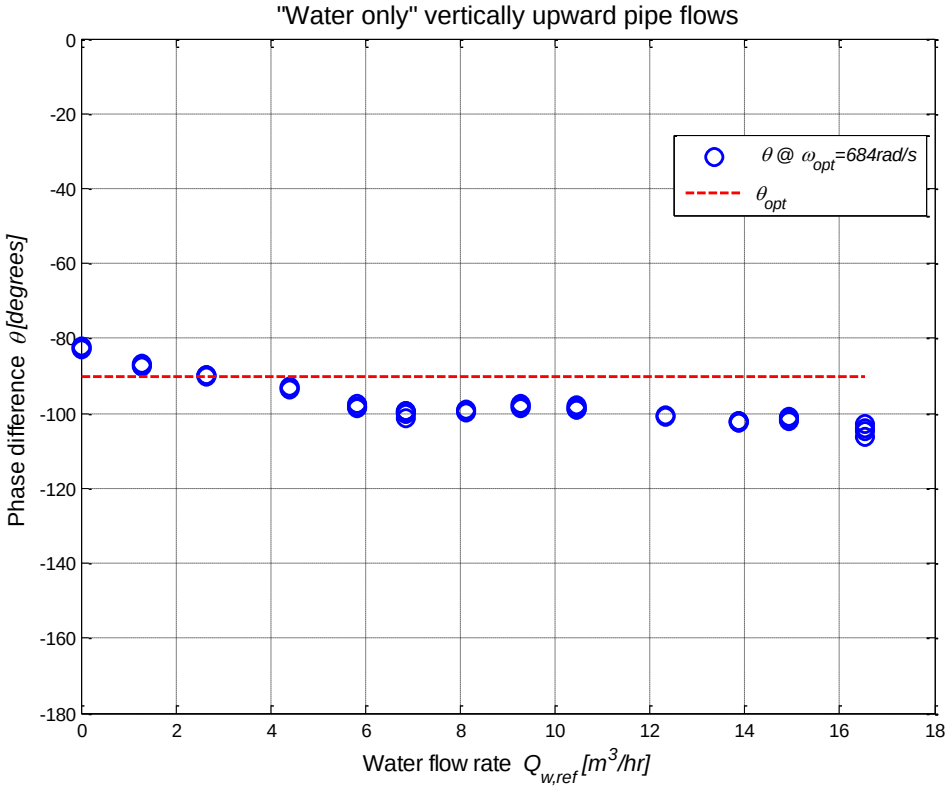

Figure 8-9: Phase difference θ versus reference water volumetric flow rate when the VDMS was operated at its optimal frequency in "water only" vertically upward pipe flows

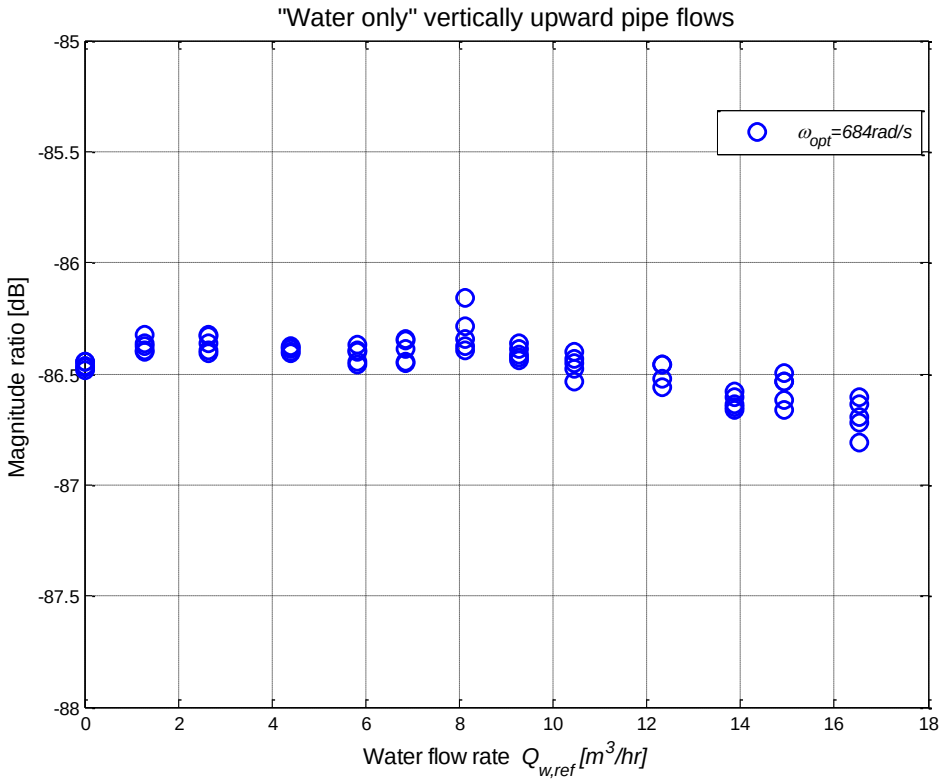

Figure 8-10: Magnitude ratio Mr versus reference water volumetric flow rate when the VDMS was operated at its optimal frequency in "water only" vertically upward pipe flows

In figure 8-6, the green dashed line representing the reference water density $\rho_{w,ref}$ was obtained as described in section 8.2 whilst the red and blue dashed lines represent -0.5% and $+0.5\%$ error bars respectively. The measurement parameters λ, $\hat{a}$, θ and Mr shown in figure 8-7 to figure 8-10 respectively, were computed using equation 4-28, equation 4-47, equation 4-49 and equation 4-50. λ_{opt} and $\hat{a}_{opt}$ represent the theoretical values of λ and $\hat{a}$ obtained when the VDMS operating frequency equals its fundamental frequency $\omega_{n,1}$ and these values were computed using equation 5-22 and equation 4-19 respectively whilst θ_{opt} represent the theoretical value of the phase difference between the displacement and force signals that will ensure the errors in the density measurement obtained using the VDMS were minimized. The values of θ_{opt} was obtained from the theoretical Bode plot shown in figure 3-3 for a 2nd order vibrating mechanical system at $\omega_{n,1}$ as -90°. Since $\rho_{w,m,n,i}$, λ and $\hat{a}$ were computed using θ and Mr obtained from the force and

displacement phasors, θ and Mr results are discussed first in this section, followed by the results obtained for $\hat{a}$, λ and $\rho_{w,m,n,i}$.

Qualitatively, the result in figure 8-9 shows that θ is -83° at no flow and it is steadily reduced to -99° as the water flow rate $Q_{w,ref}$ was increased from 0m^3/hr to 6.99m^3/hr. When $Q_{w,ref}$ was between 6.99 m^3/hr to 15.20m^3/hr, θ is observed to remain approximately constant at -99°. This result shows that θ varies between -7% and +10% from θ_{opt} for $Q_{w,ref}$ values between 0m^3/hr to 15.20m^3/hr. Additionally, the plot of Mr versus $Q_{w,ref}$ in figure 8-10 shows that the value of Mr is somewhat between -86.4dB and -86.7dB for $Q_{w,ref}$ values between 0m^3/hr to 16.77m^3/hr. Qualitatively, the trend in the phase difference θ versus water flow rate $Q_{w,ref}$ results in figure 8-9 is observed to be more similar to the results for $\rho_{w,m,n,i}$, λ and $\hat{a}$ shown in figures 8-6, 8-7 and 8-8 respectively, than the result of the magnitude ratio shown in figure 8-10. It is therefore reasonable to suggest that θ is more likely to influence the errors in $\hat{a}$ and λ and hence $\rho_{w,m,n,i}$ than Mr. From figure 8-8 and figure 8-7, the values of $\hat{a}$ and λ were found to be -0.12 and 2500 respectively at no flow condition and these values changed progressively to 0.16 and -3500 as $Q_{w,ref}$ was increased from 0m^3/hr to 6.99m^3/hr. For $Q_{w,ref}$ between 6.99m^3/hr and 16.77m^3/hr, the values of $\hat{a}$ and λ remained somewhat consistent. Since the values of $\hat{a}$ and λ obtained for $Q_{w,ref}$ between 0m^3/hr and 16.77m^3/hr were relatively close to zero, the results suggested that the errors associated with using the VDMS to obtain $\rho_{w,m,n,i}$ were minimized in this investigation. Finally, the results in figure 8-6 show that the predicted water densities $\rho_{w,m,n,i}$ obtained for the flow conditions investigated were consistently within $\pm 0.5\%$ of the reference density measurement and thus suggested that the VDMS gave an accurate estimate of the water density in the working section relative to the reference. The tight cluster observed in $\rho_{w,m,n,i}$ for all the measurements taken at each flow condition further suggested that the VDMS gave consistent and repeatable density measurements. The results shown in figure 8-6 to figure 8-10 are suggestive of the existence of a

water flow rate dependent systematic error in $\rho_{w,m,n,i}$. Given that θ obtained in this investigation is observed to vary between -7% and +10% of θ_{opt} for $Q_{w,ref}$ between 0m^3/hr and 16.77m^3/hr, which in turn resulted in deviation of $\hat{a}$, λ and hence $\rho_{w,m,n,i}$ from their respective reference values, it was instructive to quantify the errors in $\rho_{w,m,n,i}$ and this is discussed in section 8.3.4.

8.3.4 Comparison of density measurement results acquired using the VDMS at the optimal operating frequency with the reference density for "water only" vertical upward flows

This section presents a comparison of the predicted density measurements $\rho_{w,m,n,i}$ obtained using the VDMS at its optimal operating frequency and the reference density measurements $\rho_{w,ref}$ for "water only" vertically upward pipe flows. For the i^{th} density measurement taken at the nth flow condition in the current research work, a general expression was defined to compute a percentage relative error $e_{x,n,i}$ using the reference density and the predicted density for the different flow types used in this research work. This error $e_{x,n,i}$ is given by,

$$e_{x,n,i} = \frac{\rho_{x,m,n,i} - \rho_{x,ref,n,i}}{\rho_{x,ref,n,i}} \times 100 \qquad \text{Equation 8-2}$$

where x is the flow type and could be either "w" for "water only" flows or "sw" for "solids-in-water" flows or "aw" for "air-in-water" flows, i is the density measurement index for the nth flow condition and $\rho_{x,m,n,i}$ and $\rho_{x,ref,n,i}$ are the i^{th} predicted and reference density respectively, taken at the nth flow condition of flow type x. Additionally, expressions to compute the mean error $\bar{e}_{x,n}$ and the standard deviation $S_{x,n}$ of the errors $e_{x,n,i}$ in $\rho_{x,m,n,i}$ for the nth flow condition in x flow type are defined in this section. The values of $\bar{e}_{x,n}$ and $S_{x,n}$ are used for the purpose of quantitative comparison of the values of $\rho_{x,m,n,i}$ and $\rho_{x,ref,n,i}$ and are defined as follows,

$$\bar{e}_{x,n} = \frac{\sum_{i=1}^{N}(e_{x,n,i})}{N} \qquad \text{Equation 8-3}$$

$$S_{x,n} = \sqrt{\frac{\sum_{i=1}^{N}\left(e_{x,n,i} - \bar{e}_{x,n}\right)^2}{N}}$$ Equation 8-4

where $e_{x,n,i}$ represents the i[th] measured error in $\rho_{x,m,n,i}$ at the n[th] flow condition, $\bar{e}_{x,n}$ represents the mean error in $\rho_{x,m,n,i}$ at the n[th] flow condition, N represents the total number of measurements taken at each flow condition and x represents the flow type and it has been defined previously.

In "water only" experiments, the mean error $\bar{e}_{w,n}$, also referred to as the systematic error, was used to provide a means to quantify the magnitude of the deviation of the predicted water density $\rho_{w,m,n,i}$ from the reference water density $\rho_{w,ref}$ whilst the standard deviation $S_{w,n}$ of the errors $e_{w,n,i}$ in $\rho_{w,m,n,i}$ provide a means to quantify the magnitude of the scatter in $\rho_{w,m,n,i}$ about $\rho_{w,ref}$. For the flow conditions listed in table 8-3 that were used in the "water only" experiments, the mean or systematic errors $\bar{e}_{w,n}$ and standard deviation $S_{w,n}$ of the errors $e_{w,n,i}$ in the predicted density $\rho_{w,m,n,i}$ were computed using equation 8-3 and equation 8-4 respectively, and these results are shown in figure 8-11.

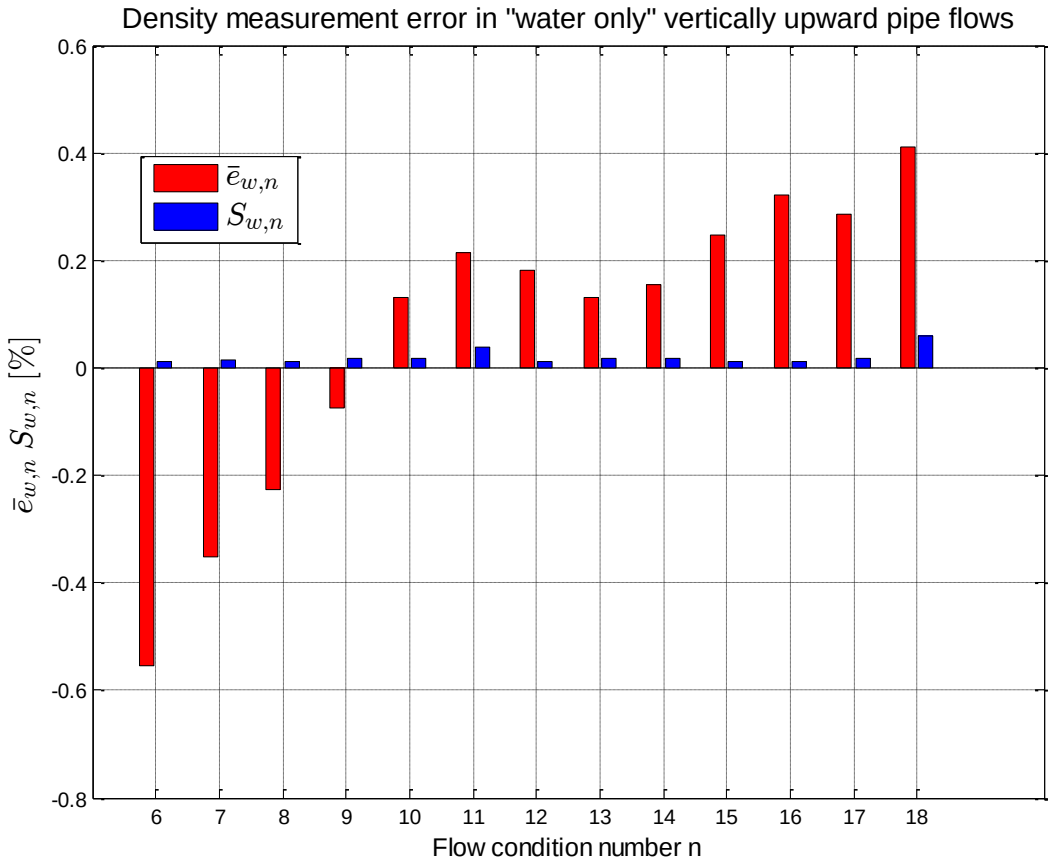

Figure 8-11: Bar graph of mean error and standard deviation of errors in $\rho_{w,m,n,i}$ when VDMS was operated at its optimal frequency in "water only" vertically upward pipe flows

Inspection of the results presented in figure 8-11 show that the mean errors $\bar{e}_{w,n}$ in $\rho_{w,m,n,i}$ increase progressively from -0.55% to +0.21% as $Q_{w,ref}$ increases from 0 (FC_w-6) to 6.99m^3/hr (FC_w-11). When $Q_{w,ref}$ was between 6.99m^3/hr and 16.77m^3/hr (i.e. between FC_w-11 and FC_w-16) the $\bar{e}_{w,n}$ values are seen to increase randomly. The results suggest a flow rate dependent systematic error in $\rho_{w,m,n,i}$ which could be minimized by appropriate calibration of the VDMS. Also, the random errors in $\rho_{w,m,n,i}$ could be reduced by increasing the number N of density measurements taken at each flow condition. Qualitatively, the trend in $\bar{e}_{w,n}$ data shown in figure 8-11 is quite similar to the phase difference θ plot shown in figure 8-9, and is again suggestive that the errors associated with computing θ may have more influence in the errors $e_{w,n,i}$ in $\rho_{w,m,n,i}$ than Mr. It is worth mentioning here that $\bar{e}_{w,n}$ was always within -0.55% to $+0.41\%$ of the reference density

measurement for all the flow conditions used in this investigation and suggest that the predicted density values obtained using the VDMS were a reasonably accurate estimation of the true water density in the flow loop working section. Furthermore, the standard deviation $S_{w,n}$ of the errors $e_{w,n,i}$ in $\rho_{w,m,n,i}$ was also consistently less than 0.06% for all the flow conditions investigated. This result also agrees with the visual observation of the scatter in the plot in figure 8-6 to figure 8-10 and indicates good repeatability and reliability of the $\rho_{w,m,n,i}$ measurements obtained using the VDMS.

Also, generalised expressions to compute the overall mean error $\bar{e}_{x,t}$ and the overall standard deviation $S_{x,t}$ of the errors in $\rho_{x,m,n,i}$ for all the measurements taken in the experiments conducted using different flow types x in the current research are defined follows,

$$\bar{e}_{x,t} = \frac{\sum_{n=1}^{N_t} \sum_{i=1}^{N} \left(e_{x,n,i}\right)}{N_t \times N} \qquad \text{Equation 8-5}$$

$$S_{x,t} = \sqrt{\frac{\sum_{n=1}^{N_t} \sum_{i=1}^{N} \left(e_{x,n,i} - \bar{e}_{x,t}\right)^2}{N_t \times N}} \qquad \text{Equation 8-6}$$

where N is the number of measurements taken at a given flow condition and N_t is the total number of flow conditions. For "water only" experiments, the overall mean error $\bar{e}_{w,t}$ and the overall standard deviation $S_{w,t}$ of the errors in $\rho_{w,m,n,i}$ were computed using equation 8-5 and equation 8-6. Note that a total of sixty-four density measurements were taken for the "water only" experiments. The values of $\bar{e}_{w,t}$ and $S_{w,t}$ were obtained as 0.07% and 0.01% respectively, which again shows that the density measurements agree well with the reference density measurements and that the results from the VDMS are also highly repeatable. The small values of $\bar{e}_{w,t}$ and $S_{w,t}$ suggest that the errors associated with the VDMS when it was operated at its selected optimal frequency and used to measure density in "water only" flows were significantly minimized. These values for $\bar{e}_{w,t}$ and $S_{w,t}$ also agrees well with quotes of accuracies and uncertainty of existing

commercial vibrating densitometry system for single phase applications [173, 174]. From the density measurement results obtained using the VDMS for the "water only" experiments, it is conceivable to say that if the VDMS is operated at its optimal frequency, it can be used to provide relatively accurate, repeatable and reliable density measurements for single phase fluids similar to that used in this research.

Lastly, it was important to identify the source(s) of the errors shown in figure 8-11 which suggested the presence of a systematic error in $\rho_{w,m,n,i}$ obtained using the VDMS. A careful observation of the VDMS measurement unit showed that the spatial position of the force sensor associated with the VDMS was offset from the sensing pipe centre by 1mm. Generally, it is expected that when the sensing pipe with "fixed end" supports undergoes lateral vibration in vertical upward pipe flows, it will be subjected to a Coriolis acceleration through the mechanical introduction of apparent rotations in the pipe [149]. The net Coriolis force at the pipe centre is expected to be zero as described by Morrison and Crossland [149] and also shown in section 8.8. Thus, if the force and displacement sensors associated with the VDMS are positioned exactly at the sensing pipe centre, the net Coriolis force at the sensing pipe centre will be zero. However, the position of the force sensor was 1mm offset from the sensing pipe centre, and it was therefore possible that a net Coriolis force was picked up by the force sensor in this investigation. This net Coriolis force is water flow rate $Q_{w,ref}$ dependent [149], and hence it is possible that the progressive increase in the mean errors observed in figure 8-11 were due to an increase in the net Coriolis force as $Q_{w,ref}$ was increased.

8.4 Density measurements obtained using VDMS and reference instruments in solids-in-water vertically upward pipe flows

This section discusses the results of experiments conducted to obtain mixture density measurements using the VDMS and reference instruments in solids-in-water vertically upward flows. In this experiment, a solids-water mixture was pumped from a reservoir (see figure 6-2) and circulated through the flow loop working section before returning to the reservoirs via the separator unit (see section 6.2). Fifteen flow conditions with different in-situ solids volume fractions were generated and used in this experiment and these flow conditions are described in section 8.4.1. As a precautionary procedure to ensure accurate measurements were taken in this experiment, the differential pressure (DP) sensor high pressure (HP) and low pressure (LP) lines were flushed with water to ensure no air was trapped in the pressure lines before measurements were taken. For each flow condition generated and used in this investigation, the vertically upward solids-in-water flow generated was circulated round the flow loop for at least 20 minutes to allow the flow mixture and its temperature to become uniform. It is important to mention here that despite allowing the solids-water mixture to circulate round the flow loop for a significant time interval before taking measurements, the flow mixture generated in the working section was not uniform. The flow became less uniform as the water volumetric flow rate was increased relative to the solids volumetric flow rate to generate flows with relatively low in-situ solids volume fractions. For each flow condition generated, the VDMS was operated at a relevant frequency obtained as described in section 8.4.1 and the data acquisition unit was then used to simultaneously measure the force and displacement signals from the VDMS and the differential pressure ΔP across a one meter axial length of the flow loop working section. Additionally, the reference instruments were used to measure the solids and water volumetric flow rates in the working section. For each flow condition used in the investigation, an average of either five or ten different measurements was taken

dependent upon specific flow condition, in order to minimize the random errors in the measurement. The measurement results obtained in this experiment are presented and discussed in section 8.4.2.

8.4.1 Flow conditions investigated using the VDMS and reference instruments to measure mixture density in solids-in-water vertically upward pipe flows

The flow conditions generated in this investigation were achieved using either a multiphase pump as a standalone pump or in combination with a single-phase pump (see
figure 6-2) depending on the in-situ volume fraction of solids required to be generated in the flow mixture. The flow rate of the solids-water mixture passing through the working section was adjusted by using one of the following three methods; (i) controlling the speed of the multiphase pump using a variable frequency drive (VFD), (ii) manually adjusting "valve 1" (see
figure 6-2), (iii) by combining both (i) and (ii). In this investigation, two operating sequences were used to generate flow conditions with either relatively low or high in-situ solids volume fraction. In order to generate flow conditions with relatively low in-situ solids volume fraction, where the water flow rate was required to be relatively high compared to the solids flow rate, method (i) was used. Conversely, to generate flow conditions with relatively high in-situ solids volume fraction, where the water flow rate was required to be relatively low compared with the solids flow rate, method (iii) was used. It was also important to determine an appropriate VDMS optimal operating frequency for each of the flow conditions generated, since the optimal operating frequency was required to obtain density measurements with minimal errors. From the magnitude ratio and phase difference results shown in figure 5-17 and figure 5-18 and obtained from the bench testing described in section 5.8 using solids-water mixture, an operating frequency range that was within $\pm 1\%$ of the VDMS resonant frequency was selected as 680rad/s to 693rad/s. This frequency range represents the resonant frequency obtained for solids-water mixture for test mixtures 6 and 7 (see table 5-3).

In order to reduce the number of measurements required to select an appropriate (optimal) VDMS operating frequency for a given flow condition used in this investigation, a decision was taken to firstly perform a preliminary test where the VDMS was operated at 680rad/s and 690rad/s and then the measured phase difference θ between the displacement and force signals obtained at these frequencies was used to estimate an optimal operating frequency by linear interpolation, where the phase difference of the VDMS response was predicted to be -90°. The VDMS operating frequencies obtained for the different flow conditions used in this investigation are presented in table 8-4.

Table 8-4: Flow conditions used in the investigation to obtain mixture density measurements using the VDMS and the reference instruments in solids-in-water vertically upward pipe flows

Flow condition number n	Flow condition name	VDMS operating frequency ω_{opt}(rad/s)	Water flow rate, $Q_{w,ref}$ (m^3/hr)	Solids flow rate, $Q_{s,ref}$ (m^3/hr)
1	FC_{sw}-1	687.44	10.95	0.18
2	FC_{sw}-2	687.20	15.88	1.35
3	FC_{sw}-3	687.92	10.23	0.25
4	FC_{sw}-4	686.72	7.15	0.20
5	FC_{sw}-5	685.76	10.24	0.50
6	FC_{sw}-6	685.59	6.44	0.55
7	FC_{sw}-7	685.13	6.27	0.54
8	FC_{sw}-8	682.16	6.05	0.53
9	FC_{sw}-9	681.92	6.27	0.54
10	FC_{sw}-10	682.10	6.44	0.55
11	FC_{sw}-11	685.16	5.69	0.50
12	FC_{sw}-12	685.35	6.09	0.53
13	FC_{sw}-13	682.16	5.69	0.50
14	FC_{sw}-14	684.84	6.05	0.53
15	FC_{sw}-15	681.95	6.09	0.53

8.4.2 Results obtained when the VDMS was used to predict the mixture density in solids-in-water vertically upward pipe flows for the range of flow conditions given in table 8-4

This section presents and discusses the results obtained when the VDMS and the reference instruments were used to measure, independently, the mixture density in solids-in-water vertically upward pipe flows for the flow conditions given in table 8-4. For each flow condition investigated, the force and displacement signals were acquired from the VDMS using the data acquisition unit and these measurements were then used to obtain ω, $\hat{a}$, $\hat{b}$ and λ using the signal processing technique described in section 4.5 and the relevant equations. The VDMS operating frequency ω and lambda λ values were then applied to the density prediction model given in equation 4-29 and equation 4-30 to compute the solids-in-water mixture density $\rho_{sw,m,n,i}$. Additionally, the differential pressure ΔP and water $Q_{w,ref}$ and solids $Q_{s,ref}$ volumetric flow rates were used to compute the frictional pressure loss F_m in the flow using equation 6-39. The frictional pressure loss F_m, differential pressure ΔP and reference water density $\rho_{w,ref}$ were then applied to equation 6-17 to compute the reference mixture density $\rho_{sw,ref,n,i}$ for the solids-in-water vertically upward flow. The predicted mixture density $\rho_{sw,m,n,i}$ and reference mixture density $\rho_{sw,ref,n,i}$ obtained for all the measurements taken in this investigation are shown in figure 8-12.

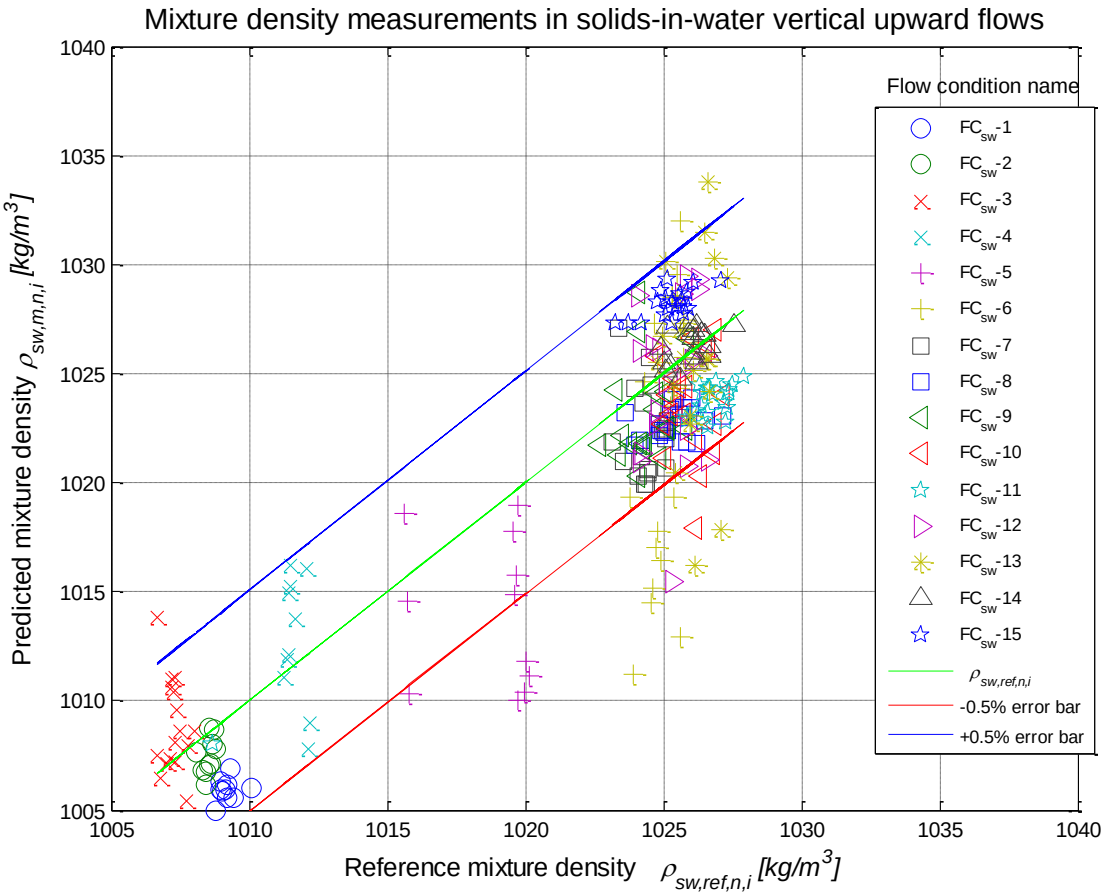

Figure 8-12: Mixture density measurements obtained using VDMS and reference instruments in solids-in-water vertically upward flows

In figure 8-12, the blue and red lines representing $+0.5\%$ and -0.5% error bars were computed using equation 8-7 and equation 8-8 respectively, whilst the different flow conditions investigated (see table 8-4) are represented by different plot colours and symbols.

$$+0.5\%\ \text{error bar} = 1.005 * \rho_{sw,ref,n,i} \qquad \text{Equation 8-7}$$

$$-0.5\%\ \text{error bar} = 0.995 * \rho_{sw,ref,n,i} \qquad \text{Equation 8-8}$$

From figure 8-12, it is apparent that the predicted mixture densities $\rho_{sw,m,n,i}$ obtained using the VDMS for the different flow conditions used in the investigation were mostly within $\pm 0.5\%$ of the reference density measurements apart from FC_{sw}-5, FC_{sw}-6 and FC_{sw}-10. Qualitatively, the results suggested that the VDMS gave relatively accurate estimates of the solids-water mixture density in the flow loop working section for the vast majority of the measurements taken. However,

the large scatters observed in the plots are also suggestive of the existence of large random errors in $\rho_{sw,m,n,i}$ which may be caused by the inhomogeneous solids-water mixtures in the working section. Thus, it was very likely that in the solids-water experiments the average mass of the solids-water mixture measured in the working section using the VDMS, for a given data acquisition period, may be inconsistent. It is observed in figure 8-12 that for a given flow condition the values of $\rho_{sw,m,n,i}$ varied more than $\rho_{sw,ref,n,i}$. For example, in FC_{sw}-3, the predicted mixture densities $\rho_{sw,m,n,i}$ varied between 1005kg/m^3 and 1014kg/m^3 whilst the reference mixture densities $\rho_{sw,ref,n}$ varied between 1006kg/m^3 and 1008kg/m^3. Qualitatively, the variation of the values of $\rho_{sw,m,n,i}$ and $\rho_{sw,ref,n,i}$ obtained for the different flow condition used in this investigation indicated that there is evidence of random error in the density measurements obtained using the VDMS and reference instrument. One way to reduce these random errors was by averaging all the measurements taken at a given flow condition. Thus, a mean of the predicted solids-water mixture density $\bar{\rho}_{sw,m,n}$ and a mean of the reference solids-water mixture density $\bar{\rho}_{sw,ref,n}$ were computed for each flow condition using equation 8-9 and equation 8-10 respectively.

$$\bar{\rho}_{sw,m,n} = \frac{\sum_{i=1}^{N}\left(\rho_{sw,m,n,i}\right)}{N} \qquad \text{Equation 8-9}$$

$$\bar{\rho}_{sw,ref,n} = \frac{\sum_{i=1}^{N}\left(\rho_{sw,ref,n,i}\right)}{N} \qquad \text{Equation 8-10}$$

where $\rho_{sw,m,n,i}$ represents the ith value of the measured solids-water mixture density obtained at the nth flow condition, $\rho_{sw,ref,n,i}$ represents the ith value of the reference solids-water mixture density obtained at the same flow condition and N is the total number of density measurements taken at each flow condition. Additionally, the mean values of Mr, θ, $\hat{a}$ and λ obtained for a given flow condition were computed using the generalized expression,

$$\bar{\Gamma} = \frac{\sum_{i=1}^{N}(\Gamma_i)}{N} \qquad \text{Equation 8-11}$$

where Γ_i represents the i[th] measurement of a parameter at a given flow condition and can either be θ, Mr, $\hat{a}$ or λ and $\bar{\Gamma}$ represents the mean value of the same parameter for a given flow condition. The values of $\bar{\rho}_{sw,m,n}$ and $\bar{\rho}_{sw,ref,n}$ obtained using equation 8-9 and equation 8-10 respectively, were then used to define a mean density ratio $\chi_{sw,m,n}$ at a given flow condition as follow,

$$\chi_{sw,m,n} = \frac{\bar{\rho}_{sw,m,n}}{\bar{\rho}_{sw,ref,n}} \qquad \text{Equation 8-12}$$

The results of $\chi_{sw,m,n}$ and the mean values of the density measurement parameters $\bar{\Gamma}$ are shown in figure 8-13 to figure 8-17.

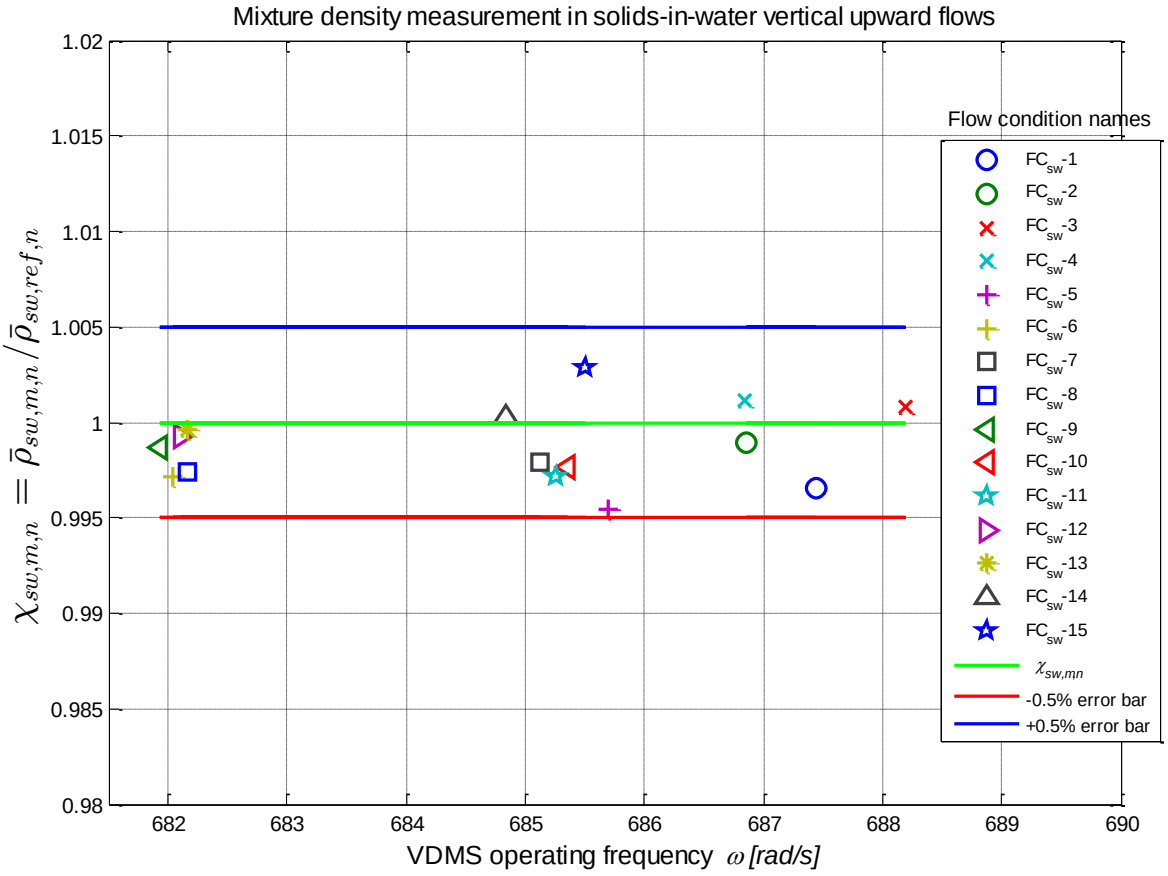

Figure 8-13: Solids-water mixture density ratio versus VDMS operating frequency obtained using VDMS and reference instruments in solids-in-water vertically upward pipe flows.

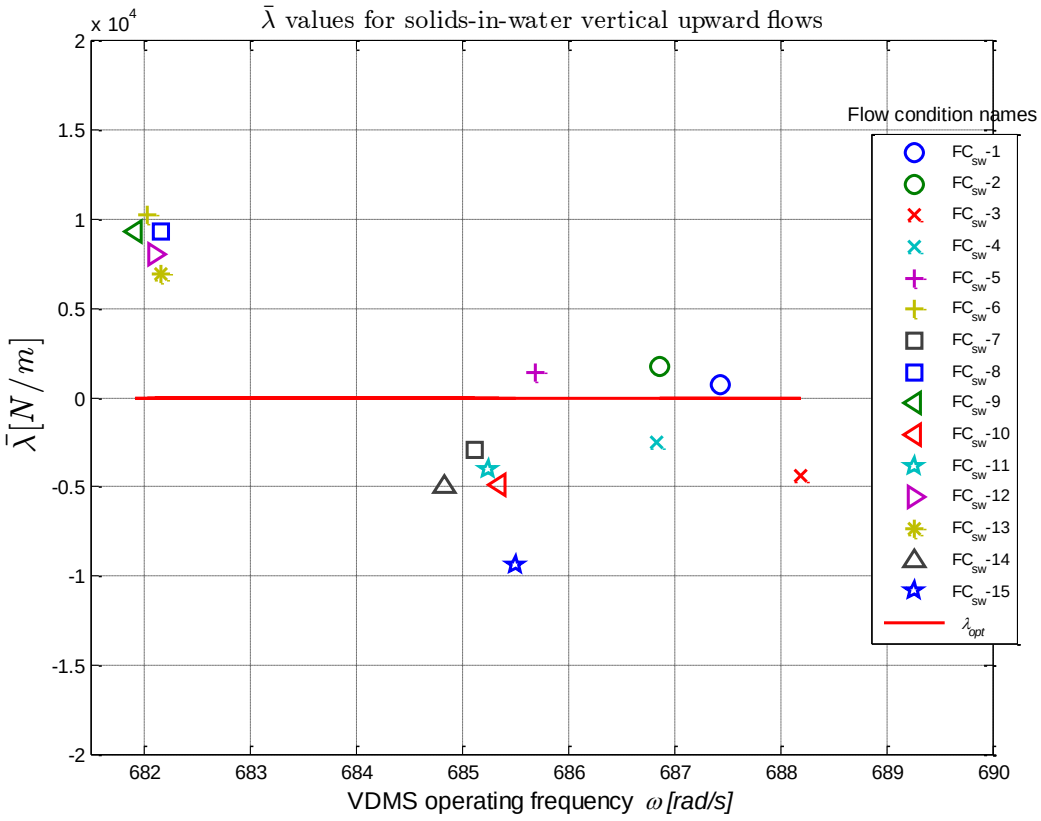

Figure 8-14: Mean lambda $\bar{\lambda}$ values versus VDMS operating frequency obtained using in solids-in-water vertically upward pipe flows

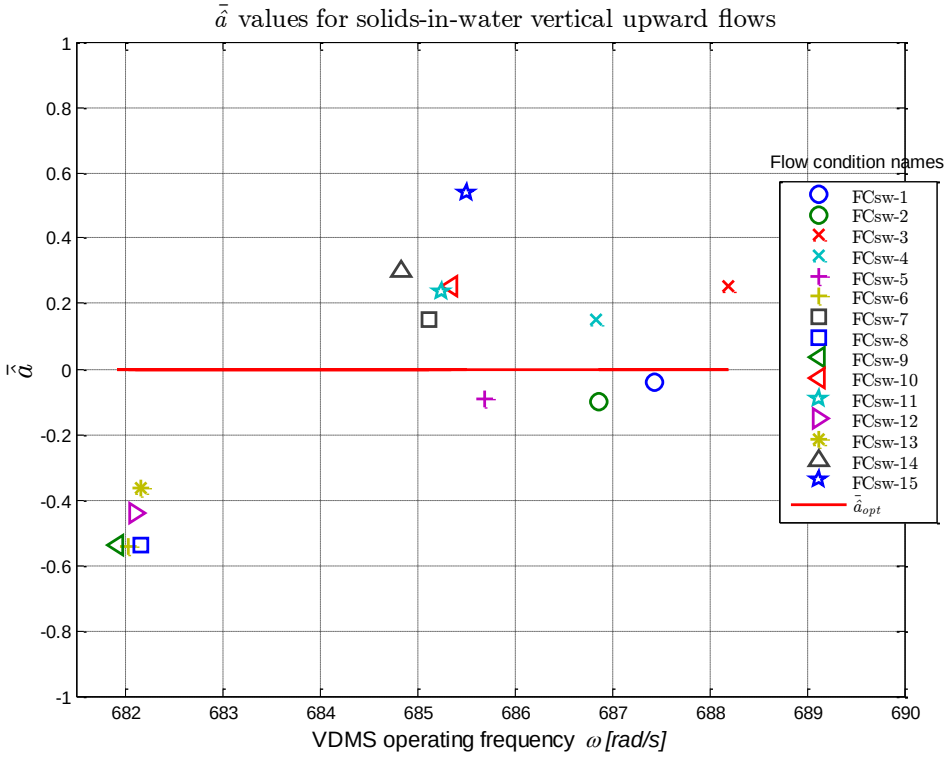

Figure 8-15: Mean $\hat{a}$ value versus VDMS operating frequency obtained using VDMS in solids-in-water vertically upward pipe flows

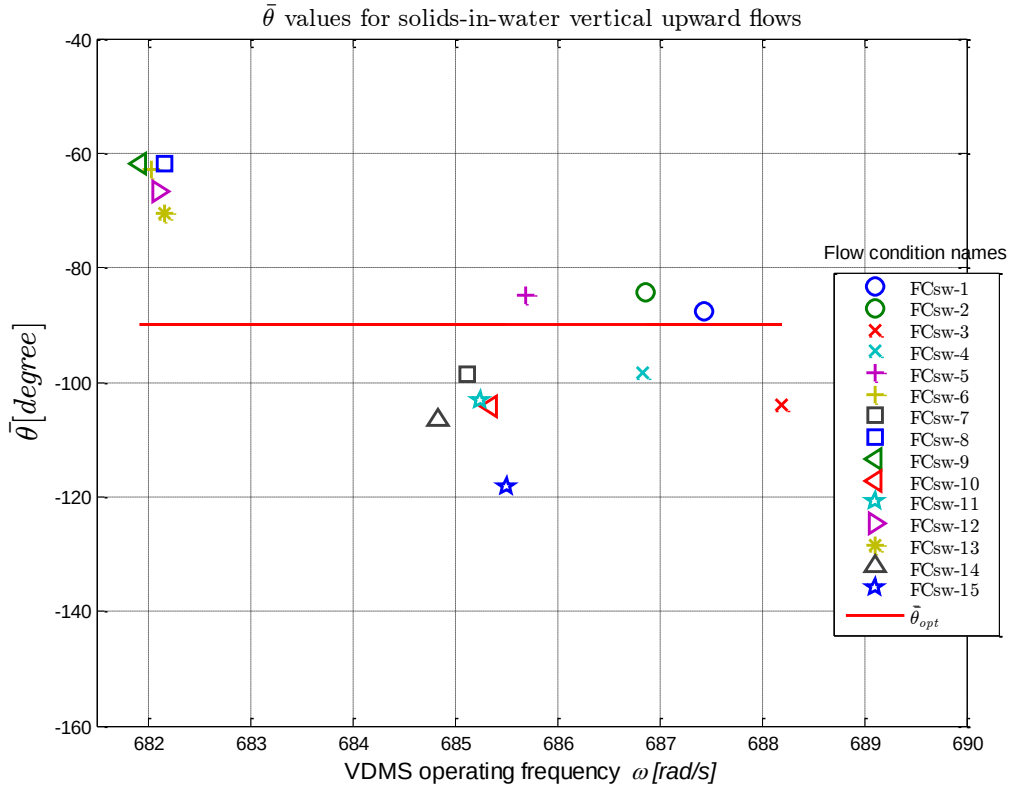

Figure 8-16: Mean values of the phase difference $\overline{\theta}$ versus VDMS operating frequency obtained using VDMS in solids-in-water vertically upward pipe flows

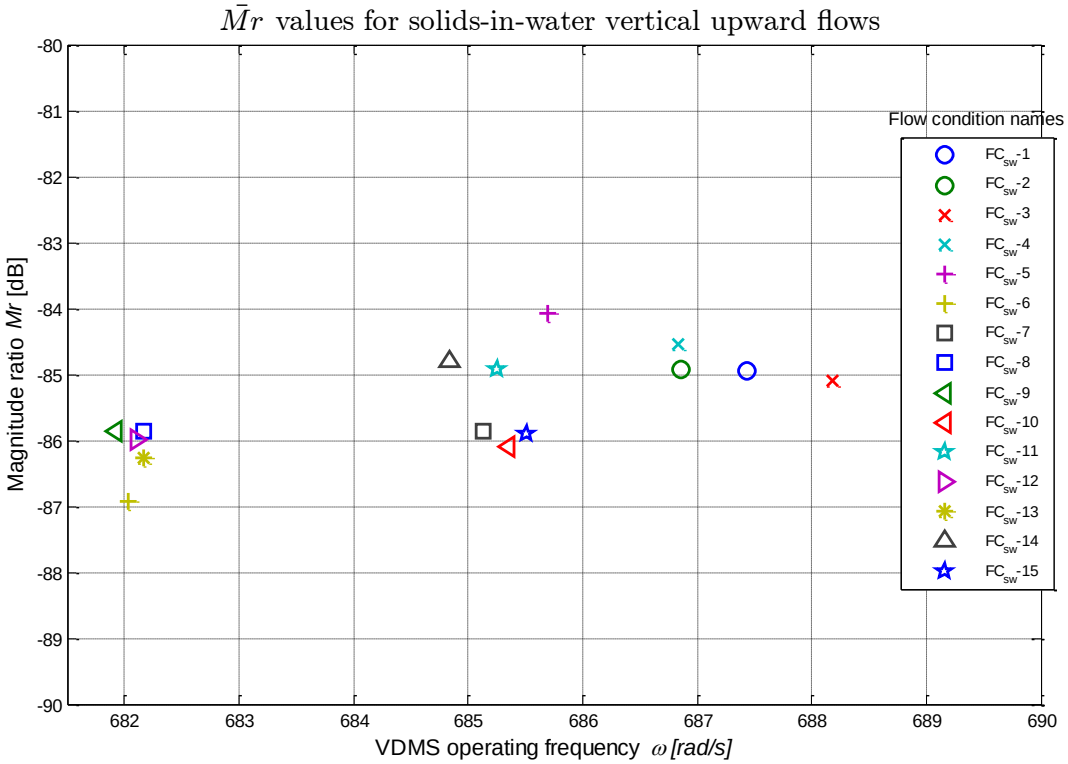

Figure 8-17: $\overline{Mr}$ versus VDMS operating frequency obtained using VDMS in solids-in-water vertically upward pipe flows

The plots in figure 8-13 to figure 8-17 provided a means to evaluate the suitability of the selected VDMS operating frequencies ω used in the different flow conditions in the solids-water experiments and its influence on the measurement errors in $\rho_{sw,m,n,i}$. In figure 8-13, the blue and red lines represent $+0.5\%$ and -0.5% error bars and were computed using equation 8-13 and equation 8-14 respectively. The error bars are defined by,

$$+0.5\%\ \text{error bar} = 1.005 * \chi_{sw,ref,n} \qquad \text{Equation 8-13}$$

$$-0.5\%\ \text{error bar} = 0.995 * \chi_{sw,ref,n} \qquad \text{Equation 8-14}$$

where $\chi_{sw,ref,n}$ represents a reference measurement where the ratio of mean mixture densities obtained using the VDMS and the reference instruments at a given flow condition is one. The results presented in figure 8-13 to figure 8-17 will now be discussed in order to understand the influence of the selected VDMS operating frequency on the accuracy of the predicted solids-water mixture density.

The magnitude ratio versus frequency plot shown in figure 8-17 contains insufficient information to be used as a "independent" result to determine whether the selected VDMS operating frequency ω was optimal for each flow condition investigated and to investigate the influence of ω on the errors in $\rho_{sw,m,n,i}$. In order to use figure 8-17 for this purpose, more than two density measurements will be required at frequencies around the resonant frequency for a given flow condition. However, the mean phase difference $\bar{\theta}$ versus frequency result shown in figure 8-16 can be used as a "independent" result to determine whether the selected VDMS operating frequency was optimal for a given flow condition and hence evaluate the influence of ω on the errors in $\rho_{sw,m,n,i}$. From figure 8-16, it is observed that $\bar{\theta}$ values for the solids-in-water flows investigated (see table 8-4) are noticeably different from the $\bar{\theta}_{opt}$ curve. The values of $\bar{\theta}$ vary between $-62°$ and $-118°$ which represents about $\pm 30\%$ deviation from $\bar{\theta}_{opt}$. In order to discuss the reason(s) for the seemingly large variation observed in the plot of $\bar{\theta}$ versus ω, it is expedient to restate two important results

obtained in sections 3.3 and 5.8.2. Firstly, it was shown in figure 3-3 that for a second order system with low damping properties, the system phase response will change very rapidly from 0° to $-180°$ at frequencies around ω_n and secondly, the VDMS frequency response plots obtained from bench testing using solids-water test mixtures (see figure 5-17 and figure 5-18) showed identical responses to figure 3-3 and thus suggested that the VDMS response can be correctly described as a modified second order system. In this investigation, visual observation of the solids-water mixture composition in the flow loop working section showed that the mixture volume composition was somewhat inhomogeneous and varied with time. The mixture composition became more inhomogeneous as the volume fraction of the dispersed solids phase was reduced relative to the continuous water phase and this may have caused the mass of the mixture in the working section to vary with time. Since the selected VDMS operating frequencies for the flow conditions used in this investigation (see table 8-4) were obtained by linear interpolation of the θ value obtained from preliminary tests conducted at 680rad/s and 690rad/s, it is very likely that changes in the volume composition of the solids-water mixture in the working section may have resulted in changes to the flow mixture mass and hence the resonant frequency associated with the flows. Change to the flow resonant frequency will cause the VDMS operating frequency to deviate from the actual ω_{opt} which could have caused θ to change rapidly and significantly from the value of $-90°$ predicted from the preliminary tests. This probably explains the reason for the large deviation of $\bar{\theta}$ from $\bar{\theta}_{opt}$ observed in figure 8-16. A theoretical analysis to evaluate the effect of errors in $\bar{\theta}$ on the predicted solids-water mixture density was therefore carried out using equation 4-29 and equation 4-30 and the average values of ω, θ and Mr obtained from FC_{sw}-1 experiments. It was found from the theoretical analysis that variation in θ between $\pm 30\%$ from θ_{opt} will result in a maximum error of $\pm 1.13\%$ in the predicted density. The analysis result further indicates that the density prediction model developed in equation 4-29 and equation 4-30 was very robust.

The results of the mean values of λ and $\hat{a}$ versus frequency shown in figure 8-7 and figure 8-8 shows similarity with the result of $\bar{\theta}$ versus frequency. Inspection of figure 8-7 and figure 8-8 shows appreciable deviations of λ and $\hat{a}$ from zero which is indicative of their dependance on θ. The mean lambda values $\bar{\lambda}$ were between ± 9000 and the $\bar{\hat{a}}$ values were between ± 0.5. From figure 8-13, the ratio of the mean densities $\chi_{sw,m,n}$ obtained using the VDMS and reference instruments is observed to be less than one for all of the flow conditions used in this investigation apart from FC_{sw}-3, FC_{sw} -4, FC_{sw} -14 and FC_{sw} -15. When $\chi_{sw,m,n}$ is less than one, the result suggests that $\bar{\rho}_{sw,m,n}$ is underestimated with respect to the reference density and when $\chi_{sw,m,n}$ is greater than one, $\bar{\rho}_{sw,m,n}$ is overestimated with respect to the reference density. Further statistical analysis was required to establish a basis for quantitative comparison between the mixture density measurements obtained using the VDMS and the reference instruments. This analysis and the results obtained are presented and discussed in section 8.4.3.

8.4.3 Comparison of mixture density measurements obtained using VDMS and reference instruments in solids-in-water vertically upward pipe flows

In this section, a quantitative comparison of the mixture density measurements obtained from the VDMS and the reference instruments is presented. A percentage relative error $e_{sw,n,i}$ was computed for the i^{th} density measurement taken at the n^{th} flow condition. This was computed using an expression similar to equation 8-2 and required the predicted solids-water mixture density $\rho_{sw,m,n,i}$ obtained using the VDMS and the reference mixture density $\rho_{sw,ref,n,i}$ obtained using the reference instruments. The $e_{sw,n,i}$ values were then used to compute the mean errors $\bar{e}_{sw,n}$ and the standard deviation $S_{sw,n}$ of the errors in $\rho_{sw,m,n,i}$ obtained at the n^{th} flow condition using expressions similar to equation 8-3 and equation 8-4. These two statistical tools were used to quantitatively describe the systematic measurement errors and random measurement errors

respectively. For each flow condition given in table 8-4, the values for $\bar{e}_{sw,n}$ and $S_{sw,n}$ obtained for the solids-in-water experiments are presented in figure 8-18.

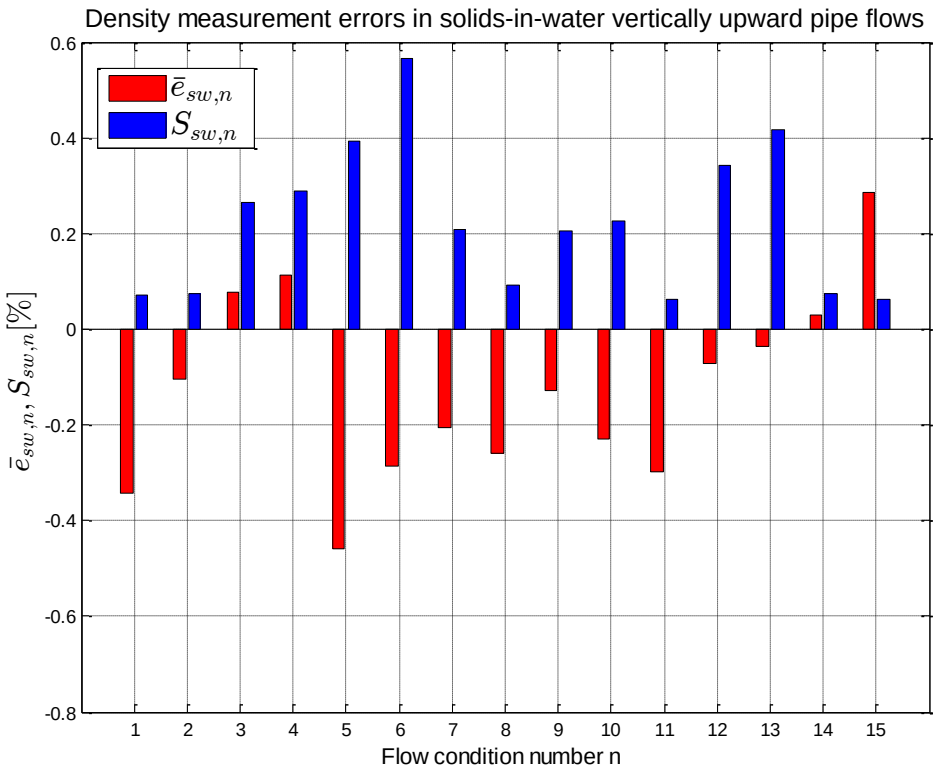

Figure 8-18: Bar graph of mean error and standard deviation of errors in measured mixture density when VDMS was used in solids-in-water vertically upward pipe flows

Qualitatively, the mean error results presented in figure 8-18 shows similarity with the results of $\chi_{sw,m,n}$ versus ω shown in figure 8-13. It is observed that for the different flow conditions used in this investigation, the mean error $\bar{e}_{sw,n}$ in $\rho_{sw,m,n,i}$ relative to $\rho_{sw,ref,n,i}$ is negative for all the flow conditions with the exceptions of FC_{sw}-3, FC_{sw}-4, FC_{sw}-14 and FC_{sw}-15, which also corresponds to the flow conditions where $\chi_{sw,m,n}$ was greater than one. A positive $\bar{e}_{sw,n}$ value is indicative of a positive offset in the systematic error and conversely, a negative $\bar{e}_{sw,n}$ value indicates a negative offset in the systematic error. The results in figure 8-18 where $\bar{e}_{sw,n}$ is positive thus suggests that $\rho_{sw,m,n,i}$ may have been overestimated with reference to $\rho_{sw,ref,n,i}$ at a given flow condition and similarly $\rho_{sw,m,n,i}$ may have been underestimated with reference to $\rho_{sw,ref,n,i}$ when $\bar{e}_{sw,n}$ is negative. In the solids-in-water experiments, the values of $\bar{e}_{sw,n}$ varied between

-0.46% and $+0.29\%$ for all the flow conditions investigated. The largest $\bar{e}_{sw,n}$ value was -0.46% at FC_{sw}-5 while the smallest $\bar{e}_{sw,n}$ value was -0.03% and 0.03% at FC_{sw}-13 and FC_{sw}-14 respectively. The largest and smallest standard deviation $S_{sw,n}$ of the errors in $\rho_{sw,m,n,i}$ were observed at FC_{sw}-6 and FC_{sw}-13 as 0.57% and 0.06% respectively.

In order to properly understand the source(s) of the mean errors $\bar{e}_{sw,n}$ shown in figure 8-18, it was important to critically analyse the method for obtaining $\rho_{sw,m,n,i}$ and $\rho_{sw,ref,m,n,i}$ since these measurements were used to compute $e_{sw,n,i}$ which was in turn used to compute $\bar{e}_{sw,n}$. From the density prediction model given in equation 4-29 and equation 4-30, it is seen that $\rho_{sw,m,n,i}$ is dependent upon accurate measurement of ω, β, K_1 and λ. The sensing pipe stiffness K_1 and β are constant variables that respectively describes the sensing pipe resistance to an applied force and its frequency characteristic due to its "fixed end" supports (section 5.3.2). In this investigation, it was unlikely that K_1 and β caused random variation in $\rho_{sw,m,n,i}$. However, it cannot be completely ruled out that the values of K_1 and β obtained in section 5.3.2 and 5.8.2 respectively, may contain errors and that K_1 may also be affected by temperature variations in the sensing pipe, although the experiments were performed in a temperature regulated environment and care was taken to ensure the temperature of the flow mixture was uniform before measurements were taken. Conversely, ω and λ were both obtained from the measured force and displacement signals as described in section 4.5. Since accurate measurement of the λ value is dependent on accurate measurement of the force and displacement signals at the relevant optimal VDMS operating frequency and given that considerable variation existed in the volume composition of the solids-water mixture in the flow loop working section during this investigation, which caused noticeable deviation of ω from ω_{opt}, it is plausible that the errors associated with the measured force and displacement signals were not minimized in all of the measurements taken in this investigation and hence the solids-water mixture density.

Additionally, equation 6-17 shows that $\rho_{sw,ref,n,i}$ is dependent on accurate measurement of the frictional pressure loss F_m of the flowing mixture and the differential pressure ΔP across a one metre axial length of the working section. In this experiment, the differential pressure was computed using the output signal from the DP sensor current-to-voltage converter circuit (see section 6.5.1) while the frictional pressure loss F_m was estimated using the Fanning friction factor f_F and the homogeneous solids-in-water mixture flow velocity $u_{h(sw)}$ obtained using the gravimetric measurement system (see section 6.8). It is therefore possible that the reference mixture density measurements $\rho_{sw,ref,n,i}$ obtained using equation 6-17 may cause significant measurement errors if F_m and ΔP are either overestimated or underestimated for the flow. Notably, variation in the average mass of the solids-in-water mixture flowing through the working section can cause the measured differential pressure to vary and so may introduce errors in the measurement. However, investigation of the variation in ΔP on the measurement accuracy for solids-in-water flows, showed that this error is probably insignificant. At present, this is the best reference mixture density measurement system available for two-phase solids-in-water flow experiments.

Lastly, the overall mean error $\bar{e}_{sw,t}$ and the standard deviation $S_{sw,t}$ of the errors in $\rho_{sw,m,n,i}$ were computed for all the measurements taken in the solids-water flow experiments using expressions similar to equation 8-5 and equation 8-6 respectively as -0.12% and 0.33%. These $\bar{e}_{sw,t}$ and $S_{sw,t}$ values indicate that the VDMS density measurements agree well with the reference density measurements and were also repeatable and reliable. From the results presented in this section, it can be concluded that the VDMS can be used to provide accurate and reliable two phase solids-water mixture density measurements for flows similar to the type used in this investigation.

8.5 Mean in-situ solids volume fraction measurement obtained using the VDMS and reference instruments in solids-in-water vertically upward pipe flows

Once the VDMS had been used to predict the mixture density in solids-in-water flows, its capability was extended to predict in-situ solids volume fraction. This section describes the results obtained when the VDMS and the reference instruments were used to independently obtain solids volume fraction measurements in two phase, solids-in-water vertically upward pipe flows, where solid particles formed the dispersed phase and water formed the continuous phase. These measurements can be used to provide information on the respective phase volume fractions in a two phase flow. For example, solids volume fraction is an important measurement to ensure efficient sewage sludge treatment. It is also important in pulp processing and hydraulic transportation of solids in the mining and paper production industries.

8.5.1 Mean in-situ solids volume fraction measurement results obtained using VDMS and reference instruments in solids-in-water vertically upward pipe flows

A major intention of this investigation was to extend the operation of the VDMS to measure the mean in-situ solids volume fraction in flows where the solids-water mixture was homogeneous. In this investigation, however, the homogeneity of the flow mixture in the flow loop working section often varied considerably with time at specific flow conditions (mainly flows with relatively low solids volume composition). The expression given in equation 6-15 was adopted to derive an expression to compute the predicted solids volume fraction $\alpha_{s,m,n,i}$ for the ith measurement taken at a given flow condition as follows,

$$\alpha_{s,m,n,i} = \frac{\rho_{sw,m,n,i} - \rho_{w,ref}}{\rho_{s,ref} - \rho_{w,ref}} \qquad \text{Equation 8-15}$$

where $\rho_{sw,m,n,i}$ is the ith value of the measured solids-water mixture density obtained at the nth flow condition, $\rho_{s,ref}$ is the reference density of the solids and $\rho_{w,ref}$ is the reference water density. The value of $\rho_{s,ref}$ used in this investigation was 1340kg/m^3 and $\rho_{w,ref}$ was obtained as described

in section 8.2. In the current research, the values of $\alpha_{s,m,n,i}$ obtained for a given flow condition was computed using equation 8-15. Additionally, an expression for computing the reference solids volume fraction, previously derived in equation 6-16, was used in this section to compute $\alpha_{s,ref,n,i}$. The expression used the estimated frictional pressure loss F_m of the flow in the working section, the differential pressure ΔP measured across an axial length L of one meter in the working section, the acceleration of gravity g, the reference solids density $\rho_{s,ref}$ and the reference water density $\rho_{w,ref}$ to compute $\alpha_{s,ref,n,i}$ for a given measurement. The values of $\alpha_{s,m,n,i}$ and $\alpha_{s,ref,n,i}$ were respectively used to compute the mean values of $\bar{\alpha}_{s,m,n}$ the predicted solids volume fraction and $\bar{\alpha}_{s,ref,n}$ the reference solids volume fraction at each flow condition, using the relationships

$$\bar{\alpha}_{s,m,n} = \frac{\sum_{i=1}^{N} \alpha_{s,m,n,i}}{N}$$ Equation 8-16

$$\bar{\alpha}_{s,ref,n} = \frac{\sum_{i=1}^{N} \alpha_{s,ref,n,i}}{N}$$ Equation 8-17

where $\alpha_{s,m,n,i}$ represents the ith measured solids volume fraction at a given flow condition and $\alpha_{s,ref,n,i}$ represents the ith reference solids volume fraction at the given flow condition. N represents the total number of measurements made at each flow condition. The values of $\bar{\alpha}_{s,m,n}$ and $\bar{\alpha}_{s,ref,n}$ were computed in this work using equation 8-16 and equation 8-17 and the results obtained are shown in figure 8-19.

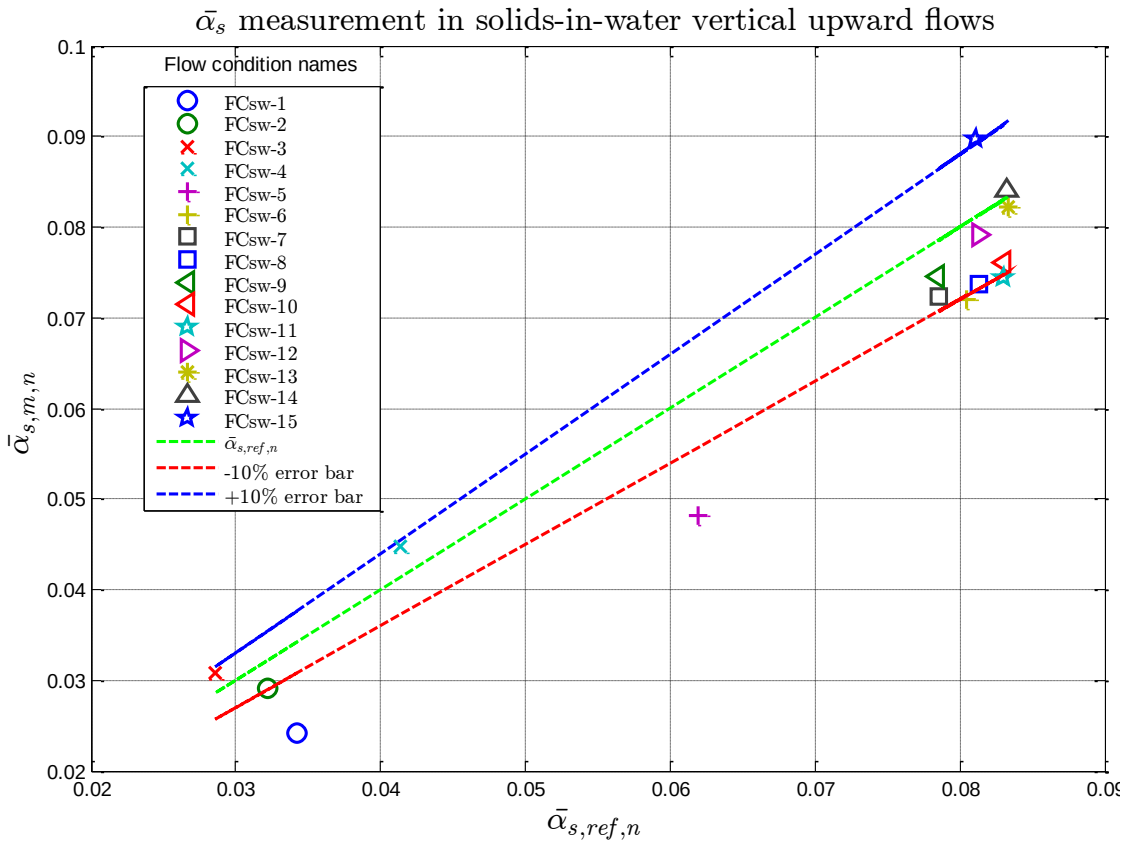

Figure 8-19: Mean solids volume fraction measurements acquired using the VDMS and the reference instruments in solids-in-water vertically upward pipe flow at 15 different flow conditions

In figure 8-19, the values of $\bar{\alpha}_{s,m,n}$ and $\bar{\alpha}_{s,ref,n}$ were computed for the flow conditions given in table 8-4 and these flow conditions are represented by different plot colours and symbols in the legend. The blue and red dashed lines represent the $+10\%$ and -10% error bars respectively in figure 8-19 and were obtained as follows,

$$+10\% \text{ error bars} = 1.1 * \bar{\alpha}_{s,ref,n} \qquad \text{Equation 8-18}$$

$$-10\% \text{ error bars} = 0.90 * \bar{\alpha}_{s,ref,n} \qquad \text{Equation 8-19}$$

From figure 8-19, it is observed that $\bar{\alpha}_{s,m,n}$ is consistently within $+10\%$ and -10% of $\bar{\alpha}_{s,ref,n}$ for the fifteen flow conditions used in the investigation with the exceptions of FC_{sw}-1 and FC_{sw}-5. Qualitatively, the results suggest that the mean in-situ solids volume fractions obtained, independently, using the VDMS and reference instruments were indeed representative of the true mean solids volume fractions which existed in the solids-water mixtures flowing through the

working section. The results show that $\bar{\alpha}_{s,m,n}$ was below the $\bar{\alpha}_{s,ref,n}$ curve for all of the flow conditions investigated with the exceptions of FC_{sw}-3, FC_{sw}-4, FC_{sw}-14 and FC_{sw}-15. This result suggests that $\bar{\alpha}_{s,m,n}$ may have been underestimated relative to $\bar{\alpha}_{s,ref,n}$ in all of the flow conditions investigated except FC_{sw}-3, FC_{sw}-4, FC_{sw}-14 and FC_{sw}-15 where $\bar{\alpha}_{s,m,n}$ may have been overestimated relative to $\bar{\alpha}_{s,ref,n}$.

The similarity of this result to that of the mean errors $\bar{e}_{sw,n}$ in $\bar{\rho}_{sw,m,n}$, presented in figure 8-18, shows the dependence of $\bar{\alpha}_{s,m,n}$ on $\rho_{sw,m,n,i}$. For the solids-water experiments where the solids volume fraction in the mixture was greater than 6.5% (see table 8-4), it was visually observed that the homogeneity of the components of the flow mixture in the working section was much more uniformly distributed across the pipe cross sectional area when compared with flows where the solids volume fraction in the flow mixture was less than 6.5%. Thus, FC_{sw}-1 to FC_{sw}-5 which, denote the flow conditions where the solids volume fraction was less than 6.5% shows much larger deviations in $\bar{\alpha}_{s,m,n}$ from $\bar{\alpha}_{s,ref,n}$. The result generally suggests that the accuracy of $\bar{\alpha}_{s,m,n}$ may improve if the homogeneity of the flow mixture varies less with time. Quantitative analysis of the systematic and random errors in $\bar{\alpha}_{s,m,n}$ for a given flow condition are presented in section 8.5.2. These measurements provided a statistical tool for analysing the accuracy and reliability of the $\bar{\alpha}_{s,m,n}$ and $\bar{\alpha}_{s,ref,n}$ measurements obtained using the VDMS and the reference instruments respectively.

8.5.2 Comparison of the mean solids volume fraction measurement results acquired using the VDMS and the reference instruments in solids-in-water vertically upward pipe flows

In order to quantitatively compare the mean phase volume fraction measurement results obtained using the VDMS and the reference instruments in the two-phase, vertically upward pipe flows used in this research, a relative percentage error $e_{q,n,i}$ was computed for the i^{th} dispersed phase

volume fraction $\alpha_{q,m,n,i}$ measurement taken at a given flow condition using the generalised expression,

$$e_{q,n,i} = \frac{\alpha_{q,m,n,i} - \alpha_{q,ref,n,i}}{\alpha_{q,ref,n,i}} \times 100 \qquad \text{Equation 8-20}$$

where $\alpha_{q,m,n,i}$ represents the ith measured volume fraction of the dispersed q phase obtained at a given flow condition and $\alpha_{q,ref,n,i}$ represents the ith reference volume fraction of the dispersed q phase and at the same flow condition. The symbol q which denote the measured dispersed phase was either "s" for solids phase or "a" for gas phase. Equation 8-20 was used in this thesis to compute the error $e_{q,n,i}$ in the ith measured dispersed phase volume fraction at a given flow condition in solids-in-water and air-in-water experiments. The value of $e_{q,n,i}$ was in turn used to compute the mean error $\bar{e}_{q,n}$ and the standard deviation $S_{q,n}$ of the errors in $\alpha_{q,m,n,i}$ using expressions similar to equation 8-3 and equation 8-4 and replacing x with q.

For the solids-in-water experiments described in this thesis, the value of the error $e_{s,n,i}$ in the ith measured solids volume fraction $\alpha_{s,m,n,i}$ measurement taken at a given flow condition was computed using equation 8-20 whilst the mean error $\bar{e}_{s,n}$ and standard deviation $S_{s,n}$ of the errors in $\alpha_{s,m,n,i}$ at the same flow condition were computed using equation 8-3 and equation 8-4 and are shown in table 8-5.

Table 8-5: Mean error and standard deviation of error when the VDMS and the reference instruments were used to predict the solids volume fraction $\alpha_{s,m,n,i}$ in solids-in-water vertically upward pipe flows

Flow condition number, n	Flow condition name	Mean solids volume fraction [%]	$\bar{e}_{s,n}$ Mean error [%]	$S_{s,n}$ Standard deviation of error [%]
1	FC_{sw}-1	2.41%	-29.49%	5.67%
2	FC_{sw}-2	2.91%	-9.49%	6.89%
3	FC_{sw}-3	3.09%	8.35%	27.74%
4	FC_{sw}-4	4.47%	8.30%	20.32%
5	FC_{sw}-5	4.82%	-21.19%	18.53%
6	FC_{sw}-6	7.20%	-10.81%	21.21%
7	FC_{sw}-7	7.24%	-7.77%	7.93%
8	FC_{sw}-8	7.36%	-9.46%	3.16%
9	FC_{sw}-9	7.46%	-4.84%	7.88%
10	FC_{sw}-10	7.61%	-8.26%	8.06%
11	FC_{sw}-11	7.65%	-10.45%	2.18%
12	FC_{sw}-12	7.92%	-2.55%	12.63%
13	FC_{sw}-13	8.23%	-1.21%	14.89%
14	FC_{sw}-14	8.41%	1.11%	2.70%
15	FC_{sw}-15	8.96%	10.62%	2.56%

The result in table 8-5 suggests evidence of a relatively large random error in $\bar{\alpha}_{s,m,n}$ obtained using the VDMS. The values of $\bar{e}_{s,n}$ and $S_{s,n}$ vary between -29.49% and 10.62% and 2.18% and 27.24% respectively for the flow conditions used in the solids-water experiment. It can be seen that absolute value of the largest mean error $|\bar{e}_{s,n}|$ in $\bar{\alpha}_{s,m,n}$ was 29.49% at FC_{sw}-1 whilst the absolute value of the smallest mean error $|\bar{e}_{s,n}|$ in $\bar{\alpha}_{s,m,n}$ was 1.11% at FC_{sw}-14. Additionally, FC_{sw}-3 has the largest standard deviation $S_{s,n}$ of the errors in $\bar{\alpha}_{s,m,n}$ of 27.74% whilst FC_{sw}-11 has the smallest standard deviation $S_{s,n}$ of the relative errors in $\bar{\alpha}_{s,m,n}$ of 2.18%. It is important to state here that the mean errors $\bar{e}_{s,n}$ in $\bar{\alpha}_{s,m,n}$ presented in table 8-5 are heavily reliant on the accuracy of

the values of $\rho_{sw,m,n,i}$ and $\rho_{sw,ref,n,i}$ obtained using the VDMS and the reference instruments respectively, hence the discussion presented in section 8.4.2 on the source(s) of errors in $\rho_{sw,m,n,i}$ and $\rho_{sw,ref,n,i}$ is also applicable to $\alpha_{s,m,n,i}$. The relatively large values of $\bar{e}_{s,n}$ and $S_{s,n}$ observed in table 8-5 indicates that further improvement is required in order to use the VDMS to obtain accurate and reliable $\bar{\alpha}_{s,m,n}$ measurement in solids-in-water flows. However, it is worth mentioning that $\bar{e}_{s,n}$ obtained in this investigation compares very nicely with the results obtained by Muhamedsalih [1] using an impedance cross correlation ICC flow meter for similar flow types.

8.6 Density measurements obtained using the VDMS and reference instruments in bubbly air-in-water vertically upward pipe flows

As part of a series of experiments that were conducted in this research work to investigate the capability of of the VDMS to accurately predict the mixture density of multiphase flows, it was also used in air-in-water vertically upward pipe flows, where air bubbles formed the dispersed phase and water formed the continuous phase. This section presents a description of the experiments conducted and a discussion of the results obtained. In this experiment, a single phase centrifugal pump was used to pump "water only" from the water reservoir through the flow loop while air was introduced into the base of the flow loop working section (see
figure 6-2). The air bubbles were introduced in the working section from four equally spaced inlet points that were 1m upstream of the VDMS (12 times the diameter of the VDMS) to ensure the good homogeneity of the air-water mixture during measurements. The volumetric flow rate of water in the working section was measured using the turbine flow meter while the air volumetric flow rate was computed using the technique described in section 6.7.1. Different flow conditions were generated in this experiment by adjusting the volumetric flow rate of water and/or air in the flow loop working section. These flow conditions are described in section 8.6.1. Additionally, the connections of the pressure lines to the DP sensor (as shown in figure 6-7) were reversed to ensure

the frictional pressure loss F_m of the flow was correctly measured. The computer based VDMS control system described in chapter 7 was used in this experiment (i) to generate an excitation signal that was sent to the VCA coil, (ii) to determine the optimal operating frequency and (iii) to obtain mixture density measurements. Before measurements were taken in this investigation, the DP sensor pressure lines were flushed with water to ensure no air was trapped. During experimentation, air-in-water flow was generated and circulated in the flow loop for an average of 20 minutes to ensure homogeneity of the flow mixture and uniformity of the flow temperature. Next, the data acquisition unit settings and amplitude of the VCA excitation signal were defined via the user interface of the computer based VDMS control system (see Appendix F). The control system was then used to generate an excitation signal that was sent to the VCA coil. The control system uses a "proportional plus integral" PI controller to determine the optimal VDMS operating frequency as described in section 7.5.3. The proportional gain and integral time of the controller were automatically determined by the PI controller "auto-tune" feature. Once the controller output was steady, the control system was used to save the force, displacement, temperature, VCA coil current and differential pressure signals to a measurement file. The predicted mixture density and reference mixture density were also computed online and saved to a measurement file. Unlike in the previous experiments to measure density in "water only" and solids-in-water flows where the VDMS was operated over a range of frequency in order to determine an optimal frequency to operate the VDMS at a given flow condition, the computer based VDMS control system used in the air-in-water experiment offers the advantage that it is able to automatically compute the optimal frequency to operate the VDMS using the frequency control system and hence significantly reduces the time required to complete an experiment. In this investigation, an average of five measurements was taken at each flow condition.

8.6.1 Flow conditions investigated

The flow conditions used in this experiment were generated by varying the flow rates of water and air flowing through the working section of the flow loop. The total flow rate of the air-water mixture in the flow loop working section was varied by either adjusting "valve 1" to change the water flow rate or by adjusting the air valve or air pressure regulator to change the air flow rate (see

figure 6-2). Eleven different flow conditions with varying compositions of air and water, of which ten were in the bubbly flow regime and one in the slug flow regime, were generated for this investigation and these flow conditions are shown in table 8-6.

Table 8-6: Flow conditions used in air- in-water flow experiment

Flow condition number, n	Flow condition name	Water flow rate $Q_{w,ref}$ [m^3/hr]	Air flow rate $Q_{a,ref}$ [m^3/hr]	VDMS operating freq. ω_{opt} [rad/s]	Reference air-water mixture density $\rho_{aw,ref,n}$ [kgm^{-3}]	Reference air volume fraction in mixture $\alpha_{a,ref,n}$ [%]
1	FC_{aw}-1	15.47	0.10	689.11	997.00	0.1
2	FC_{aw}-2	15.09	0.32	691.27	985.74	1.2
3	FC_{aw}-3	15.47	0.48	692.70	977.62	2.0
4	FC_{aw}-4	3.66	0.16	696.82	958.97	3.9
5	FC_{aw}-5	15.47	1.18	701.58	936.77	6.1
6	FC_{aw}-6	9.39	0.79	704.91	920.69	7.7
7	FC_{aw}-7	9.39	1.01	709.63	901.14	9.7
8	FC_{aw}-8	7.16	1.25	714.56	876.94	12.1
9	FC_{aw}-9	8.47	1.32	716.92	867.74	13.0
10	FC_{aw}-10	12.94	2.29	718.67	857.50	14.1
11	FC_{aw}-11	9.44	2.91	754.77	772.07	22.6

8.6.2 Measurement results obtained when the VDMS and the reference instruments were used to predict the mixture density in air-in-water vertically upward pipe flows

This section presents a discussion of the measurement results obtained using the VDMS and the reference instruments to obtain mixture density in air-in-water flows. For all of the experiments conducted using the flow conditions given in table 8-6, the computer based VDMS control system was used to obtain the following measurements; (i) a frequency, force and displacement data which were applied to the signal processing technique to compute the predicted mixture density offline, (ii) differential pressure and water flow rate data to compute the reference mixture density offline and (iii) predicted and reference mixture densities that were computed online. The online program routine for computing the mixture density has been described in section 7.5.4. The results of the mixture density measurements obtained using the VDMS and the reference instruments are shown in figure 8-20. Note that the density measurement results in figure 8-20 include $\rho_{aw,m,n,i}$ computed offline and online.

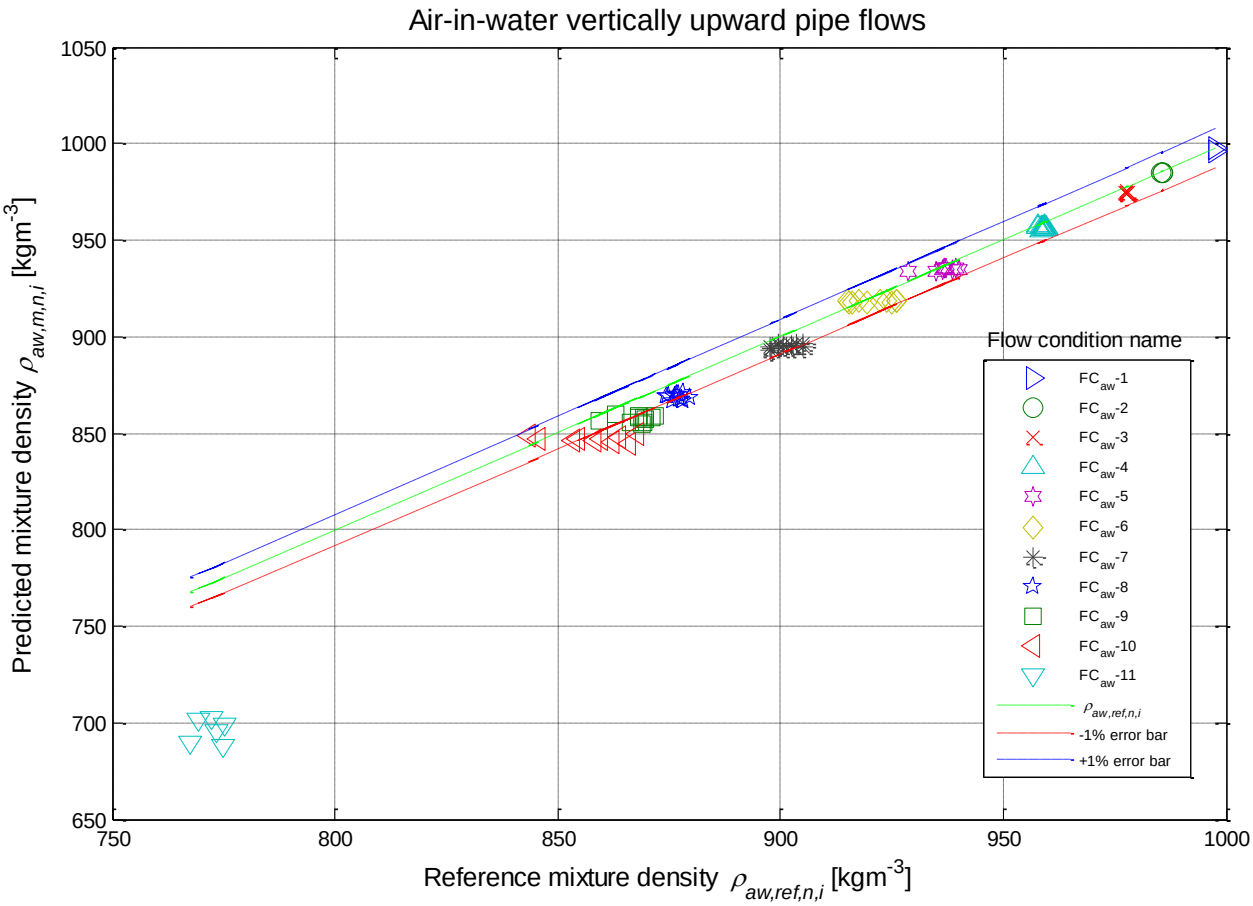

Figure 8-20: Mixture density measurements acquired using the VDMS and the reference instruments in air-in-water vertically upward pipe flow

In figure 8-20, the different flow conditions used in the investigation (see table 8-6) are represented by different colours and symbols in the legend whilst the blue and red dashed lines represents $+1\%$ and -1% error bars respectively, and were computed as follows,

$$+1\%\ \text{error bar} = 1.01 * \rho_{aw,ref,n,i} \qquad \text{Equation 8-21}$$

$$-1\%\ \text{error bar} = 0.99 * \rho_{aw,ref,n,i} \qquad \text{Equation 8-22}$$

where $\rho_{aw,ref,n,i}$ is the ith reference mixture density obtained at a given flow condition in air-in-water flow and was computed using equation 6-22 (see section 6.5). From figure 8-20, it is seen that the vast majority of the predicted mixture density $\rho_{aw,m,n,i}$ values obtained using the VDMS, for the flow conditions investigated, were consistently within the $\pm 1\%$ error bars with the exception of FC$_{aw}$-11. Quantitatively, the $\rho_{aw,m,n,i}$ values obtained are observed to be in good

agreement with the $\rho_{aw,ref,n,i}$ reference density and are tightly clustered for all density measurements taken for a given flow condition with the exception of FC_{aw}-11. Visual observation of the results in figure 8-20 shows that the mixture density obtained in FC_{aw}-1 to FC_{aw}-4, with mixture density between 1000kg/m^3 to 950kg/m^3, are on the green plot representing the reference mixture densities at the different flow conditions and these results are also very tightly clustered. The results suggest that for these flow conditions (FC_{aw}-1 to FC_{aw}-4), the computer based VDMS control system gave an accurate estimate of the air-water mixture density in the flow loop working section relative to the reference density. It is also observed that as the mixture density of the flow was reduced below 950kg/m^3, the values of $\rho_{aw,m,n,i}$ show an increasing deviation from the reference $\rho_{aw,ref,n,i}$ plot (see figure 8-20) towards the -1% error bar. A majority of the measured values of $\rho_{aw,m,n,i}$ are observed to be outside the -1% error bar when the flow mixture density was less than 900kg/m^3. Generally, the results also show an increased scatter in the values of $\rho_{aw,ref,n,i}$ obtained using the reference instruments between FC_{aw}-5 and FC_{aw}-11. At FC_{aw}-11, the values of $\rho_{aw,m,n,i}$ obtained were far away from the $\pm 1\%$ error bars and the scatter between the ith density measurements $\rho_{aw,m,n,i}$ are observed to be larger than for FC_{aw}-1 to FC_{aw}-10. From the results presented in figure 8-20, it can be inferred that the accuracy of the predicted mixture densities $\rho_{aw,m,n,i}$ obtained using the VDMS decreases with decrease in $\rho_{aw,ref,n,i}$ values (see table 8-6). In order to analyse the trend in the mixture density results obtained using the computer based VDMS control system and its capability to accurately determine a relevant optimal VDMS operating frequency for each flow condition that will ensure the measurement errors are minimized, the measurement parameters θ, Mr, $\hat{a}$ and λ used to compute $\rho_{aw,m,n,i}$ were required. These results are shown in figure 8-21 to figure 8-26.

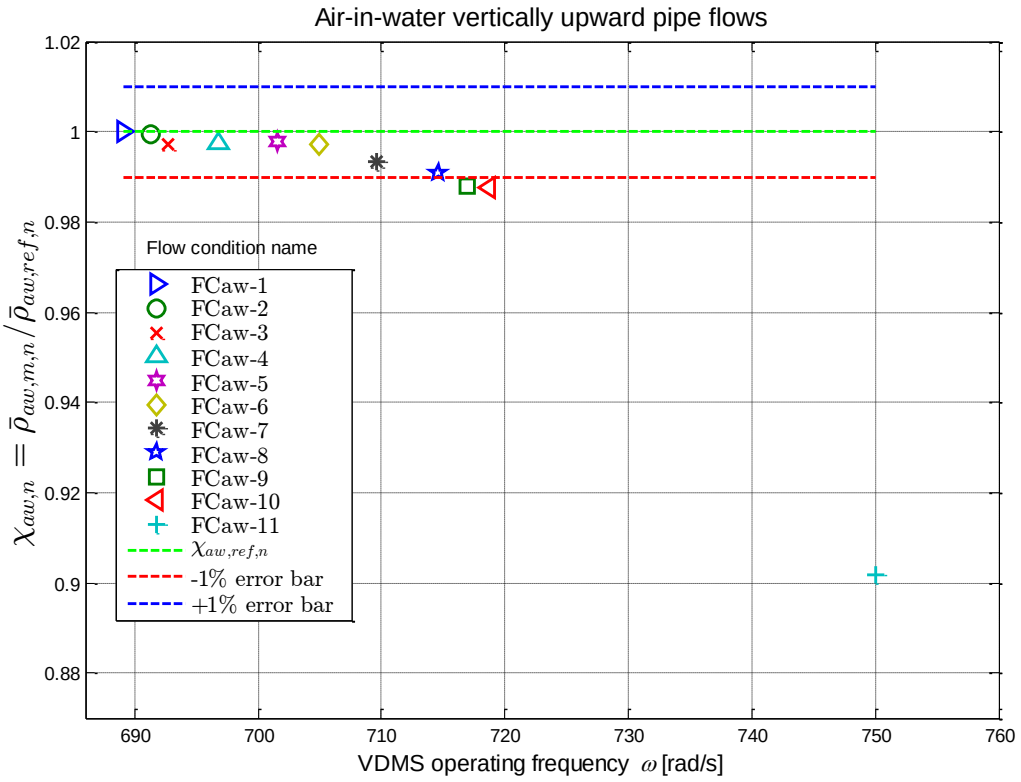

Figure 8-21: Ratio of mean mixture density $\chi_{aw,m,n}$ obtained using the VDMS and the reference instruments versus operating frequency in air-in-water vertically upward pipe flows.

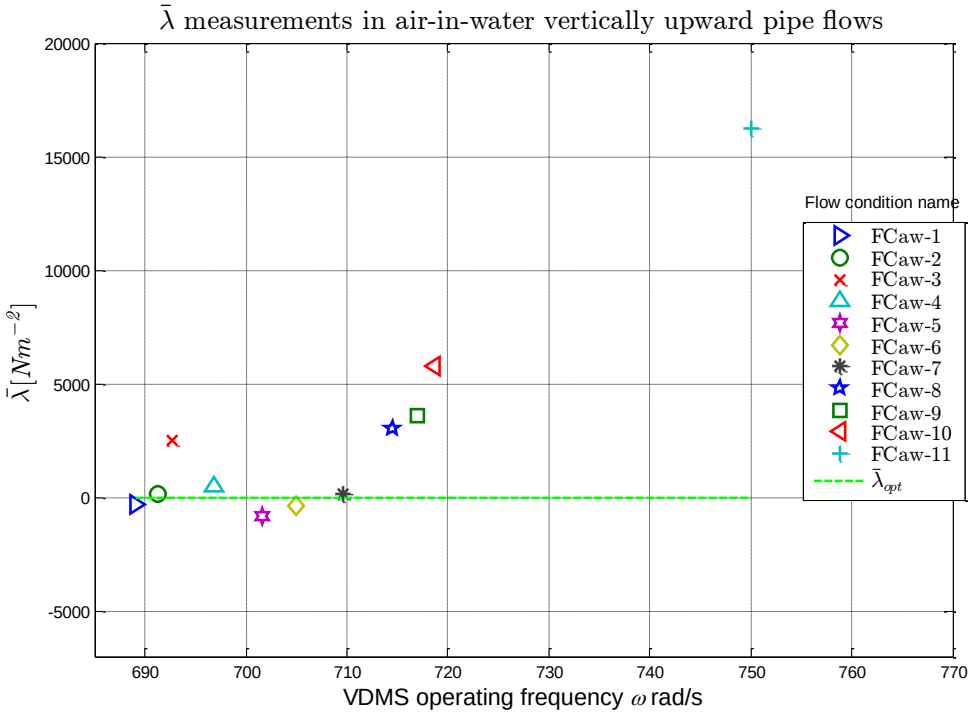

Figure 8-22: Mean value of lambda $\bar{\lambda}$ versus operating frequency using VDMS in air-in-water vertically upward pipe flows

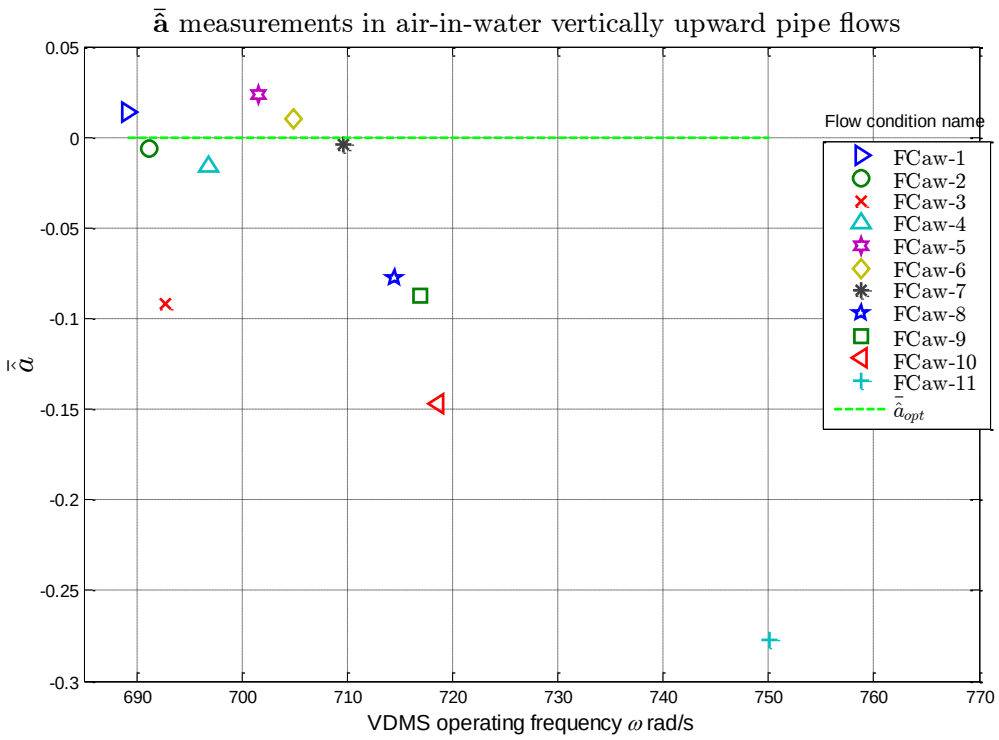

Figure 8-23: Mean value of $\hat{a}$ versus operating frequency obtained using VDMS in air-in-water vertically upward pipe flows

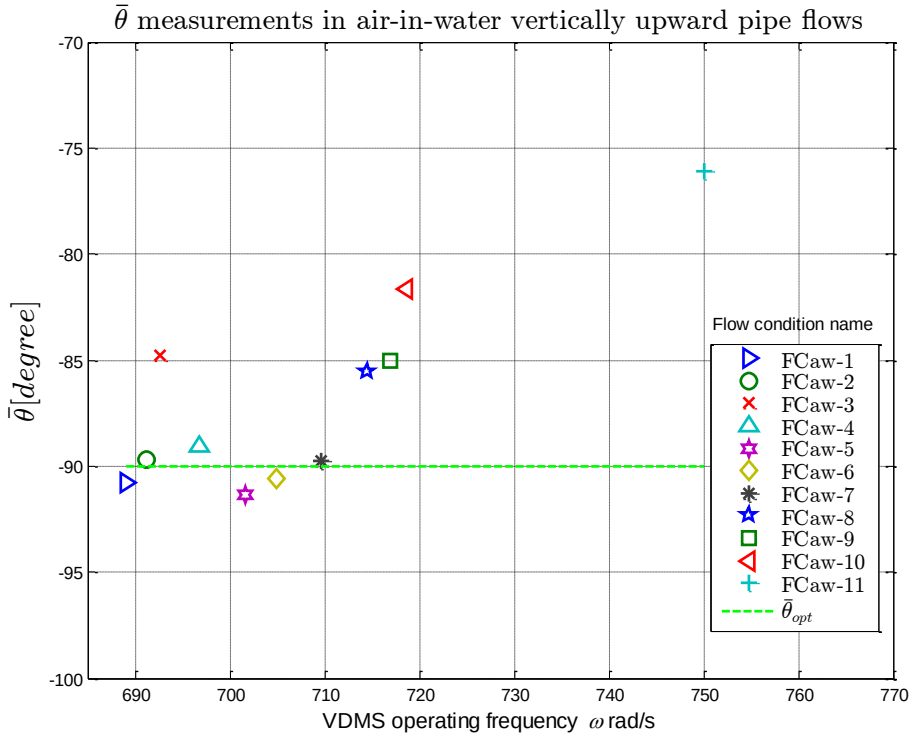

Figure 8-24: $\bar{\theta}$ values versus operating obtained using VDMS in air-in-water vertically upward pipe flows

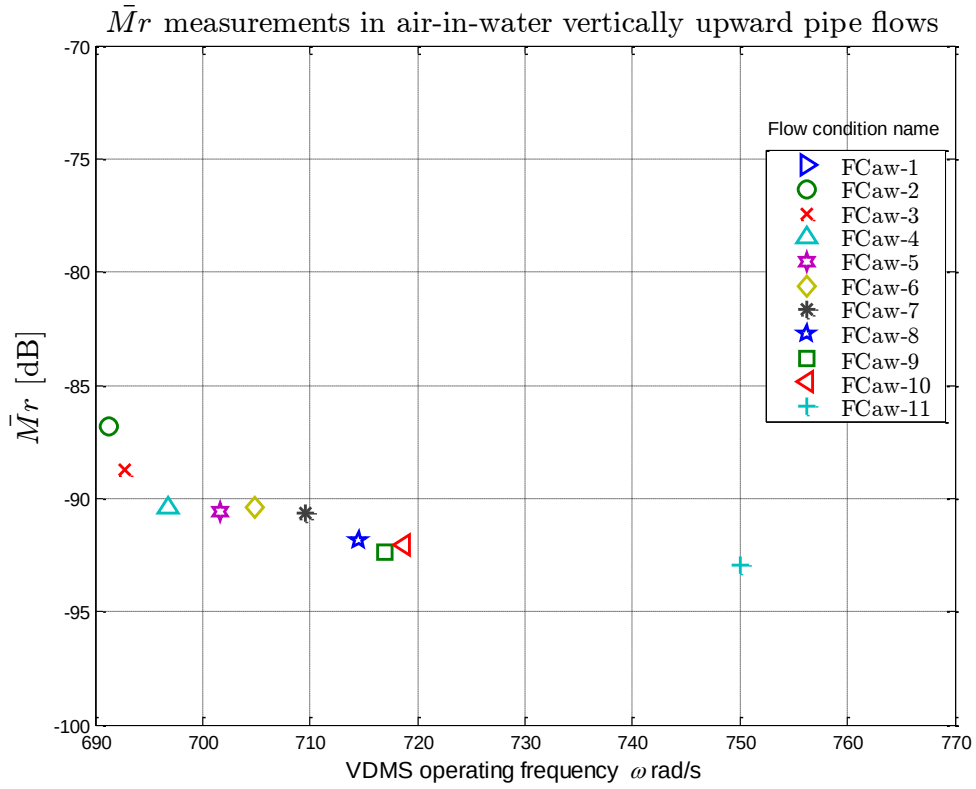

Figure 8-25: $\overline{Mr}$ values versus operating frequency obtained using VDMS in air-in-water vertically upward pipe flow

For all the plots shown in figure 8-21 to figure 8-25, the different flow conditions are represented by different symbols and colours. Also, the reference densities of the air-water mixture at FC_{aw}-1 to FC_{aw}-11 has been presented in table 8-6 and it ranges from 997.00kg/m^3 to 772.07kg/m^3. Figure 8-21 shows the plot of the ratio of the mean of the air-water mixture density $\chi_{aw,m,n}$ obtained using the VDMS and the reference instruments versus the VDMS operating frequency ω for the flow conditions used in air-water flow experiments. The values of $\chi_{aw,m,n}$ computed using equation 8-23 provided a measure of the deviation of the mean predicted air-water mixture density from the mean reference air-water mixture density at a given flow condition.

$$\chi_{aw,m,n} = \frac{\bar{\rho}_{aw,m,n}}{\bar{\rho}_{aw,ref,n}} \qquad \text{Equation 8-23}$$

where $\bar{\rho}_{aw,m,n}$ represents the mean of the i[th] $\rho_{aw,m,n,i}$ measurement obtained at a given flow condition and $\bar{\rho}_{aw,ref,n}$ represents the mean of the i[th] $\rho_{aw,ref,n,i}$ measurement obtained at the same flow condition. The values of $\bar{\rho}_{aw,m,n}$ and $\bar{\rho}_{aw,ref,n}$ at a flow condition n were obtained as follows,

$$\bar{\rho}_{aw,m,n} = \frac{\sum_{i=1}^{N}(\rho_{aw,m,n,i})}{N} \quad \text{Equation 8-24}$$

$$\bar{\rho}_{aw,ref,n} = \frac{\sum_{i=1}^{N}(\rho_{aw,ref,n,i})}{N} \quad \text{Equation 8-25}$$

where N is the total number of measurements taken at the n^{th} flow condition. The curves representing $+1\%$ and -1% error bars in figure 8-21 were also computed using the following expressions,

$$+1\% \text{ error bar} = 1.01 * \chi_{aw,ref,n} \quad \text{Equation 8-26}$$

$$-1\% \text{ error bar} = 0.99 * \chi_{aw,ref,n} \quad \text{Equation 8-27}$$

where $\chi_{aw,ref,n}$ represents the ratio of the mean reference air-water mixture density at the n^{th} flow condition. Additionally, the mean values of λ, $\hat{a}$, θ and Mr shown in figure 8-22 to figure 8-25 respectively, were computed using the generalized expression,

$$\bar{\Gamma} = \frac{\sum_{i=1}^{N}(\Gamma_i)}{N} \quad \text{Equation 8-28}$$

where Γ_i represent the i[th] measured parameter used in the investigation and can either be θ, Mr, $\hat{a}$ or λ and $\bar{\Gamma}$ represent the mean of the same parameter. From the plot of the mean values of the magnitude ratio versus VDMS operating frequency shown in figure 8-25, it is observed that the values of the magnitude ratio (representing the ratio of the amplitudes of the displacement signal to the force signal) decreases as the air-water mixture density (see table 8-4) associated with a given flow condition name decreases from FC_{aw}-1 to FC_{aw}-11. Unlike the existing vibrating densitometers which tend to stall when they encounters air-in-water flow with relatively low mixture density [142], the VDMS used in the air-water flow experiments shows good robustness

to continue to provide displacement and force measurements for flows with mixture density from 997.00kg/m^3 to 772.07kg/m^3. Thus the VDMS used in this research is capable of providing reliable mixture density measurements when used in air-in-water flows, inasmuch as the force and displacement sensors attached to the VDMS are able to accurately measure a representative displacement and force signals of the vibrating sensing pipe. The VDMS will continue to provide the necessary data to the computer based control system which is then used to generate an appropriate excitation signal to maintain its operation and to compute the flow mixture density. These results obtained using the VDMS therefore indicate an improvement in the performance of the vibrating densitometer when it is used to measure mixture density in air-water flows.

Before discussing the results shown in figure 8-21 to figure 8-25, it is important to note that FC_{aw}-11 used in this experiment has an air volume fraction 23% which differs significantly from the ranges of air volume fraction used for the other flow conditions (FC_{aw}-1 to FC_{aw}-10) used in this experiment (see table 8-6). The reason for generating a flow condition with such high air volume fraction was to understand how well the VDMS could provide mixture density measurement in similar flow condition. Figure 8-24 shows the results of the mean phase difference $\bar{\theta}$ variation with the VDMS optimal operating frequency ω_{opt} at the different flow conditions used in this investigation and it was used to analyse the accuracy of ω_{opt} values obtained using the computer based VDMS control system at each of the flow conditions with respect to the accuracy of the predicted mixture densities. In figure 8-24, it is seen that $\bar{\theta}$ values obtained at the different flow conditions investigated are centred about $\bar{\theta}_{opt}$ with the exceptions of FC_{aw}-3 and FC_{aw}-8 to FC_{aw}-11. For FC_{aw}-8 to FC_{aw}-11, the values of $\bar{\theta}$ are observed to deviate further from the $\bar{\theta}_{opt}$ line. Furthermore, the plots of the $\bar{\hat{a}}$ against ω_{opt} and $\bar{\lambda}$ against ω_{opt} show a similar trend as figure 8-24 which is suggestive of the dependence of the values of $\bar{\hat{a}}$ and $\bar{\lambda}$ on $\bar{\theta}$ values. Consequently, $\bar{\hat{a}}$ and $\bar{\lambda}$ values shown in figure 8-22 and figure 8-23 respectively, are observed to be close to zero

between FC_{aw}-1 and FC_{aw}-2 and FC_{aw}-4 and FC_{aw}-7 which correspond to the flow conditions where the values of $\bar{\theta}$ are within $\pm 1\%$ of $\bar{\theta}_{opt}$. Additionally, it is observed that, with the exception of FC_{aw}-3, the flow conditions where the flow mixture density was less than 890kg/m^3 (FC_{aw}-8 to FC_{aw}-11) has values of $\bar{\hat{a}}$ and $\bar{\lambda}$ that deviates further from zero which is indicative of a reduction in the VDMS measurement accuracy at these flow conditions. The plot of $\chi_{aw,m,n}$ versus ω_{opt} presented in figure 8-21 shows that $\chi_{aw,m,n}$ is less than one at all of the flow conditions investigated and it suggests that $\bar{\rho}_{aw,m,n}$ may have been underestimated relative to $\bar{\rho}_{aw,ref,n}$. Also, the values of $\chi_{aw,m,n}$ are observed to decrease progressively from FC_{aw}-1 to FC_{aw}-11 and was outside the $\pm 1\%$ error bars at the flow conditions where the mixture density was less than 890kg/m^3. It was therefore necessary to further analyse the measurement error.

8.6.3 Comparison of mixture density measurement results acquired using VDMS and reference instruments in air-in-water vertically upward pipe flows

In this section, the measurement errors obtained using the VDMS and reference instruments in air-in-water vertically upward pipe flows are presented and discussed. Two statistical tools, namely; (i) the mean and (ii) the standard deviation of the errors were used to establish a basis for quantitative comparison of $\rho_{aw,m,n,i}$ and $\rho_{aw,ref,n,i}$ measurements. For the ith measured air-water mixture density $\rho_{aw,m,n,i}$ obtained using the VDMS at a given flow condition, a percentage error $e_{aw,n,i}$ was first computed using equation 8-2. The error $e_{aw,n,i}$ was then used to compute the mean error $\bar{e}_{aw,n}$ and the standard deviation $S_{aw,n}$ of the errors at that flow condition. The values of $\bar{e}_{aw,n}$ and $S_{aw,n}$ were computed for the flow conditions given in table 8-6 using the generalised expression given in equation 8-3 and equation 8-4 and these results are shown in figure 8-26.

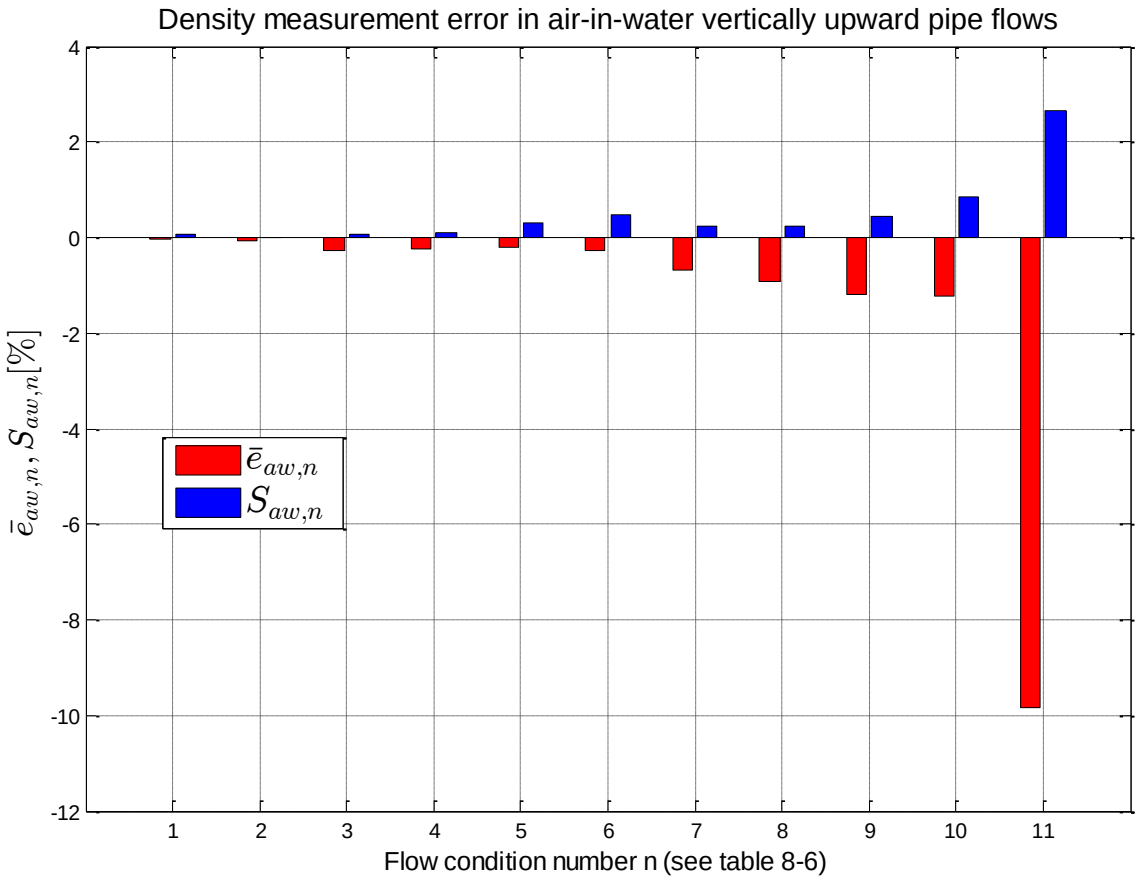

Figure 8-26: Bar graph of mean error and standard deviation of errors obtained using VDMS to measure the mixture density in air-in-water vertically upward pipe flows

From figure 8-26, the results show that the mean errors $\bar{e}_{aw,n}$ in $\rho_{aw,m,n,i}$ obtained at a given flow condition increases as the air volume fraction in the mixture increases which suggests evidence of an air volume fraction dependent systematic error in $\rho_{aw,m,n,i}$ obtained using the VDMS. It is seen that the mean error $\bar{e}_{aw,n}$ in $\rho_{aw,m,n,i}$ increases progressively from -0.03% to -9.83% with corresponding increase in the mixture air volume fraction associated with the flow conditions from 0.1% to 23% (see FC_{aw}-1 to FC_{aw}-11 in table 8-6). From the results shown in figure 8-26, the largest $\bar{e}_{aw,n}$ and $S_{aw,n}$ values are obtained at FC_{aw}-11 as -9.66% and 2.66% respectively whilst the smallest $\bar{e}_{aw,n}$ and $S_{aw,n}$ values are obtained at FC_{aw}-1 as -0.03% and 0.06% respectively. For flows where the mean in-situ the air volume fraction in the mixture was less than 10% (i.e. between FC_{aw}-1 and FC_{aw}-8), $\bar{e}_{aw,n}$ is observed to be less than 1% of the reading. Also, $S_{aw,n}$ is

impressively very small (less than 0.5%). Given that the computer based VDMS control system was used in this experiment to determine the VDMS optimal operating frequency at each of the flow conditions investigated, it was expected that the errors associated with the force and displacement measurements will be minimized in this investigation.

In order to thoroughly understand the reason(s) for the systematic errors $\bar{e}_{aw,n}$ shown in figure 8-26, it was important to critically analyse the methods for obtaining $\rho_{aw,m,n,i}$ and $\rho_{aw,ref,n,i}$ since these measurements were used to compute the values of $e_{aw,n,i}$ which were used to compute $\bar{e}_{aw,n}$ and $S_{aw,n}$. From equation 6-22, it is seen that $\rho_{aw,ref,n,i}$ is dependent on accurate measurement of the differential pressure ΔP across a one meter length of the flow loop working section and as well as the frictional pressure loss F_m in the working section. In this experiment, it is likely that these measurements (ΔP and F_m) could either have been overestimated or underestimated and may thus contribute to the errors observed. The method for estimating ΔP using the output from the DP sensor current-to-voltage converter circuit and the method for computing the air volumetric flow rate which was used to estimate F_m could also introduce error into $\rho_{aw,ref,n,i}$. If either, or both, ΔP and F_m are overestimated, $\rho_{aw,ref,n,i}$ will be greater than $\rho_{aw,m,n,i}$ and this will give a negative $e_{aw,n,i}$. Similarly, if either, or both, ΔP and F_m are underestimated the $\rho_{aw,ref,n,i}$ measurement will be less than $\rho_{aw,m,n,i}$ measurement and will give a positive measurement error $e_{aw,n,i}$. In this investigation, the negative mean errors $\bar{e}_{aw,n}$ shown in figure 8-26 suggest that either, or both, ΔP and F_m may have been overestimated. The negative measurement errors observed are fairly typical of two phase air-in-water mixture density measurements as described in [138], however, the magnitude of the errors in the current work are relatively smaller.

Since the density prediction model given in equation 4-29 was assumed to be valid for incompressible flows, the systematic errors $\bar{e}_{aw,n}$ could also have been caused by modelling errors. From equation 4-29 and equation 4-30, it is seen that $\rho_{aw,m,n,i}$ is dependent on ω,

β_{opt}, K_1, V_{pipe} and λ therefore the likely influence of these measurement variables on errors $e_{aw,n,i}$ in $\rho_{aw,m,n,i}$ will be discussed independently. Firstly, the variable λ was obtained from the measured force and displacement signals and, since the computer based VDMS control system was used to select an optimal frequency ω_{opt} in this experiment, it was expected that the errors associated with the λ measurement would be minimized. This can be seen in the results for $\bar{\theta}$ vs ω shown in figure 8-24 where $\bar{\theta}$ is observed to be within $\pm 5\%$ of $\bar{\theta}_{opt}$ at all the flow conditions investigated with the exception of FC_{aw}-11. Also, only incompressible test mixtures (i.e. liquid only, liquid-liquid and solids-liquid) were used in the bench testing (see section 5.8) to determine the value of β_{opt} that was used to compute $\rho_{aw,m,n,i}$ in this investigation. It is therefore plausible that the value of β_{opt} that was used to compute $\rho_{aw,m,n,i}$ could also have introduced error in the measurement. Also, temperature variation in the sensing pipe may likely cause small changes in the actual values of K_1 and V_{pipe} and may also introduce error in $\rho_{aw,m,n,i}$.

Gysling [136] has shown that for air-in-water flows, the mixture will exhibit a "springiness" property which is dependent on the mixture compressibility. For air-in-water mixtures at ambient temperature and pressure, the flow mixture compressibility will increase by a factor of 250 for every 1% increases in the air volume fraction. In this experiment, it is plausible that the vibration dynamics of the VDMS may not have been correctly described by the mathematical model given in equation 4-12, and used to develop the density prediction model in equation 4-29, due to the "springiness" property introduced by the air-in-water mixture at relatively high gas volume fraction. It is likely that the modelling error in equation 4-29 becomes larger as the "springiness" property of the flow mixture increases. This may explain the reason for the air volume fraction dependent systematic errors observed in $\rho_{aw,m,n,i}$ shown in figure 8-26. The result shows that for flows with air volume fraction greater than 10% (FC_{aw}-8 to FC_{aw}-11) the mixture density measurement errors becomes larger and also the reliability of the measurement is reduced. Other

factors that could also have affected the measurement errors in $\rho_{aw,m,n,i}$ include bubble size [175], bubble flow rate[176] and flow regime [177]. Since the results in figure 8-26 indicate evidence of an air volume fraction dependent systematic error when the VDMS was used to obtain $\rho_{aw,m,n.i}$ measurements in air-in-water flows, it became necessary to develop an improved density prediction model that can be used to obtain accurate $\rho_{aw,m,n,i}$ measurements in such flows. The improved model developed for this purpose is described in chapter 9.

8.7 Mean air volume fraction measurements obtained using the VDMS and the reference instruments in air-in-water vertically upward pipe flows

In the current work, the VDMS was also used to measure the mean air volume fraction in two phase, air-in-water vertically upward pipe flows. This type of measurement is particularly important in applications where knowledge of the phase volume fractions of the mixture is critical to their efficient management. For example, in a gas injection oil well accurate measurement of the gas volume fraction is required to calculate the pressure gradient in the well. It is also used in modelling oil well "blowouts" and to calculate gas volumetric flow rate when used in combination with the gas velocity.

8.7.1 Mean in-situ air volume fraction measurement results acquired using the VDMS and the reference measurement instruments in air-in-water vertically upward pipe flows

This section present and discusses the results of the mean in-situ air volume fraction measurements that were obtained using the VDMS and the reference instruments for the flow conditions given in table 8-6. Equation 6-20 was adopted to derive an expression to compute the ith measured value $\alpha_{a,m,n,i}$ of the in-situ air volume fraction at a given flow condition used in this investigation. This expression is given by,

$$\alpha_{a,m,n,i} = \frac{\rho_{w,ref} - \rho_{aw,m,n,i}}{\rho_{w,ref}} \qquad \text{Equation 8-29}$$

where $\rho_{aw,m,n,i}$ represents the i[th] measured air-water mixture density obtained at a given flow condition using the VDMS and $\rho_{w,ref}$ represents the reference water density. Also, a reference $\alpha_{a,ref,n,i}$ air volume fraction measurement was also computed in the current research work using equation 6-27. This expression used the differential pressure ΔP measured across a one meter axial length L of the flow loop working section, the estimated frictional pressure loss F_m of the flow, the acceleration of gravity g and the reference water density $\rho_{w,ref}$ to compute $\alpha_{a,ref,n,i}$. Additionally, the mean of the measured $\bar{\alpha}_{a,m,n}$ and the reference $\bar{\alpha}_{a,ref,n}$ in-situ air volume fractions at a given flow condition were computed as follows,

$$\bar{\alpha}_{a,m,n} = \frac{\sum_{i=1}^{N} \alpha_{a,m,n,i}}{N}$$ Equation 8-30

$$\bar{\alpha}_{a,ref,n} = \frac{\sum_{i=1}^{N} \alpha_{a,ref,n,i}}{N}$$ Equation 8-31

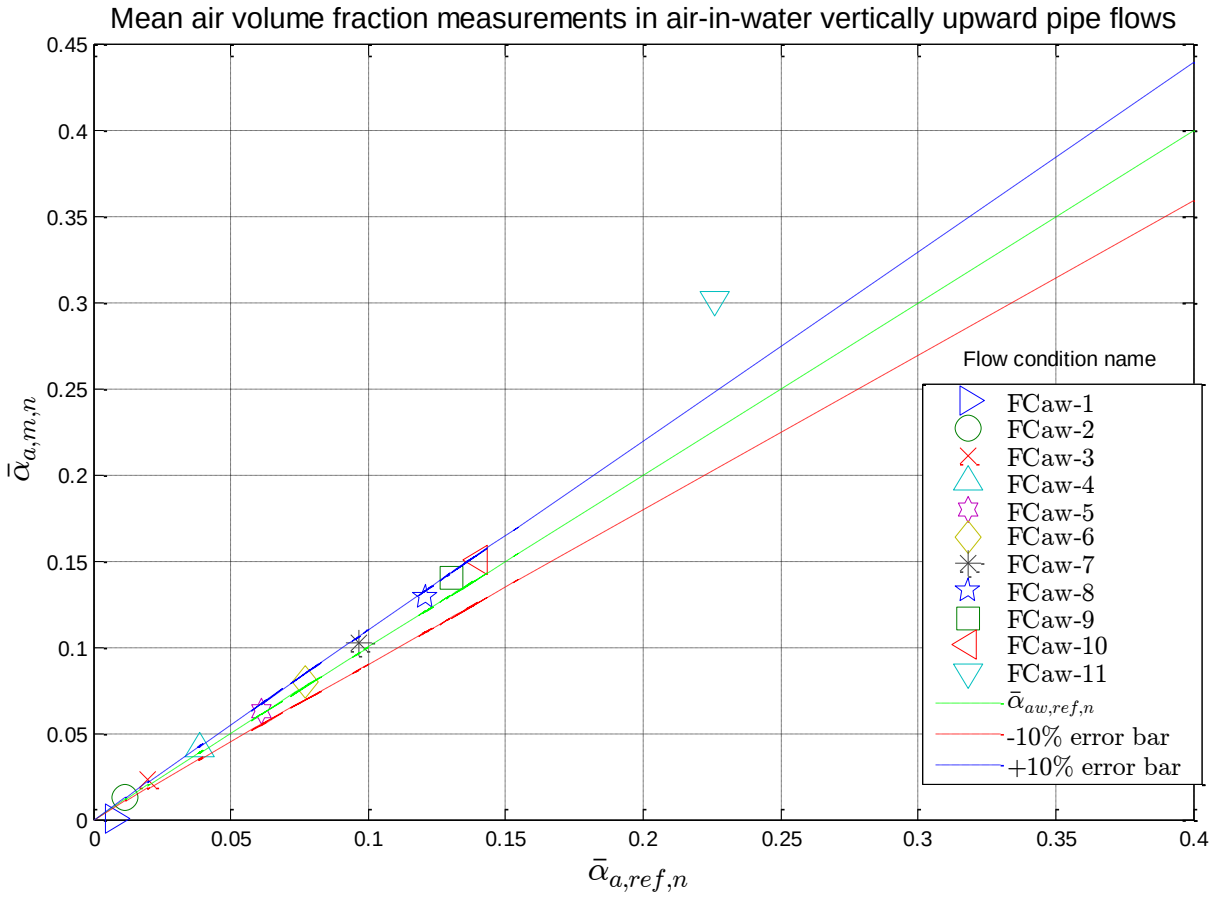

Figure 8-27: Mean air volume fraction measurements acquired using VDMS and reference instruments in air-in-water vertically upward pipe flow

The flow conditions for which $\bar{\alpha}_{a,m,n}$ and $\bar{\alpha}_{a,ref,n}$ were computed were the same as the flow conditions given in table 8-6. In figure 8-27, the different flow conditions are represented by different colours and symbols in the legend and the blue and red dashed lines represents the $+10\%$ and -10% error bars respectively and were computed using the following expressions,

$$+10\% \text{ error bar} = 1.10 * \bar{\alpha}_{a,ref,n} \quad \text{Equation 8-32}$$

$$-10\% \text{ error bar} = 0.90 * \bar{\alpha}_{a,ref,n} \quad \text{Equation 8-33}$$

It is apparent from the results presented in figure 8-27 that for a given flow condition, the mean of the in-situ air volume fraction values $\bar{\alpha}_{a,m,n}$ obtained using the VDMS are consistently within $\pm 10\%$ of the reference mean in-situ air volume fraction values $\bar{\alpha}_{a,ref,n}$ with the exception of FC_{aw}-11. These results suggest that the mean air volume fractions $\bar{\alpha}_{a,m,n}$ obtained using the VDMS were a reasonably accurate representation of the true air volume fraction in the flow loop working section. However, the deviation of $\bar{\alpha}_{a,m,n}$ from $\bar{\alpha}_{a,ref,n}$ tended to increase as the air composition in the mixture was increased from FC_{aw}-1 to FC_{aw}-11. The results shown in figure 8-27 are also similar to the results in figure 8-20 which is indicative of the dependency of the measured value of $\bar{\alpha}_{a,m,n}$ on $\rho_{aw,m,n,i}$ measurement. Hence, the discussion on the sources of errors in $\rho_{aw,m,n,i}$ presented in section 8.6.3 are also applicable to $\bar{\alpha}_{a,m,n}$.

8.7.2 Comparison of mean air volume fraction measurements acquired using the VDMS and the reference instruments in air-in-water vertically upward pipe flows

The purpose of this section is to quantitatively compare the values of $\bar{\alpha}_{a,m,n}$ obtained using the VDMS and the reference $\bar{\alpha}_{a,ref,n}$ data for each flow condition used in the air-in-water experiments. Two statistical tools, namely; mean error $\bar{e}_{a,n}$ and standard deviation $S_{a,n}$ of the errors in $\alpha_{a,m,n,i}$ were defined using expressions similar to equation 8-3 and equation 8-4 respectively, and were used for the purpose of quantitative comparison of the errors $e_{a,n,i}$ in $\alpha_{a,m,n,i}$. The values of $\bar{e}_{a,n}$

and $S_{a,n}$ were used to measure the magnitude of the deviation of $\alpha_{a,m,n,i}$ from the reference $\alpha_{a,ref,n,i}$ and the reliability and uncertainty in the measurements taken. These statistical quantities obtained for the air-in-water experiments are shown in figure 8-28.

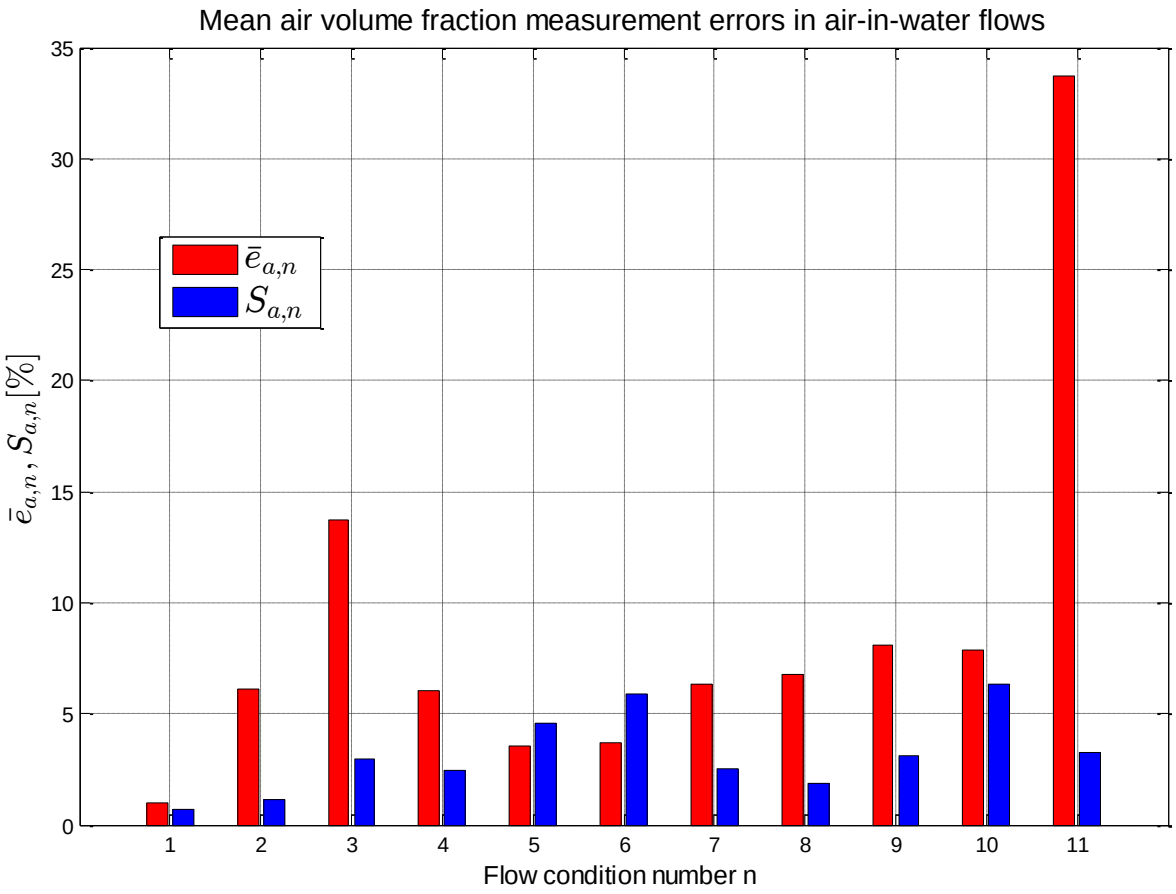

Figure 8-28: Bar graph of mean errors and standard deviation of the errors in $\alpha_{a,ref,n,i}$ obtained using VDMS in air-in-water vertically upward pipe flows

The results in figure 8-28 suggest evidence of random measurement error in $\alpha_{a,m,n,i}$. The results also show that the mean error $\bar{e}_{a,n}$ in $\alpha_{a,ref,n,i}$ at each flow condition used in the experiment is less than $+10\%$ of reading for all the flow conditions used in this investigation with the exceptions of FC_{aw}-3 and FC_{aw}-11 where $\bar{e}_{a,n}$ is +13.74% and +33.18% respectively. Also, the value of $S_{a,n}$ is less than 7% for all the flow conditions used in this investigation, which indicates that the measurements obtained were repeatable. At FC_{aw}-3, it is observed that deviation of $\bar{\theta}$ from $\bar{\theta}_{opt}$ is approximately 5% and the mean error $\bar{e}_{a,n}$ in $\alpha_{a,ref,n,i}$ is +13.74% and this result suggests that the

error in the measured force and displacement signals used in computing $\alpha_{a,ref,n,i}$ may not have been entirely minimized and thus likely explains the reason for the relatively large error $\bar{e}_{a,n}$ value observed at FC_{aw}-3. Furthermore, the results obtained at FC_{aw}-11, where the mixture air volume fraction was approximately 23%, is believed to contain modelling error due to the change in dynamic property of the air-water mixture and hence the VDMS gave inaccurate estimates of the true air volume fraction $\alpha_{a,m,n,i}$ in the flow loop working section. Since the value of $\bar{\alpha}_{a,m,n}$ is dependent on the value of $\rho_{aw,m,n,i}$ obtained using the VDMS and the reference $\bar{\alpha}_{a,ref,n}$ value is dependent on the values of F_m and ΔP obtained using the reference instruments, the discussion of the sources of errors in $\rho_{aw,m,n,i}$ and $\rho_{aw,ref,n,i}$ presented in section 8.6.3 also applies to $\alpha_{a,m,n,i}$ and $\alpha_{a,ref,n,i}$ respectively. It can be concluded from the results presented in figure 8-28 that the computer based VDMS control system can be used to obtain relatively accurate and reliable estimate of the mean in-situ air volume fraction for the type of air-in-water flows, where the air volume fraction is less than 10%, described in this research.

8.8 Effect of Coriolis force on accuracy of density measurements

In section 8.3.3, a flow rate dependent systematic error was observed when the VDMS was used to measure $\rho_{w,m,n,i}$ in "water only" vertically upward flows. It was therefore important to investigate the source(s) of the flow rate dependent systematic errors, in order to better understand the measurement capability of the VDMS. Given that a pipe with "fixed end" supports and undergoing vibration will experience a Coriolis force which is dependent on the velocity of the vibrating body, it was decided that the effect of the Coriolis force on the $\rho_{w,m,n,i}$ obtained using the VDMS should be investigated. This section presents a discussion of the effect of the Coriolis force on $\rho_{w,m,n,i}$. Generally, when fluid passes through a vertical pipe with "fixed end" supports and undergoing lateral vibration, it is expected to experience, (i) an acceleration along the flow direction and (ii) an acceleration perpendicular to the flow direction. Morrison and Crossland [149]

have described this phenomenon using an analogy of a sliding block R connected to a rotating link "OX" as shown figure 8-29. According to Morrison and Crossland, if the sliding block R is assumed to move with an angular velocity ω and a radial velocity $\dot{r}$ on a rotating link OX, then the acceleration of the block relative to the rotating link will have two components namely, (a) a Coriolis acceleration $\ddot{x}$ component due to the angular velocity of the block along the link and (b) a Coriolis acceleration $\ddot{y}$ component due to the radial velocity $\dot{r}$ of the block and tangential to the link.

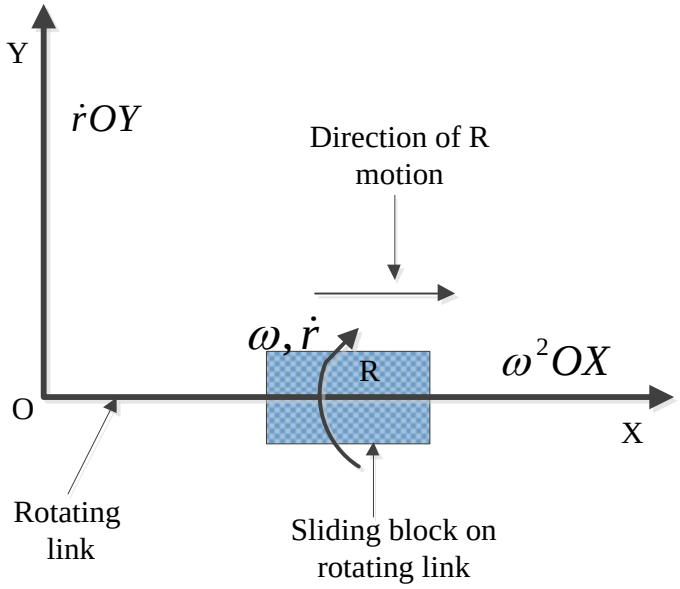

Figure 8-29: Diagram of sliding block R on a rotating link OX

In figure 8-29, R represents the sliding block moving in the "x-direction" along the rotating link "OX" which is fixed at point "O" and the "y-direction" is perpendicular to the "x-direction". The centripetal acceleration $\ddot{x}$ and the tangential acceleration $\ddot{y}$ of the sliding block R moving in the "x-direction" on the rotating link "OX" shown in figure 8-29 are given by these expressions,

$$\ddot{x} = \ddot{r} - \omega^2 r \qquad \text{Equation 8-34}$$

$$\ddot{y} = 2\omega\dot{r} + \dot{\omega}r \qquad \text{Equation 8-35}$$

where $\ddot{r}$ is the component of the acceleration along the link, $\omega^2 r$ is the centripetal acceleration of the sliding block along the link, $2\omega\dot{r}$ is the component of the acceleration tangential to the link and $\dot{\omega}r$ is the centripetal acceleration of the sliding block perpendicular to the link.

Considering that the VDMS was vertically installed in the flow loop working section and when measurements were taken during experimentation, it undergoes lateral vibration with fluid flowing through, the system described in figure 8-29 can be related to the VDMS and the flowing fluid. The sliding block R is assumed to represent the flowing fluid in the pipe with an angular velocity ω and radial velocity $\dot{r}$ and the rotating link "OX" is also assumed to represent a symmetrical half of the pipe which has "fixed end" supports and undergoing vibration when a force is applied at the center (see figure 8-30).

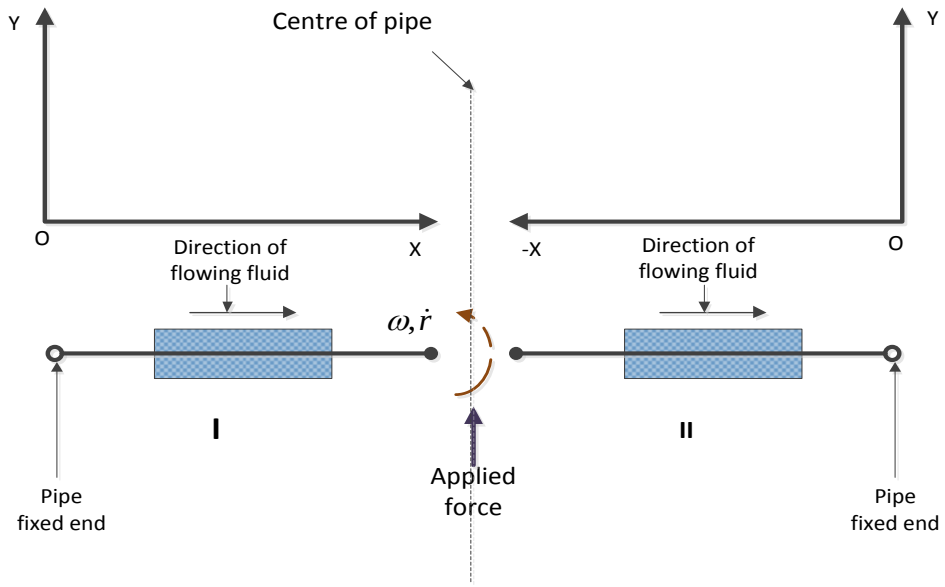

Figure 8-30: Acceleration diagram of VDMS

In figure 8-30, the sensing pipe is shown split into two symmetrical halves, I and II, and the fluid flows in the positive "x-direction" as indicated by the arrows whilst the sensing pipe vibration is in the "y-direction" (i.e. the direction of applied force). When a force is applied at the pipe centre, the resulting Coriolis acceleration in the "y-direction" can be described using equation 8-35 while the Coriolis acceleration along the flow direction has negligible effect on the pipe vibration and

can be ignored. The tangential Coriolis acceleration acting in section I and II of the sensing pipe can therefore be written as,

$$\ddot{y}_I = 2\dot{r}\omega + r\dot{\omega} \quad \text{Equation 8-36}$$

$$\ddot{y}_{II} = -2\dot{r}\omega + r\dot{\omega} \quad \text{Equation 8-37}$$

where $\ddot{y}_I$ and $\ddot{y}_{II}$ are the tangential acceleration of the fluid in section I and II of the sensing pipe respectively. In equation 8-36 and equation 8-37, the acceleration component due to $\dot{r}$ in the "y-direction" are equal and in opposite direction, hence they have opposite signs while the acceleration component due to r in the "y-direction" are equal and in the same direction hence, they have the same signs. The total tangential acceleration $\ddot{y}_T$ of the fluid acting at the sensing pipe centre can be obtained as the summation of $\ddot{y}_I$ and $\ddot{y}_{II}$. This is given by,

$$\ddot{y}_T = \ddot{y}_I + \ddot{y}_{II} = 2r\dot{\omega} \quad \text{Equation 8-38}$$

From equation 8-36, equation 8-37 and equation 8-38, the acceleration component due to fluid radial velocity $\dot{r}$ in the "y-direction" should have no effect on the force applied to the pipe since they cancel out each other whilst the acceleration component ωr do not cancel each other out, but do not depend on $\dot{r}$. Therefore, the total acceleration $\ddot{y}_T$ should have negligible effect on the magnitude of the applied force measured at the pipe centre and therefore should not influence the VDMS density measurement accuracy. Hence, provided the force is applied exactly at the sensing pipe centre, its measured value should be independent of the flow velocity and thus not expected to affect the predicted density. However, it was observed that the force sensor associated with the VDMS used in the current research work was offset by 1mm from the sensing pipe centre due to imperfect manufacture and may therefore have caused a non-zero net Coriolis force to be measured by the force sensor and may possibly have resulted in the flow rate dependent systematic error observed in $\rho_{w,m,n,i}$.

8.9 Summary

Several experiments conducted using a multiphase flow loop facility at the University of Huddersfield have been described in this chapter. These included experiments to determine the capability of the VDMS and the reference instruments to measure fluid density in "water only", solids-in-water and air-in-water vertically upward pipe flows. Several flow conditions were generated and used in these investigations and have been described. The results of the density measurement obtained using the VDMS and reference instruments were also presented and discussed. The VDMS and reference instruments were also used to estimate mean phase volume fraction in solids-in-water and air-in-water flows and the results obtained were discussed. The density and hence phase volume fraction measurement errors were computed and discussed as well as the likely source(s) of these errors. Lastly, the effect of the Coriolis force on the measurement error were discussed. The density measurements obtained using the VDMS was found to agree well with the reference measurement for "water only", solids-in-water and bubbly air-in-water flow and hence suggested that the VDMS can be used to provide relatively accurate and reliable density measurements for the flow type described in this research.

Chapter 9

MODIFIED MATHEMATICAL MODEL FOR PREDICTING MIXTURE DENSITY IN AIR-IN-WATER PIPE FLOWS

9.1 Introduction

This chapter presents a new mathematical model that was developed for predicting density in both compressible and incompressible pipe flows and for clarity, it is referred to as model-2 to distinguish it from the previous mathematical model developed in section 4.2 which is referred to as model-1 in this chapter. The need to develop a new mathematical model that could be used to accurately predict mixture density in both compressible and incompressible flows was necessitated by the relatively large measurement errors observed when model-1 was used to predict the mixture density in air-in-water flows as observed in section 8.6.2. Additionally, validation of the new mathematical model, (model-2) using the experimental and theoretical frequency response data for air-in-water flows with different air volume fractions compositions (in the bubbly and slug flow regimes), is presented is this chapter. Lastly, the density measurement errors obtained when model-1 and model-2 were used to independently compute the predicted mixture density of the air-in-water flows given in table 8-6 is presented and discussed.

9.2 Development of a new mathematical model for predicting mixture density in compressible and incompressible pipe flows

In order to develop a new mathematical model that could be used to accurately predict mixture density in both compressible and incompressible pipe flows, the model of the vibrating mechanical system comprising of a mass, spring and damper element as shown in figure 4-1, was modified to attempt to account for the change in the dynamic vibration characteristics of the system when an air-in-water mixture flows through it. Gysling [136] showed that the sensing pipe and its content

can be considered as two interacting vibrating mechanical systems which are coupled by the stiffness property of the air-in-water mixture and this is shown in figure 9-1.

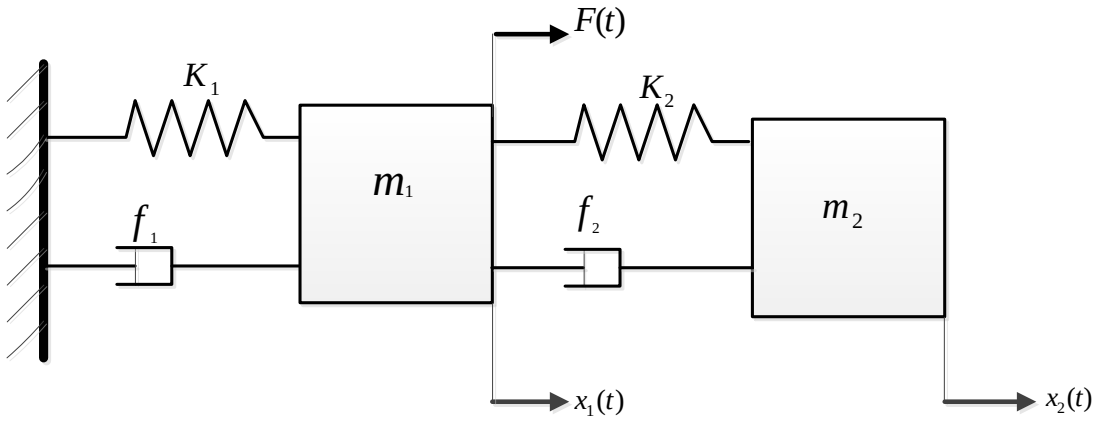

Figure 9-1: Diagram of spring mass damper elements of sensing pipe and multiphase mixture contained within it.

The following definitions apply to the variables in the diagram shown in figure 9-1, K_1 denotes the sensing pipe stiffness constant while K_2 represents the stiffness associated with the coupling between the sensing pipe and the pipe contents, m_1 is the true mass of the sensing pipe and is related to its modified mass $\hat{m}_1$ by the expression,

$$m_1 = \beta^2 \hat{m}_1 \qquad \text{Equation 9-1}$$

where β is the VDMS constant which was discussed in section 4.2 and 5.8.1. The true mass of the sensing pipe contents is denoted as m_2 and it is related to its modified mass $\hat{m}_2$ by the expression,

$$m_2 = \beta^2 \hat{m}_2 \qquad \text{Equation 9-2}$$

The true damping constant of the sensing pipe f_1 is related to the modified damping constant $\hat{f}_1$ by the expression,

$$f_1 = \beta \hat{f}_1 \qquad \text{Equation 9-3}$$

Since the VDMS is operated at an optimal frequency, its motion will be more freely driven and hence the fluid damping f_2 can be neglected. The harmonic forcing function $F(t)$ applied to the sensing pipe is defined as,

$$F(t) = \mathbf{F}e^{j\omega t}$$ Equation 9-4

where **F** is a complex force phasor with magnitude and phase, and ω is the forcing frequency. Additionally, $x_1(t)$ and $x_2(t)$ are the time dependent displacements of the sensing pipe and its contents respectively, and are defined by the following expressions,

$$x_1(t) = \mathbf{X}_1 e^{j\omega t}$$ Equation 9-5

$$x_2(t) = \mathbf{X}_2 e^{j\omega t}$$ Equation 9-6

where $\mathbf{X_1}$ and $\mathbf{X_2}$ are complex phasors with magnitude and phase. It is important to state here that the displacement $x_2(t)$ of the sensing pipe contents is assumed to be an absolute displacement which is relative to the static, shaded, region in figure 9-1 and is not relative to the sensing pipe. The time dependent velocities of the sensing pipe $\dot{x}_1(t)$ and the pipe contents $\dot{x}_2(t)$ can be obtained by differentiating equation 9-5 and equation 9-6. This gives,

$$\dot{x}_1(t) = j\omega\mathbf{X}_1 e^{j\omega t}$$ Equation 9-7

$$\dot{x}_2(t) = j\omega\mathbf{X}_2 e^{j\omega t}$$ Equation 9-8

The accelerations of the sensing pipe and the pipe contents are defined as $\ddot{x}_1(t)$ and $\ddot{x}_2(t)$ respectively and can be obtained by differentiating the expressions for the respective velocities giving,

$$\ddot{x}_1(t) = -\omega^2\mathbf{X}_1 e^{j\omega t}$$ Equation 9-9

$$\ddot{x}_2(t) = -\omega^2\mathbf{X}_2 e^{j\omega t}$$ Equation 9-10

The free body diagram depicting the forces acting on the sensing pipe and the pipe contents, and the resultant motions of the pipe and pipe contents, when a harmonic forcing excitation $F(t)$ is applied to the sensing pipe is shown in figure 9-2.

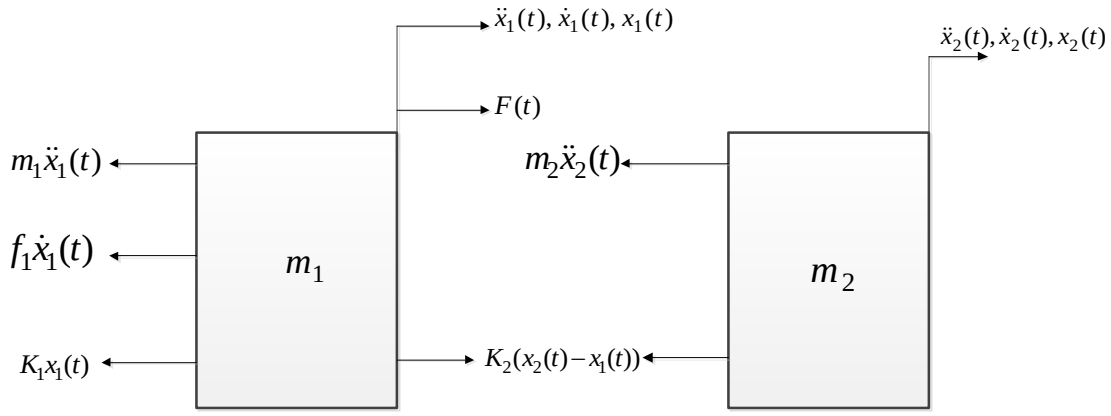

Figure 9-2: Free body diagram showing the forces acting on the sensing pipe and its contents when a harmonic forcing excitation is applied to the sensing pipe

Note that the free body diagram forces are expressed in terms of the true masses m_1 and m_2 and the true damping constant f_1 and these can be related to the modified masses and damping constants using the expressions given in equation 9-1 to equation 9-3. In order to generate the equations of motion for the free body diagram in figure 9-2, the system is considered as having two degrees of freedom due to the two interacting inertia from the sensing pipe and its contents. The equation of motion for the sensing pipe and its contents is thus given in terms of its modified masses and modified damping constants by,

$$\hat{m}_1\ddot{x}_1(t) + \hat{f}_1\dot{x}_1(t) + (K_1 + K_2)x_1(t) - K_2x_2(t) = F(t) \quad \text{Equation 9-11}$$

$$\hat{m}_2\ddot{x}_2(t) + K_2(x_2(t) - x_1(t)) = 0 \quad \text{Equation 9-12}$$

Equation 9-11 and equation 9-12, are expressed in terms of the modified masses and modified dampings in order to take into account the vibration dynamics of the sensing pipe with "fixed end" supports. Equation 9-5 to equation 9-10 is then substituted into the equations of motion given in equation 9-11 and equation 9-12 respectively and the resulting expressions obtained are given as follows,

$$\hat{m}_1\left(-\omega^2\mathbf{X}_1e^{j\omega t}\right) + j\omega\hat{f}_1\mathbf{X}_1e^{j\omega t} + (K_1 + K_2)\mathbf{X}_1e^{j\omega t} - K_2\mathbf{X}_2e^{j\omega t} = \mathbf{F}e^{j\omega t} \quad \text{Equation 9-13}$$

$$\hat{m}_2\left(-\omega^2\mathbf{X}_2e^{j\omega t}\right) + K_2(\mathbf{X}_2 - \mathbf{X}_1)e^{j\omega t} = 0 \quad \text{Equation 9-14}$$

These expressions can be simplified further by dividing through by $e^{j\omega t}$ giving,

$$\{-\omega^2\hat{m}_1 + j\omega\hat{f}_1 + (K_1 + K_2)\}\mathbf{X}_1 - K_2\mathbf{X}_2 = \mathbf{F} \quad \text{Equation 9-15}$$

$$(-\omega^2\hat{m}_2 + K_2)\mathbf{X}_2 - K_2\mathbf{X}_1 = 0 \quad \text{Equation 9-16}$$

$\mathbf{X}_2$ is now made the subject of the formula in equation 9-16 giving,

$$\mathbf{X}_2 = \frac{K_2\mathbf{X_1}}{\{-\omega^2\hat{m}_2 + K_2\}} \quad \text{Equation 9-17}$$

Equation 9-17 is substituted into equation 9-15 to obtain an expression for describing the vibration characteristics of the sensing pipe and its contents as follows,

$$\left\{\left(K_1 - \omega^2\hat{m}_1 - \frac{\omega^2\hat{m}_2K_2}{\{K_2 - \omega^2\hat{m}_2\}}\right) + j\omega\hat{f}_1\right\}\mathbf{X}_1 = \mathbf{F} \quad \text{Equation 9-18}$$

The real part in equation 9-18 is simplified giving,

$$K_1 - \omega^2\hat{m}_1 - \frac{\omega^2\hat{m}_2K_2}{\{K_2 - \omega^2\hat{m}_2\}} = K_1 + \frac{-\omega^2K_2(\hat{m}_1 + \hat{m}_2) + \omega^4\hat{m}_1\hat{m}_2}{K_2 - \omega^2\hat{m}_2} \quad \text{Equation 9-19}$$

Equation 9-19 is then substituted into equation 9-18 to obtain the expression,

$$\left\{\left(K_1 + \frac{-\omega^2K_2(\hat{m}_1 + \hat{m}_2) + \omega^4\hat{m}_1\hat{m}_2}{K_2 - \omega^2\hat{m}_2}\right) + j\omega\hat{f}_1\right\}\mathbf{X}_1 = \mathbf{F} \quad \text{Equation 9-20}$$

Equation 9-20 gives an expression that can be used to describe the oscillatory motion of the system described in figure 9-1 when the input is a harmonic excitation. From equation 9-20, the force-displacement relationship of the sensing pipe and its contents when undergoing vibration due to a harmonic forcing is given by the expression,

$$\frac{\mathbf{X}_1}{\mathbf{F}} = \frac{1}{\left[\left\{K_1 + \frac{-\omega^2K_2(\hat{m}_1 + \hat{m}_2) + \omega^4\hat{m}_1\hat{m}_2}{K_2 - \omega^2\hat{m}_2}\right\} + j\omega\hat{f}_1\right]} \quad \text{Equation 9-21}$$

This expression is used to develop a new mathematical model that can be used to accurately predict the density of compressible and incompressible pipe flows. Equation 9-21 is a complex expression that can be standardized by rationalization. This is given by,

$$\frac{\mathbf{X_1}}{\mathbf{F}} = \frac{\left\{K_1 + \frac{-\omega^2 K_2(\hat{m}_1 + \hat{m}_2) + \omega^4 \hat{m}_1 \hat{m}_2}{K_2 - \omega^2 \hat{m}_2}\right\} - j\{\omega \hat{f}_1\}}{\left\{K_1 + \frac{-\omega^2 K_2(\hat{m}_1 + \hat{m}_2) + \omega^4 \hat{m}_1 \hat{m}_2}{K_2 - \omega^2 \hat{m}_2}\right\}^2 + \{\omega \hat{f}_1\}^2}$$ Equation 9-22

Equation 9-22 is a complex phasor with real and imaginary terms and it is identical to equation 4-13. Therefore, the in-phase and out-of-phase components of the system response described by equation 9-22 are given by,

$$\frac{\mathbf{X_1}(\omega)}{\mathbf{F}(\omega)} cos\,\theta(\omega) = \frac{\left\{K_1 + \frac{-\omega^2 K_2(\hat{m}_1 + \hat{m}_2) + \omega^4 \hat{m}_1 \hat{m}_2}{K_2 - \omega^2 \hat{m}_2}\right\}}{\left[\left\{K_1 + \frac{-\omega^2 K_2(\hat{m}_1 + \hat{m}_2) + \omega^4 \hat{m}_1 \hat{m}_2}{K_2 - \omega^2 \hat{m}_2}\right\}^2 + \{\omega \hat{f}_1\}^2\right]}$$ Equation 9-23

$$\frac{\mathbf{X_1}(\omega)}{\mathbf{F}(\omega)} sin\,\theta(\omega) = \frac{-\{\omega \hat{f}_1\}}{\left[\left\{K_1 + \frac{-\omega^2 K_2(\hat{m}_1 + \hat{m}_2) + \omega^4 \hat{m}_1 \hat{m}_2}{K_2 - \omega^2 \hat{m}_2}\right\}^2 + \{\omega \hat{f}_1\}^2\right]}$$ Equation 9-24

where $\frac{\mathbf{X_1}(\omega)}{\mathbf{F}(\omega)}$ is the ratio of the magnitudes of the sensing pipe displacement and applied force phasors at ω and θ is the phase difference between the phase angle of the sensing pipe "displacement" and "applied force" phasors. Equation 9-23 and equation 9-24 can now be used to derive new expressions for the parameters $\hat{a}$ and $\hat{b}$ which, with reference to equation 4-17 and equation 4-18, may also be defined in terms of the displacement and force measurements obtained from the VDMS. These new expressions for $\hat{a}$ and $\hat{b}$ are given by,

$$\hat{a} = \frac{-\left\{K_1 + \frac{-\omega^2 K_2(\hat{m}_1 + \hat{m}_2) + \omega^4 \hat{m}_1 \hat{m}_2}{K_2 - \omega^2 \hat{m}_2}\right\}}{\{\omega \hat{f}_1\}}$$ Equation 9-25

$$\hat{b} = \frac{\left\{K_1 + \frac{-\omega^2 K_2(\hat{m}_1 + \hat{m}_2) + \omega^4 \hat{m}_1 \hat{m}_2}{K_2 - \omega^2 \hat{m}_2}\right\}}{\left[\left\{K_1 + \frac{-\omega^2 K_2(\hat{m}_1 + \hat{m}_2) + \omega^4 \hat{m}_1 \hat{m}_2}{K_2 - \omega^2 \hat{m}_2}\right\}^2 + \{\omega \hat{f}_1\}^2\right]}$$ Equation 9-26

If both sides of equation 9-25 are squared, the resulting expression when rearranged is given by,

$$\{\omega \hat{f}_1\}^2 = \frac{\left\{K_1 + \frac{-\omega^2 K_2(\hat{m}_1 + \hat{m}_2) + \omega^4 \hat{m}_1 \hat{m}_2}{K_2 - \omega^2 \hat{m}_2}\right\}^2}{\hat{a}^2}$$ Equation 9-27

Equation 9-26 and equation 9-27 can then be combined and simplified to obtain an expression for $\hat{b}$ in terms of $\hat{a}$, the forcing frequency ω, and the system properties $\hat{m}_1$, $\hat{m}_2$, K_1 and K_2 as follows,

$$\hat{b} = \frac{1}{\left[\left\{K_1 + \frac{-\omega^2 K_2(\hat{m}_1 + \hat{m}_2) + \omega^4 \hat{m}_1 \hat{m}_2}{K_2 - \omega^2 \hat{m}_2}\right\}\left(1 + \frac{1}{\hat{a}^2}\right)\right]} \qquad \text{Equation 9-28}$$

A mathematical expression for computing the modified mass $\hat{m}_2$ of the sensing pipe contents can then be obtained by making $\hat{m}_2$ the subject of formula in equation 9-28. Following a sequence of mathematical manipulations shown in Appendix G, the modified mass $\hat{m}_2$ of the sensing pipe contents is obtained as,

$$\hat{m}_2 = \frac{\left[\frac{1}{\omega^2}\left(K_1 - \frac{1}{\hat{b}\left(1 + \frac{1}{\hat{a}^2}\right)}\right) - \hat{m}_1\right]}{1 + \frac{\omega^2}{K_2}\left[\frac{1}{\omega^2}\left(K_1 - \frac{1}{\hat{b}\left(1 + \frac{1}{\hat{a}^2}\right)}\right) - \hat{m}_1\right]} \qquad \text{Equation 9-29}$$

From equation 9-2 and equation 9-29, the expression to compute the true mass m_2 of the contents within the sensing pipe is given by,

$$m_2 = \beta^2 \left\{ \frac{\left[\frac{1}{\omega^2}\left(K_1 - \frac{1}{\hat{b}\left(1 + \frac{1}{\hat{a}^2}\right)}\right) - \hat{m}_1\right]}{1 + \frac{\omega^2}{K_2}\left[\frac{1}{\omega^2}\left(K_1 - \frac{1}{\hat{b}\left(1 + \frac{1}{\hat{a}^2}\right)}\right) - \hat{m}_1\right]} \right\} \qquad \text{Equation 9-30}$$

Equation 9-30 gives an expression for computing the true mass m_2 of the sensing pipe contents in terms of the sensing pipe modified mass $\hat{m}_1$, where $\hat{m}_1$ is defined in equation 9-1, the sensing pipe stiffness constant K_1, the forcing frequency ω, the measurement parameters $\hat{a}$ and $\hat{b}$, the VDMS constant β and the stiffness constant K_2 of the coupling between the pipe contents and the sensing pipe. The predictive density model developed in equation 9-30 represents a novel contribution of this work and it can be used to provide a relatively more accurate mixture density measurement in

compressible flows provided the coupling stiffness constant K_2 between the flow mixture and the pipe can be correctly estimated, in addition to ω and λ.

For an incompressible flow mixture, e.g. "water only" and solids-in-water flow, where the compressibility of the flow mixture is approximately zero, the coupling stiffness constant K_2 of the mixture will be infinite and so equation 9-30 can be simplified as shown below,

$$m_2 = \beta^2 \left\{ \left[\frac{1}{\omega^2} \left(K_1 - \frac{1}{\hat{b}\left(1 + \frac{1}{\hat{a}^2}\right)} \right) - \hat{m}_1 \right] \right\} \qquad \text{Equation 9-31}$$

which is the same as the original mathematical expression for m_2 derived in section 4.2 and given by equation 4-27. Equation 9-30 provides an improved model which considers the coupling between the contents of the sensing pipe and the pipe when the VDMS undergoes dynamic vibration.

9.3 Method to estimate the coupling stiffness constant K_2 between the air-in-water mixture and the VDMS in vertical upward pipe flows.

For a compressible fluid mixture, e.g. air-in-water, the stiffness term K_2 must be known in order to use equation 9-30 to predict the mixture density. Thus, knowledge of the overall coupling stiffness constant of the mixture is required. A technique that can be used to estimate K_2 will now be described here.

The thermodynamic relationship for the adiabatic expansion or compression of the gas in the air-water mixture can be written as,

$$PV^{\gamma} = C \qquad \text{Equation 9-32}$$

where P is the gas pressure, V is the volume occupied by the gas phase in the mixture, C is a constant and γ is the ratio of the specific heats for air and it is defined by,

$$\gamma = \frac{C_p}{C_v} \qquad \text{Equation 9-33}$$

where C_p is specific heat of the gas phase at constant pressure and C_v is specific heat of the gas at constant volume. In order to rearrange the expression in equation 9-32 into a form that can be simplified, a new variable "u" is introduced and is defined by,

$$u = V^{\gamma} \qquad \text{Equation 9-34}$$

By substituting equation 9-34 into equation 9-32 and differentiating the resulting expression with respect to a new dummy variable "x" gives,

$$P\frac{du}{dx} + u\frac{dP}{dx} = 0 \qquad \text{Equation 9-35}$$

Also, equation 9-34 is differentiated with respect to x and the resulting differential substituted into equation 9-35 to give,

$$P\gamma V^{\gamma-1}\frac{dV}{dx} + V^{\gamma}\frac{dP}{dx} = 0 \qquad \text{Equation 9-36}$$

By rearranging equation 9-36, the compressibility of the gas in the mixture can now be obtained as follows,

$$\frac{-dP}{dV} = \frac{P\gamma}{V} \qquad \text{Equation 9-37}$$

For an air-in-water mixture flowing through the sensing pipe, the following assumptions are made about the flow in order to simplify the model to obtain the mixture coupling stiffness constant K_2, (i) the bubbles are all spherical in shape and have a radius r and (ii) the air bubbles are arranged in such a manner that they form springs which acts in series with each other. Many such "series springs" in the mixture may be considered as acting in parallel with each other when they interact in the direction parallel to the direction of the vibratory motion. It is assumed here that there are N bubbles in each vertical column and M × M bubbles in each horizontal plane. A simplified diagram showing the air bubbles in the pipe is shown in figure 9-3.

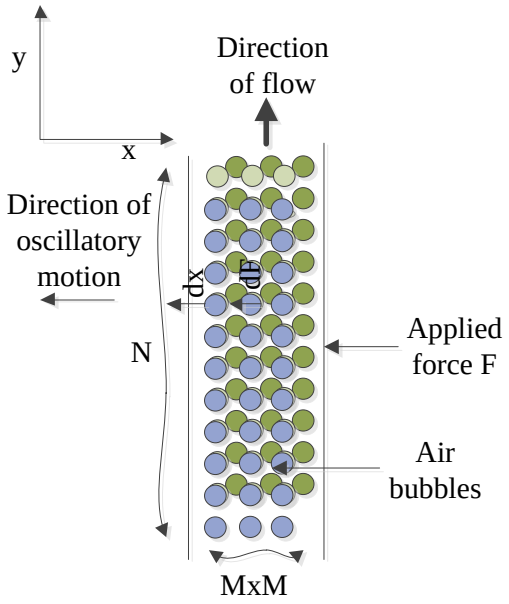

Figure 9-3: Diagram of air-in-water flow with air bubbles acting as springs in parallel

For the air-in-water mixture, the mixture coupling stiffness constant K_2^* of a single gas bubble is given by,

$$K_2^* = \frac{dF}{dx}$$ Equation 9-38

where dF is the change in the force exerted on the gas bubble by the mixture and dx is the resulting displacement of the bubble due to this change in force. dF and dx are in the direction of the oscillatory motion of the mixture and may be approximated by the expressions,

$$dF = AdP$$ Equation 9-39

$$dx = \frac{-dV}{A}$$ Equation 9-40

where A is the cross sectional area of the gas bubble, dP is the pressure exerted by mixture on the bubble and dV is the change in volume of the gas bubble. The negative sign in equation 9-40 indicates that there is a decrease in the gas volume when it is compressed. By substituting equation 9-39 and equation 9-40 into equation 9-38, an approximate expression for computing the stiffness constant of the gas bubble is obtained as,

$$K_2^* = -A^2 \frac{dP}{dV}$$ Equation 9-41

By combining equation 9-37 and equation 9-41, an expression to compute the coupling stiffness constant K_2^* of a single gas bubble in the air-in-water flow is obtained as,

$$K_2^* = A^2 \frac{P_i{}^* \gamma}{V^*}$$ Equation 9-42

where V^* is the volume of each individual gas bubble and $P_i{}^*$ is the internal pressure of each gas bubble and is defined by [178]

$$P_i{}^* = P_o + \frac{2\sigma}{r}$$ Equation 9-43

where P_o is the atmospheric pressure acting against the external wall of the bubble, σ is the air-water interfacial surface tension and r is the bubble radius. For the type of air-in-water flows described in figure 9-3, the total number of bubbles T in the mixture can be defined by,

$$T = N \times (M \times M)$$ Equation 9-44

In the direction of the oscillatory motion of the pipe, each horizontal row of M bubbles can be considered as springs acting in series with each other and so will have an effective stiffness K_M given by,

$$K_M = \frac{K_2^*}{M}$$ Equation 9-45

With reference to figure 9-3, there are $N \times M$ effective gas bubble columns which may be considered to form springs with stiffness K_M and acting in parallel with each other. Therefore the overall stiffness K_2 of the mixture is given by,

$$K_2 = K_M \times N \times M = NK_2^*$$ Equation 9-46

Note that K_2 may also be considered as being the stiffness of the coupling between the pipe and its contents. The following approximation is made here in order to simplify the expression for obtaining the total number of air bubbles T in the sensing pipe.

$$\frac{N}{M} = \frac{L}{D}$$ Equation 9-47

where L and D are the sensing pipe length and diameter respectively. By making M the subject of formula in equation 9-47 and firstly, substituting M into equation 9-44 and then substituting the resulting expression into equation 9-46, an equation to obtain an approximate estimate of the overall coupling stiffness K_2 of the air-in-water mixture can be obtained as follows,

$$K_2 = NK_2^* = K_2^* T^{\frac{1}{3}} \left(\frac{L}{D}\right)^{\frac{2}{3}}$$ Equation 9-48

If the air volume fraction in the flow pipe in figure 9-3 is α_a, then the total number of bubbles contained in the mixture can also be defined by,

$$T = \frac{\alpha_a V_{pipe}}{V^*}$$ Equation 9-49

where V_{pipe} is the sensing pipe volume and V^* is the volume of the individual air bubbles. Therefore, the coupling stiffness K_2 for T gas bubbles is given by,

$$K_2 = \left[5.58\gamma r^{-3}\left(P_o + \frac{2\sigma}{r}\right)(\alpha_a V_{pipe})^{\frac{3}{2}}\left(\frac{L}{D}\right)^{\frac{2}{3}}\right]$$ Equation 9-50

Equation 9-50 gives an expression that was used in the current research work to compute an approximate value of the coupling stiffness constant K_2 in air-water flows. From equation 9-50, it is seen that the expression for computing K_2 is related to the volume fraction α_a of air in the mixture and the radius r of the air bubbles. As α_a becomes close to zero (approaching a single phase flow), the bubble radius become zero and the value of K_2 tend to infinity. Conversely, K_2 will decrease as α_a increases and the bubble radius become bigger. It is important to state here that the model given in equation 9-50 is only valid for homogeneous, bubbly air-water flows where the air bubbles are uniformly distributed.

9.4 Modified VDMS constant for air-in-water pipe flows

It will be recalled that the bench testing described in section 5.10.1 from which the VDMS constant β_{opt}, which was used to compute $\rho_{aw,m,n,i}$ in chapter 8, was obtained using test mixtures which were incompressible (liquid only, liquid-liquid and solids-liquid) (see table 5-3). It is plausible that this value of β_{opt} could increase the modelling errors observed in section 8.6 and 8.7 when the VDMS was used to obtain $\rho_{aw,m,n,i}$ and $\bar{\alpha}_{a,m,n}$ respectively. Since the VDMS constant β is influenced by the mass distribution of the contents of the vibrating pipe, it was therefore decided that a modified β value that is well suited for air-in-water flows be derived from bench testing using both incompressible and compressible test mixtures. Further bench tests were thus required to determine this modified VDMS constant. Two additional test mixtures were formulated using polystyrene balls, water and vegetable oil. Eleven polystyrene balls were interconnected using a thin thread to form a ring. The ring was placed inside the sensing pipe, and across its length, to act as air bubbles.

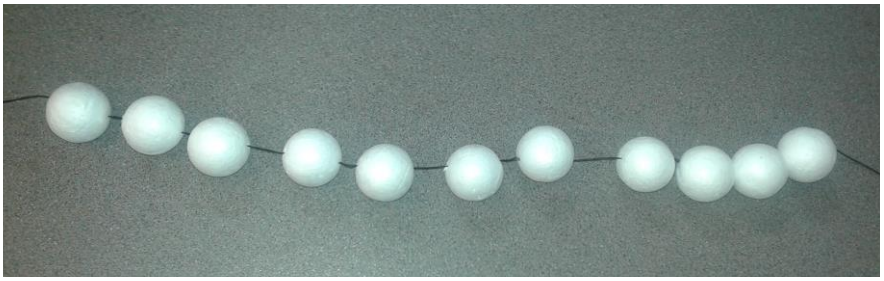

Figure 9-4: Ring of polystyrene balls to represent air bubbles

The two test mixtures were prepared using the polystyrene balls and oil and the polystyrene balls and water and their properties are shown in Table 9-1

Table 9-1: Composition of additional test mixtures to determine the modified VDMS constant for compressible and incompressible flows

Test mixture (S/No)	Test mixture name	Components of test Mixture	Actual mass of VDMS (m_1+m_2) [Kg]	Density of test mixture [kg/m^3]
TM-8	Test mixture 8	Sensing pipe(2.2kg)+v.oil(2.22kg)+polystyrene balls(8.2g)	4.428	797.43
TM-9	Test mixture 9	Sensing pipe(2.2kg)+water(2.45kg)+polystyrene balls(8.2g)	4.658	879.75

For each of these test mixtures, the VDMS operating frequency was varied from 0rad/s to 950rad/s at predefined frequency intervals and at each of these measurement frequency points, the displacement and force signals were measured and then applied to the signal processing technique described in section 4.5 to compute the magnitude and phase frequency responses of the system whilst the theoretical magnitude and phase frequency responses were computed using equation 9-52. The iteration technique described in section 5.9 was then used to obtain the values of β which gave the best fit between the theoretical and experimental magnitude and phase frequency response data. These values of β are shown in table 9-2 while the magnitude and phase frequency response plots for test mixture (8) and (9) are shown in figure 9-5 and figure 9-6 respectively.

Table 9-2: Bench test result for VDMS constant in gas-liquid mixture

S/No	**Components of test Mixture**	**VDMS constant, β**
Test mixture 8	Sensing pipe(2.2kg)+v.oil(2.22kg)+polystyrene balls(8.2g)	1.3198
Test mixture 9	Sensing pipe(2.2kg)+water(2.45kg)+ polystyrene balls(8.2g)	1.2980

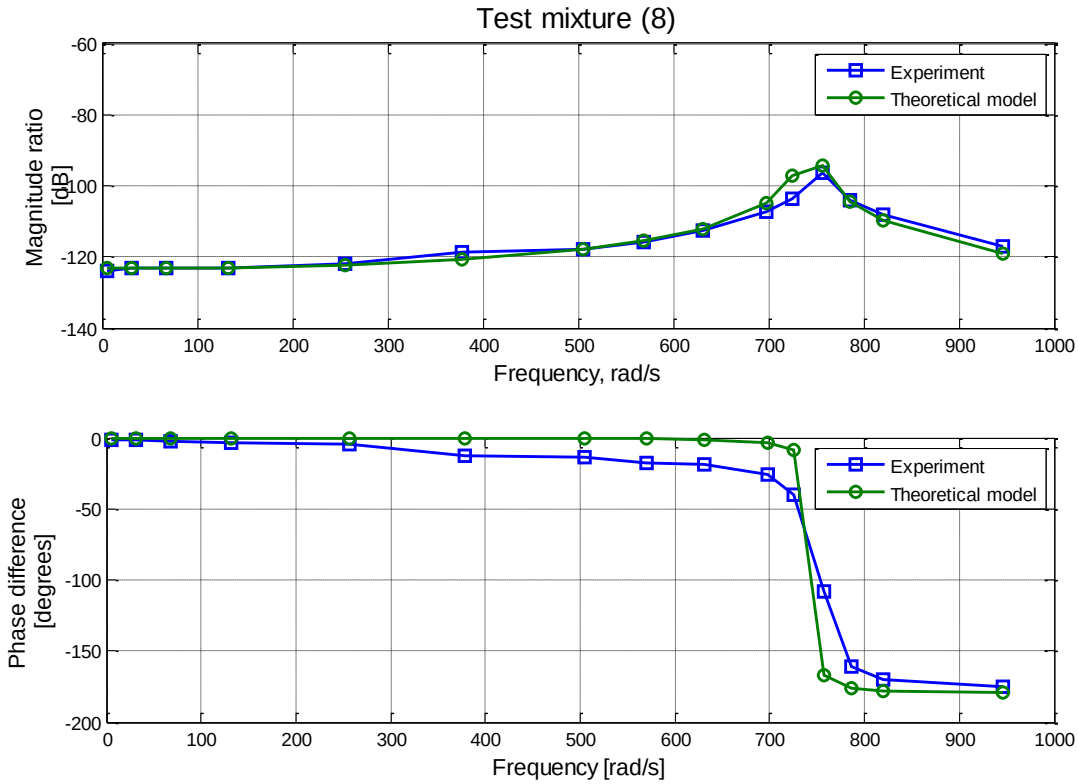

Figure 9-5: Experimental and theoretical frequency response plots for test mixture (8)

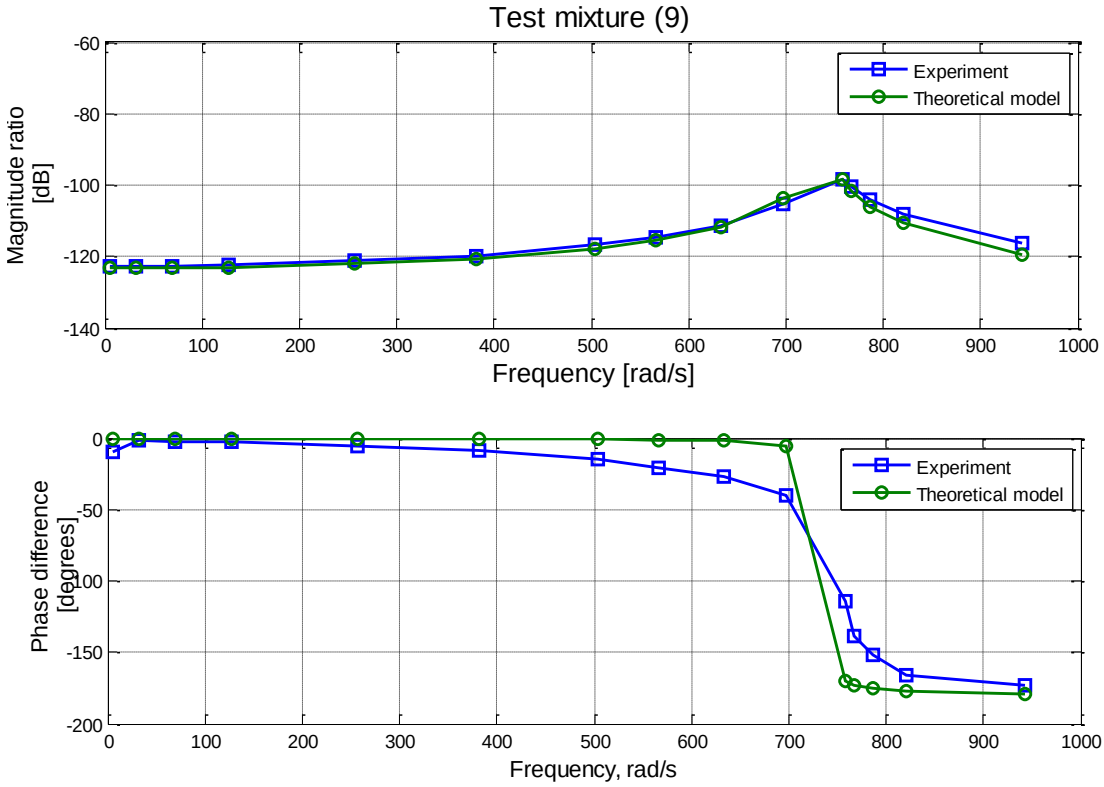

Figure 9-6: Experimental and theoretical frequency response plots for test mixture (9)

Following on from the grouping of the "test mixtures" shown in table 5-5, test mixture (8) and (9) were grouped as "gas-liquid" and the average value of β for this group was obtained as 1.3089 from table 9-2. Furthermore, a single value of β for the "liquid-liquid" and "gas-liquid" test mixture groups was then obtained by taking the average of the values of β for these two groups of test mixtures. The value of β_{mod} was obtained as 1.2966. This modified value of the VDMS constant β_{mod} was used in computing all results in this chapter, which required the use of model-2.

Next, experimental frequency response data were obtained using the dynamic flow loop described in section 6.2 for air-in-water flows with 3% and 23% air volume fraction respectively, and these results were compared with the theoretical frequency response data obtained using model-1 and model-2 for the same flow types. These frequency response data provided a basis for qualitative and quantitative comparison of the agreement between model-2, model-1 and the experimental data obtained for the type of air-in-water flows that were used in the investigation with the new β_{mod} value. In this experiment, the VDMS was operated from 0rad/s to 890rad/s at pre-selected frequency points. This frequency range for which the VDMS was operated was selected to show characteristics of the system up to and just beyond the first fundamental frequency. The computer based VDMS control system described in section 7.5.3 was operated in "manual mode" and was used to obtain the measured displacement and force signals which were used to provide the relevant displacement, force and frequency data that were applied to the signal processing technique described in section 4.5 to compute the experimental frequency response data. Additionally, the theoretical frequency response data were obtained for model-1 and model-2 respectively as follows,

$$\left|\frac{\mathbf{X_1}}{\mathbf{F}}\right| = 20\,log_{10}\frac{1}{\sqrt{\left(K_1 - \omega^2(\hat{m}_1 + \hat{m}_2)\right)^2 + (\omega\hat{f}_1)^2}} \qquad \text{Equation 9-51}$$

$$\left|\frac{\mathbf{X_1}}{\mathbf{F}}\right| = 20\,log_{10}\frac{1}{\sqrt{\left\{\left(K_1-\omega^2\hat{m}_1-\frac{\omega^2K_2\hat{m}_2}{K_2-\omega^2\hat{m}_2}\right)^2+(\omega\hat{f}_1)^2\right\}}}$$

Equation 9-52

In this experiment, it was visually observed that for the flows with 3% air volume fraction, the bubble sizes were relatively small (between 5mm to 10mm) and moved in a streamlined pattern in the flow loop working section. However, for the experiment with 23% air volume fraction, the air bubbles were observed to agglomerate into larger structures at the pipe centre and formed bigger size air bubbles. The bubble pattern was also observed to be very chaotic. In equation 9-52, the value of K_2 was computed using equation 9-50.

9.5 Comparison of the theoretical and the experimental frequency response results of the VDMS when used in air-in-water vertically upward pipe flows

In this section, the theoretical frequency response data were obtained using model-1 and model-2, given by equation 9-51 and equation 9-52 respectively, and the experimental frequency response data were obtained using equation 4-50, for flows with 3% and 23% air volume fraction respectively. The magnitude frequency response data provided a tool for comparison of the theoretical frequency responses obtained using model-1 and model-2 and the experimental frequency responses and these results are shown in figure 9-7 and figure 9-8.

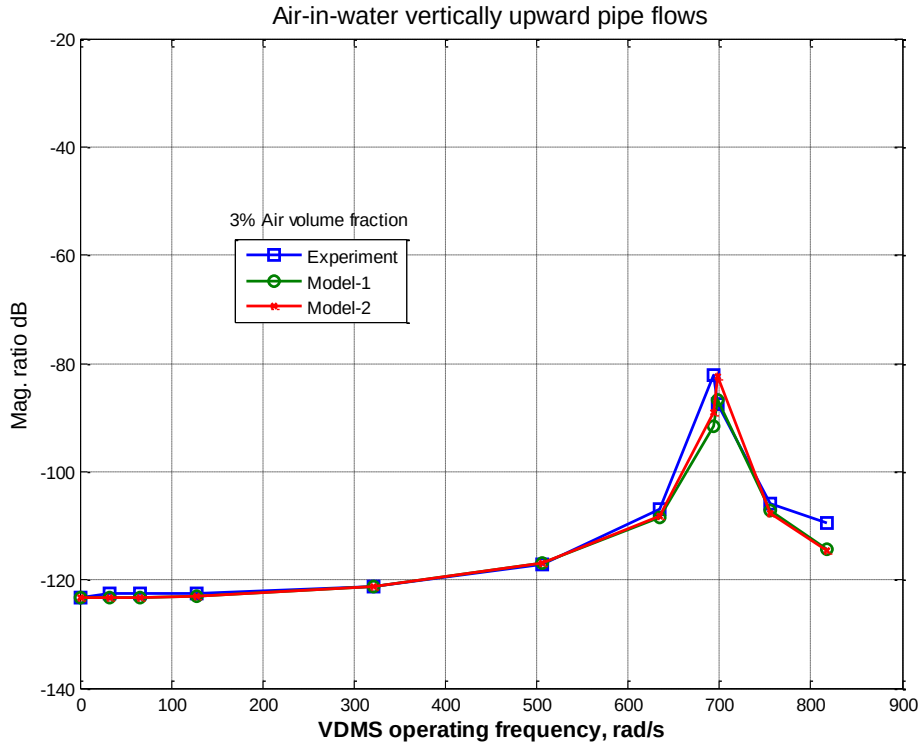

Figure 9-7: Magnitude ratio versus VDMS operating frequency plots for air in water flows with 3% air volume fraction

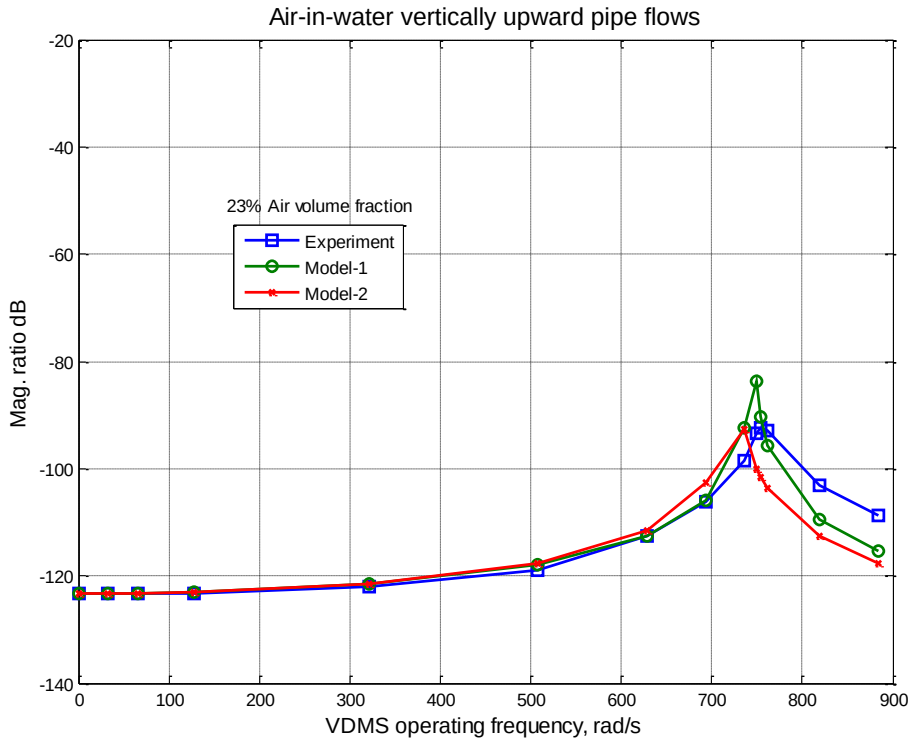

Figure 9-8: Magnitude ratio versus VDMS operating frequency plots for air in water flows with 23% air volume fraction

In the results shown in figure 9-7 and figure 9-8, the values of $\hat{m}_1$, $\hat{m}_2$ and $\hat{f}_1$ used in model-1 and model-2 were obtained using equation 9-1 to equation 9-3 respectively where m_1 and f_1 were gotten from the bench testing described in section 5.4 and 5.5 while m_2 was computed using the air-water mixture density and air volume fraction. From the results shown in figure 9-7, it is seen that the respective magnitude ratio versus frequency plots obtained using model-1 and model-2 for flows with 3% air volume fraction show good agreement with the experimental data for the VDMS operating frequencies ω between 0rad/s to 750rad/s. However, when ω was at the resonant frequency, the value of the system magnitude ratio obtained using model-1 is seen to be less than that obtained using model-2 and the experimental data, which are similar. This may be because model-1 does not account for the flow mixture compressibility property. These results suggest that model-2 is likely to give a more accurate description of the actual dynamic response of the flow than model-1. Additionally, the results in figure 9-8 shows that for the experiments conducted using air-in-water mixture with 23% air volume fraction, the magnitude ratio versus VDMS operating frequency ω plots obtained using the experimental data, model-1 and model-2 respectively were in good agreement for values of ω from 0rad/s to frequencies around the resonant frequency. For values of ω at the resonant frequency and beyond, the results show a significant difference between the magnitude ratio responses obtained using the experimental data, model-1 and model-2 respectively. These results suggest that neither model-1 nor model-2 gave an accurate description of the actual dynamic response of the system for the experiment using 23% air volume fraction for values of ω at the resonant frequency and beyond. The variation observed between the experimental data, model-1 and model-2 results shown in figure 9-8 is predictable given that model-1 does not take into account the "springiness" properties of the air-water mixture and the mathematical model given in equation 9-50 to compute the air-water flow coupling stiffness constant K_2 associated with model-2 is only valid for homogeneous bubbly flows (flows

with air volume fraction less than 10%). From the results presented in figure 9-7 and figure 9-8, it is plausible that model-2 will give a more accurate value of $\rho_{aw,m,n,i}$ for bubbly flows compared with model-1. The modelling error in $\rho_{aw,m,n,i}$ is likely to increase as the mixture air volume fraction increases. These results further explain the likely reason for the air volume fraction dependent systematic errors observed in the air-in-water flow experiment results presented in section 8.6. Hence, the experiments where the air volume fraction of the flow mixture was 1% had a mean error $\bar{e}_{aw,m,n}$ that was significantly lower when compared with the experiments where the air volume fraction of the flow mixture was 23%. It was therefore instructive to compare the air volume fraction dependent systematic errors in the predicted mixture density $\rho_{aw,m,n,i}$ obtained using model-1 and model-2 for the air-water flows given in table 8-6.

9.6 Comparison of predicted mixture density obtained using model-1 and model-2 in air-in-water vertically upward flows where air volume fraction is less than 10%

The main intention in this section is to compare the accuracies of the predicted air-water mixture density obtained using the VDMS when model-1 and model-2 are separately implemented using the signal processing technique described in section 4.5 for air-in-water flows with less than 10% air volume fraction. The air-water mixture densities $\rho_{aw,m,n,i}$ were computed using model-1, as defined in equation 4-29, and model-2, as defined in equation 9-30, for the air-in-water vertically upward pipe flow conditions given in table 8-6 where the air volume fraction in the mixture is less than 10% i.e FC_{aw}-1 to FC_{aw}-7. For the i^{th} density measurement $\rho_{aw,m,n,i}$ taken at a given flow condition used in this experiment, a percentage relative error $e_{aw,n,i}$ in $\rho_{aw,m,n,i}$ values obtained using model-1 and model-2 was computed using equation 8-2. The value of $e_{aw,n,i}$ obtained was then used to compute the mean error $\bar{e}_{aw,n}$ in $\rho_{aw,m,n,i}$ using equation 8-3 and these results are shown in figure 9-9.

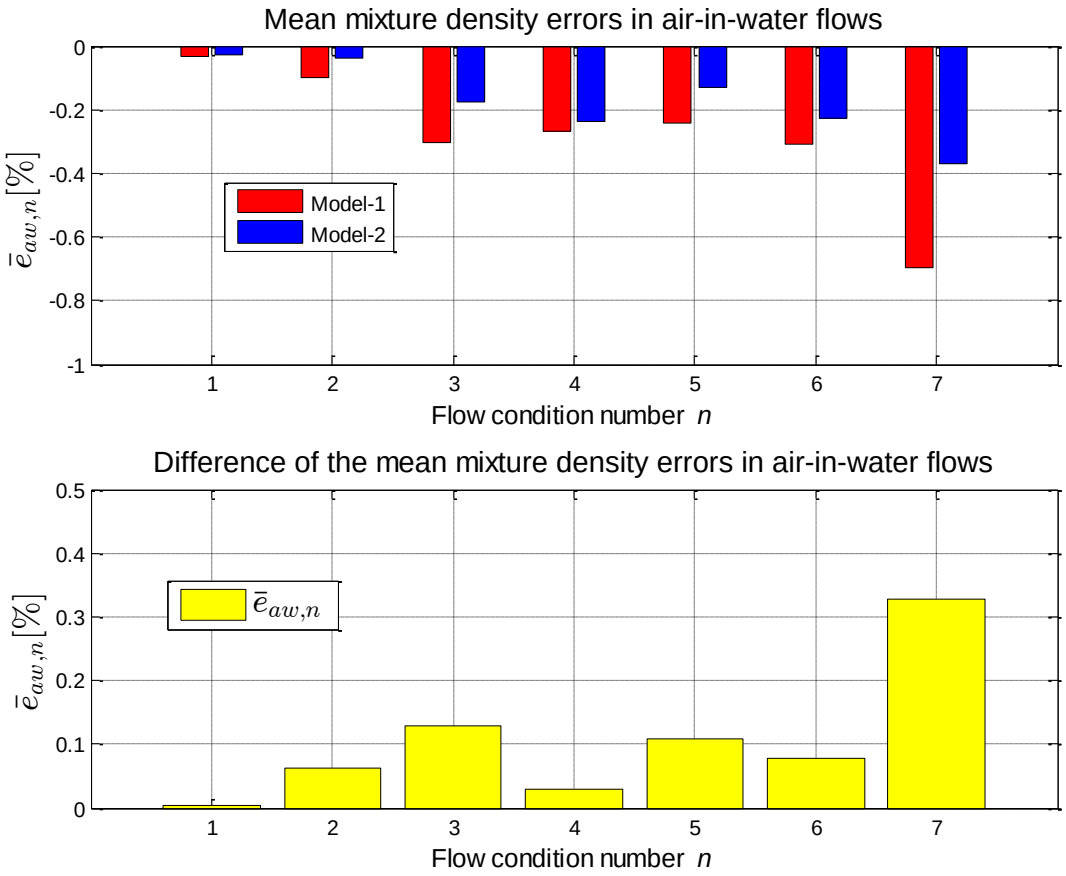

Figure 9-9:(a) Comparison of mean errors in air-in-water flows(b) absolute difference in mean errors obtained using model-1 and model-2

The vertical axis in figure 9-9(a) represent the mean error $\bar{e}_{aw,n}$ in $\rho_{aw,m,n,i}$ obtained using the model-1 and model-2 whilst the vertical axis in figure 9-9(b) represent the difference between $\bar{e}_{aw,n}$ obtained using model-1 and model-2 respectively. From the results shown in figure 9-9 (a) and (b), it is seen that for FC_{aw}-1 to FC_{aw}-7 the mean errors $\bar{e}_{aw,n}$ in $\rho_{aw,m,n,i}$ obtained using model-2 is smaller in magnitude when compared to the mean error obtained using model-1 for a similar flow condition. This result suggests that for FC_{aw}-1 and FC_{aw}-7 where the air volume fraction of the air-water flow mixture was between 0.07% and 9.7%, it was possible to obtain a relatively accurate estimate of the flow mixture coupling stiffness K_2 using the mathematical model given in equation 9-50 and hence a more accurate value of $\rho_{aw,m,n,i}$ was obtained using model-2 than model-1. Comparatively, the overall mean error $\bar{e}_{aw,t}$ obtained using model-1 and model-2 at

FC_{aw}-1 to FC_{aw}-7 was reduced by 39% from -0.28% to -0.17%. From the results shown in figure 9-9(a) and (b), it is therefore possible to say that the method given in equation 9-50 for obtaining K_2 value and the modified density prediction model (model-2) given in equation 9-31 can be used to obtain relatively accurate estimates of the air-water mixture density $\rho_{aw,m,n,i}$ for the type of bubbly flows used in this investigation where the air volume fraction is less than 10%. It is plausible that the modelling error in the estimation of K_2 will increase significantly when used in air-water flows with air volume fraction greater than 10% due to the model assumption that the flow is bubbly and homogenous.

Gysling and Banach [138] have used a speed of sound based gas volume fraction measurement technique to account for the compressibility effect in air-water flows and have obtained air-water mixture density measurements with relative accuracy of about 2% for air volume fractions up to 5%. Also, Juhl [179] obtained mean errors up to 12% when using a Coriolis flow meter to measure the mixture density in air-water flows for air volume fractions from 0% to 10%.

The air-water mixture density results obtained using the VDMS thus indicates that the modified density prediction model (model-2) presented in this chapter can be used in bubbly flows (of the type used in this investigation) to provide relatively accurate and reliable mixture density measurement provided that the mixture coupling stiffness can be correctly estimated.

9.7 Summary

A modified mathematical model to accurately predict the mixture density in air-in-water flow has been presented in this chapter. The modified mathematical model requires knowledge of the flow mixture coupling stiffness constant K_2 in addition to ω, K_1, β and λ to predict the air-water mixture density. Also, a method was developed for computing the coupling stiffness constant K_2 between the air-water mixture and the sensing pipe. Further bench tests were conducted to determine a modified VDMS constant β_{mod} that was used in the air-water flow experiments to describe the

dynamic behaviour of the VDMS and to compute the mixture density. This chapter also presents and discusses the comparison between the experimental and theoretical frequency responses of the VDMS for experiments using air-water flow mixtures with 3% and 23% air volume fractions respectively. The results obtained showed that the frequency responses of the VDMS obtained using model-1 and model-2 agreed nicely with the experimental frequency response data for the experiments with 3% air volume fraction and showed large variation for the experiments with 23% air volume fraction. Lastly, the mean of the mixture density error obtained using the model-1 and model-2 were compared for a similar set of air-in-water flow conditions and the results showed that model-2 provided a more accurate mathematical model for predicting mixture density for flows with air volume fraction less than 10%.

Chapter 10

CONCLUSIONS AND FUTURE WORK

10.1 Conclusions

This chapter presents the main conclusions drawn from this research. It describes how well the research work has met the aims and objectives presented in section 2.4 and section 2.5 respectively. It also summarizes the contribution to knowledge made by this research and the authors' recommendations for future work. The key aim of this research work was to design and develop a novel, non-invasive densitometry system that could be used to predict the mixture density in single phase and multiphase pipe flow without the need for a radioactive source and which will be inexpensive and relatively accurate compared to existing densitometry systems. The current research work has achieved the primary aims stated in section 2.4 by designing, developing and successful testing a non-invasive densitometry system which uses the mechanical vibration characteristics of a pipe and the pipe contents to predict the flow density in single phase and multiphase pipe flows. The densitometry system developed consists of three essential units; (i) a measurement unit comprising a sensing pipe, a force actuator, a force sensor, a displacement sensor, a coil current sensor and a temperature sensor; (ii) a signal conditioning and processing unit comprising of the relevant electronic circuits that ensures the measurement signals do not contain noise and are at a measureable level; and (iii) a data acquisition unit to acquire and save the measurement signals to a computer for further processing. The usability of the densitometry system developed in the current research was also extended to predict the mean phase volume fractions in homogeneous two-phase solids-in-water and air-in-water flows.

A novel mathematical model for computing the fluid density in single phase and multiphase pipe flows was developed using the mechanical vibration theory for a beam with two ‘fixed end’ supports and having a forced excitation. This mathematical model uses the stiffness constant K_1

and mass m_1 of the sensing pipe, the forcing frequency ω, a defined density measurement parameter λ and a constant β to compute the mass of the pipe contents, which was then used to compute its density. A signal processing technique was developed to implement the density prediction model and it used the DFT technique to compute the phase difference θ between the sensing pipe displacement $\mathbf{X}_1$ and applied force **F** phasors and their respective peak magnitudes which were in turn used to compute the parameter λ. The signal processing technique was also used to obtain the forcing frequency ω.

Several bench tests were carried out to determine the sensing pipe mass m_1, pipe stiffness constant K_1 and VDMS constant β which were required to implement the density prediction model. A bench test was also conducted to verify that the sensing pipe maximum displacement was at its centre when a load was applied to its centre and hence determine the spatial location of the displacement and force sensors on the sensing pipe. The respective signal conditioning circuits were calibrated to ensure accurate measurements were obtained from the sensors associated with the measurement unit before the data acquisition unit was configured. Once the densitometry system was completed, several 'test mixtures' comprising 'liquid only', 'liquid-liquid' and solids-liquid' mixtures with different properties were developed (see table 5-3) to conduct frequency response tests on the densitometry system. For each of the test mixtures developed, the VDMS was operated over a specific frequency range and the force and displacement signals obtained from the dynamic response of the system were used to generate experimental Bode plots while the theoretical Bode plots were generated from the mathematical model given in equation 4-12. The results obtained from the frequency response tests were used to determine the VDMS constant β using an iterative technique developed using Microsoft Excel solver. This value for β gave the best agreement between the experimental and theoretical frequency responses of the VDMS for the test mixtures used in the investigation and are presented in figure 5-12 to figure 5-18 in section 5.8.2.

Once the VDMS constant β was obtained, bench experiments were conducted to investigate the capability of the constructed densitometry system to accurately predict mixture density in a pipe flow. These experiments were conducted using the same test mixtures which had been used for the frequency response investigation. For a given test mixture, the VDMS was operated at preselected frequency points between 500rad/s to 760rad/s and the measured force and displacement signals were used with the signal processing technique to compute the predicted density. A relative percentage error was then computed for each measurement taken for a test mixture. Two statistical tools, namely, mean error and the standard deviation of the error were used to compare the density measurements obtained using the VDMS and the reference density. For a given test mixture used in the investigation, the mean error $\bar{e}_{tm}$ and standard deviation S_{tm} of the errors in the predicted density obtained at each i^{th} operating frequency were computed using equation 5-16 and equation 5-17 respectively. The results obtained (see figure 5-19) showed that for all the measurements taken using the seven test mixtures described in table 5-3, the vast majority of the mean errors in the predicted density were within $\pm 5\%$ of reading as the VDMS operating frequency was varied between 500rad/s and 760rad/s. The magnitude of these errors was appreciably large and it was thus necessary to optimize the operation of the densitometry system to reduce these errors. The method for computing the predicted mixture density and the results obtained from the bench experiment were analysed and used to define optimal operating conditions for the VDMS. These optimal operating conditions included a reduced frequency range (660rad/s-710rad/s) for operating the VDMS which ensured the measurement errors associated with the force and displacement sensors were minimized, an optimized VDMS constant β_{opt} and an appropriate sampling frequency which ensured the resolution of the DFTs was increased and hence the VDMS operating frequency ω was more accurately measured. The mean error associated with the VDMS when it was used to measure the density of a test mixture at a given operating frequency was significantly

reduced from $\pm 5\%$ to $\pm 1\%$ by using the optimized operating conditions. Also, the standard deviation of the errors in the measured densities was reduced from 1.81% to 1%.

The VDMS was then installed in a multiphase flow loop facility at the University of Huddersfield which is capable of generating 'water only', 'solids-in-water' and 'air-in-water' vertical and inclined upward flows. The reference instruments included in the flow loop were firstly calibrated before use. Experiments were then performed using the VDMS to predict the mixture density in 'water only', 'solids-in-water' and 'air-in-water' vertically upward flows and for each of these flow types, several flow conditions were generated. A computer based control system was designed and developed using LabVIEW to ensure the VDMS could be operated at its optimal frequency and also to provide an online computation of the flow mixture density. The system includes a set of LabVIEW routines (i) to generate an excitation signal that is sent to the VCA, (ii) to measure the force, displacement, coil current and temperature signals from the respective sensors, (iii) to compute the VDMS optimal operating frequency and (iv) to implement the signal processing technique online.

When the VDMS was operated at its optimal frequency of 684rad/s and used to measure water density in 'water only' vertically upward flows, the mean error $\bar{e}_{w,n}$ observed in the predicted density $\rho_{w,m,n,i}$ for each of the thirteen flow conditions investigated were within $\pm 0.50\%$ of the reference density measurement. The overall mean error $\bar{e}_{w,t}$ and standard deviation $S_{w,t}$ of the errors in $\rho_{w,m,n,i}$ across all the flow conditions were obtained as 0.07% and 0.01% respectively. When the VDMS was used in solids-in-water vertically upward flows to the predict the mixture density $\rho_{sw,m,n,i}$, the mean of the mixture density measurement errors $\bar{e}_{sw,n}$ associated with the measurements taken at a given flow condition using the VDMS were again observed to be within $\pm 0.50\%$ of the reference mixture density measurement. The overall mean error $\bar{e}_{sw,t}$ and standard deviation $S_{sw,t}$ of the errors in $\rho_{sw,m,n,i}$ across all of the solids-in-water flow conditions

investigated were obtained as -0.13% and 0.19% respectively. Additionally, the predicted mean solids volume fractions $\bar{\alpha}_{s,m,n}$ obtained using the VDMS in solids-in-water flows were within $\pm 10\%$ of the reference $\bar{\alpha}_{s,ref,n}$ mean solids volume fraction measurements for the vast majority of the flow conditions used in the investigation. It was observed that the values of the mean error $\bar{e}_{s,n}$ and standard deviation $S_{s,n}$ of the errors in $\alpha_{s,m,n,i}$ were larger for the flow conditions where $\bar{\alpha}_{s,ref,n}$ in the flow pipe working section was relatively small and the solids-water mixtures were inhomogeneous.

Lastly, the computer based VDMS control system was used in air-in-water experiments to obtain the VDMS optimal operating frequency ω_{opt} for the different flow conditions used in the investigation and to obtain relevant air-water mixture density $\rho_{aw,m,n,i}$ measurements. In this experiment, the mean error $\bar{e}_{aw,n}$ in the air-water mixture density $\rho_{aw,m,n,i}$ measurements obtained using the VDMS were within $\pm 1\%$ of the reference $\rho_{aw,ref,n,i}$ air-water mixture density for the different flow conditions investigated where the air volume fraction in the mixture was less than 10% (see figure 8-21). It was observed that an air volume fraction dependent systematic error existed in $\rho_{aw,m,n,i}$ measurements. Additionally, the mean errors $\bar{e}_{a,n}$ in the predicted $\alpha_{a,m,n,i}$ air volume fraction obtained using the VDMS at a given flow condition were within $\pm 10\%$ of the reference $\alpha_{a,ref,n,i}$ air volume fraction for air-in-water flows were the air volume fraction was less than 10%. These errors $\bar{e}_{a,n}$ were observed to increase significantly for air-water flows with air volume fractions that were greater than 10%.

A modified density prediction model, referred to as model-2 in chapter 9, was then developed to attempt to minimize the air volume fraction dependent systematic errors $\bar{e}_{aw,n}$ (see figure 8-26) observed when the VDMS was used to obtain mixture densities $\rho_{aw,m,n,i}$ in air-in-water flows. The modified density prediction model, given in equation 9-30, required a correct estimation of the coupling stiffness K_2 between the pipe and the pipe contents for air-water mixtures. Correct

values for ω, K_1, β and λ were also necessary to correctly predict the density of the mixture. A method to obtain an approximate estimate of the coupling stiffness K_2 between the pipe and the air-in-water mixture was also developed. Further experiments were also conducted using air-in-water flows with 3% and 23% air volume fractions respectively and the results obtained were used to compare the VDMS experimental frequency responses and theoretical frequency responses obtained using model-1 and model-2. The results of the experiments (see figure 9-7 and figure 9-8) showed that the frequency response plots obtained using the theoretical models (model-1 and model-2) agreed closely with the experimental data for the flow with 3% air volume fraction. However, for the flows with 23% air volume fraction the frequency response plots obtained using the experimental data, model-1 and model-2 all showed significant variation from each other at frequencies around the resonant frequency. This seemingly large variation between the frequency response plots suggested the existence of large modelling errors when the VDMS is used in such flow types. The modelling errors may have been caused by inaccurate estimation of the K_2 given the validity conditions (see section 9.3) associated with the mathematical model that was used to compute K_2 and the fact that model-1 does not account for the coupling stiffness constant between the pipe and the air-water mixture. The modified (model-2) and initial (model-1) density prediction models given in equation 4-29 and equation 9-30 respectively were again used to obtain the air-water mixture density $\rho_{aw,m,n,i}$ for a range of flow conditions (see table 8-6) having air volume fractions between 0.07% and 9.7%. Comparison of the mean errors $\bar{e}_{aw,n}$ in $\rho_{aw,m,n,i}$ obtained using the VDMS with model-1 and model-2 respectively showed significant reduction in $\bar{e}_{aw,n}$ for flows with air volume fraction less than 10%. Also, the overall mean error $\bar{e}_{aw,t}$ value in $\rho_{aw,m,n,i}$ obtained using the VDMS with model-2 across the flow conditions with less than 10% air volume fraction showed a 39% reduction of $\bar{e}_{aw,t}$ from -0.21% to -0.11% when compared with $\bar{e}_{aw,t}$ value obtained using the VDMS with model-1 for the same flow conditions.

10.2 Novel Features and Contribution to Knowledge

The research work presented in this thesis has made the following contribution to knowledge in the area of density and mean volume fraction measurement.

- A novel non-invasive densitometry system to measure fluid density in single phase and multiphase flows have been designed and developed. The device has been successfully tested for vertically upward pipe flows. A notable attractiveness of this device is that it does not require a radioactive source and it is relatively inexpensive and accurate.
- The mean errors and standard deviation of the errors in the predicted densities obtained using the VDMS for (i) "water only" flows were 0.07% and 0.01% respectively (ii) solids-in-water flows were -0.21% and 0.33% respectively and (iii) air-in-water flows with less than 10% air volume fraction were -0.21% and 0.25% respectively. The mean errors and standard deviation of the errors obtained from these experiments can be related to the VDMS accuracy and repeatability.
- The novel densitometry system developed can also be used to measure mean phase volume fraction in homogenous two phase flows. The device was successfully used to measure mean volume fraction of the dispersed air phase and solids phase in air-in-water flows and solids in water flows respectively.
- Two novel density prediction models were developed, using the vibration characteristics of a mechanical system, to predict the density in single phase or multiphase pipe flows. Both density prediction models have been implemented in the signal processing scheme developed for the densitometry system.
- A novel signal processing technique using the DFT technique was developed to implement the density prediction models. The signal processing technique uses the DFT technique to compute the peak force $|F_{max}|$ amplitude, peak displacement $|X_{max}|$ amplitude, the forcing

frequency ω and the phase difference θ between the displacement and force signals which are in turn used to compute the density measurement parameters $\hat{a}$ and $\hat{b}$ required in the density prediction model.

- A computer based control system was developed to ensure the VDMS could be operated at its optimal frequency and also to provide online mixture density measurement. The control system was developed using LabVIEW and have been used in the experiments involving air-in-water flows in this research.
- A bench test rig and bench testing technique have been developed and used to obtain the densitometry system calibration constants.
- A mathematical model for estimating the value of the coupling stiffness constant between a pipe and the pipe contents have been developed and this model was used in the air-in-water flow experiments to obtain relatively accurate estimates of the coupling stiffness constants for flows with less than 10% air volume fractions.

10.3 Recommendation for further work

The results obtained from the current research and the conclusions reached suggest a number of investigations that could be considered for further work. These recommendations are given below;

- Since the densitometry system meter constant β is influenced by the mass distribution of the multiphase mixture any error in β can increase the modelling errors in the predicted density result. It is therefore recommended that β should be obtained in a dynamic flow using the actual fluids with which the VDMS is to be used. Additionally, a quick, reliable and repeatable method for obtaining β in such dynamic flow loop should be developed.
- The optimal frequency range at which the densitometry system is operated can be extended by improving the flexibility properties of the sensing pipe (i.e. by using a sensing pipe with low stiffness constant). A more flexible pipe will ensure measurable deflections can be

obtained at frequencies further away from the system resonant frequency. Other options are to use a more accurate and sensitive displacement sensor and a force actuator with higher capacity, although these options may increase the cost of the VDMS construction and also its power requirements.

- It is also recommended that the method for estimating the mixture coupling stiffness K_2 between the sensing pipe and the air-in-water mixture needs further investigation to accurately evaluate this property in greater detail.
- Generally, the reference instruments in the flow loop at the University of Huddersfield that were used in the current research performed well. However, it is suggested that improvements are required in the separation unit included in the gravimetric measurement system used to obtain solids and water volumetric flow rates in solids-in-water flows.
- The densitometry system can be combined with an electromagnetic flow meter EMF to measure the phase volumetric flow rates in two phase flows where the continuous phase is a conducting fluid. The VDMS will provide the mixture density of the flow and hence the volume fractions of the phases while the EMF will be used to measure the velocity of the continuous phase.
- Commercial development of the VDMS could be undertaken as a low cost, relatively accurate densitometery system that is safe to use and which poses no risks to personnel or the environment.

References

1. Muhamedsalih, Y. M., *Two-phase flow meter for determining water and solids volumetric flow rate in vertical and inclined solids-in-water flows*, in *School of Computing and Engineering*. 2014, University of Huddersfield: Huddersfield.
2. Leeungculsatien, T. and Lucas, G. P., *Measurement of velocity profiles in multiphase flow using a multi-electrode electromagnetic flow meter*. Flow Measurement and Instrumentation, 2013. **31**(Supplement C): p. 86-95.
3. Wehrs, D. *Detection of plugged impulse lines using statistical process monitoring technology*. 2006. Available from: http://www2.emersonprocess.com/siteadmincenter/pm%20rosemount%20documents/3051s%20plugged%20line%20detection_white%20paper_dec06.pdf. Retrieved 10/03/2016
4. Alloui, T. *10 worst issues affecting instruments in oil and gas facilities-part 1: Pressure transmitters*. 2015. Available from: https://www.linkedin.com/pulse/10-worst-issues-affecting-instruments-oil-gas-part-tahar. Retrieved 04/04/2017
5. Tuvnel *Impulse lines for differential-pressure flow meters*. 2010. Available from: http://www.tuvnel.com/_x90lbm/Impulse_Lines_for_Differential-Pressure_Flow_Meters.pdf. Retrieved 12/03/2016
6. Iaea, *Regulations for the safe transport of radioactive material*, Agency, I.a.E., Editor. 2012.
7. Hauptmann, P., *Ultrasonic density measurement with acoustic reference path*, in *Sensor and Measurement technology*. 2003.
8. Bjorndal, E., Froysa, K.-E., and Engeseth, S.-A., *A novel approach to acoustic liquid density measurements using a buffer rod based measuring cell.* IEEE Transactions on Ultrasonics, Ferroelectronics and Frequency control, 2008. **55**(8): p. 1794-1808.
9. Falcone, G., Hewitt, G. F., and Alimonti, C., eds. *Multiphase flow metering : Principles and application*. 1st ed. Developments in petroleum science. Vol. 54. 2009, Elsevier: Oxford. 47-108.
10. Pietro-Fiorentini. *Multiphse flow measurement*. 2014; Available from: file:///C:/Users/u1075971/Desktop/PHD/LIBRARY/Pietro%20Fiorentini%20Multiphase%20flow%20meter.pdf.
11. Framo-Engineering *Framo multiphase flow meters phasewatcher vx*. 2003. Available from: http://imistorage.blob.core.windows.net/imidocs/99123p001%20framo%20multiphase%20flowmeters%20-%20phasewatcher%20vx.pdf. Retrieved 12/03/2016
12. Onesubsea *Onesubsea phasewatcher subsea multiphase and wet gas flow meter with vx technology*. 2013. Available from: https://www.onesubsea.com/~/media/Files/onesubsea/brochures/phasewatcher.pdf. Retrieved 12/03/2016
13. Zhou, J., *Flow patterns in vertical air/water flow with and without surfactant*, in *The School of Engineering* 2013, University of Dayton
14. Cory, J., *The measurement of volume fraction and velocity profiles in vertical and inclined multiphase flows*, in *School of Computing and Engineering*. 1999, University of Huddersfield: Huddersfield.
15. Hewitt, G. F. and Hall-Taylor, N. S., *Annular two-phase flow*. 1970, Oxford: Pergamon Press.
16. Spedding, P. L., Woods, G. S., Raghunathan, R. S., and Watterson, J. K., *Vertical two-phase flow: Part i: Flow regimes.* Chemical Engineering Research and Design, 2008. **76**(5): p. 612-619.
17. Bratland, O., *Multiphase flow assurance*. 2013.
18. Kippax, V. *Mempulse mbr system vs traditional mbr systems*. 2011; Available from: http://www.thembrsite.com/wp-content/uploads/2013/11/MemPulse_aeration_configs_cj.gif. Date accessed:20/10/2016.
19. Peker, S. M. and Helvaci, S. S., *Solid-liquid two pahse flow*. 1st ed. 2011, NL: Elsevier Science.
20. Garic´-Grulovic, R. V., Grbavcˇ Ic´, Z. E. B., and Arsenijevic´, Z. L., *Heat transfer and flow pattern in vertical liquid–solids flow.* Powder Technology, 2004. **145**: p. 163-173.

21. H.H.Hu, *Direct simulation of flows of solid-liquid mixtures.* International Journal of Multiphase Flow, 1996. **22**(2): p. 335-352.
22. Koos, V. and Lardere, J. a. D. *Environmental management in oil and gas exploration and production*. 1997. Available from: http://www.ogp.org.uk/pubs/254.pdf. Retrieved 22/04/2016
23. Tiab, D. and Donaldson, E., *Petrophysics: Theory and practice of measuring reservoir rock and fluid transport properties*. 2004, Elsevier.
24. Norman, H. *Nontechnical guide to petroleum geology, exploration, drilling and production*. 2012. 113-124. Available
25. Devold, H., *Oil and gas production handbook: An introduction to oil and gas production, transport, refining and petrochemical industry*. 2013.
26. Teeic. *Oil and gas production activities*. 2016; Available from: http://teeic.indianaffairs.gov/er/oilgas/activities/act/index.htm. Date accessed:10/05/2016.
27. Allioli, F., Cretoiu, V., Mauborgne, M.-L., Evans, M., Griffiths, R., Haranger, F., Stoller, C., Murray, D., and Reichel, N., *Formation density from a cloud, while drilling*, in *Oilfield review*. 2013.
28. Reichel, N., Evans, M., Allioli, F., Mauborgne, M.-L., Nicoletti, L., Haranger, F., Laporte, N., Stoller, C., Cretoiu, V., El-Hehiawy, E., and Rabrei, R. *Neutron-gamma density(ngd): Principles, field test results and log quality control of a radioisotope-free bulk density measurement*. in *SPWLA 53rd Annual logging Symposium*. 2012. Cartagena, Colombia.
29. Azar, J. J. and Samuel, R. G., *Drillings engineering*. 2007, PenWell Corportation: Tulsa, US.
30. Geehan, T. and Mckee, A., *Drilling mud: Monitoring and managing it.* Oilfield Review, 1989. **1**(2): p. 41-52.
31. Bloys, B., Davis, N., Smolen, B., Bailey, L., Fraser, L., and Hodder, M., *Designing and managing drilling fluid.* Oilfield Review, 1994. **6**(2): p. 33-43.
32. Moore, P. L., *Drilling practices manual*. 1986, PenniWell Books: Oklahoma.
33. Emerson, *Introduction to drilling fluids monitoring*. 2012.
34. G.Falcone, Hewitt, G. F., Alimonti, C., and B.Harrison, *Multiphase flow metering: Current trends and future developments.* Society of Petroleum Engineers, 2001. **71474**: p. 1-13.
35. Berthold *Density, concentration and solids content: Non contacting measurement*. 2014. Available
36. Mun, T. C., *Production of polyenthylene using gas fluidized bed reactors.* 2003.
37. Kissin and Yury, V., *Polyethylene - end-use properties and their physical meaning*. 2013, Hanser Publishers.
38. Gabriel, L. H., *History and physical chemistry of hdpe*.
39. Kažys, R. and Rekuvienė, R., *Viscosity and density measurement methods for polymer melts.* ULTRASOUND, 2011. **66**(4).
40. Abu-Zahra, N. H., *Measuring melt density in polymer extrusion processes using shear ultrasound waves.* The International Journal of Advanced Manufacturing Technology, 2004. **24**(9): p. 661-666.
41. Endress+Hauser *Density measurement for quality monitoring and process control*. 2012. Available from: www.endress.com. Retrieved 10/12/2016
42. Sadeghbeigi, R., *Fluid catalytic cracking handbook*. 2012, Elsevier: Oxford.
43. Valentine, J. *Micro motion meters used to close the material balance for a refiner's fluid catalytic cracking process*. 2004. Available from: http://www2.emersonprocess.com/siteadmincenter/PM%20Micro%20Motion%20Documents/Fluidized-Catalytic-Crakcer-WP-00521.pdf. Retrieved 10/12/2016
44. Khandalekar, P. D., *Control and optimization of fluidized catalytic cracking process* in *CHEMICAL ENGINEERING* 1993, Texas Tech University.
45. W.H.O, *Bulk density and tapped density of powders*, in *International pharmacopoeia*. 2012.
46. Ansel, H. C., *Pharmaceutical calculations*. 13th ed. 2010, Philadelphia: Lippincott Williams & Wilkins.
47. Thomas, S. *Measuring solutions for the pharmaceutical industry from anton paar*. 2013. Available from: http://www.selectscience.net/product-news/measuring-solutions-for-the-pharmaceutical-industry-from-anton-paar/?artID=28206. Retrieved 10/12/2016

48. Azom *Maximizing solid dose production using accurate bulk density measurement*. 2013. Available from: http://www.azom.com/article.aspx?ArticleID=8060. Retrieved 10/12/2016
49. Azom *Precise test for computing bulk density in solid dose tablet manufacture*. 2015. Available from: http://www.azom.com/article.aspx?ArticleID=11648. Retrieved 10/12/2016
50. Sahoo, P. K. *Pharmaceutical technology: Tablets*. 2007. Available
51. Palou, A., Cruz, J., Blanco, M., Tomas, J., Rios, J. D. L., and Alcala, M., *Determination of drug, excipients and coating distribution in pharmaceutical tablets using nir-ci*. Journal of Pharmaceutical Analysis, 2011. **2**(2): p. 90-97.
52. Siemens *Process instrumentation and analytics: Food and beverage industry*. 2012. Available from: www.siemens.com/sensors/food-beverage. Retrieved 10/12/2016
53. Olaniran, A. O., Maharaj, Y. R., and Pillay, B., *Effects of fermentation temperature on the composition of beer volatile compounds, organoleptic quality and spent yeast density*. Journal of Biotechnology, 2011.
54. Yokogawa *Automatic and continuous monitoring of the beer fermentation process (with a liquid density meter)*. 2011. Available from: http://web-material3.yokogawa.com/AN10T01K01-01E.pdf. Retrieved 29/11/2016
55. Rudolph Research *Measuring alcohol concentration for proof by measuring the density of alcohol*. 2016. Available from: http://rudolphresearch.com/wp-content/uploads/2014/08/Measuring-Alcohol-Concentration.pdf.
56. Anton-Paar *Determination of the alcohol concentration of alcoholic beverages*. 2008. Available Retrieved 19/12/2016
57. Anton-Paar *Sugar inversion and brix in soft drinks: Process application note*. Available
58. Mettler Toledo *Food and beverages analysis*. 2009. Available from: http://us.mt.com/dam/labdiv/campaigns/food2012/downloads/sugar_guide_en.pdf. Retrieved 21/11/2016
59. Anton-Paar *Density measurement in dairy industry*. 2009. Available from: http://www.mep.net.au/foodlab/FL_5/MEP_DMA35_dairy.pdf. Retrieved 10/12/2016
60. Molteberg, D. and Hoibo, O., *Development and variation of wood density, kraft pulp yield and fibre dimensions in young norway spruce (picea abies)*. Wood and science technology, 2006. **40**(3): p. 173-189.
61. Pecora, J. E., Ruiz, A., and Soriano, P., *Minimization of the wood density variation in pulp and paper production*. INFOR, 2007. **45**(4): p. 187-196.
62. Mercangoz, M. and Doyle, F. J., *Model-based control in the pulp and paper industry*. IEEE control systems magazine, 2006: p. 30-39.
63. Berthold-Technologies *Solutions for pulp and paper production: Mass flow, density measurement, level and moisture measurement*. 2016. Available
64. Charbucinski, J. *Nucleonic gauges in the australian mining and exploration industries*. 35-48. Available from: http://www.iaea.org/inis/collection/NCLCollectionStore/_Public/31/024/31024450.pdf. Retrieved 10/12/2016
65. Paterson, A. J. C., *High density slurry and paste tailings, transport systems -paterson*, in *International Platinum Conference*. 2004.
66. Endress+Hauser-Australia-Pty-Ltd *Optimising thickener efficiency*. Sustainability matter, 2009. Available from: http://www.sustainabilitymatters.net.au/content/wastewater/article/optimising-thickener-efficiency--1370645427. Retrieved 10/12/2016
67. Webster, J. G., ed. *The measurement, instrumentation, and sensors handbook*. Density measurement, ed. Eren, H. 1999, CRC Press LLC: Florida. 563-576.
68. Gillum, D. R., *Industrial pressure,level and density measurement*. 2009, ISA: Newyork City.
69. Liptak, B. G., *Instrument engineers handbook*, in *Process Measurement and Analysis*. 2003, CRC Press: Washington. p. 809-864.
70. Kuroki, H., *How did archimedes discover the law of bouyancy by experiment?* Front Mech. Eng., 2016. **11**(1): p. 26-32.
71. Boyes, W., ed. *Instrumentation reference book*. 4th ed. 2010, Elsevier: Oxford. 135-143.

72. Boyes, W., ed. *Instrumentation reference book*. 2009, Butterworth Heinemann.
73. Godwin, A. R. H., ed. *Measurement of the thermodynamic properties of single phases*. 1st ed. Experimental thermodynamics. Vol. VI. 2003, Elsevier: London. pp127-225.
74. Bjorndal, E., *Acoustic measurement of liquid density with applications for mass measurement of oil*. 2007, University of Bergen, Norway: Bergen.
75. Wagner, W., Brachthauser, K., Kleinrahm, R., and Losch, H. W., *A new, accurate single sinker densitometer for temperatures from 233 to 523k at pressures up to 30mpa*. International Journal of Thermophysics, 1995. **16**(2): p. 399-411.
76. Wagner, W. and Kleinrahm, R., *Densimeters for very accurate density measurements of fluids over large ranges of temperature, pressure, and density*. Metrologia, 2004. **41**: p. 24-39.
77. Greene, G. J., *Densitometer*, Office, U.S.P., Editor. 1968, UGC instruments, Inc, Houston.
78. Wagner, W., Brachthauser, K., Kleinrahm, R., and Losch, H. W., *A new,accurate single sinker densitometer for temperatures from 233 to 523k at pressures up to 30mpa*. International Journal of Thermophysics, 1995. **16**(2): p. 399-411.
79. Anderson, N. A., *Instrumentation for process measurement and control*. Chilton Company: Pennsylvania.
80. Dyer, S. A., ed. *Survey of instrumentation and measurement*. 2001, John Wiley & Sons, Inc: New York.
81. Batey, R. H., *A non-nuclear density meter & mass flow system for dredging slurries*. Western Dredging Association (XXXII) Technical conference and Texas A&M University 2012. **43 Dredging Seminar**.
82. Eren, H., *Density measurement*. 1999, CRC Press LLC.
83. Jones, E. B., *Instrument technology*, in *On-line analysis instruments*. 1976, Butterworths: London.
84. He, P. and Zheng, J., *Acoustic dispersion and attenuation measurement using both transmitted and reflected pulses*. Ultrasonics, 2001. **39**: p. 27-32.
85. Gysling, D. L., *Fluid density measurement in pipes using acoustic pressures*. 2005, Google Patents.
86. Difoggio, R., *Method and apparatus for an acoustic pulse decay density determination*, Patent, U.S., Editor. 2006, Baker Hughes Inc: US.
87. Kazys, R., Sliteris, R., Rekuviene, R., Zukauskas, E., and Mazeika, L., *Ultrasonic technique for density measurement of liquids in extreme conditions* Sensors, 2015. **15**: p. 19393-19415.
88. Puttmer, A., Hauptmann, P., and Henning, B., *Ultrasonic density sensor for liquids*. IEEE Transactions on Ultrasonics, Ferroelectronics and Frequency control, 2000. **47**: p. 85-92.
89. Bamberger, J. A. and Greenwood, M. S., *Measuring fluid amd slurry density and solid concentration non-invasively*. Ultrasonics, 2004. **42**: p. 563-567.
90. Cheeke, N. and David, J., *Fundamentals and applications of ultrasonic waves*. 2002, CRC Press LLC.
91. Piche, L., *Ultrasonic density measurement*, Patent, U.S., Editor. 1987, Canadian patents and DEvelopment limited: US.
92. Rowell, W., Dzbikowicz, Z., Janssebs-Maenhout, G., and Howell, J., *Ultrasonic densitometer for non-invasive infield detection of illicit liquids in suspect containers* 2009, Institute for the Protection and security of the Citizen: Italy.
93. Sinha, D. N., *Noninvasive method for determining the liquid level and density inside of a container*. 2000, The Regent of the University of Califonia: United State.
94. Sinha, D. N., *Non-invasive fluid density and viscosity measurement*. 2012, Los Alamos National Security, LLC.
95. Pope, N. G., Viers, K. D., and Claytor, T. N., *Fluid density and concentration measurement using noninvasive insitu ultrasonic resonance interferometry*, in *Ultrasonics Symposium*. 1992, The Regents of the University of California, office of technology transfer.
96. Greenwood, M. S. and Lail, J. C., *Ultrasonic fluid densitometry and densitometer*, Patent, U., Editor. 1998.
97. M.S.Greenwood, *Ultrasonic fluid densitometer for process control*, Patent, U., Editor. 2000, Battelle Memorial Institute.

98. Chakhlov, V. L., Cheprasov, A. I., and Shaverin, N. V., *Measurements of the density of petroleum products and their mixtures by the ultrasonic method.* Russian Journal of Nondestructive Testing, 2002. **38**(6): p. 472-476.
99. Higuti, R. T. and Adamowski, J. C., *Ultrasonic densitometer using a multiple reflection technique.* IEE Transanctions on Ultrasonic, Ferroelectric, and Frequency Control, 2002. **49**(9): p. 1260-1268.
100. Hoche, S., Hussein, M. A., and Becker, T., *Ultrasound-based density determination via bugger rod techniques: A review.* Journal of sensors and sensors systems, 2013(2): p. 103-125.
101. Park, H.-S. and Chung, H.-H., *Design and application of a single-beam gamma densitometer for void fraction measurement in a small diameter stainless steel pipe in a critical flow condition.* NUCLEAR ENGINEERING AND TECHNOLOGY, 2007. **39**(4): p. 349-358.
102. Hewitt, G. F., *Measurement of two-phase flow parameters*. 1978, Academic Press: New York.
103. Golgoun, S. M., Sardari, D., Sadeghi, M., Ebrahimi, M., Aminipour, M., and Davarpanah, M. R., *Combined backscatter and transmission method for nuclear density gauge*, in *EPJ*. 2015, EDP sciences.
104. Shivaramu, Priyada, P., Margret, M., and Ramar, R., *Intercomparison of gamma ray scattering and transmission techniques for fluids interface level and density determination*, in *5th Pan American Conference for NDT* 2011: Cancun, Mexico.
105. Kulik, A., Esin, A. J., Baturin, N., Sen, S., and Brosseau, M. G., *Density profile measurement by detecting backscattered radiation with position-sensitive detector*. 2013, Thermo Fisher Scientific Inc.
106. Tjugum, S. A., Johansen, G. A., and Holstad, M. B., *The use of gamma radiation in fluid flowmeasurements.* Radiation Physics and Chemistry, 2001. **61**: p. 797-798.
107. Khorsandi, M., Feghhi, S. a. H., Salehizadeh, A., and Roshani, G. H., *Developing a gamma ray fluid densitometer in petroleum products monitoring applications using artificial neural network.* Radiation Measurements, 2013. **59**: p. 183-187.
108. Nelson, G. and Relly, D. *Gamma-ray interactions with matter*. 27-42. Available from: http://www.lanl.gov/orgs/n/n1/panda/00326397.pdf. Retrieved 05/1/2017
109. Ball, A. J., Solomon, C. J., and Zarnecki, J. C., *The response of gamma backscatter density gauges to spatial inhomogeneity ± an extension of the single scattering model.* nUCLEAR INstruments and Methods in Physics Research, 1998. **140**: p. 449-462.
110. Tjugum, S. A., Johansen, G. A., and Holstad, M. B., *The use of gamma radiation in fluid flow measurements.* Radiation physics and chemistry, 2001. **61**: p. 797-798.
111. Tjugum, S. A., *X-ray based densitometer for multiphase flow measurements*, Patent, U.S., Editor. 2012, Roxar flow measurement As: Norway.
112. Mcchesney, M., *Shock tube beta-ray densitometer*. JOURNAL OF ScIENTIFlC INSTRUMENTS, 1961. **38**: p. 496-500.
113. Rousseau, J. C., Czerney, J., and Riegel, B., *Viod fraction measurements during blowdown by neutron absorption or scattering methods*, in *European Two-phase flow meeting*. 1976: Erlangen.
114. Banerjee, S., *Two-phase flow void fraction measurements using neutron beams.* Trans. Am. Nucl. Soc., 1980. **34**: p. 799-802.
115. The Secretary of State, *Ionisng radiations regulations 1999 (irr99)*, in *1999 No3232*, Safety, H.A., Editor. 1999, 4620711001.
116. Sharaf, S., Da-Silva, M., Hampel, U., Zippe, C., Beyer, M., and Azzopard, B., *Comparison between wire mesh sensor and gamma densitometry void measurements in two-phase flows.* Measurement Science and Technology, 2011. **22**(10): p. 1-13.
117. Schlieper, G., *Principles of gamma ray densitometry.* Metal power report, 2000. **55**(12): p. 20-23.
118. Peyvandi, R. G., Tootkaleh, S. R., Islamirad, S. Z., and Hosseinzadeh, R., *Influence of temperature on the performance of gamma densitometer*. Instruments and Experimental Techniques, 2014. **57**(6): p. 667-670.
119. Kratky, O., Leopold, H., Stabinger, H., and Angew, Z., *Dichtemessung an flüssigkeiten und gasen auf 10-6g/m3 bei 0,6 cm3 pro-benvolumen.* Physik, 1969. **27**: p. 273-277.
120. Atkinson, D. I. H. and Stansfeld, J. W., *Improvements in single vibrating tube transducers*, Office, E.P., Editor. 1989, Schlumberger: United Kingdom.

121. Atkinson, D. I. H. and Rudkin, M. J., *Fluid transducer*, Office, E.P., Editor. 1993, Schlumberger: United Kingdom.
122. Stemme, E., Ekelof, J., and Nordin, L., *Measuring liquid density with a turning fork transducer*. IEEE Transactions on Instrumentation and Measurements, 1983. **32**: p. 434.
123. Drobkov, V., Melnikov, V., and Shustov, A., *Fluid density measurement device*. 2014, Nest International N.V.
124. Singh, S. K., *Industrial instrumentation & control*. 2nd ed. 2003, New Delhi: McGraw-Hill.
125. Storm-Jr, B. H., Masino, J., Proett, J., and Pelletier, M. T., *Single tube densitometer*. 2004, Halliburton Energy Services, Inc.: United State America.
126. Janssen, S., *Device for measuring the density of a fluid*, Patent, U.S., Editor. 1973, Campagnie Des Compteurs.
127. Smith, J. E., *Parallel path coriolis mass flow rate meter*, Patent, U.S., Editor. 1985, Micro Motion Inc: US.
128. Headrick, D. C., *High pressure resonant vibrating tube densitometer*, Patent, U.S., Editor. 2009, Halliburton Energy Services, Inc.
129. Pelletier, M. T., Proett, M. A., Bruce H. Storm, J., Birchak, J. R., and Ritter, T. E., *Downhole densitometer*. 2002, Halliburton Energy Services, Inc.
130. Donzier, E., *Density and viscosity sensor and measuring method*. 2013: United Kingdom.
131. Zheng, D., Shi, J., and Fan, S., *Design and theoretical analysis of a resonant sensor for liquid density measurement.* Sensors, 2012. **12**(6): p. 7905-7916.
132. Lorefice, S. and Sardi, M., *Calibration of a reference vibrating tube densimeter*, in *XX IMEKO World Congress*. 2012: Republic of Korea.
133. Bouchot, C. and Richon, D., *An enhanced method to calibrate vibrating tube densimeters.* Fluid Phase Equilibria, 2001. **191**: p. 189-208.
134. Lampreia, I. M. S. and Castro, C. a. N. D., *A new and reliable calibration method for vibrating tube densimeters over wide ranges of temperature and pressure.* Journal of Chemical Thermodynamics, 2011. **43**: p. 537-545.
135. Woolger, C. *Invar-nickel iron alloy*. 1996; Available from: http://www.nickel-alloys.net/invar_nickel_iron_alloy.html. Date accessed:12/10/2016.
136. Gysling, D. L., *An aeroelastic model of coriolis mass and density meters operating on aerated mixtures.* Flow Measurement and Instrumentation, 2007. **18**(2): p. 69-77.
137. Billingham, J., *Modelling the response of vibrating element density meter in two-phase mixture.* Journal of Fluid mechanics, 1997. **340**: p. 343-360.
138. Gysling, D. L. and Banach, T., *Enhanced density measurement using speed of sound augmented coriolis meters*, in *ISA*. 2004: Houston.
139. Ltd, S. M. *Solartron density transducers*. 2002. Available
140. Zheng, D., Shi, J., and Fan, S., *Design and theoretical analysis of a resonant sensor for liquid density measurement*

Sensors, 2012. **12**: p. 7905-7916.
141. Patten, T., *Keep metering problems from bubbling up*, in *Chemical Processing*. 2005, Putman.
142. Zamora, M. and Henry, M. P., *An fpga implementation of a digital coriolis mass flow metering drive system.* IEEE Transactions on industrial electronics, 2008. **55**(7): p. 2820-2831.
143. Kelly, S. G., *Mechanical vibrations theory and applications*. 2012, Cengage Learning: Stamford.
144. Schmitz, T. L. and Smith, K. S., *Mechanical vibrations: Modeling and measurement*. Springer: New York.
145. Sinha, A., *Vibration of mechanical systems*. 2010, Cambridge University Press: New York.
146. Silva, C. W. D., *Vibration: Fundamentals and practice*. 2000, CRC Press: New York.
147. Stokanovic, V. and Kozic, P., *Vibrations and stability of complex beam systems*. 2015, Springer International Publishing.
148. Rao, S. S., *Mechanical vibrations*. 2011, Pearson Education Inc.: New Jersey.
149. Morrison, J. L. M. and Crossland, B., *An introduction to mechanics of machines*. 1970: Longman Group Limited. 237-291.

150. Sundararajan, D., *Discrete fourier transform: Theory, algorithms and applications*. 2001, World Scientific Publicshing Co.: Singapore.
151. Lyons, R. G., *Understanding digital signal processing*. 2004, Pearson Education Ltd: London.
152. Chaparro, L. F., *Signals and systems using matlab*. 2010: Academic Press.
153. Solidworks. 2016; Available from: http://www.solidworks.co.uk/. Date accessed:10/05/2016.
154. Brauer, J. R., *Magnetic actuators and sensors*. 2006, John Wiley & Sons, Inc.,: New Jersey. p. 83-100.
155. Geeplus, *Voice coil motor*. 2015.
156. Piersol, A. G. and Paez, T. L., eds. *Harris' shock and vibration handbook*. 6th ed. 2010, McGraw Hill: New York.
157. Geeplus, *Vm6340 datasheet*. 2014.
158. Lcm-Systems-Ltd. *Dce stainless steel stud type tension and compression load cell datasheet*. 2015; Available from: http://www.lcmsystems.com/DCE_Stainless_Steel_Stud_Type_Tension_abd_Compression_Load_Cell. Date accessed:19/01/2017.
159. Rdpe-Group. *D5 & d6 lvdt displacement transducer datasheet*. 2014; Available from: http://www.rdpe.com/uk/d5-d6.pdf. Date accessed:14/08/2016.
160. *Linear variable differential transformer*. Available from: http://www.te.com/usa-en/industries/sensor-solutions/insights/lvdt-tutorial.html. Date accessed:14/08/2016.
161. ; Available from: https://www.ukas.com/services/accreditation-services/laboratory-accreditation-isoiec-17025/calibration/.
162. *Https://www.Zeiss.Co.Uk/metrology/products/systems/bridge-type-cmms/contura.Html*. Date accessed:03/07/2017.
163. Solidworks. *Linear static analysis*. 2016; Available from: http://help.solidworks.com/2012/English/SolidWorks/cworks/IDH_Analysis_Background_Linear_Static_Analysis.htm?id=98fbbe618ac14f6ca1cfb77b4cfea4f9#Pg0&ProductType=&ProductName=. Date accessed:10/05/2016.
164. Timoshenko, S., *Strength of materials*. 2nd ed. 1955: Van Nostrand. 134-208.
165. *Https://support.Office.Com/en-gb/article/define-and-solve-a-problem-by-using-solver-5d1a388f-079d-43ac-a7eb-f63e45925040*. Date accessed:22/09/2016.
166. Lucas, G. P., Cory, J., Waterfall, R. C., Loh, W. W., and Dickin, F. J., *Measurement of the solids volume fraction and velocity distributions in solids–liquid flows using dual-plane electrical resistance tomography*. Flow Measurement and Instrumentation, 1999. **10**(4): p. 249-258.
167. Able *Nt industrial type turbine flowmeter*. 2010. Available from: https://able.co.uk/media/2013/12/able-turbine-datasheet.pdf.
168. S.Baz-Rodriguez, Aguilar-Corona, A., and Soria, A., *Rising velocity for single bubbles in pure liquids.* Revista Mexicana de Ingenieria Quimica, 2012. **11**: p. 269-278.
169. Romeo, E., Royo, C., and Monzón, A., *Improved explicit equations for estimation of the friction factor in rough and smooth pipes.* Chemical Engineering Journal, 2002. **86**(3): p. 369-374.
170. National Instruments *Signal generation in labview*. 2016. Available from: http://www.ni.com/white-paper/4087/en/.
171. *Designing pid controllers with pid tuner*. Available from: https://uk.mathworks.com/help/control/getstart/designing-pid-controllers-with-the-pid-tuner-gui.html. Date accessed:08/01/2017.
172. National Instrument. *Hardware integration with ni labview*. 2013; Available from: http://www.ni.com/white-paper/14555/en/. Date accessed:1/10/2016.
173. Thermo-Scientific, *Thermo scientific sarasota fd910 and fd950 liquid density meters: For use in general industrial and chemical applications*. 2015.
174. Emerson Process Management, *Micro motion® technical overview and specification summary*. 2016.
175. Seeger, M., *Coriolis flow measurement in two phase flow*. IEE Computing and Control Engineering, 2005.

176. Grumski, J. T. and Bajura, R. A., *Performance of a coriolis-type mass flow meter in the measurement of two-phase (air–liquid) mixtures.* ASME Fluids Engineering Division, 1984. **17**.
177. Lui, R. P., Fuent, M. J., Henry, M. P., and Duta, M. D., *A neural network to correct mass flow errors caused by two phase flow in a digital coriolis mass flow meter.* Flow Measurement and Instrumentation, 2001. **12**: p. 53-63.
178. Westerhof, N., Stergiopulos, N., and Noble, M. I. M., *Law of laplace*, in *Snapshots of hemodynamics: An aid for clinical research and graduate education*. 2010, Springer US: Boston, MA. p. 45-48.
179. Juhl, K. A., *Aerated flow measurement and modelling of a coriolis flow meter*, in *Department of Energy Technology*. 2014, Aalborg University.
180. Jacobs, T. *Ultrasonic drilling mud measurement to improve drilling*. Journal of Petroleum technology. Available from: http://www.spe.org/jpt/img/posts/p9224/ma3_768.jpg.
181. National Instruments. *Ni usb-6211 device specification*. Available from: http://www.ni.com/pdf/manuals/375195c.pdf. Date accessed:10/08/2017.

Appendices

Appendix A: MATLAB CODE TO COMPUTE DFT'S OF THE MEASURED DISPLACEMENT AND FORCE SIGNALS

```
clear all
clc
%.....................................................................
% -MATLAB code to compute DFT of sampled displacement data
t = xlsread('C:\Users\u1075971\Desktop\try1.xlsx',1,'a2:a65537');% read sampled time data
y = xlsread('C:\Users\u1075971\Desktop\try1.xlsx',1,'g2:g65537');% read sampled lvdt data
N=length(y);% compute the number of data samples N
dt=t(2)-t(1);%compute the sample period dt
fs=1/dt;  % compute the sampling frequency
%create a for loop to compute the ensemble average of the complex DFT of the displacement
for k=1:N/2;  % set values of k up to the Nyquist frequency
   XAB(k)=0; % set the initial value of of the complex DFT of the displacement XAB(k)=0
End
% Ensemble averaging of the complex DFT of the displacement data
for k=1:10; % Set number of averaging to be done
fn = fs/2;  % compute Nyquist frequency of data sample
f=linspace(0,fn,N/2);% create a row vector for frequency up to the Nyquist frequency
X = fft(y)/N; % Compute DFT of sampled displacement data
XA =X(1:N/2);% Extract DFT of displacement data up to the Nyquist freq
XAB=XAB+XA;
XABb=XAB/k ; % Perform averaging
XAR=real(XABb);%Extract real part of the DFT of displacement signal
XAI=imag(XABb);%Extract Img part of the DFT of displacement signal
subplot(2,2,1);
plot(f,XAR); %plot the real part of the DFT component of displacement signal against frequency
title('DFT of Displacement signal-Real part');
ylabel('X(f)_{Re}(mm)');
xlabel('Frequency(Hz)')
subplot(2,2,2);
plot(f,XAI);%plot the imaginary part of the DFT component of displacement signal against
frequency
title('DFT of Displacement signal-Img part');
ylabel('X(f)_[180](mm)');
xlabel('Frequency(Hz)');
end
hold on
%% -MATLAB code to compute DFT of sampled Force data
y1 = xlsread('C:\Users\u1075971\Desktop\try1.xlsx',1,'h2:h65537');% read sampled load cell data
```

```
N=length(y1);% compute Number of data samples
%create a for loop to compute the new values for the complex DFT of the force signal for k values
for k=1:N/2 ;  % set values of k up to the Nyquist frequency
   XAB1(k)=0; % set initial value of the complex DFT of the force data,XAB1(k)=0
end
for k=1:10;
fn = fs/2;  % Nyquist frequency
f = linspace(0,fn,N/2);% create a row vector for frequency up to the Nyquist frequency
X1 = fft(y1)/N; % Compute DFT of sampled force data
XA1=X1(1:N/2);%Extract DFT of sampled force signal up to the Nyquist freq
XA1=transpose(XA1);
XAB1=XAB1+XA1;
XAB1b=XAB1/k ; % Perform ensemble averaging
XAR1=real(XAB1b);%Extract the real part of the DFT of sampled force data
XAI1=imag(XAB1b); % Extract the Img part of the DFT of sampled force data
subplot(2,2,3);
plot(f,XAR1); % plot the real part of sampled force data against frequency
title('DFT of Force signal-Real part');
ylabel('P(f)_{Re}(N)');
xlabel('Frequency(Hz)')
subplot(2,2,4);
plot(f,XAI1);%plot the imaginary part of sampled force data against frequency
title('DFT of Force signal-Img part');
ylabel('P(f)_[180](N)');
xlabel('Frequency(Hz)');
end
hold off
```

Appendix B

METHOD FOR CONVERTING A DISCRETE SIGNAL FROM CARTESIAN FORM TO POLAR FORM

For the discrete sinusoidal signal represented in Cartesian form as given below,

$$x(t_r) = C\,cos(t_r) + jD\,sin(t_r)$$ Equation B-1

where $C\cos(t_r)$ is the real part of the discrete sinusoid and $D\sin(t_r)$ is the imaginary part of the discrete sinusoid. The constants C and D in equation b-1 can be defined in terms of the amplitude and phase angle of the sinusoid as follows,

$$C = A\,cos\,\theta$$ Equation B-2

$$D = A\,sin\,\theta$$ Equation B-3

where A and θ respectively, are the amplitude and phase angle of the discrete sinusoid. For a discrete sinusoid where the real and imaginary parts of the signal are known, he amplitude and phase can be computed as follows,

$$A = \sqrt{C^2 + D^2}$$ Equation B-4

$$\theta = tan^{-1}\left(\frac{D}{C}\right)$$ Equation B-5

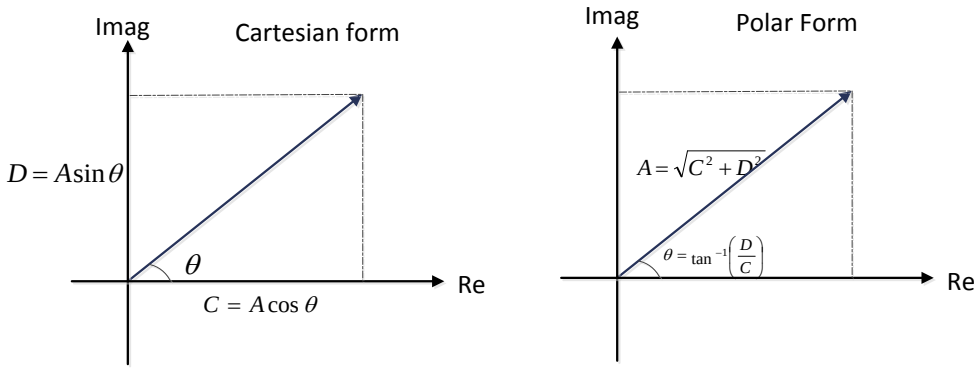

Figure B-1: Cartesian form and polar form representation of a sinusoid

Appendix C

LVDT DATASHEET

5. SPECIFICATION

Supply		±6 to ±18V dc or 12 to +36V dc at 50mA typical
Voltage Output –	dual supply	±4±10V into 2kΩ } Refer to
	single supply	±4V to ±10V into 10kΩ } Fig.4
	Regulation	0.5mV/V typical
Current Output-	both supplies	4-20mA into 100/550Ω max. Overload internally limited to 30mA max. This is an active output that should not be connected to any external power supply as this will damage unit.
	Regulation	1µA/V typical
Oscillator Output		1V rms. at 5kHz standard. 25mA maximum.
Oscillator Temperature Coefficient		0.005%/°c typical
Demodulation		Synchronous
Amplifier Gain		x.07 to x500 in 8 ranges with fine control interpolation
Zero Range		±5V minimum
Linearity		0.1% of full scale
Input Resistance		130k ohm differential
Zero Stability	Voltage Output	0.002% of FS typical/°C (optimum at ±10V o/p)
	Current Output	0.005% of FS typical/°C
Gain Stability	Voltage Output	0.005% of FS typical/°C (optimum at ±10V o/p)
	Current Output	0.01% of FS typical /°C
Bandwidth		Dc to 500Hz (flat)
Noise -Voltage Output		5mV peak to peak typical 10µA peak to peak typical
EMC Specification		When subjected to radiated electro-magnetic energy (as EN61000-4-3) an additional error can occur at certain frequencies:

Field Strength	Typical Maximum Error
10V/m	1.5%
3V/m	0.1%

Temperature Range	-10°C to +60°C
Dimensions	98 x 64 x 34 mm (3.9 x 2.5 x 1.5 inches)
Weight	260 g (0.57 lb)
Gland Cable Diameter	3 to 6.5 mm (0.12 to 0.26 inches)
Seals	IP65 specification

14

Figure C-1: Specification of the LVDT signal conditioning circuitry [159]

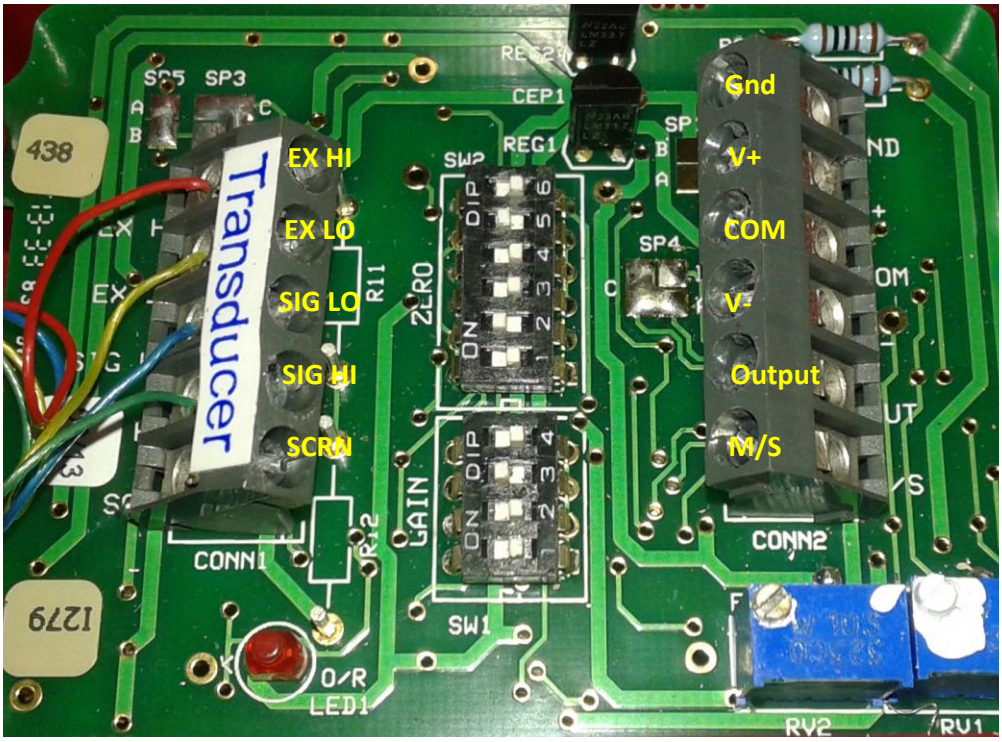

Figure C-2: Picture of the LVDT signal conditioning circuitry [159]

Appendix D

LOAD CELL ABRIDGED DATA SHEET [158]

Specification

Rated load (Newtons)	100, 250, 500 750
(Kilonewtons)	1, 2.5, 5, 7.5, 10, 25, 50
Proof load	150% of rated load
Ultimate breaking load	>300% of rated load
Maximum side load	10% of rated load
Output	1.5mV/V at rated load (nominal)
Non-Linearity	<±0.25% of rated load
Non-Repeatability	<±0.1% of rated load
Excitation voltage	10vdc recommended, 15vdc maximum
Bridge resistance	350Ω (25kN and 50kN: 700Ω)
Insulation resistance	>500MΩ @500vdc
Operating temperate range	-20 to +70°C
Compensated temperature range	-10 to +50°C
Zero temperature coefficient	<±0.01% of rated load/°C
Span temperature coefficient	<±0.01% of rated load/°C
Environmental protection level	IP65
Connection type	2 metres 4-core screened PVC cable
Wiring connections	+ve supply: Red -ve supply: Blue +ve signal: Green -ve signal: Yellow

Figure D-1: load cell abridged data sheet [158]

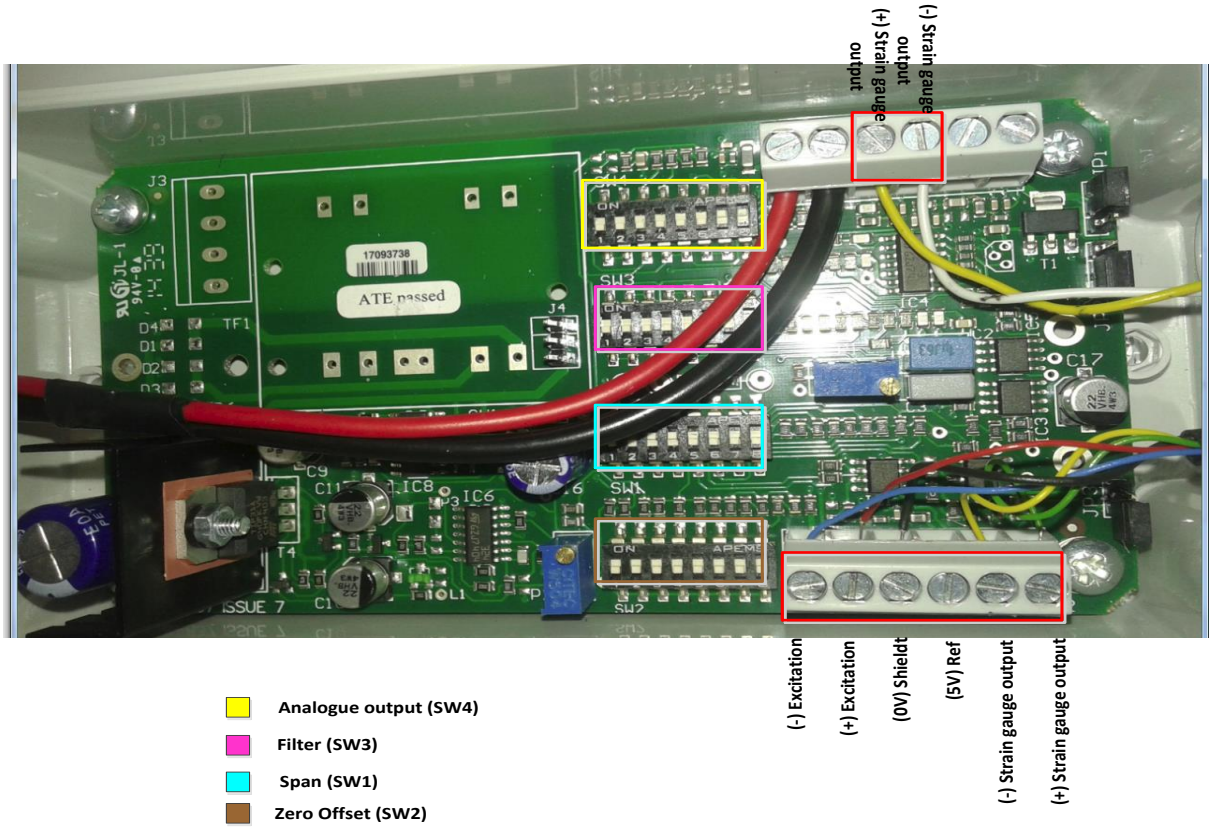

Figure D-2: Picture of load cell signal conditioning circuitry [158]

Appendix E

NI USB-6211 DEVICE SPECIFICATION

Analog Input

Number of channels	8 differential or 16 single ended
ADC resolution	16 bits
DNL	No missing codes guaranteed
INL	Refer to the *AI Absolute Accuracy* section
Sample rate	
Single channel maximum	250 kS/s
Multichannel maximum (aggregate)	250 kS/s
Minimum	0 S/s
Timing accuracy	50 ppm of sample rate
Timing resolution	50 ns
Input coupling	DC
Input range	±0.2 V, ±1 V, ±5 V, ±10 V
Maximum working voltage for analog inputs (signal + common mode)	±10.4 V of AI GND

CMRR (DC to 60 Hz)	100 dB
Input impedance	
Device on	
AI+ to AI GND	>10 GΩ in parallel with 100 pF
AI- to AI GND	>10 GΩ in parallel with 100 pF
Device off	
AI+ to AI GND	1,200 Ω
AI- to AI GND	1,200 Ω
Input bias current	±100 pA
Crosstalk (at 100 kHz)	
Adjacent channels	-75 dB
Non-adjacent channels	-90 dB
Small signal bandwidth (-3 dB)	450 kHz
Input FIFO size	4,095 samples
Scan list memory	4,095 entries
Data transfers	USB Signal Stream, programmed I/O
Overvoltage protection for all analog input and sense channels	
Device on	±30 V for up to two AI pins
Device off	±20 V for up to two AI pins
Input current during overvoltage condition	±20 mA maximum/AI pin

Analog Output

Number of channels	2
DAC resolution	16 bits
DNL	±1 LSB
Monotonicity	16 bit guaranteed
Maximum update rate	
1 channel	250 kS/s
2 channels	250 kS/s per channel
Timing accuracy	50 ppm of sample rate
Timing resolution	50 ns
Output range	±10 V
Output coupling	DC
Output impedance	0.2 Ω
Output current drive	±2 mA
Overdrive protection	±30 V
Overdrive current	2.4 mA
Power-on state	±20 mV
Power-on glitch	±1 V for 200 ms
Output FIFO size	8,191 samples shared among channels used
Data transfers	USB Signal Stream, programmed I/O
AO waveform modes	Non-periodic waveform, periodic waveform regeneration mode from onboard FIFO, periodic waveform regeneration from host buffer including dynamic update
Settling time, full-scale step, 15 ppm (1 LSB)	32 µs
Slew rate	5 V/µs

Device Pinout

Figure 3. NI USB-6211 Pinout

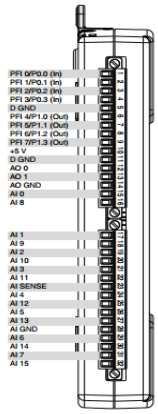

Figure E-3: NI USB-6211 device pinouts [181]

Appendix F

COMPUTER BASED VDMS CONTROL SYSTEM

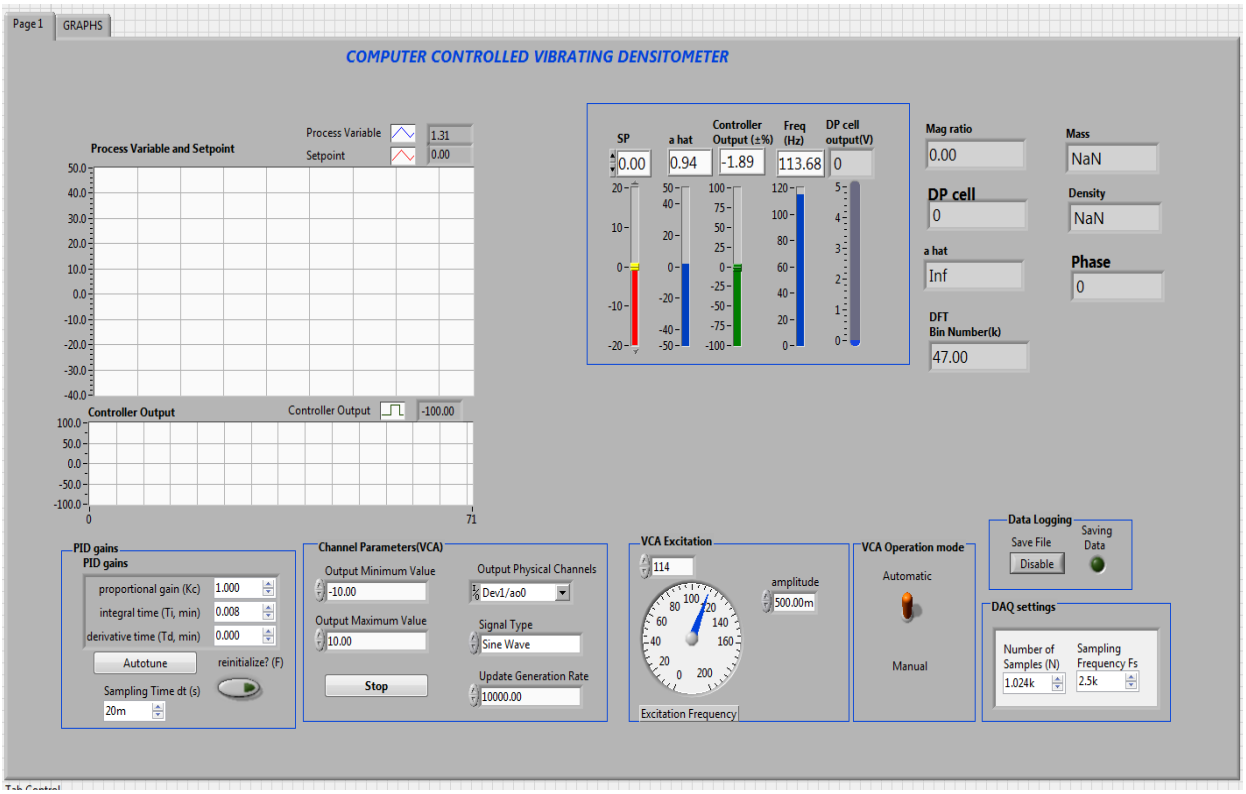

Figure F-1: User interface of the computer based VDMS control system

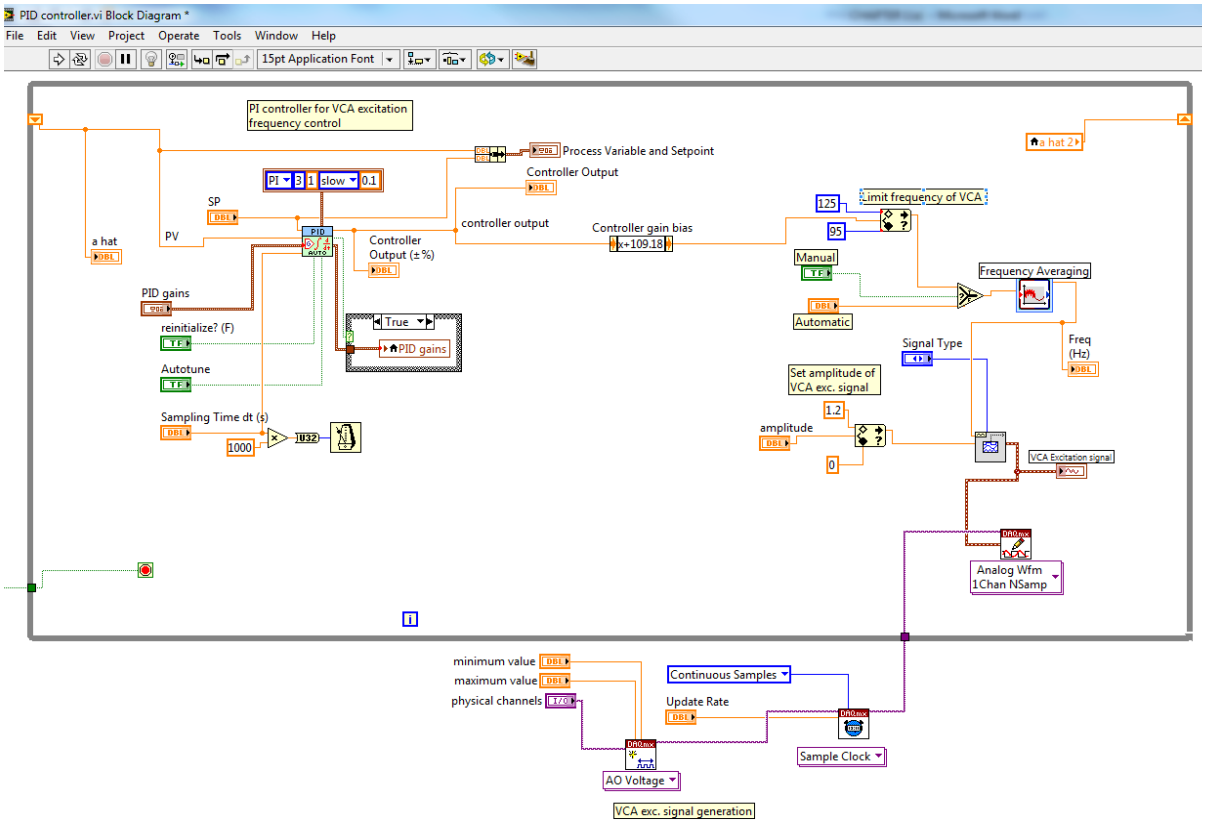

Figure F-2: Frequency control and VCA excitation signal generation program routines used in computer based VDMS control system

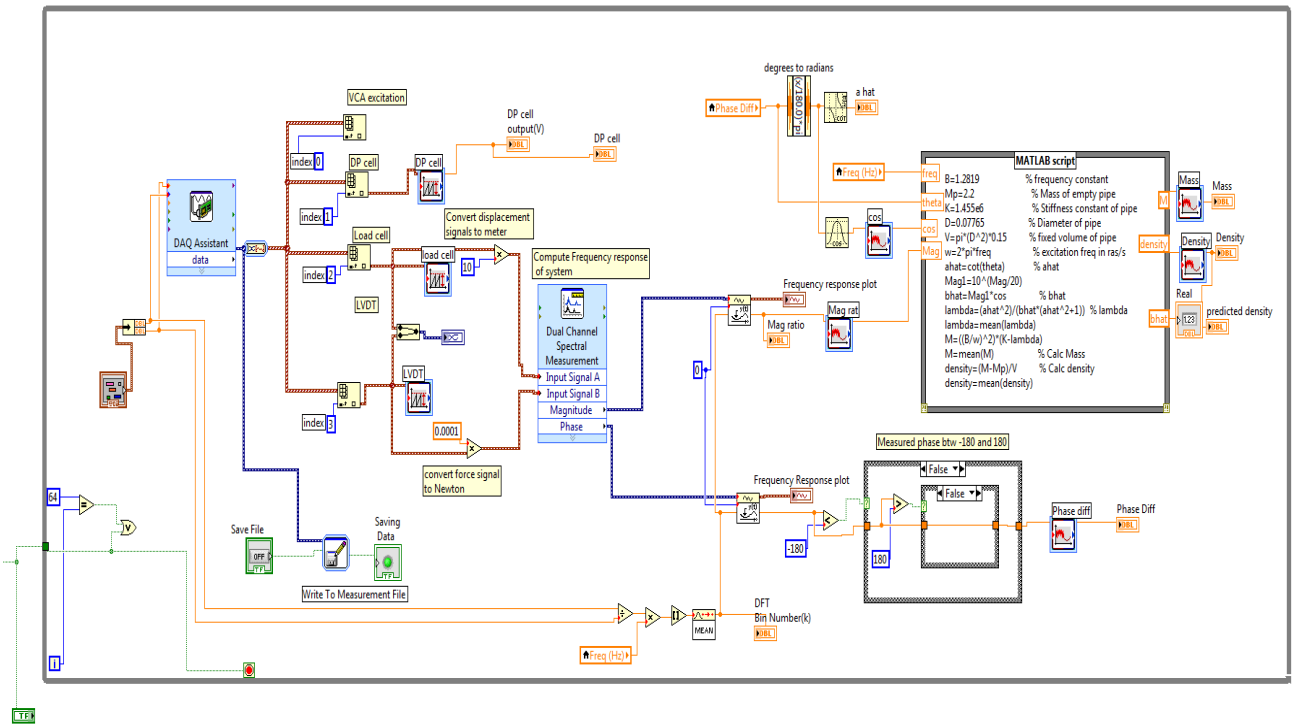

Figure F-3: Data acquisition and online signal processing technique program routines used in computer based VDMS control system

Appendix G

MATHEMATICAL MANIPULATION TO OBTAIN $\hat{m}_2$ FROM equation 9-28

From equation 9-28,

$$\hat{b} = \frac{1}{\left[\left\{K_1 + \frac{-\omega^2 K_2(\hat{m}_1 + \hat{m}_2) + \omega^4 \hat{m}_1 \hat{m}_2}{K_2 - \omega^2 \hat{m}_2}\right\}\left(1 + \frac{1}{\hat{a}^2}\right)\right]} \quad \text{Equation 9-1}$$

Since the measurement parameters $\hat{a}$ and $\hat{b}$ can be obtained from the force and displacement phasors, these variables are rearranged as given in Equation below.

$$\hat{b}\left(1 + \frac{1}{\hat{a}^2}\right) = \frac{1}{\left[\left\{K_1 + \frac{-\omega^2 K_2(\hat{m}_1 + \hat{m}_2) + \omega^4 \hat{m}_1 \hat{m}_2}{-\omega^2 \hat{m}_2 + K_2}\right\}\right]} \quad \text{Equation G-1}$$

The sensing pipe stiffness constant K_1 can also be obtained from static bench testing as described in section 5.3. Thus, equation G-1 can be rearranged as follows,

$$K_1 - \frac{1}{\hat{b}\left(1 + \frac{1}{\hat{a}^2}\right)} = \left\{\frac{-\omega^2 K_2(\hat{m}_1 + \hat{m}_2) + \omega^4 \hat{m}_1 \hat{m}_2}{-\omega^2 \hat{m}_2 + K_2}\right\} \quad \text{Equation G-2}$$

Furthermore, the forcing frequency ω of the system can be obtained from the DFT of the force or displacement signal, hence equation G-2 can be simplified as shown below.

$$\frac{1}{\omega^2}\left\{-K_1 + \frac{1}{\hat{b}\left(1 + \frac{1}{\hat{a}^2}\right)}\right\} = \left\{\frac{-K_2(\hat{m}_1 + \hat{m}_2) + \omega^2 \hat{m}_1 \hat{m}_2}{-\omega^2 \hat{m}_2 + K_2}\right\} \quad \text{Equation G-3}$$

Also, the terms in the right hand side of equation G-3 can be simplified as follows,

$$\left\{\frac{-K_2(\hat{m}_1 + \hat{m}_2) + \omega^2 \hat{m}_1 \hat{m}_2}{-\omega^2 \hat{m}_2 + K_2}\right\} = -\hat{m}_1 - \frac{K_2 \hat{m}_2}{K_2 - \omega^2 \hat{m}_2} \quad \text{Equation G-4}$$

Equation G-4 can then be combined with the simplified expression given in equation G-3 and the resulting expression is obtained as.

$$\frac{K_2 \hat{m}_2}{K_2 - \omega^2 \hat{m}_2} = \frac{1}{\omega^2}\left\{K_1 - \frac{1}{\hat{b}\left(1 + \frac{1}{\hat{a}^2}\right)}\right\} - \hat{m}_1 \quad \text{Equation G-5}$$

From equation G-5 the term $\frac{K_2 \hat{m}_2}{K_2 - \omega^2 \hat{m}_2}$ is simplified further by dividing through with $K_2 \hat{m}_2$,

Equation G-6

$$\frac{1}{\frac{1}{\hat{m}_2}-\frac{\omega^2}{K_2}}=\left[\frac{1}{\omega^2}\left\{K_1-\frac{1}{\hat{b}\left(1+\frac{1}{\hat{a}^2}\right)}\right\}-\hat{m}_1\right]$$

The mass $\hat{m}_2$ of the sensing pipe contents can then be made the subject of formula in the expression given in equation G-6. This is obtained as,

Equation G-7

$$1=\left(\frac{1}{\hat{m}_2}-\frac{\omega^2}{K_2}\right)\left[\frac{1}{\omega^2}\left\{K_1-\frac{1}{\hat{b}\left(1+\frac{1}{\hat{a}^2}\right)}\right\}-\hat{m}_1\right]$$

From equation G-7, $\hat{m}_2$ is obtained as shown below.

Equation G-8

$$1+\frac{\omega^2}{K_2}\left[\frac{1}{\omega^2}\left\{K_1-\frac{1}{\hat{b}\left(1+\frac{1}{\hat{a}^2}\right)}\right\}-\hat{m}_1\right]=\frac{1}{\hat{m}_2}\left[\frac{1}{\omega^2}\left\{K_1-\frac{1}{\hat{b}\left(1+\frac{1}{\hat{a}^2}\right)}\right\}-\hat{m}_1\right]$$

Equation 9-30

$$\hat{m}_2=\frac{\left[\frac{1}{\omega^2}\left\{K_1-\frac{1}{\hat{b}\left(1+\frac{1}{\hat{a}^2}\right)}\right\}-\hat{m}_1\right]}{1+\frac{\omega^2}{K_2}\left[\frac{1}{\omega^2}\left\{K_1-\frac{1}{\hat{b}\left(1+\frac{1}{\hat{a}^2}\right)}\right\}-\hat{m}_1\right]}$$